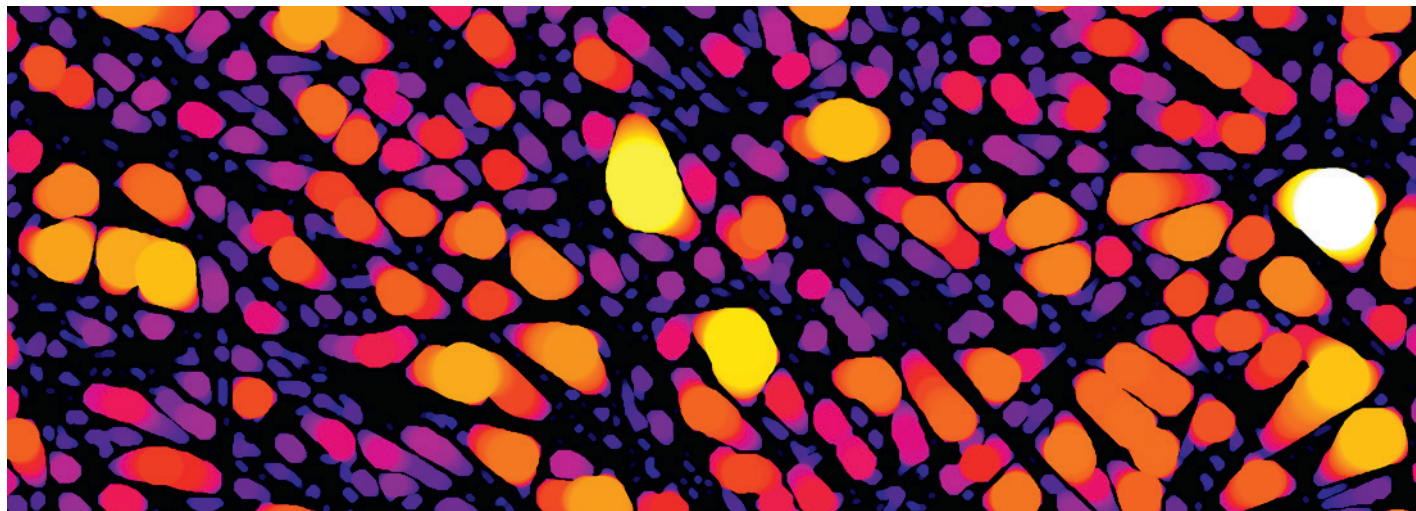


PAUL SCHERRER INSTITUT



# Annual Report 2015

Electrochemistry Laboratory

**Cover**

X-ray tomography image of gas diffusion layer for fuel cells with color coded pore size distribution.

PAUL SCHERRER INSTITUT



# Annual Report 2015

Electrochemistry Laboratory

**Paul Scherrer Institut**  
Electrochemistry Laboratory  
5232 Villigen PSI  
Switzerland

**Secretary**  
Phone +41 56 310 29 19  
Fax +41 56 310 44 15

**Hardcopies of this report  
are available from**

Cordelia Gloor  
cordelia.gloor@psi.ch  
Paul Scherrer Institut  
5232 Villigen PSI  
Switzerland



A full version of this report is also available on the web  
<http://www.psi.ch/lec>

**Publisher**

Electrochemistry Laboratory  
Paul Scherrer Institut  
5232 Villigen PSI  
Switzerland

**Editorial Team**

Cordelia Gloor/Peter Lutz  
Lorenz Gubler  
Thomas J. Schmidt

**Printing**

Paul Scherrer Institut

ISSN 1661-5379

DOI: 10.3929/ethz-a-007047464

PSI Electrochemistry Laboratory :: Annual Report 2015

© Paul Scherrer Institut

## CONTENTS

3	Editorial		
4	The Electrochemistry Laboratory at a Glance		
6	The Swiss Competence Center for Energy Research – Heat & Electricity Storage		
9	<b>SCIENTIFIC ACHIEVEMENTS 2015</b>		
	FUEL CELLS & ELECTROLYSIS – SYSTEMS & DIAGNOSTICS		
10	Impact of the active area on cold start capability of fuel cells		
12	Water/gas distribution in electrolyzers with gas diffusion layers of different pore sizes		
14	Optical imaging characterization for optimization of an evaporatively cooled Polymer Electrolyte Fuel Cell (PEFC)		
16	Combined neutron imaging and small angle scattering study of water management in fuel cells		
18	Operating a HT-PEFC with hydrogen from a formic acid reformer		
19	Water evaporation in partially saturated gas diffusion layers		
21	The influence of phosphoric acid loss on HT-PEFC performance and long term durability		
23	H <sub>2</sub> /O <sub>2</sub> PEFC system in an uninterruptible power supply application with extended autonomy time		
24	Analysis of image quality of reduced scan time operando X-ray tomographic microscopy of PEFC		
26	Why does electrolyzer performance not care about pressure?		
	FUEL CELLS & ELECTROLYSIS – MATERIALS		
28	Open circuit voltage hold test of radiation grafted membranes		
29	ETFE based e-beam grafted membranes for fuel cells with GMA comonomer		
31	Ionic conductivity of radiation grafted membranes doped with phosphoric acid		
33	Tuning the wettability of gas diffusion layers		
	BATTERIES – MATERIALS		
36	Synthesis and characterization of carbon with tuneable porosity		
38	Poly(ethylene oxide)-coated double-layer separator for lithium-sulfur battery		
40	Polysulfides confined! New design of the separator for enhanced lithium sulfur cell performance		
41	Mitigation of the voltage fade of high-energy lithium nickel-manganese-cobalt oxides (HE-NCM) as cathodes for lithium-ion batteries		
43	Comparative study of Ni <sub>2</sub> SnP as negative electrode for Na-ion and Li-ion batteries		
45	CuSbS <sub>2</sub> vs. Sb <sub>2</sub> S <sub>3</sub> as negative electrode for Li-ion and Na-ion batteries		
47	Cr-Nasicon Li <sub>3</sub> Cr <sub>2</sub> (PO <sub>4</sub> ) <sub>3</sub> /C as a new cathode material with two redox couples		
49	LiFe <sub>x</sub> Mn <sub>1-x</sub> methylene diphosphonate (x = 0, 0.2, 0.5, 0.8, 1.0): mixed transition metal diphosphonate positive electrode materials for Li-ion batteries.		
51	Effect of carbon additive on the cycling stability of the Li-S electrodes with high sulfur loading		
	BATTERIES – DIAGNOSTICS		
54	H <sub>2</sub> and PO <sub>F</sub> <sub>3</sub> gases as markers for the formation of ROH species in carbonate electrolytes		
55	Contribution of 5 V cathodes to the surface layer formation at the anodes in Li-ion batteries		
57	Impact of FEC on HE-NCM half- and full-cells investigated by online electrochemical mass spectrometry		
58	XPS surface analysis of silicon thin films as model anode for Li-ion batteries		
60	Ageing phenomena in high-voltage aqueous supercapacitors investigated by <i>in situ</i> gas analysis		
62	Transition metal dissolution in the Li <sub>1+x</sub> (Ni <sub>a</sub> Co <sub>b</sub> Mn <sub>1-a-b</sub> ) <sub>1-x</sub> O <sub>2</sub> /graphite full-cell		
64	Improved cylindrical cell for operando neutron powder diffraction of LiNi <sub>0.5</sub> Mn <sub>1.5</sub> O <sub>4</sub> vs. graphite		

- 66 Combining operando X-ray diffraction and operando Raman spectroscopy to understand the reaction mechanisms of  $\text{LiNi}_{0.5}\text{Mn}_{1.5}\text{O}_4$  in Li-ion batteries
- 68 A bulk investigation of  $\text{CoSn}_2$  and  $\text{FeSn}_2$  as anodes for Na-ion batteries
- 70 PEEM spectroscopy: a promising technique to study the surface of commercial-like battery electrodes at the nanoscale
- 72 Microstrain and its impact on the electrochemical performance of  $\text{LiNi}_{0.80}\text{Co}_{0.15}\text{Al}_{0.05}\text{O}_2$
- 73 Impact of operating conditions on the cycling performance of all-vanadium redox flow batteries

#### ELECTROCATALYSIS & INTERFACES

- 76 Activity and stability of high surface area  $\text{IrO}_2$
- 77 Oxygen evolution reaction on  $\text{Ba}_{0.5}\text{Sr}_{0.5}\text{Co}_{0.8}\text{Fe}_{0.2}\text{O}_3$  perovskite
- 78 Compared stability of carbon-supported Pt-nanoparticles vs. unsupported Pt-aerogels for  $\text{O}_2$ -reduction in PEFCs
- 80 Pt coverage of model catalysts: active vs inactive area and its consequences on ORR limiting currents in a flow cell
- 82 Oxide supported Pt catalyst for low temperature polymer electrolyte fuel cell application in MEAs: performance and stability
- 84 The non-uniformly accessible wall-jet electrode: a numerical study of the current distribution and its implications for inhomogeneously covered model electrodes
- 86 Carbon surface modification by introduction of oxygen defects – influence on vanadium (V) reduction activity
- 88 Fundamental study towards the development of perovskite ( $\text{LaMO}_3$ ) oxygen evolution catalysts in alkaline environment
- 90 Bimetallic Pt-Ni aerogels for electrocatalysis of the oxygen reduction
- 92 Use and misuse of Pourbaix diagrams: Instability of metal oxide catalysts for oxygen evolution
- 93 Physical and electrochemical investigation of strained Pt model catalysts prepared by pulsed laser deposition

## 95 THE ELECTROCHEMISTRY LABORATORY

### FACTS & FIGURES

- 96 Structure 2015
- 97 Personnel 2015
- 100 Dissertations 2015
- 101 Exchange Students, Diploma Theses, Summer Students, Guest Scientists
- 103 Seminar, Invited Speakers
- 105 Awards
- 106 Conferences – Symposia
- 108 Review Activities of the Laboratory
- 110 Industrial Partners
- 111 Documentation
- 111 Project Collaborations with External Partners
- 113 Teaching Activities
- 114 Publications
- 119 Talks
- 124 Patent Applications
- 124 Posters
- 126 Conferences & Workshops Organizations
- 127 Members in External Committees
- 128 Editorial Work

## EDITORIAL



Electrochemical Energy Conversion and Storage are major topics in the quest of a sustainable, environmentally friendly energy system, being it in the industrial, public or mobility sector. PSI's Electrochemistry Laboratory is therefore also a major player in Research & Development of electrochemical energy conversion and storage devices. As Switzerland's largest Electrochemistry R&D unit, the Laboratory is

not only playing this leading role within our own country, but is also internationally very well recognized as one of the leading centers for all topics related to Li-ion batteries, polymer electrolyte fuel cells and water electrolysis.

Since 2014, we also took the responsibility of leading the Swiss Competence Center for Energy Research (SCCER) Heat & Electricity Storage, the virtual Competence Center of 23 academic groups from R&D institutions all over the country. The Center is successfully operated now in its third year and is leaving already its footprints in the Swiss energy research landscape.

In this Annual Report 2015, you will not only find details on PSI's Electrochemistry Laboratory and the SCCER Heat & Electricity Storage, but also some short insights into ongoing projects and activities, summarized in more than 47 short reports authored by our researchers demonstrating some of our contributions to the grand challenge of electrochemical energy storage and conversion. In addition, some key facts and figures from 2015 are given, including a full list of our more than 70 publications and numerous talks demonstrating the leading role PSI's Electrochemistry Laboratory is playing internationally.

For the first time in May 2015, our annual international PSI Electrochemistry Symposium was organized as a joint 2-day event together with the Spring Symposium of the SCCER Heat & Electricity Storage. Our Symposium entitled *Electrochemical Energy Storage – A Key for Future Energy Systems* was one of the most successful events we organized in this series of symposia with almost 200 participants from Europe, demonstrating the great interest in the topic of our research. The internationally well-known speakers (N. Lewis, CalTech; G. Centi, University of Messina; D. Stolten, Research Center Jülich; M. Winter, University of Münster; J.-M. Tarascon, Collège de France) certainly helped to attract this interested audience; details of this event you will find also in this annual report on page 109.

Personally, being at PSI now for five years, I also would like to share with you my own highlight of the past year: In November, my first two PhD students successfully passed their final exam at ETH Zürich. Accompanying and supporting students arriving at PSI after their Master program over the period of a PhD thesis and seeing them leaving as matured scientists is probably one of the most rewarding experiences I had in my academic career. I wish both of them all the best for their future professional life.

At this point it needs to be mentioned that all our projects and results could not have been achieved without the funding we received over the years from industrial partners and the different funding agencies in Switzerland and abroad. We, therefore, would like to take this opportunity to thank all our funding sources hoping to continue our successful collaborations in the years to come.

Thomas J. Schmidt

# THE ELECTROCHEMISTRY LABORATORY AT A GLANCE

## Our Mission

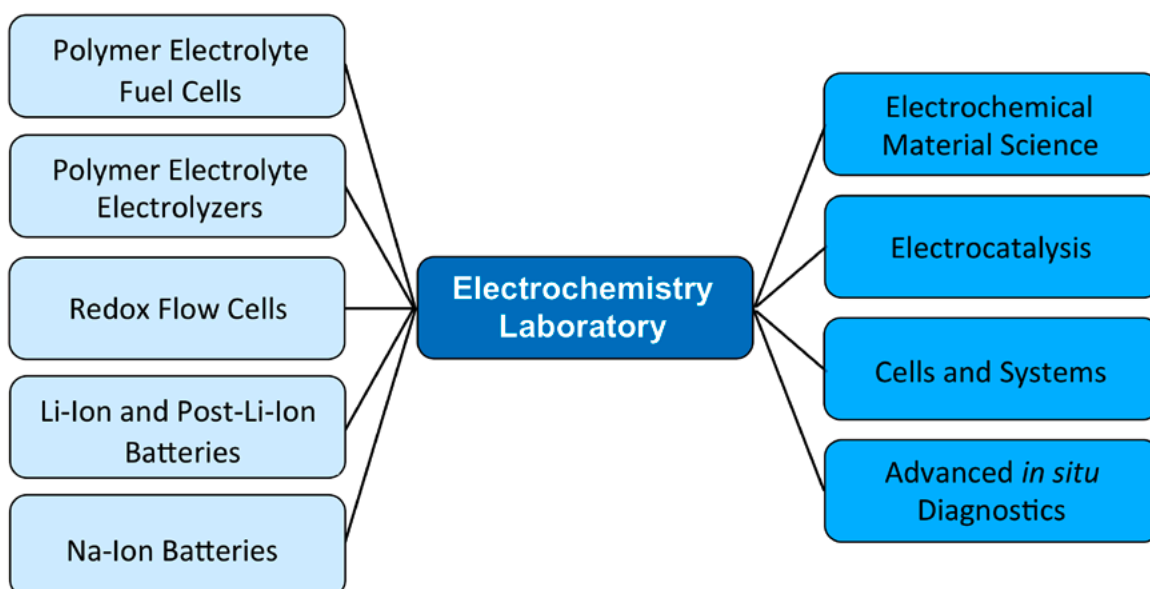
### Advancement of electrochemical energy storage and conversion by

- **developing novel electrochemical materials, cells and devices;**
- **providing insights into electrochemical materials, cells and device properties.**

PSI's Electrochemistry Laboratory is Switzerland's largest Center for Electrochemical Research with around 70 employees. Our mission is to advance the scientific and technological understanding of electrochemical energy storage and conversion specifically in the context of a sustainable energy system, in which renewable energy is required to be stored in secondary batteries or chemicals (as e.g., hydrogen) and (re-)converted into electricity. Our applied fundamental R&D, hence, is focused on devices like secondary batteries – specifically Li-based systems –, polymer electrolyte fuel cells and electrolyzers, respectively.

As a research institute's laboratory we are bridging the gap between fundamental science and applied engineering by combining both academically as well as industrially relevant questions. For all outlined devices we not only develop fundamental understanding of materials on atomic and molecular level (electrochemical materials sciences and electrocatalysis), but also on the applied development of technical cells and devices, e.g., fuel cell systems.

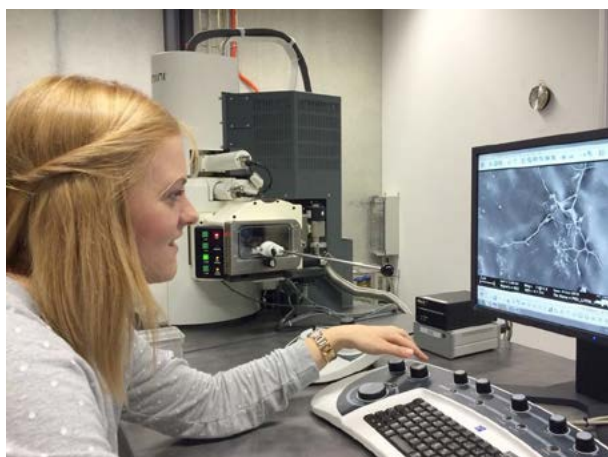
On all technical complexity levels, we are developing and utilizing advanced *in situ* diagnostic tools to gain insights on properties and processes from the nanometer to the centimeter scale, respectively, often making use of PSI's unique large scale facilities.



## Electrochemical Energy Storage

The vision of the Electrochemical Energy Storage Section is the development of the best energy storage system.

We work on rechargeable batteries, mainly lithium based. The scientific goal is a profound understanding of electrochemical processes in complex nonaqueous systems. In particular, of utmost scientific interest are the numerous interactions of all components of electrochemical energy storage systems (batteries, supercapacitors) determining the safety and life time of such systems.



*SEM/EDX technique to probe morphology of battery components.*

The work equally considers the synthesis of novel materials for electrochemical energy storage, the modification of known materials (e.g., carbon) and material characterization, keeping in mind the entire span from basic science to industrial applications. To answer the scientific questions, we develop various sophisticated *in situ* methods for use in the field of nonaqueous solid-state electrochemistry and investigate the physical and electrochemical properties of insertion materials and electrochemical interfaces *in situ*. Also, we do electrochemical engineering work on threedimensional electrodes and characterize industrial batteries and battery systems.

## Electrochemical Energy Conversion

The Electrochemical Energy Conversion Section is focused on the development and in-depth understanding of materials, processes and devices for the conversion of renewable energy into electricity or chemical energy carriers. Especially in the context of a sustainable energy system utilizing hydrogen as an energy carrier and its electrochemical energy conversion is of particular importance.

In this topical context our goal is the in-depth understanding of technologies like Polymer Electrolyte Fuel Cells (PEFC), Polymer Electrolyte Water Electrolyzers (PEWE) and processes like the co-electrolysis of CO<sub>2</sub> and water, respectively.

The R&D strategy involves activities on four pathways:

- system, stack and cell engineering;
- membrane development based on PSI's own radiation-grafting technology and the development of cell components;
- research in electrocatalysis and the reaction kinetics of the important reactions (e.g., the oxygen electrode reactions) for improved understanding of intrinsically limiting factors; and
- the development and application of advanced *in situ* diagnostic tools on stack, cell and component levels including analyses of the electrode-electrolyte interface.



*Fuel cell system testing. Experimental set-up for advanced start/stop investigation.*

# ENERGY STORAGE RESEARCH IN SWITZERLAND

## THE SWISS COMPETENCE CENTER FOR ENERGY RESEARCH (SCCER) HEAT AND ELECTRICITY STORAGE

To stop the threatening climate change, the CO<sub>2</sub> emissions will have to be reduced. The national states apply different approaches. In Denmark and Germany as well as in Switzerland the nuclear phase-out is planned targeting a replacement by renewable energies. The capacity of the renewable energy sources – sun, wind and water – is considered to be sufficient for the energy supply in Switzerland. Yet, storing the electricity from wind and sun is necessary to adapt the production to the consumption.

Jörg Roth, Thomas J. Schmidt

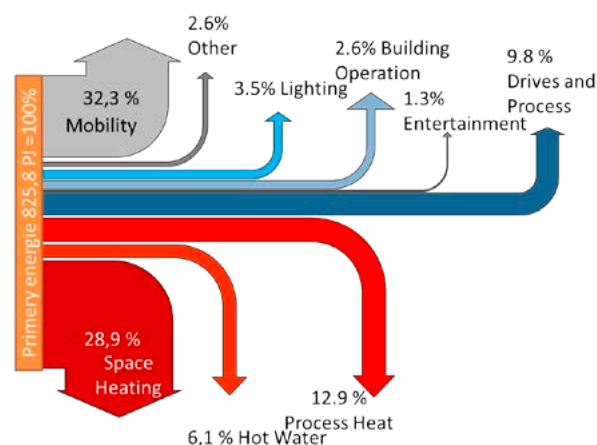
The electricity production from wind and solar energy is by nature subjected to strong temporal fluctuations, which is indispensably connected to their storage ability. Short-term storage in the time frame of minutes to hours as well as long-term seasonal storage is of relevance. In the early stages of the deployment of renewable energies the short-term storage facilities suffice, but with increasing share of renewable energies, seasonal storage facilities become more important. The analysis of the energy use by modern industrial societies shows that half the prime energy is used for heat production (Figure 1), and a third of the heat is used for heating buildings.

Today, commercially available systems for short-term energy storage are batteries, water-based heat storage or pump storage. A great potential and also a necessity still exists in research and development for seasonal energy storage.

The Swiss Competence Center for Energy Research (SCCER) Heat and Electricity Storage is a network of 23 academic groups who contribute to the development of future storage solutions with their individual competences. The scope of the considered technologies comprises the development of lithium and sodium based batteries, the production and storage of hydrogen and low-molecular carbon on water basis and carbon dioxide.

A separate working group is developing heat storage facilities for the use in the industrial as well as the domestic sector on the basis of storage materials for sensible, latent and sorption heat, respectively. To understand the topic in its entirety the different technologies are investigated in the context of a complete system by an interdisciplinary team. This group is focused on the questions of eco-balances, life expectancy, reliability and safety of storage technologies.

The degree of maturity of the investigated technologies ranges from elemental material development to system prototypes with the goal to provide both short- and long-term project results.



Quelle: Analyse des schweizerischen Energieverbrauchs 2000 - 2014 nach Verwendungszwecken BFE 2015; Prognos, TEP, Infras 2015

Figure 1. Primary energy consumption in Switzerland 2014.

### Electrical Energy

The secondary battery is the only possibility to store large amounts of electrical energy for an almost indefinite amount of time. The advantages for the stationary storage are: no moving parts, a single-stage and an almost reversible process, a good scalability due to the modular structure and an unique dynamic response characteristic. The biggest disadvantages are costs, life expectancy and safety. Therefore batteries are suitable for short-term storage (minutes/hours) in terms of renewable energies. The high investment costs demand a high cycle frequency, which can be achieved through peak shaving and frequency compensation.

In case of a massive application of Li-ion technology as a grid energy storage system, an increase of the costs for batteries has to be considered due to potentially increasing raw material prices for lithium and copper (current collector) with rising demand. The increase of mass production, however, will have an compensating effect on the price development (economy of scale).

A long-term goal is the improvement of the actual Li-ion-systems with specific (nano-)structuring of the electrodes and also the development of sodium-ion cells, which exhibit the similar durability, power and capacity as the Li-ion cells. Due to this, stationary battery applications could be more

cost-effective. The materials for anode, cathode and electrolyte, however, cannot be transferred directly from the lithium-sodium batteries enforcing new materials development for Na-ion systems. Last year, first results with a multiple electrochemical cell stack, containing a sodium-vanadium cathode and a cobalt-zinc anode were successfully achieved.

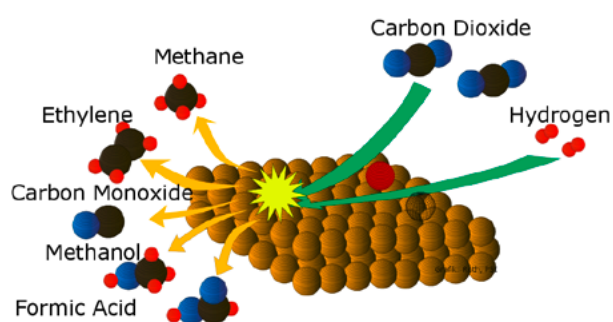


**Figure 2.** Extraction approach for renewable energy sources and raw materials by CO<sub>2</sub> reduction.

## Thermal Energy

Heat storage devices, as well as batteries are able to use the source of energy without the downstream transformation step, which is an advantage for efficiency reasons. At present, heat storage systems are used in industry to increase the overall efficiency of the systems through optimization of the thermal flow. For domestic heat use, solar thermal collectors are integrated for hot water supply and (floor-)heating. Isolated water tanks are often used, which are designed for a storage range from hourly to seasonal storage. These storage tanks are simple and cost effective, but have a low storage density and a low temperature range, which is limited, on the one hand, by the water vapor pressure curve and, on the other hand, by the water freezing point. This is only partially suitable for industrial processes. An alternative are mineral storage materials, that are suitable for temperature ranges between 500 °C to 1000 °C. Molten salt is often used if a combination of heat storage and heat transport is required.

Apart from the heat storage of sensible heat (the temperature of the storage medium changes during the heat transfer, like in a water bath), there also exists latent heat (the storage

medium keeps the temperature, even though heat is transferred, like in melting ice).

A special feature, which is investigated in the Competence Center, is the combination of sensible heat storage with latent heat storage. In this way the best from both systems can be combined. The low costs of sensible heat storage, combined with the constant-temperature transfer of latent heat storage is an interesting economic solution. Especially for the development of latent heat storage for high temperatures (1000 °C) there is a necessity for intensive material development, which is a specialty of the SCCER.

## Chemical Energy

The economic hydrogen production and storage is a challenge which is closely related to the energy transition. Hydrogen is an attractive option due to the variety of ways of production and usage. In the context of production of synthetic fuels, hydrogen is an important raw material for the conversion of CO<sub>2</sub> into high-value chemicals which can be used as current fossil fuels in combustion engines or stored for long periods of time (seasonal). It is very attractive to utilize the surplus of renewably generated electricity to produce hydrogen, due to the fact that the needed raw materials, water and electricity, are cheap.

To date most of hydrogen is produced by thermochemical processes from cost effective fossil raw materials, oil and gas. The hydrogen production based on electrolysis is insignificant due to the presently high costs of electrolyzers.

Within the SCCER a search for precious metal free catalysts for hydrogen production is being conducted for the classical electrolysis as well as for the direct photochemically driven hydrogen production. The long-term vision are solar collectors which can produce hydrogen via photoelectrolysis. Molybdenum sulfate based catalysts are promising candidates. The challenge is to process the material to thin films, without them losing their excellent characteristics.

Besides the hydrogen production also the hydrogen storage is a field which has great development potential due to its gravimetric energy density that is very high (33,3 kWh/g) and three times bigger than the energy density of gasoline. However, the volumetric energy density is low and depends on the storage form (gaseous, 200 bar: 0.53 kWh/l) and is therefore five times

lower than natural gas under the same conditions. The energy density in liquid hydrogen storage is still a factor of three below the one for gasoline. The aim is to store the hydrogen under mild conditions with highest possible storage density. Low molecular organic compounds, e.g., formaldehyde or formic acid, can be extracted by catalytic processes from carbon dioxide and hydrogen and they can just as easily be decomposed. In the context of the SCCER systems are developed to produce and decompose formic acid as hydrogen storage medium that look like a hydrogen battery to the end-user.

One step further is the synthesis of the already mentioned hydrocarbon from  $\text{CO}_2$ , water and (electric) energy. At present this approach is taken by methanation pilot plants. This process is based on the Sabatier reaction and relies on the availability of hydrogen, which is mainly produced by means of electrolysis (in a renewable scenario). Methane is produced on the basis of metal(-oxide) catalysts at temperatures up to  $400^\circ\text{C}$  [1]. The vision of the further development of this idea is to extract hydrocarbons (e.g. methanol) from water and carbon dioxide directly. The approach of the groups within the Competence Center is to examine metal-organic catalysis for  $\text{CO}_2$  reduction as well as the direct electrochemical conversion of  $\text{CO}_2$  and water to methane, ethane and methanol etc. (Figure 2). The advantage of the first approach is the possibility to apply highly selective catalysts under mild process conditions, with a positive effect on the costs and the plant size. The direct electrochemical reduction of  $\text{CO}_2$  is far from the technical implementation, but its feasibility has been demonstrated. The selectivity and the durability of the electrodes are being optimized. On a long-term basis the extraction of basic chemicals from excess energy for the organic-chemical industry should be possible.

## System analysis

All these technologies develop their value only in interplay with the system. Therefore it is necessary to perform a theoretical and practical system analysis with respect to ecological, social and environmental aspects. A good example is the Energy System Integration (ESI) Platform at Paul Scherrer Institut (Figure 3).

Besides working on large scale demonstrators the questions regarding safety analysis, manufacturing processes, especially

for batteries, as well as the study of business models for the energy transition are assessed. It is a known fact that changes in the energy-sector have to be made, because the traditional structures of a central electricity production are under pressure. The classical business model for pump storage does not exist anymore; the running of large-scale inflexible plants is simply not profitable. At the same time there are existing wide legal gaps in Europe, because the term «energy storage» is not defined in the legislation.

As long as the responsibilities of running the storage systems are not clearly assigned to either the consumers or the producers and as long as there is no tariff consent, it is impossible to create real business models. Sound legal security is indispensable to justify investments by private industry in research and development of energy storage technology. To be able to store renewable energy within 15 years, we urgently need to start the research and development now. Research ideas and methods exist, but the engagement to implement them needs to be increased. If the legislative authority decides to close the legal gap, then the industry would be willing to invest into energy storage.

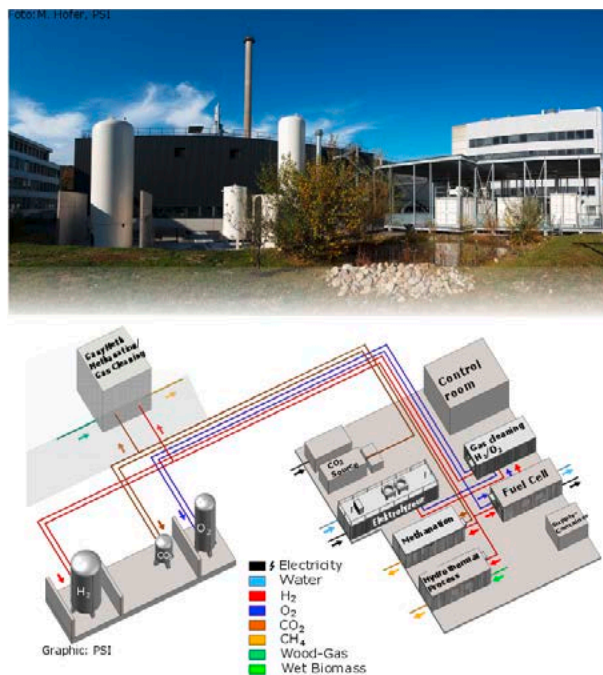


Figure 3. The Energy System Integration (ESI) Platform.

# SCIENTIFIC ACHIEVEMENTS 2015

FUEL CELLS & ELECTROLYSIS –

SYSTEMS & DIAGNOSTICS

## Impact of the active area on cold start capability of fuel cells

J. Biesdorf, P. Stahl<sup>1</sup>, M. Siegart, T.J. Schmidt, P. Boillat

phone: +41 56 310 5727, e-mail: johannes.biesdorf@psi.ch

Polymer electrolyte fuel cells (PEFCs) are a promising candidate to replace fossil fuel based power generators for stationary and mobile applications. However before their successful and profitable commercialization for mass markets, several improvements like durability, performance or the cold start capability need to be performed in order to ensure a reliable operation under real operating conditions.

As has already been reported in previous publications of our group [1], strongly differing explanations regarding the aggregate state of water are reported in literature. The predominant number of publications assumes that all product water produced during the start-up freezes inside the catalyst layer of the cathode. Consequently, the operating time is assumed to be defined by deterministic parameters such as the pore space of the catalyst layer or the water uptake of the membrane. However, these findings were contradicted by experiments which indirectly [1] and directly [2] identified super-cooled water inside the fuel cell.

In literature, the presence of supercooled water was exclusively reported for small scale fuel cells with active areas significantly below 10 cm<sup>2</sup> whereas ice was predominantly identified in large scale fuel cells. Besides differences in the aggregate state, differences in the operating behaviour are reported. Large scale fuel cells show repeatable and short operating times whereas stochastic and long operating times are generally measured with small scale fuel cells. In order to understand the differences between the two regimes, experimental results of subzero isothermal start-up experiments with two different cell sizes of 1 and 50 cm<sup>2</sup> will be presented. Subsequently the experimental results of the small scale fuel cell will be used to predict the freezing behaviour in larger fuel cells with a Monte Carlo simulation.

### Experimental

*Cell designs* – The experiments were performed with two different cell designs. Cell type 1 is a differential fuel cell with an active area of 1 cm<sup>2</sup> operating at high stoichiometries. Details about cell design can be found in ref [3]. Cell type 2 is a 50 cm<sup>2</sup> fuel cell operated with technical stoichiometries. Further details can be found in ref [4]. Both cells were assembled with catalyst coated membranes (CCM) (Primea 5710, Gore Ltd., USA) with Pt-loadings of 0.1 mg<sub>Pt</sub> cm<sup>-2</sup> on the anode and 0.4 mg<sub>Pt</sub> cm<sup>-2</sup> on the cathode side. The GDLs from the SGL Carbon Group Series 24BC were used.

*Operating conditions* – All tests were performed with gas pressures slightly above the atmospheric pressure. The cell flows were set to 0.1 Nl/min on the anode and cathode side for both cell designs which translates into stoichiometries of 140/60 for the 1 cm<sup>2</sup> and 2.8/1.2 for the 50 cm<sup>2</sup>. The isothermal start-up protocol used during these experiments is similar to the protocol presented in ref [1] and consists of the following steps:

- (I) drying,
- (II) preconditioning of the membrane,
- (III) cooling down the cell,
- (IV) feed gases,
- (V) apply current until failure of the fuel cell, and
- (IV) heating up.

*Simulation* – Based on previously presented measurement protocol, approximately 250 cold starts were executed with the small scale fuel cell to obtain a probability distribution of cell failure as function of the operating time. This experimentally obtained distribution can be used as input for a Monte Carlo simulation to predict the failure probability of larger fuel cells. The probability distribution of the small scale fuel cell can be used for upscaling under the following two assumptions:

- (I) the behaviour of every 1 cm<sup>2</sup> segment is identical and
- (II) the water cluster can be considered of being continuous across the cell.

According to these assumptions, each small section of the cell can be assumed to be independent from the other in terms of freezing probability. Consequently, the operating time of a fuel cell with an area of n cm<sup>2</sup> is calculated as the minimum value of n independent variables following the probability distribution of freezing of the 1 cm<sup>2</sup> cell.

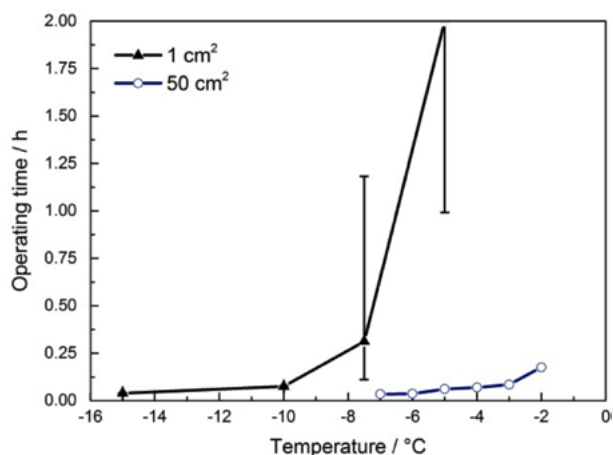
### Results

Figure 1 shows the experimentally obtained operating times as a function of the temperature for both cell configurations; the solid points represent median values, the error bars the lower and higher quartile.

In general, the operating time is strongly decreasing with decreasing temperature. As expected, the differential cell shows at all temperatures the highest operational times, whereas lower cold start capabilities are obtained with 50 cm<sup>2</sup> cell. At -7.5 °C, more than 25% of the cells of the small scale cells and more than 75% at -5 °C did not fail during 1 h. In contrast, significantly lower operating times are obtained with the 50 cm<sup>2</sup> fuel cell, with failures of less than 15 min of operation for all temperatures. Even though only a single experiment was performed at each temperature with this cell configuration, the continuous trend suggests a repeatable behaviour. Although strong differences can be identified in the repeatability and operating times, both cell configurations converge towards a common lower limit of operating time, which will be explained subsequently.

In order to link both results of the small and larger scale fuel cell, a Monte Carlo simulation was executed based on the probability distribution extracted from the experiments with the cell of 1 cm<sup>2</sup> at 7.5 °C. Figure 2 shows the numerical results of the predicted operating time as a function of the cell size. As can be seen, the probability of cell failure strongly increases with increasing cell size, and converges towards a lower limit of operating times for cell sizes above 10 cm<sup>2</sup>, which is around 5 minutes at this temperature of -7.5 °C. Another observation

is the strong decrease of the error bars with larger cell sizes. Thus variabilities of more than 1 h are obtained with cells of  $1 \text{ cm}^2$ , whereas cells above  $10 \text{ cm}^2$  show more repeatable operating times. Both, the repeatability as well as the operating times, nicely correlate with the experimental results presented in Figure 1.



**Figure 1.** Experimental results of the cold start capability of two different cell sizes at various subfreezing temperatures. The points show median values, error bars indicate the upper and lower quartiles.

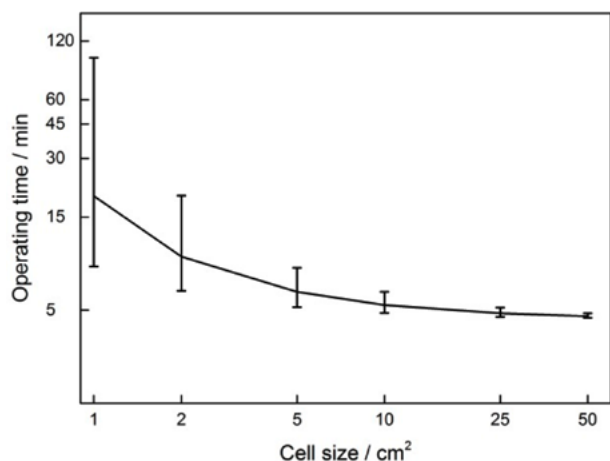


**Figure 2.** Operation times as a function of the cell size obtained from Monte-Carlo simulation. This simulation is based on the experimental data of the  $1 \text{ cm}^2$  cell shown in figure 1.

## Discussion

In general, all effects observed in previous experiments and simulations can be explained by the existence of supercooled water inside the fuel cell. Supercooled water is a metastable aggregate state of liquid water which exists below  $0 \text{ °C}$ . The phase transition to frozen state occurs spontaneously and is dependent on several parameters such as the temperature, cluster volume or surface properties [5].

*Operating times* – Based on the simulation results, the stochastic nature of the water–ice transition of small scale fuel cells could be linked to the deterministic behaviour of the larger fuel cells: above cell sizes of  $10 \text{ cm}^2$ , the freezing probability is so high that the operation time is only limited by deterministic factors such as the water uptake of the membrane or the pore space of the catalyst layer.

*Temperature dependence* – It has been reported in literature that the probability of phase transition from supercooled to frozen water is strongly temperature dependent [5]. This characteristic might explain the strongly decreasing operating times with reduced temperatures. Similar to previous explanation, a higher probability of phase transitions leads to a more repeatable freezing behaviour.

*Lower limit of charge produced* – During our experiments, a minimal operating time was obtained for both cell configurations. This minimal time can be explained by deterministic parameters such as the water uptake of the membrane and the ionomer inside the catalyst layer, as well as the filling of the pore space of the catalyst layer until the active sites of the catalyst layer are blocked.

## Conclusion

In this work, the influence of the size of the active area on the freezing mechanism was studied. It was found out that the probability of freezing increases with increasing active areas, resulting in long and stochastic operation times for small cells and short and reproducible operation times for large cells. This effect was explained by a higher probability of phase transition from supercooled to ice in large scale fuel cell.

## References

- [1] P. Oberholzer, P. Boillat, R. Siegrist, R. Perego, A. Kästner, E. Lehmann, G.G. Scherrer, A. Wokaun, *J. Electrochem. Soc.* **159**, B235 (2011).
- [2] J. Biesdorf, P. Oberholzer, F. Bernauer, A. Kaestner, P. Vontobel, E.H. Lehmann, T.J. Schmidt, P. Boillat, *Phys. Rev. Lett.* **112**, 248301 (2014).
- [3] P. Oberholzer, P. Boillat, R. Siegrist, A. Kästner, E.H. Lehmann, G.G. Scherer, A. Wokaun, *Electrochem. Com.* **20**, 67–70 (2012).
- [4] P. Stahl, J. Biesdorf, P. Boillat, J. Kraft, K.A. Friedrich, *J. Electrochem. Soc.* **162** (7), F677–F685 (2015).
- [5] Y. Ishikawa, M. Shiozawa, M. Kondo, K. Ito, *Int. J. Heat Mass Transfer* **74**, 215–227 (2014).

## Water/gas distribution in electrolyzers with gas diffusion layers of different pore sizes

J. Seweryn, J. Biesdorf, D. Scheuble, T.J. Schmidt, P. Boillat

phone: +41 56 310 5034, e-mail: pierre.boillat@psi.ch

Polymer Electrolyte Electrolyzers (PEEC) are of significant interest for the production of hydrogen fluctuating from renewable sources, thanks to their ability of fast start-up and shut-down. In order to minimize the impact of costly precious metal catalysts, as well as the impact of gas crossover through the membrane, operation at the highest possible current density is desired. One well-known limitation to this is the resistance of the membrane resulting in increased loss at higher current densities. A further possible limitation is the apparition of mass transport losses, due to the limited supply of water to the anode electrode. The latter, in relation with the distribution of water and gas in the porous media and flow channels of the electrolyzers, have only been scarcely studied in the past. Due to their high penetration through various materials – including the titanium sinter used as porous media in electrolyzers, and their good contrast for water, neutrons are a very interesting probe for the study of *in situ* water/gas distribution in operating electrolyzers.

### Experimental

Building on the imaging techniques previously developed for the imaging of water in operating fuel cells [1, 2] experiments were conducted on small scale (1 cm<sup>2</sup>) electrolysis cells. The cell design included a flow field made of 5 parallel channels (depth and width 1 mm) made of aluminum and coated with gold. Titanium sinters from Sika (T5, 1 mm) were used as a diffusion media. Preliminary results were presented in a previous report [3] and are further analyzed here.

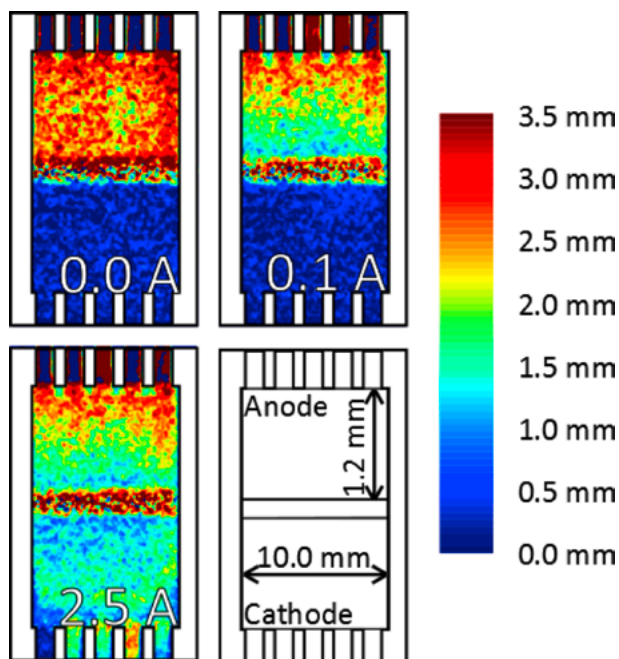


**Figure 1.** In-plane radiograms of electrolyzer cell obtained during first measurement campaign in December 2014, converted to water content. Transmission in the membrane region was insufficient for reliable analysis. Cell operated at 50 °C and 2 bar (symmetric).

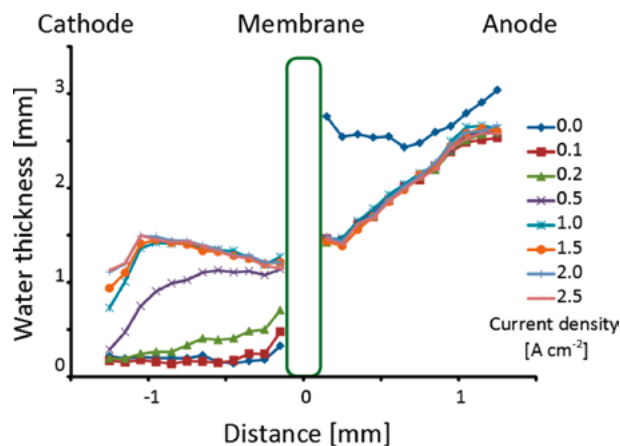


**Figure 2.** Water content in anodic porous layer as a function of current density in December 2014. Cell operated at 50 °C and 2 bar (symmetric).

The possibility to perform a *through-plane* imaging was investigated as well; however the amount of information obtained in this mode for a differential cell is very limited. This mode might be much more useful for a future investigation of full-sized cells.

### Experimental

The measurements performed in December were described in [3]; recent ones have been performed at the NEUTRA beamline of the PSI, using the operating conditions module built for a previous campaign, with extended pressure capability. The cell was adapted from a project of M. Cochet and D. Scheuble, with 1 cm<sup>2</sup> active area; this novel design enabled quick replacement of flowfields and MEAs. The measurements were performed in in-plane mode, with flow channels perpendicular to the beam.

The examined porous layers were sintered Ti powders (SIKA from GKN) with porosity of 20–30 %, selected as follows:

- T5, T10 and T20 – thickness ca 1.2 mm
- T5 and T20 – thickness ca 2 mm

T5, T10 and T20 are names given by the manufacturer, and correspond roughly to the pore size expressed in  $\mu\text{m}$ .

For 1.2 mm thick samples also the experiments involving pressure variation at constant current of 2 A cm<sup>-2</sup> were performed:

- 2, 5, 10 and 20 bar<sub>abs</sub>, symmetrically
- oxygen side 2 bar<sub>abs</sub>, hydrogen side: 20 bar<sub>abs</sub>
- hydrogen side 2 bar<sub>abs</sub>, oxygen side: 20 bar<sub>abs</sub>

The remaining operating parameters were kept constant: 50 °C, water flow 50 ml min<sup>-1</sup>.

## Results

Since the last measurement campaign was ended very recently, the full analysis of results, especially the image processing, is not finished yet. At this point it can be said, basing on electrochemical performance data, that some of the cells were behaving incorrectly (see Figure 3).

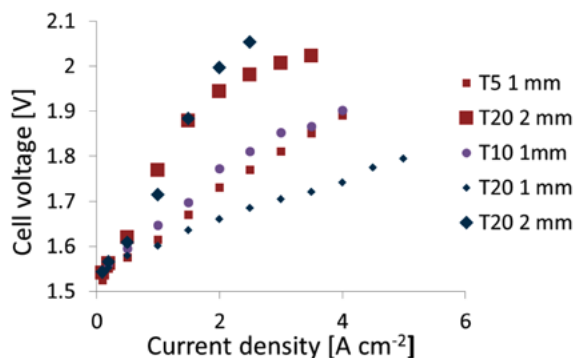


**Figure 3.** IR-free VI curves registered for cells comprising different porous layers. Except for T20 1 mm, they exhibit anomalous overvoltage and shape.

It is unclear what the reason was; the most probable explanation is insufficient compression of active area. The current setup involves large area of PTFE gasket with the compression force distributed between it and the porous layer; given viscoelastic properties of this material it is almost impossible to control force exerted on active area. It might be reasonable to use some of perfluorinated elastomers in the future instead of PTFE.

## Acknowledgement

The support from the Swiss Federal Office of Energy (SFOE) through project 8100066 is gratefully acknowledged.

## References

- [1] P. Boillat, PhD thesis Nr 18397 (2009), ETH Zürich, Switzerland.
- [2] P. Boillat, G. Frei, E.H. Lehmann, G.G. Scherer, A. Wokaun, *Electrochem. Solid-State Lett.* **13**, B25 (2010).
- [3] J. Seweryn, J. Biesdorf, T.J. Schmidt, P. Boillat, *Annual Report – Electrochemistry Laboratory 2014*. 16. DOI: 10.3929/ethz-a-007047464 (2014).

## Optical imaging characterization for optimization of an evaporatively cooled Polymer Electrolyte Fuel Cell (PEFC)

M. Cochet, P. Gröninger, A. Forner-Cuenca, D. Scheuble, P. Boillat

phone: +41 56 310 5256, e-mail: magali.cochet@psi.ch

An evaporative cooling concept for a Polymer Electrolyte Fuel Cell (PEFC) is being developed at PSI, where cooling is managed by injecting liquid water in the fuel cell itself. In this concept, water is brought through flowfields channels parallel to the gas channels, and wicked by capillary forces through the Gas Diffusion Layers (GDL) towards the membrane, where it finally evaporates. Two elements are central to this scheme: first, the GDL, a thin hydrophobic porous media transporting reactant gases to the membrane, has been modified. A synthetic method developed at PSI [1, 2] transforms some portions of the GDL into hydrophilic lines. These lines, parallel and equally spaced, define separate pathways for liquid water and avoid flooding (Figure 1). The second element is the flowfield supporting the parallel channels in which the liquid water and the gases flow.

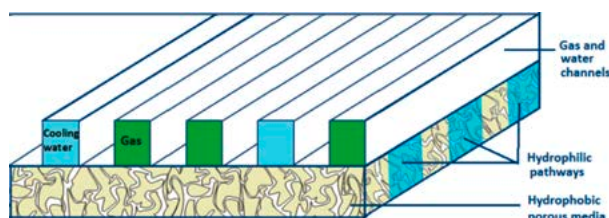


**Figure 1.** Modified GDL with hydrophilic lines, and flowfields channels including channels for the liquid water.

In order to prove this concept, a thermal test bench equipped with Heat Flux Sensors (HFS) was built, in order to simulate thermal boundary conditions representative of a fuel cell stack, and to test the performances of a cell with evaporative cooling. In this report, we present a preliminary study which aims at proving the possibility of getting water from the flow-field channels into the modified GDL without strong overpressure, comparing the capacity of the heat flux sensors of determining an evaporation rate to a liquid flow meter and studying the impact of capillary pressure and air mass flow rate on the evaporation rate within the cell.

### Experimental

For this study focused on evaporation without cell operation, one of the sides was replaced by a compression body with a Plexiglas visualisation window. The other side is composed of a compression body in aluminum, three HFS, a flowfield with six channels dedicated to gas transport and five channels for water transport, a PTFE gasket and a GDL, either fully hydrophobic or modified. Images of the channels and the GDL are recorded through the Plexiglas window with a digital camera to monitor the imbibition of the GDL and the appearance of water in the gas channels (see Figure 3). For this study, the gas used is air. The compression body is warmed with heating cartridges up to 50 °C, and the temperature is regulated with a thermocouple positioned on the bottom surface and a PID regulation. The Heat Flux Sensors are devices that create a voltage proportional to the heat flux going through the sensor. Three individual HFS with three embedded thermocouples are used on the anode side directly under the flow-

fields. The middle HFS is positioned below the GDL, and the two others are positioned below the channels and the PTFE gasket, upstream and downstream of the GDL.

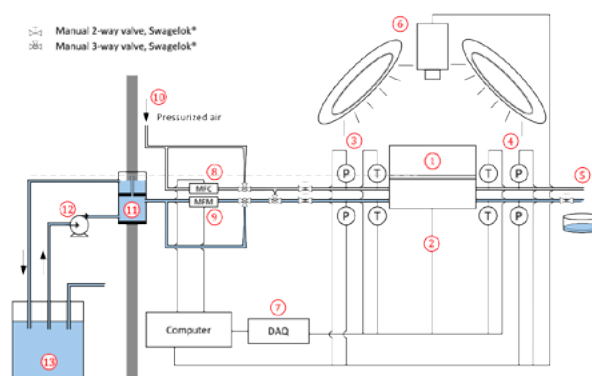


**Figure 2.** Experimental setup.

Figure 2 presents the experimental set-up. Air and water are fed from the same side into the cell and flow in the same direction. The air was delivered from a pressurized tank and flown out of the cell to the atmosphere. The air flow was controlled by a mass flow controller with a nominal mass flow rate of 1549 NmL/min. Water was in dead-end mode and its pressure  $P_{\text{water}}$  was controlled by the water tank's height. For water and gas, pressures and temperatures were measured at the inlet and outlet of the cell. The capillary pressure, an important parameter that controls the saturation of the GDL, is defined as:

$$P_{\text{cap}} = P_{\text{water}} - P_{\text{air}} \quad \text{Equation 1}$$

Any flow of air creates a pressure drop in the cell. Assuming that the pressure drops upstream and downstream of the GDL are equal, the pressures were computed as the averages of the inlet and outlet values. Before evaporation was measured, a visual test was made to see the imbibition of the GDL versus capillary pressure without flowing air. The breakthrough pressure is defined as the minimal capillary pressure at which water gets into the GDL. For the modified GDL, the breakthrough pressure was found to be -12 mbar, in agreement with the results of another study (see ref [3]). For a fully hydrophobic GDL, it is equal to +35 mbar. Figure 3 shows water getting into the GDLs at breakthrough pressure.

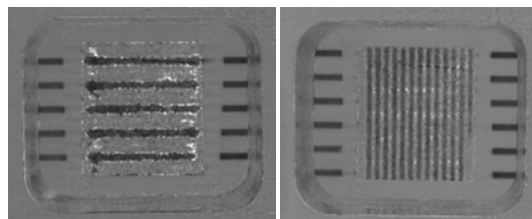


**Figure 3.** Water in the hydrophobic GDL (left) and modified GDL (right) at breakthrough pressure.

Another useful value is the value for which the water starts dripping from the GDL into the air channels. For the patterned

GDL, it is equal to +4.5 mbar, and for the hydrophobic GDL, to +38 mbar. The evaporation rates were computed in two different ways. First, a liquid flow meter measured the mass flow rates of water going into the cell. Since the water is in dead-end mode, it is assumed that the rate of water going into the cell is equal to the evaporation rate. The second method involves the 3 HFS. With no water in the channels, the heat flux measured by the HFS includes the heat flux lost by the convection of the gases as well as the heat flux lost by conduction to the ambient air. With water in the cell, it also includes the heat flux lost because of evaporation. Therefore, the evaporation heat  $\phi^{\text{evap}}$  can be found by measuring first the values given by the HFS without evaporation, and then subtracting the results from the heat fluxes measured with evaporation:

$$\phi^{\text{evap}} = \phi_{\text{with evap}}^{\text{HFS}} - \phi_{\text{no evap}}^{\text{HFS}} \quad \text{Equation 2}$$

From there the evaporation rate  $\dot{m}_{\text{evap}}$  is computed as:

$$\dot{m}_{\text{evap}} = \phi^{\text{evap}} / L_{\text{LV}} \quad \text{Equation 3}$$

with  $L_{\text{LV}}$  the latent heat of vaporization of water at 50 °C.

## Results

Figure 4 shows the evaporation rate measured by the two different methods versus the capillary pressure for the modified GDL for low capillary pressure values.

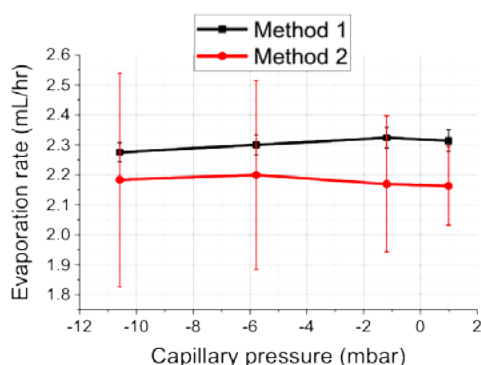


**Figure 4.** Evaporation rate versus capillary pressure.

Both methods show an evaporation rate independent of the capillary pressure. A previous investigation [3] showed that the modified GDL has a saturation of 30% at -12 mbar, and of 35% for 1 mbar. Thus, the evaporation is apparently not influenced by the capillary pressure probably because the saturation of the GDL is not significantly changed in this range. Increasing the capillary pressure further, from 1 mbar to 70 mbar, changes the saturation from 35% to 83%. It is however impossible to check these higher values with this set-up because, as mentioned before, higher capillary pressures lead to water in the air channels. It must also be noted that, although Figure 4 shows more precise results for Method 1 than for Method 2, it was an exception. Considering all the experiments, Method 1 actually was the least precise of both methods and clearly had the lowest repeatability.

The effect of the air flow rate on the evaporation rate was also investigated. The capillary pressure was set to 1 mbar so that the water penetrated the pores of the GDL but did not reach the air channels. It was kept constant by increasing the height of the tank when the air flow rate increased. The measurements were conducted at air flow rates between 0 and 1000 NmL/min.

Figure 5 shows the evaporation rate for the modified and the classic GDLs at breakthrough pressure.

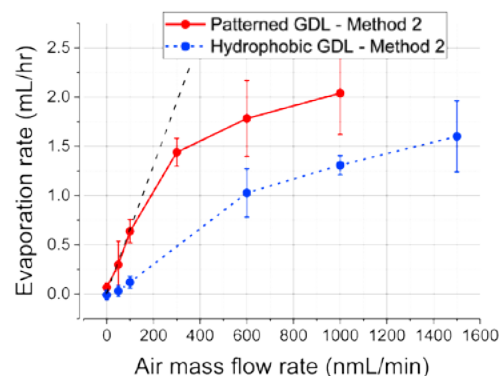


**Figure 5.** Evaporation rate in the modified GDL and the hydrophobic GDL at breakthrough pressure. The black dashed line shows the vapor uptake capacity of the gas at 50°C.

For both GDLs, the evaporation rate increases strongly at first with the mass flow rate of air, before stalling for higher values. Figure 5 also shows higher evaporation rates for the patterned GDL than for the hydrophobic GDL. As can be seen in Figure 3, at breakthrough pressure the water is mostly concentrated in the pores above the water channels in the hydrophobic GDL, whereas for the patterned GDL, the hydrophilic lines ensure that water reaches the air channels allowing direct contact to the air flow. As a result evaporation is driven only by convection, whereas for the hydrophobic GDL, evaporation is slowed down by diffusion of the water vapour through the porous media. It is worth to be noted that, for the modified GDL, the evaporation rates perfectly matches the maximum vapour uptake capability of the gas flow.

In summary, direct visualisation shows that the hydrophilic lines are soaked as expected for very small capillary pressures. Comparison between two methods of establishing the evaporation rate shows that HFS method is more reliable. The study of evaporation for the patterned GDL does not show an impact of the capillary pressure on the evaporation rate, which is probably only due to the too small range of saturation levels tested. Measurements as a function of the air flow did show that, for the modified GDL, the evaporation rate is initially only limited by the gas flow vapour uptake, with other limitations starting around 200 NmL/min.

## Acknowledgement

The authors would like to thank the Swiss Competence Center for Energy Research (SCCER) – Mobility and the Swiss National Science Foundation (project n° 143432) for their financial support.

## References

- [1] P. Boillat, A. Forner-Cuenca, L. Gubler, C. Padeste, F. Büchi, European patent application 15165516.6–1360, 2015.
- [2] A. Forner-Cuenca, J. Biesdorf, L. Gubler, P.M. Kristiansen, T.J. Schmidt, P. Boillat, *Adv. Mater.* **27** (41), 6317–6322 (2015).
- [3] A. Lamibrac, «Modified GDL for improved water management in PEFC», Poster for 2<sup>nd</sup> SCCER Mobility Annual Conference, 2015.

## Combined neutron imaging and small angle scattering study of water management in fuel cells

P. Boillat, A. Morin<sup>1</sup>, A. Forner-Cuenca, S. Lyonnard<sup>1</sup>, G. Gebel<sup>1</sup>

phone: +41 56 310 2743, e-mail: pierre.boillat@psi.ch

Water management in polymer electrolyte fuel cells (PEFCs) plays a crucial role due to the dual role of water being on one side necessary in the membrane to ensure proton conduction and on the other side detrimental in the gas flow channels and porous media. Neutron based methods (imaging and scattering) are of high interest for *in situ*, operando measurements because of the high penetration of neutrons through fuel cell construction materials and the high sensitivity to hydrogen containing compounds such as water. Imaging and small angle scattering can provide complementary results, the first one being able to measure the water distribution with high spatial resolution [1], and the latter giving information about the membrane hydration state [2]. Here, we present a combined imaging and small angle scattering study on the water distribution in a small scale fuel cell, giving an unprecedented insight in the water management of fuel cells.

### Experimental

A small scale fuel cell (active area 13 x 17 mm<sup>2</sup>) with a single serpentine channel having a developed length of 10 mm was used. The width of the channel was 1 mm and the width of the ribs 0.8 mm, while the channel depth was 0.5 mm. The polymer electrolyte membrane having a thickness of 50 μm (Nafion 212, Dupont) was hot-pressed between two gas diffusion electrodes based on a carbon paper with a microporous layer (GDL24BC, SGL Carbon Group) on which CEA in-house developed catalyst layer were applied (0.5 mg<sub>Pt</sub>/cm<sup>2</sup>). The flow fields were machined directly into the aluminum compression plates having a thickness of 30 mm, which were subsequently coated with gold. The cell was designed so that no disturbing elements (e.g. gas ports, heaters) were placed in the path of the beam, allowing three different measuring configurations (through plane and in plane imaging plus small angle scattering) as illustrated in Figure 1.

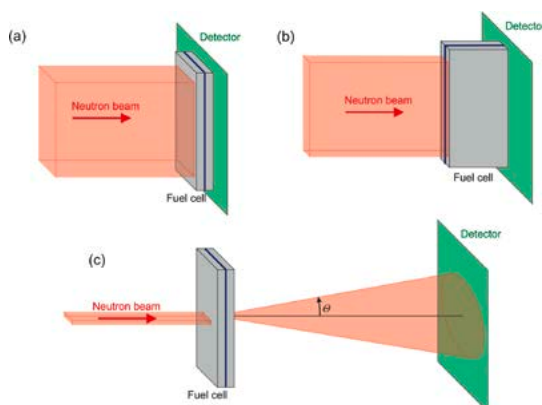


**Figure 1.** Illustration of the three different measurement configurations: Through plane imaging (a), in plane imaging (b) and small angle scattering (c).

The cell was operated on technically relevant stoichiometries (1.2 on the anode side, 2.0 on the cathode side), at a temperature of 70 °C, a pressure of 1.5 bar<sub>abs</sub> and with a relative humid-

ity of the gas flows set to 50%. The gases were fed in counterflow configuration with the hydrogen flowing from top to bottom and the air flowing for bottom to top.

The SANS experiments were conducted at the PAXY instrument of the Laboratoire Léon Brillouin (LLB, CEA Saclay, France). In order to measure small angle scattering patterns corresponding to different regions of the cells, a mask consisting of 3 slits having a width of 0.5 mm and a center-to-center distance matched to the cell channel pitch of 1.8 mm was placed in the beam. Using this mask, the ribs and channel regions of the cell were successively measured at three different positions (top, middle and bottom sections of the cell), resulting in a total of 6 measurement regions for one experiment. The measurement time for each region was set to 30 minutes, resulting in a total measurement duration of 3 hours per experiment. Additionally to the operando measurements, the scattering pattern of the dry cell as well as reference scattering patterns with nitrogen at different relative humidities between 50% and 100% were recorded. The imaging (through plane and in plane) experiments were conducted at the ICON instrument [3] of the SINQ neutron source (Paul Scherrer Institute, Switzerland). For the in plane high resolution measurements, the specific anisotropic enhancement methods previously developed at PSI [1] were applied. For referencing purposes, images of the dry cells were recorded besides the operando measurements. To ensure to best possible reproducibility, the same fuel cell test infrastructure was used for the measurements at PAXY and at ICON. After the experiments at PAXY, the cell was dried and purged with nitrogen and sealed until the experiments at ICON.

### Results

An example of SANS results is given in Figure 2, corresponding to the reference measurement at a relative humidity of 100%. As can be seen in the top part of the figure, the amplitude of the useful signal is relatively small compared to the scattering intensity from the cell body. However, after adequate intensity correction and subtraction of the dry cell pattern, a signal with sufficient quality was obtained (bottom part of Figure 2). Two features were mostly used for extracting useful information from this pattern: The position of the ionomer peak is related to the swelling state of the membrane, and the constant background at high  $q$  values ( $> 0.3 \text{ \AA}^{-1}$ ) corresponds to the incoherent scattering from liquid water. The obtained pattern was fitted using the following function:

$$I = A_{ion} \cdot e^{-\frac{(q-m_{ion})^2}{2 \cdot s_{ion}^2}} + I_{incoh} + A_{sa} \cdot e^{-\frac{q}{q_{sa}}} \quad (1)$$

Where the first term corresponds to the ionomer peak represented as a Gaussian function (amplitude  $A_{ion}$ , central position  $m_{ion}$  and standard deviation  $s_{ion}$ ), the second term ( $I_{incoh}$ ) represents the incoherent scattering from liquid water and the last term is an arbitrary exponential function used to account for the additional scattering at low  $q$  values. The fitting val-

<sup>1</sup> Commissariat à l'Énergie Atomique et aux Énergies Alternatives (CEA), Grenoble, France

ues used for further analysis are  $m_{\text{ion}}$  (position of the ionomer peak) and  $I_{\text{incoh}}$ . The  $m_{\text{ion}}$  value is converted to an «equivalent RH» value using a linear regression of  $m_{\text{ion}}$  as a function of RH obtained from the reference measurements.

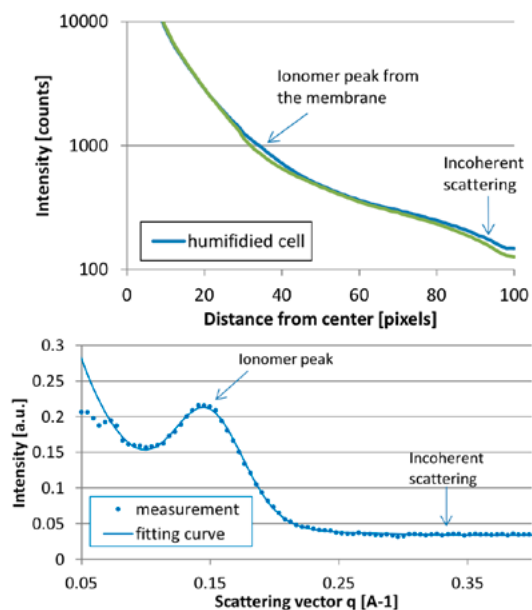


**Figure 2.** Results of the SANS measurements for the cell humidified with  $N_2$  at 100% RH. Top: raw diffraction patterns of the dry and humidified cell. Bottom: diffraction pattern after proper intensity correction and subtraction of the dry cell.

Exemplary results of the imaging (operation at  $1 \text{ A/cm}^2$ ) are given in Figure 3, with the amount of water displayed in false colour (yellow corresponding to low amounts of water and blue corresponding to high amounts of water). As can be seen, a good qualitative agreement is obtained between the through plane and in plane measurements. While the through plane measurements allow the visualisation of water droplets and slugs in the channels, the in plane images complement this information by allowing the location of the water across the cell structure.

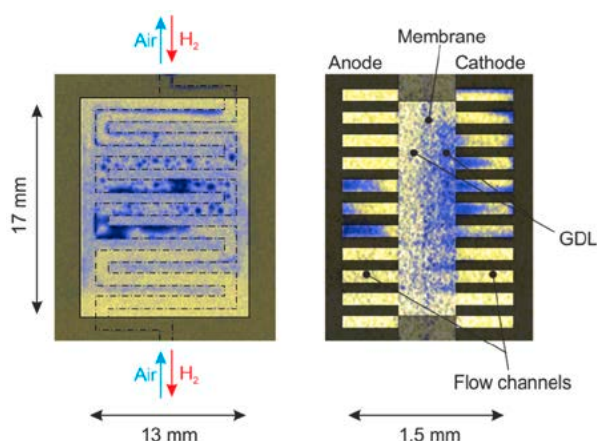


**Figure 3.** Through plane (left) and in plane (right) neutron imaging results for operation at  $1 \text{ A/cm}^2$ .

The measurement of the incoherent scattering from the SANS experiment is in principle redundant with the imaging measurement. As can be seen from Figure 4 (right), a good qualitative agreement is obtained between SANS and imaging results as well, with the water accumulation in the channels being the highest in the middle of the cell, having an intermediate value

in the top of the cell (air outlet) and being very low at the bottom of the cell. On the contrary and consistently with the imaging experiments, the quantity of water in the ribs region is similar for the three cell sections.

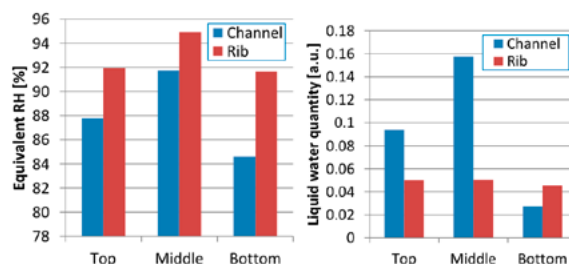


**Figure 4.** SANS results for the operation at  $1 \text{ A/cm}^2$ . Left: membrane hydration state. Right: quantity of liquid water.

Finally, the hydration state of the membrane is the information which we obtain from the SANS experiment only (Figure 4 left). The membrane hydration is highest at the middle of the cell which is explainable by the used counterflow operation mode. The driest part is the air inlet, where a significant ( $\sim 7\%$ ) difference of equivalent relative humidity is observed between the rib and channel areas. This difference is explained by the fact that the produced water is less efficiently removed for the ribs region due to the longer diffusion path to the flow channels.

In summary, neutron imaging and scattering measurement were conducted on a small scale fuel cell with three different configurations (through plane imaging, in plane imaging, small angle scattering). The overlapping part of information shows a good qualitative agreement between the three measurements, while each measurement additionally provides unique information:

- The droplets/slugs position and movement for the through plane imaging.
- The distribution of liquid water across the cell structure for the in plane imaging.
- The membrane hydration for small angle scattering.

Thus, the combined measurements with these three methods provide a unique insight useful both for direct analysis and as a support for the validation of numerical simulations.

## Acknowledgement

The support of Jacques Jestin and Michel Thévenoz (LLB, CEA, Saclay) for the conduction of the experiments at the PAXY instrument, as well as the support of Lionel Porcar (ILL, Grenoble) for the manufacturing of the masks is gratefully acknowledged. This work was conducted with the support of the European Community. We appreciate the support of the European Research Infrastructure H2FC (funded under the FP7 specific programme Capacities, Grant Agreement Number 284522).

## References

- [1] P. Boillat, G. Frei, E.H. Lehmann, G.G. Scherer, A. Wokaun, *Electrochem. Solid. St.* **13** (3), B25–B27 (2010).
- [2] A. Morin, F. Xu, G. Gebel, O. Diat, *Fuel Cells* **12** (2), 156–161 (2011).
- [3] A.P. Kaestner, S. Hartmann, G. Kuhne, G. Frei, C. Grunzweig, L. Josic, F. Schmid, E.H. Lehmann, *Nucl. Instrum. Meth. A* **659** (1), 387–393 (2011).

## Operating a HT-PEFC with hydrogen from a formic acid reformer

J. Halter, R. Bérard, A. Dalebrook<sup>1</sup>, M. Grasmann<sup>1</sup>, G. Laurenczy<sup>1</sup>, L. Gubler, F.N. Büchi  
 phone: +41 56 310 4131, e-mail: jonathan.halter@psi.ch

Formic acid (HCOOH) has attractive features as a medium for hydrogen storage as it has reasonably high theoretical energy densities with respect to volume (2086 Wh/l) and weight (1700 Wh/kg) [1]. Formic acid reforming to hydrogen and carbon dioxide can be performed at temperatures as low as 26 °C [2].

High temperature polymer electrolyte fuel cells (HT-PEFC), based on phosphoric acid imbibed polybenzimidazole membranes are operated between 160 °C and 200 °C. Operation at these elevated temperatures dramatically improves the tolerance versus CO and impurities (as compared to standard low temperature PEFC), which allows for using lower quality hydrogen, such as from the reforming of hydrocarbons.

### Experimental

The hydrogen generator was designed around a 5 l reaction vessel, containing RuCl<sub>3</sub> (0.045 mole) and Na<sub>3</sub>TPPTS (0.090 mole) catalysts in 1.5 l aqueous HCOONa solution (1 M).

All fuel cell experiments were carried out with BASF Celtec membrane electrode assemblies (MEA). The gas diffusion electrodes consist of Pt/Vulcan XC-72 supported platinum catalyst with a loading of 1 mg<sub>Pt</sub>/cm<sup>2</sup>, coated onto SGL 38 carbon paper gas diffusion layers including a microporous layer.

The HT-PEFC was operated with hydrogen ( $\lambda_{\text{an}}=1.2$ ) and air ( $\lambda_{\text{cat}}=2$ ) at 0.2 A/cm<sup>2</sup> at 160 °C and atmospheric pressure for 100 h for conditioning. The fuel was changed to 50% H<sub>2</sub> and 50% N<sub>2</sub> ( $\lambda_{\text{an}}=1.2$ ) and the cell was operated at 0.2 A/cm<sup>2</sup> for 24 h. Then the cell was fed with the hydrogen rich reformat provided by the formic acid reformer for 4 h at 0.2 A/cm<sup>2</sup> with a constant fuel flow rate of 110 nl/h ( $\lambda_{\text{an}}=14.5$  at 0.2 A/cm<sup>2</sup>). After each operating condition, a polarization curve was recorded.

### Results

Figure 1 shows the recorded polarization curves with pure H<sub>2</sub> as a fuel and air, with the 1:1 mixture of N<sub>2</sub> and H<sub>2</sub> and the formic acid reformat (about a 1:1 mixture of H<sub>2</sub> and CO<sub>2</sub>). The difference between the polarization curve measured with pure hydrogen and those with diluted hydrogen can easily be seen. This difference can be associated to the lower hydrogen partial pressure and mass transport losses for the diluted fuels. When comparing the polarization curve measured with H<sub>2</sub>/N<sub>2</sub> to the one obtained with the reformat, a slight difference in the high current density region (above 0.8 A/cm<sup>2</sup>) is observed. The additional losses with reformat can be associated with mass transport phenomena or can be seen as an indication for the presence of an increased CO concentration. Analysis of the composition of the reformat showed a CO content of around 50 ppm. Whereas this level of CO is detrimental for the LT-PEFC operating at a temperature of around 80 °C, the HT-PEFC can tolerate this amount without impact on performance. However, owing to the high concentration of CO<sub>2</sub> of 50%, it is possible, that CO is generated *in situ* by the reverse water gas shift (RWGS) reaction, at the platinum surface:



as reported by de Bruijn et. al. for LT-PEFC [3].

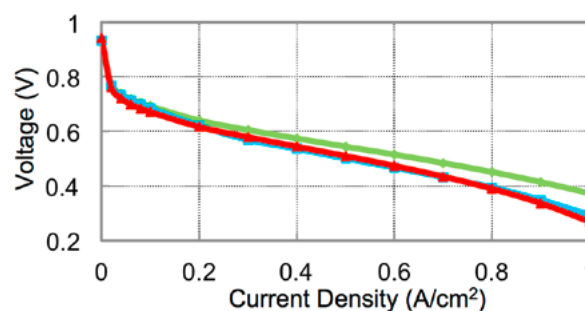


**Figure 1.** Polarization curves using H<sub>2</sub> (green), N<sub>2</sub>/H<sub>2</sub> (blue) and reformat (red) as fuel. Oxidant: air.

This hypothesis is supported by the fact that in HT-PEFC operated at 160 °C the kinetics of the RWGS reaction increases and prevents liquid water formation, which drives the reaction forward. Furthermore, the reactant gases in this study were not humidified, which again drives the RWGS forward.

Another explanation for the additional losses would be the difference in the binary diffusion coefficient of H<sub>2</sub> for equimolar mixtures of H<sub>2</sub>/N<sub>2</sub> (1.74 cm<sup>2</sup>/s at 200 °C) and H<sub>2</sub>/CO<sub>2</sub> (1.47 cm<sup>2</sup>/s at 200 °C), as reported by Marrero et. al [4]. The lower diffusivity of H<sub>2</sub> in the H<sub>2</sub>/CO<sub>2</sub> mixture can also lead to mass transport limitations in the high current density region.

### Conclusion

For the first time, a HT-PEFC was operated with hydrogen generated by a formic acid reformer. The reformat containing 50% CO<sub>2</sub> and around 50 ppm CO. The cell characteristics coincide largely with the ones for nitrogen diluted hydrogen, except at high current densities. These additional losses may be a result of the *in situ* generation of CO by the reverse water gas shift reaction at the platinum electro-catalyst.

### Acknowledgement

Financial support by the Commission for Technology and Innovation (CTI) and the Competence Center Energy and Mobility (CCEM) in the framework of the Hyform project is gratefully acknowledged. We thank T. Gloor for technical support.

### References

- [1] J. Yeom, R.S. Jayashree, C. Rastogi, M.A. Shannon, P.J.A. Kenis, *J. Power Sources* **160**, 1058–1064 (2006).
- [2] B. Loges, A. Boddien, H. Junge, M. Beller, *Angew. Chem. Int. Ed.* **47**, 3962–3965 (2008).
- [3] F.A. de Bruijn, D.C. Papageorgopoulos, E.F. Sitters, G.J.M. Janssen, *J. Power Sources* **110**, 117–124 (2002).
- [4] T.R. Marrero, E.A. Mason, *J. Phys. Chem. Ref. Data* **1**, 3–118 (1972).

## Water evaporation in partially saturated gas diffusion layers

A. Lamibrac, J. Eller, F.N. Büchi

phone: +41 56 310 2411, e-mail: felix.buechi@psi.ch

Proton exchange fuel cell (PEFC) optimal operation is closely related to water management. Produced at the cathode, water is needed in the membrane to maintain the proton conductivity. However, liquid water in the catalyst- and gas diffusion-layers (GDL) or in the channels of the flow field plates can reduce the performance since the gas access to the reaction sites becomes hindered. Therefore, better understanding of water removal is a crucial issue to address. One of the critical processes is the phase change of water in the gas diffusion layer. Here, evaporation may play a significant role to keep the optimal water balance in the porous structure. However, water evaporation in GDL is not a well understood process and has not extensively been investigated mainly because of the difficulties to measure evaporation in thin porous layers such as GDL which typically have a thickness around 200  $\mu\text{m}$ .

An experimental setup previously used [1] to inject and withdraw water from GDL has been modified to enable the measurement of the evaporation rate at different saturation levels. The experimental setup is first described here and preliminary results are presented.

### Experimental

A GDL SGL 24BA sample (6 mm in diameter) is compressed in a sample holder between a hydrophilic membrane and a flow field. The hydrophilic membrane ensures a homogeneous distribution of the water fed at the bottom edge of the GDL while the single channel of the flow field enables gas convection for evaporation on the top edge. The saturation of the GDL is controlled using a syringe pump and the capillary pressure applied is measured using a water column in parallel to the sample holder (Figure 1). The temperature of the cell is set to 30 °C by two polyimide foil heaters (Minco ref. 5569). Once a capillary pressure is set, the evaporation is measured by timing the height loss of the meniscus in the water column (1.17 mm diameter) over 1 cm. The height variation is chosen small enough so that the liquid/gas interface inside the GDL can be assumed constant during the measurement. Evaporation measurements are carried out for different capillary pressures ( saturations), different gas types (hydrogen or air) and gas flows in the upper flow field.

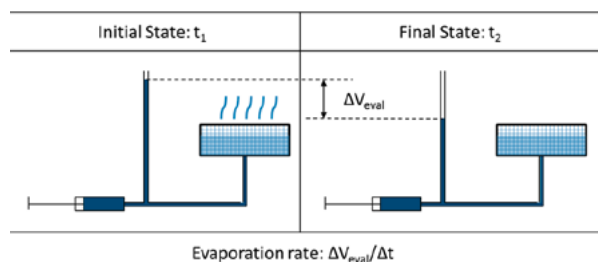


Figure 1. Schematic of evaporation experiment principle.

The procedure described can be realised in the laboratory but the evaporation rates obtained are only global, meaning that they cannot be related to a certain liquid/gas interface area for a given saturation in the GDL. To obtain the liquid/gas interface area in the GDL, the experiment was repeated at the Tomcat beamline of the Swiss Light Source (SLS). There, X-ray tomographic microscopy has been performed for different saturations and gas flow rates. Once the evaporation is known, the syringe pump is set so that it compensates the global evaporation rate and X-ray tomographic imaging is then performed. The reconstructed images show no water moving artefacts indicating that evaporation is properly compensated and that there is no significant water redistribution due evaporation/condensation processes.

### Results

Figure 2 shows that gas flow rate has limited impact on the evaporation. On the contrary, evaporation increases significantly with capillary pressure. Qualitatively, reconstructed images of the GDL indicate that the gas/liquid interface grows with capillary pressure too. The evaporation is then dependent on the water surface in contact with air. Results obtained at the Tomcat beamline present similar evolutions as the one obtained in laboratory even though the absolute values vary.

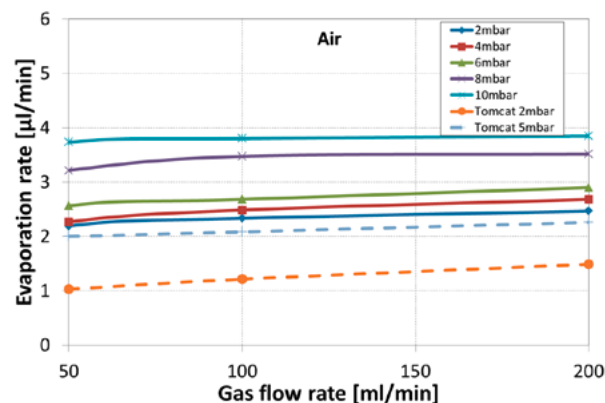
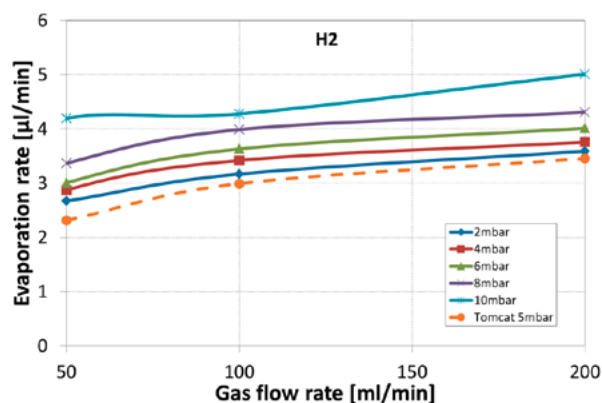


Figure 2. Global evaporations obtained in laboratory (plain lines) and at the Tomcat beamline (dashed lines) for different capillary pressures and air flow rates.

These differences may be attributed to cell assembly details, since it is difficult to accurately reproduce compression and starting capillary pressure of the injection.



**Figure 3.** Global evaporations obtained in laboratory (plain lines) and at the Tomcat beamline (dashed lines) for different capillary pressures and hydrogen flow rates.

Evaporation rates shown in Figure 3 were obtained in similar conditions as the ones in Figure 2 except that hydrogen is used instead of air. The evaporation seems to be slightly more sensitive to the hydrogen flow rate. Still capillary pressure i.e. saturation (or liquid/gas interface area) also plays a significant role. By comparing the values obtained at the same gas flow rate and capillary pressure, one can observe that evaporation is always higher when using hydrogen. This highlights the role of the diffusion in the porous substrate in the evaporation process.

Different transport mechanisms are involved during water removal. Figure 4 describes a possible scenario. First vapour has to be produced which can be idealized by discrete sources at the interface between liquid and gas. Once produced, vapour is transported from all discrete sources via diffusion towards the channel. Finally the vapour is evacuated from the channel by convection.

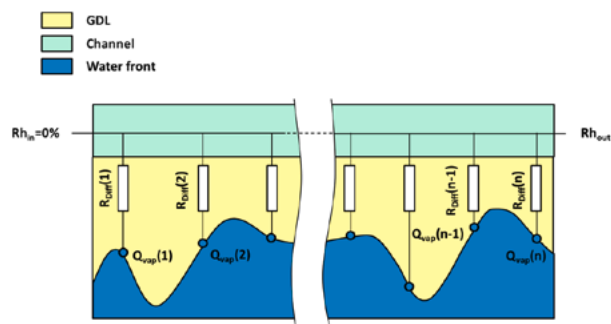


**Figure 4.** Schematic of the different vapour transport mechanisms occurring in the GDL.

Vapour production, diffusion in the GDL and convection in the channel are the relevant processes. The processes are coupled in series and one of these steps may be rate-limiting.

The local evaporation rate is assumed to be dependent on temperature and the local relative humidity. The liquid/ gas interface area may also have an influence.

The diffusional transport depends on the path length of the vapour in the porous structure and the local vapour pressure in the channel. A shorter transport distance enables faster vapour transfer from GDL to channel. High saturation, meaning an advanced water front line, will therefore promote higher vapour fluxes. In addition, it is clearly seen that diffusion of

vapour is accelerated by hydrogen as the carrier gas due to higher inter-diffusion coefficients than in air.

Finally, the convection appears to have less influence on the overall evaporation rate. This may be due to the short dimension of the channel combined with relative high gas flow rate. Nevertheless, in longer channels vapour pressure is expected to vary more. This would imply an evaporation rate gradient between the channel inlet and outlet.

This study has potential applications for all fuel cell numerical simulations considering two phase transport [2, 3]. Up to now the evaporation in these simulations was mainly accounted for based on hypothetical numbers.

## Acknowledgement

The results are part of a common project with A.Z. Weber (LBNL, Berkely) and I. Zenyuk (Tufts University, Mdeford). The authors are grateful for the technical support by Marcel Hottiger and Thomas Gloor.

## References

- [1] A. Lamibrac, J. Roth, M. Toulec, F. Marone, M. Stampanoni, F.N. Büchi, *J. Electrochem. Soc.* **163**, F202–F209 (2016).
- [2] B. Straubhaar, J. Pauchet, M. Prat, *Int. J. Hydrogen Energ.* **40**, 11668–11675 (2015).
- [3] I.V. Zenyuk, E. Medici, J. Allen, A.Z. Weber, *Int. J. Hydrogen Energ.* **40**, 16831–16845 (2015).

## The influence of phosphoric acid loss on HT-PEFC performance and long term durability

S.H. Eberhardt, T. Lochner, F.N. Büchi, T.J. Schmidt

phone: +41 56 310 2411, e-mail: felix.buechi@psi.ch

HT-PEFCs operate at temperatures of 160–190 °C. The phosphoric acid electrolyte has a small but finite vapour pressure at these intermediate temperatures and its evaporation might be a life limiting factor considering targeted life-times of 50'000 operating hours. Phosphoric acid (PA) evaporation rates can be measured for operating HT-PEFC. However, literature data [1, 2] is inconsistent and persistently given in mass per active area for a given temperature, stoichiometry and current density. Consequently, a change in operating conditions might result in vastly different electrolyte loss rates. The existing data base is not sufficient for life-time predictions.

The aim of this work is to correlate operating conditions and operating time with electrolyte inventory to predict fuel cell lifetime [3]. The focus is set on clarifying the effects of gas flow rate, cell temperature and current density on the phosphoric acid loss by evaporation. PA losses are evaluated by condensation at the outlet of 45 cm<sup>2</sup> cells and the loss rates are validated with an accelerated stress test at 190 °C where the influence of phosphoric acid inventory on different performance loss mechanisms is investigated.

### Experimental

All experiments were carried out with BASF Celtec membrane electrode assemblies (MEA). These MEAs consist of a H<sub>3</sub>PO<sub>4</sub> doped polybenzimidazole (PBI) membrane with an acid loading of 36 mg<sub>H<sub>3</sub>PO<sub>4</sub></sub> cm<sup>-2</sup> ± 6%. The electrodes consist of Pt/Vulcan XC-72 supported platinum catalyst with a loading of 1 mg<sub>Pt</sub> cm<sup>-2</sup> on anode and cathode, respectively, coated onto SGL 38 carbon paper gas diffusion layers (GDL) including a microporous layer.

Tests were performed on 45 cm<sup>2</sup> active area single cell setups. Break-in was done for 48–120 h at 160 °C and stoichiometries of  $\lambda_{H_2}/\lambda_{air} = 1.2/2.0$ . For the accelerated stress test, the fuel cell was operated at 190 °C, 0.2 A cm<sup>-2</sup> and gas flow rates of 100 NL h<sup>-1</sup>/50 NL h<sup>-1</sup> on cathode/anode side. Standard conditions (0 °C, 101'325 kPa) are indicated for gas volumes by NL. Otherwise, the volume of gas is calculated at the respective temperature.

A Tafel slope analysis was carried out to determine the different overpotential contributions [2]. Polarization curves with H<sub>2</sub>-air ( $\lambda_{H_2}/\lambda_{air} = 1.2/2$ ) and H<sub>2</sub>-O<sub>2</sub> ( $\lambda_{H_2}/\lambda_{O_2} = 1.2/9.5$ ) were recorded in time intervals of 100–200 h.

Phosphoric acid loss was determined during fuel cell operation by condensing the PA/H<sub>2</sub>O exhaust vapor in a polypropylene bottle. Sample containers were emptied every 24–300 h after flushing the PFA flange and tube between sample container and fuel cell with 50 ml of deionized water. Therefore, all phosphoric acid that condensed between cell and sample container is accounted for. The concentration of the water/phosphoric acid mixture was subsequently analyzed by ion chromatography (IC).

### Results

In Figure 1 the phosphoric acid concentration in the off-gas stream of the cathode is presented as a function of temperature from 160–190 °C and fuel cell inlet gas flow rates. It can be seen that in the temperature range of 160–180 °C the PA content in the gas scales exponentially with temperature but is independent (within measurement accuracy) of flow rate or current density. At 190 °C the evaporation rates still increase compared to lower temperatures but the PA content in the gas of the cathode deviates significantly for high gas flows. A limitation by diffusive gas phase transport or evaporation rate becomes apparent at temperatures  $\geq 190$  °C.

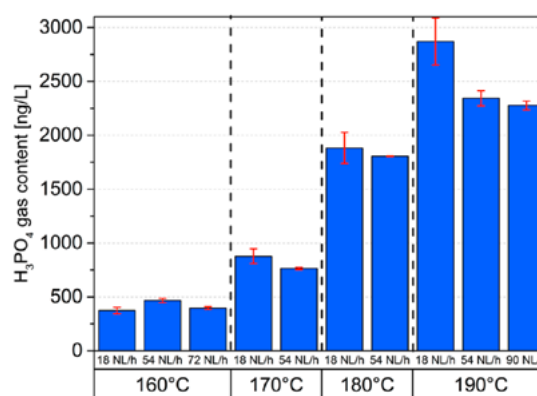


Figure 1. Phosphoric acid content in the exhaust gas stream of the cathode as a function of temperature and gas flow rate [3].

A comparison of PA gas content for a phosphoric acid fuel cell (PAFC) [4] and the cathode gas content of a HT-PEFC is shown in Figure 2. In the range of 160–180 °C the linear increase (in the semi-log plot) and overlapping values in PA gas content for both technologies further confirm the suggested PA loss by vapour saturation.

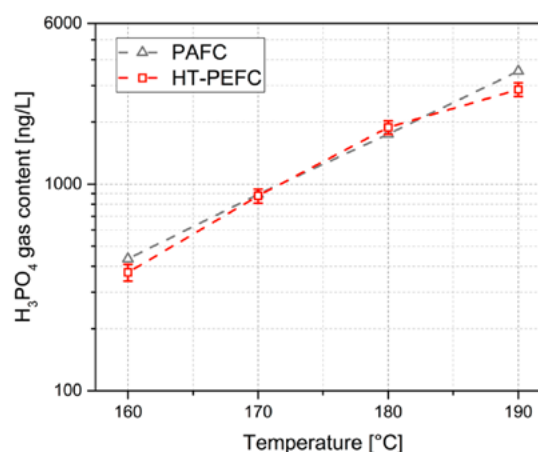
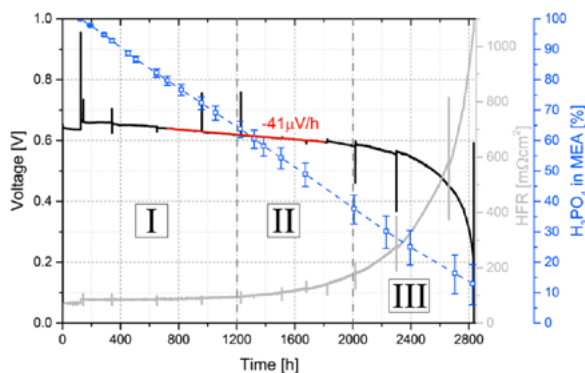


Figure 2. PA content in the exhaust gas stream of a HT-PEFC (cathode gas stream  $\lambda_{air} = 2$ ) and a PAFC (data reproduced from ref. [4]) as a function of temperature [3].

In Figure 3 voltage profile, high frequency resistance and measured PA loss of the accelerated stress test are plotted. During the first 2000 h of operation an approximately linear voltage degradation of  $41 \mu\text{V h}^{-1}$  was observed. Up to 2000 hours, the non-linear increase of the HFR is too weak to dominate voltage degradation and indicates overlapping degradation modes. Only after 2000 h the exponential increase in ohmic resistance does ultimately lead to fuel cell failure at the 2830 hour mark.



**Figure 3.** Cell voltage (black curve), high frequency resistance (HFR) (gray curve) and the measured phosphoric acid loss as a function of time. Operating conditions: 190 °C; 50 NL / 100 NL h<sup>1</sup> H<sub>2</sub>/Air; 0.2 A cm<sup>-2</sup> [3].

The overpotential contributions determined by air/O<sub>2</sub> polarization curves are depicted in Figure 4. In region I the oxygen reduction overpotential increases by about 30 mV. It has been pointed out that this decrease in cathode kinetics during the first 500–1000 h can mainly be attributed to platinum particle growth [2]. The mass transport overpotential also increases in region I. This degradation effect can most probably be attributed to changes in hydrophobicity of the catalyst layer, resulting in higher saturations with PA. This effectively increases mass transport resistances. The loss of ECSA could potentially also be attributed to a deficiency of electrolyte within the electrodes, effectively decreasing the three phase boundary but the high PA mobility and strong increase of  $\eta_{\text{mix}}$  render this highly unlikely. Performance loss due to increases in ohmic resistance can be neglected during the first 1200 h, leading to the conclusion that a loss of up to 40% PA (c.f. Figure 3) is of no concern for this kind of MEA.

Region II is characterized by a stabilization of oxygen reduction and mass transport overpotentials. Ohmic resistance on the other hand increases strongly from 1200 operating hours onwards. This can potentially be attributed to an increase of proton resistance of the membrane concomitant with an increase in contact resistance due to loss of electrolyte.

In region III, fuel cell degradation is again mainly driven by the evaporation of phosphoric acid as can be seen by a strong increase in  $\eta_{\text{IR}}$ . This corresponds well to literature data [5] where a strong decrease in ionic conductivity occurs for PPA processed m-PBI membranes for PA/PBI ratios < 8–10. Furthermore, at 2300 h, mass transport improves slightly. This can be interpreted as evaporation of excess PA in the electrodes and consequently easier access for reactant gas to the catalyst layer. Increased loss of PA from the electrodes and reduction of the three phase boundary area then cause a strong increase in oxygen reduction reaction overpotential. This is promptly followed by the fuel cell failure after 2830 h.

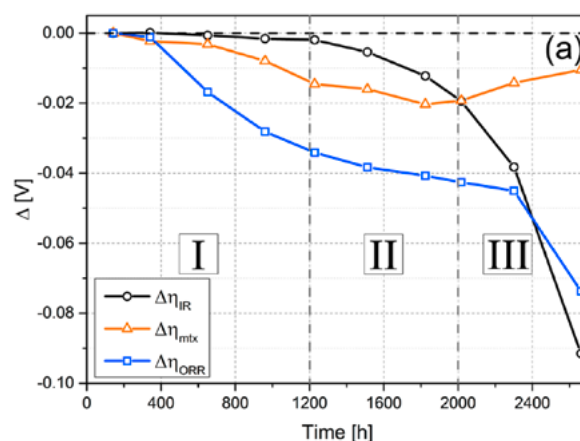


**Figure 4.** Voltage losses as a function of time at 0.2 A cm<sup>-2</sup> for oxygen reduction kinetics  $\eta_{\text{ORR}}$ , mass transport  $\eta_{\text{mix}}$  and ohmic overpotentials  $\eta_{\text{IR}}$  with respect to BoL [3].

## Conclusion

It was found that PA loss by evaporation was driven by PA gas saturation at temperatures  $\leq 180$  °C. Consequently, PA loss rates can be precisely calculated using the off-gas flow rates. Indications for diffusive gas phase transport or evaporation rate limitation at a temperature of 190 °C were found. The correlation of electrolyte inventory and fuel cell performance was explored with an accelerated stress test at 190 °C and high gas flow rates. Within 2830 h of operation  $\approx 90\%$  of the phosphoric acid was lost from the MEA. The fuel cell could sustain a loss of  $\approx 40\%$  without a significant increase in ohmic resistance. In the first 1200 h, fuel cell degradation was driven by kinetic and mass transport losses due to platinum particle growth and changes in hydrophobicity of the catalyst layer. Subsequently, phosphoric acid loss induced increased ohmic losses concomitant with kinetic and mass transport improvements, possibly due to advantageous electrolyte distribution within the electrodes. The final fuel cell failure was attributed to electrolyte starvation within the electrodes, caused by insufficient resupply of PA from the membrane or even catalyst layer detachment. To achieve lifetime requirements also at temperatures above 160 °C and high current densities, an advanced phosphoric acid electrolyte management seems inevitable.

## Acknowledgement

Financial support from BASF SE, software and electronic support by T. Gloor and support with the test bench by T. Engl are gratefully acknowledged.

## References

- [1] S. Yu, L. Xiao, B.C. Benicewicz, *Fuel Cells* **8**, 165–174 (2008).
- [2] T.J. Schmidt, in *Polymer Electrolyte Fuel Cell Durability*, F.N. Büchi, M. Inaba, T.J. Schmidt, Editors, 199–221, Springer New York (2009).
- [3] S.H. Eberhardt, T. Lochner, F.N. Büchi, T.J. Schmidt, *J. Electrochem. Soc.* **162**, F1367–F1372 (2015).
- [4] A. Seya, T. Harada, *Fuji Electr. Rev.* **47**, 11–16 (2001).
- [5] K.A. Perry, K.L. More, E. Andrew Payzant, R.A. Meisner, B.G. Sumpter, B.C. Benicewicz, *J. Polym. Sci. Part B Polym. Phys.* **52**, 26 (2014).

## H<sub>2</sub>/O<sub>2</sub> PEFC system in an uninterruptible power supply application with extended autonomy time

F. Runtsch, C. Peter, M. Ammann, U. Hannesen<sup>1</sup>, M. Birrer<sup>2</sup>, C. Zumbühl<sup>3</sup>, U. Trachte<sup>3</sup>, P. Sollberger<sup>3</sup>, F.N. Büchi

phone: +41 56 310 2886, e-mail: florian.runtsch@psi.ch

Uninterruptible Power Supplies (UPS) are used to provide emergency power for critical electrical loads like antennas, hospitals or IT centres when the input power source fails. Since for many applications, commercial UPS systems use batteries as energy source, autonomy time scales with battery capacity and thus cost and space. Polymer electrolyte fuel cell (PEFC) technology, where energy is stored more compact in hydrogen (and oxygen) offers the option to increase system autonomy time with much reduced space requirements. In order to use fuel cell technology and still maintain fast reaction to mains failure, the advantage of highly dynamic energy from batteries and the high capacity from H<sub>2</sub>/O<sub>2</sub> PEFCs are combined.

The fuel cell system was developed by Swiss Hydrogen SA (formerly Belenos Clean Power Holding Ltd) in collaboration with the Paul Scherrer Institute and integrated into the UPS system by the project partners. A special topology with three current collectors (one additional collector in the centre of the stack) was used for convenient interfacing with the ABB power inverter modules. The system will be used to provide uninterruptible energy for a gas bottling plant at PanGas AG.

### Experimental

Figure 1 shows a schematic setup of the UPS system with three different system parts (Rack 1, Rack 2, EXT). Rack 1 was realized by ABB Schweiz AG and the Lucerne University of Applied Sciences and Arts. It integrates the UPS modules responsible for the connection to the grid, the communication and the data acquisition. Rack 2 shows the UPS power source with a H<sub>2</sub>/O<sub>2</sub> PEFC system combined with batteries. The external gas supply (EXT) with H<sub>2</sub> and O<sub>2</sub> was provided by PanGas AG.

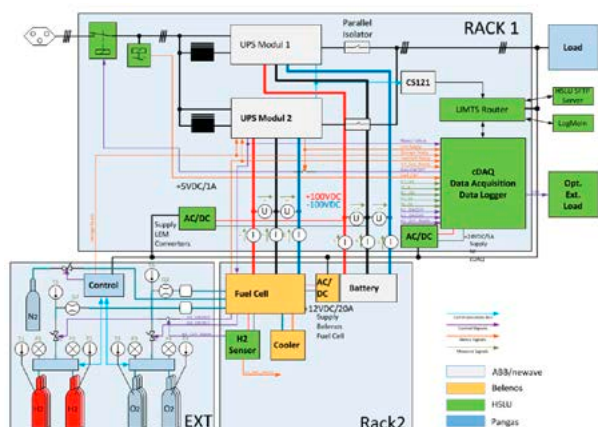


**Figure 1.** Schematic Measurement Cabinet. Rack 1: ABB UPS Modules; Rack 2: Belenos/PSI Fuel Cell rack; EXT: PanGas gas supply

### Results

The nominal power of 15 kW is provided by a H<sub>2</sub>/O<sub>2</sub> PEFC system with a 220 cell stack (located in Rack 2). A 32 lead acid battery-pack is placed below the system. Two cylinder bundles of 12x50 L bottles, each filled with 200 bar compressed gas, feed the system with H<sub>2</sub> (red) and O<sub>2</sub> (grey). An autonomy time up to 20 h at nominal power is possible. A commercial UPS with only batteries as energy storage and a comparable autonomy time would require about 10 times the space as the H<sub>2</sub>/O<sub>2</sub> PEFC system.

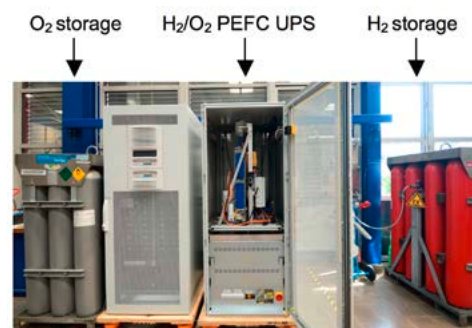


**Figure 2.** Left: ABB UPS Modules (Rack 1). Right: PSI fuel cell rack (Rack 2) with battery-pack. Two cylinder bundles (EXT) filled with H<sub>2</sub> (red) and O<sub>2</sub> (grey) were arranged close to the racks.

Figure 3 shows a current plot measured during a 5 kW load test. The graph visualises the influence of the DC/AC converter to the current drawn from all three current collectors. An oscillation with grid frequency at 50 Hz was observed at all current collectors. In addition, the individual currents vary remarkably during this period.

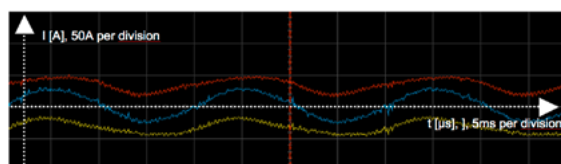


**Figure 3.** Current plot of the upper current collector (red), the lower current collector (yellow) and the central current collector (blue) during a 5 kW load test.

### Conclusions and Outlook

A H<sub>2</sub>/O<sub>2</sub> PEFC system was successfully incorporated in an UPS. The combination of a battery for quick start-ups and the H<sub>2</sub>/O<sub>2</sub> PEFC for long autonomy times was realized as a demonstrator for a possible future cost-efficient UPS solution. Long term tests will show if the oscillating currents influence the performance and durability of the H<sub>2</sub>/O<sub>2</sub> PEFC.

### Acknowledgement

Funding from the Swiss Federal Office of Energy (SFOE) is gratefully acknowledged.

<sup>1</sup> Swiss Hydrogen SA, Fribourg

<sup>2</sup> ABB Schweiz AG, Baden

<sup>3</sup> Lucerne University of Applied Sciences and Arts, Lucerne

## Analysis of image quality of reduced scan time operando X-ray tomographic microscopy of PEFC

J. Eller, F. Marone, F.N. Büchi

phone: +41 56 310 2396, e-mail: jens.eller@psi.ch

X-ray tomographic microscopy (XTM) of liquid water in polymer electrolyte fuel cells (PEFC) has proven a valuable tool in order to improve understanding of water transport in the gas diffusion layer (GDL). The visualization and quantification of liquid water in PEFC on the pore scale level is indispensable for the understanding and modeling of two-phase water transport processes and PEFC performance improvements, as recently shown by Toyota during the introduction of the PEFC powered MIRAI car [1]. So far, operando X-ray tomographic microscopy was restricted to constant operation conditions since the minimal XTM scan time of ten seconds [2] was not sufficient to capture the dynamics of the water distribution under transient operation.

In order to enable transient 4D XTM studies of liquid water in PEFC, the consequences of reduced scan times of monochromatic XTM scans on the data quality was studied. Different settings of exposure time and number of projections that result in XTM scan time around a second are evaluated in terms of signal-to-noise ratio (SNR) of the tomography data of a test cell. Based on these findings the XTM settings were selected and operando sub-second XTM imaging of a PEFC under dynamic operation was realized [3]. The evolution of the liquid water distribution in the GDL, during a current jump from 0.1 to 1 A/cm<sup>2</sup> is discussed.

### Experimental

The XTM experiments were performed at the TOMCAT beamline of the Swiss Light Source (SLS) at Paul Scherrer Institut, Switzerland. A pco.Dimax camera with 36 GB internal memory was used in combination with the 2–4x zoom microscope by ELYA solutions set to a voxel size of 3 μm. The monochromatic X-ray radiation at 13.5 keV generated by a Ru/C multilayer monochromator with an energy bandwidth of 2–3% was used during the imaging experiments.

The consequences of reduced scan times on the SNR were examined for a cell with a single channel flow field as described in [4] (termed «simplified cell») and a cell with a two channel flow field [3] (termed «realistic cell»). *Ex situ* scans with different combinations of exposure time (2 to 10 ms) and number of angular projections (201 to 1001 projections) have been taken for the simplified and realistic cell at 13.5 keV beam energy. Additionally, SNR data was extracted from operando operation of [5] at 16 keV to study the effect of increased beam energy. Since the gray scale levels of water and carbonaceous structures are very similar and for simplicity of the analysis, the SNR was characterized for the signal and noise levels of the flow field material and the void in the channel. This value can be seen as a good representative for the SNR between liquid water and void, which is difficult to determine within the GDL domain. Here, the SNR is defined as

$$SNR = \frac{MEAN(FF) - MEAN(VOID)}{STDDEV(VOID)} \quad (1)$$

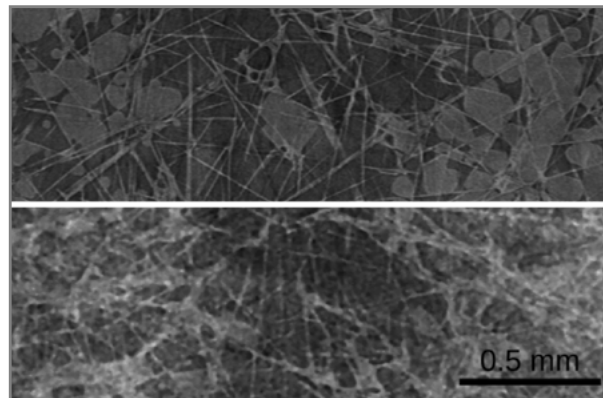


**Figure 1.** Comparison of in-plane cut of a 8 s operando XTM scan (top) and a scan of 0.75 s (bottom). While fine carbon fiber matrix can't be resolved properly in the fast sub-second scan, the larger structures of the water clusters can be identified.

where FF and VOID represent the gray scale values of a rectangular 2D domain in the flow field structure and the void in the gas channel, respectively.

For operando XTM imaging a simplified single channel cell with Toray TGP-H060 (20 %wt PTFE) GDL paper and a Solvico H200 catalyst coated membrane was used. The active area of the cell was reduced by laser processing of the CCM to 10 mm<sup>2</sup> to fit into the field of view. The cell was operated at 30 °C cell temperature with flow rates of 7.4 ml/min oxygen and 14.8 ml/min hydrogen at about 50% relative humidity of the gas feeds humidified at room temperature. The current density was increased from 0.1 A/cm<sup>2</sup> (dry conditions) to 1.0 A/cm<sup>2</sup> (flooding conditions). The development of the liquid water distribution was depicted by 30 scans (3 ms exposure time, 251 projection angles, 0.75 s scan time) every 3 s over a period of 87 s until the 36 GB of camera RAM were filled, while the current density was changed immediately after the first scan was completed.

### Results

A clearly lower image quality of the operando XTM data can be expected for a reduction of the photon count per tomographic scan by a factor of about 10. Figure 1 shows a comparison with respect to the image quality comparing a scan of 0.75 s scan time (3 ms exposure time, 251 projections) with a scan at the standard settings of 8 s scan time (8 ms exposure, 1001 projections). The dramatically increased noise level of the short scan is evident.

An analysis of the SNR of *ex situ* test scans is shown in Figure 2. On a logarithmic time scale, the SNRs of different sampling conditions show a linear dependency for the different cell types. For the simplified cell, the SNR decreases by a factor of about 3 from about 11 for a 8 s scan to SNR values of 3–4 for scans of 0.5 to 1 s. The larger cell diameter of the realistic cell reduces the SNR compared to the simplified cell by more than 30% and sets even higher requirements to the segmentation

pipeline. The freeze-start experiments of [5] at 16 keV provide a promising outlook that the SNR levels can be recovered or improved at shorter scan times with a modification of beam energy even for the realistic two-channel cell. The reduced SNR levels of the sub-second XTM data impose modifications to the segmentation workflow that was introduced for higher quality scans at steady state operating conditions [4].

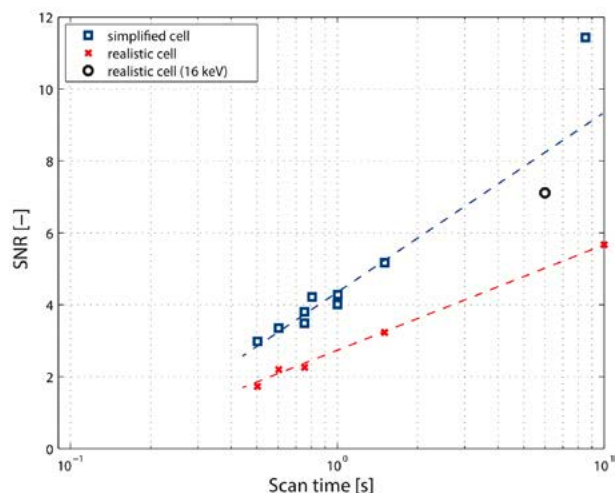


**Figure 2.** Comparison of SNR values for different scan times and different cell types; beam energy was 13.5 keV except for the measurements at 16 keV [5] (black circle) (Adapted from [3]).

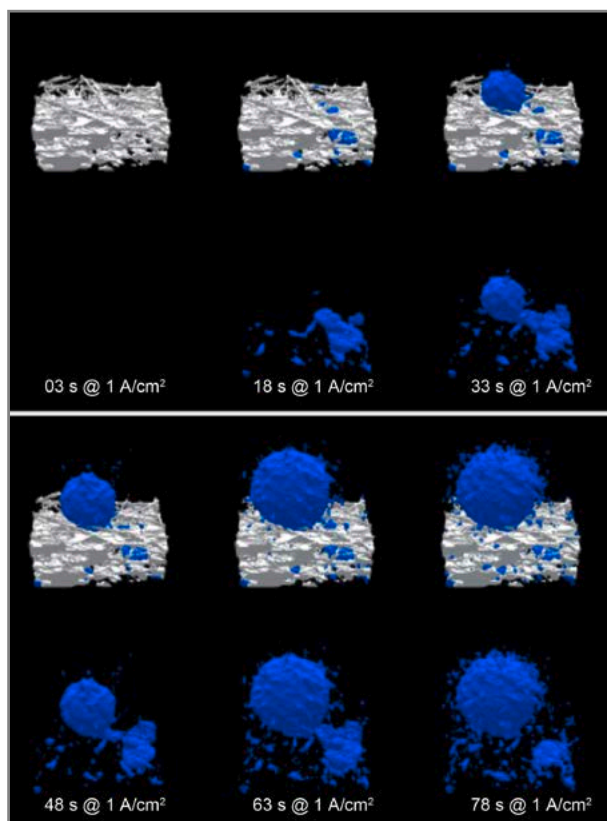


**Figure 3.** Surface rendering of the liquid water for selected XTM scans. The liquid water is shown together with (top) and without (bottom) the solid GDL for each time-step. (Adapted from [3].)

During the operando XTM experiment the temporal resolution of 3 s between the scans allowed to depict the build-up of the water saturation after increasing the current density to 1 A/cm<sup>2</sup>. Different phenomena, such as the locations of ini-

tial water break-through points, rearrangement of the water distribution over multiple connected pores, as well as breakdown of transport paths can be observed. The temporal evolution of the liquid phase in a sub-volume of the GDL under the channel is exemplary shown for a few snapshots in Figure 3. While the GDL was dry before the current density jump (0 s), a substantial amount of water has already accumulated and reached almost break-through to the GDL surface after 18 s. Interestingly, break-through for this water cluster is achieved only after a growth in in-plane direction (33 s). After break-through the droplet grows until its connection to the feeding cluster disconnects between the scans after 63 s and 78 s. The droplet can't grow any further due to the snap-off, and starts to shrink due to evaporation (not shown).

In summary, the reduced XTM scan time enables to study the evolution of the liquid water distribution in the GDL during transient PEFC operation conditions. Secondly, the shorter scan times reduce the X-ray dose to the cell and increase the number of XTM scans before radiation induced degradation biases the electrochemical properties and consequently the water distribution.

### Acknowledgement

Precise machining work by M. Hottiger, software and electronic support by T. Gloor, and support at the beamline and during preparation of the experiment by A. Lamibrac, G. Mikuljan, R. Mokso and J. Roth is gratefully acknowledged.

### References

- [1] N. Konno, S. Mizuno, H. Nakaji, Y. Ishikawa, *SAE Int. J. Alt. Power* **4**, 123 (2015).
- [2] J. Eller, J. Roth, R. Gaudenzi, S. Irvine, F. Marone, M. Stamparoni, A. Wokaun, F.N. Büchi, *ECS Trans.* **50**, 477 (2013).
- [3] J. Eller, F. Marone, F.N. Büchi, *ECS Trans.* **69** (17), 523 (2015).
- [4] J. Eller, T. Rosén, F. Marone, M. Stamparoni, A. Wokaun, F.N. Büchi, *J. Electrochem. Soc.* **158**, B963 (2011).
- [5] I. Mayrhuber, F. Marone, M. Stamparoni, T.J. Schmidt, F.N. Büchi, *ChemElectroChem.* **2** (10), 1551 (2015).

## Why does electrolyzer performance not care about pressure?

M. Suermann, M. Ammann, T. Gloor, T.J. Schmidt, F.N. Büchi

phone: +41 56 310 5763, e-mail: michel.suermann@psi.ch

Polymer electrolyte electrolysis cells (PEEC) are used to decompose water into oxygen and hydrogen. The gases are commonly stored in pressurized pipelines or gas tanks. The needed pressure level heavily depends on the final application, e. g. for mobility around 800 bar are needed. Conventionally the gases are compressed mechanically following an adiabatic or isothermal compression causing distinct losses. In contrast high pressure PEEC seems to offer more efficient electrochemical compression. Even, almost no additional losses of cell performance were reported [1]. Consequently some beneficial processes have to take place. Here we would like to give a short insight where and how those beneficial influences appear based on experimental data of up to 100 bar balanced pressure.

### Experimental

For this project a new test bench and self-made PEEC is designed for high pressure operation (Figure 1). Even if gas pressurization is done electrochemically, the water supply has to be provided at any pressure using a HPLC pump. On the anode ( $O_2$ ) the water is actively recirculated using a membrane pump, while at the cathode ( $H_2$ ) natural convection is used. The produced gases are separated from the water in the gas/liquid pressure tanks.

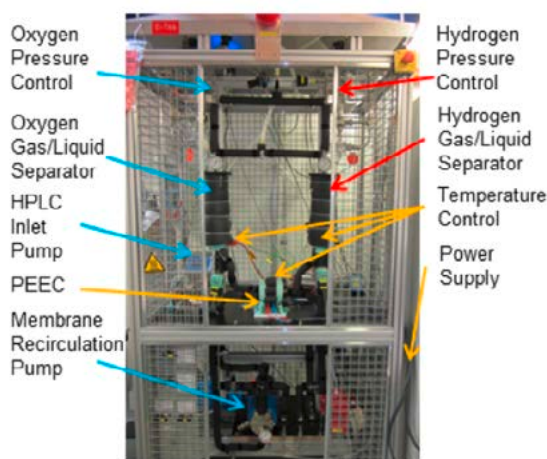


**Figure 1.** Picture shows the high pressure test bench. Labelling includes the most important valves and instruments.

### Methods

In this work galvanostatic polarization curves up to  $5 \text{ A/cm}^2$  are presented. Additionally the high frequency resistance (HFR) was measured at 1 kHz. Using the HFR different overpotentials (kinetic, ohmic and mass transport) can be distinguished as a function of pressure and current density. Using the HFR the  $iR$ -free voltage can be calculated from which at low current densities ( $< 30 \text{ mA/cm}^2$ ), where little to no mass transport losses (mtx) are assumed, the Tafel-slope is determined. Extrapolation results in the  $iR$ - and mtx-free voltage. The kinetic overpotentials are obtained from the difference between the  $iR$ - and mtx-free voltage and the pressure and

temperature dependent thermodynamic equilibrium potential, obtained from Nernst's law (Equation 1) assuming an activity of water of unity and ideal gas behavior.

$$E^0(p, T) = E^0(T) + \frac{R \cdot T}{2F} \ln \left( \frac{a(H_2) \cdot \sqrt{a(O_2)}}{a(H_2O)} \right) \quad (\text{Equation 1})$$

### Results

According to Equation 1 the thermodynamic equilibrium potential is increasing when the gas pressure is increased. Theoretically this increase is expected for the cell voltage as well. However, as shown in Figure 2 the cell voltage is almost independent from the gas pressure. According to the overpotential analysis, the beneficial influences of pressurized PEEC result from the kinetic losses between the  $iR$ - and mtx-free voltage and the thermodynamic equilibrium potential. Only at very low current densities the cell voltage increase due to higher operating pressure was observed (inset in Figure 2).

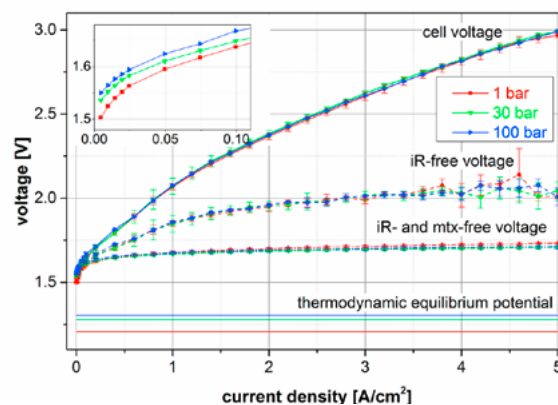


**Figure 2.** Polarization curves at  $50 \text{ }^\circ\text{C}$  for 1, 30 and 100 bar pressure using a commercial Nafion 117 catalyst coated membrane ( $4 \text{ cm}^2$  active area); inset shows low current densities.

### Conclusions and Outlook

It is (again) shown that the cell performance of a PEEC is almost independent from the operating pressure. This means that even the theoretical losses of electrochemical compression are compensated by a reduction of mainly the kinetic overpotentials. This may be due to a better penetration of the water in the porous catalyst layer, a better wetting of small catalyst pores or even a change in the reaction mechanism – further research is required.

### Acknowledgement

Funding by Swiss Federal Office of Energy (SFOE) and Belenos Clean Power is gratefully acknowledged.

### References

- [1] S.A. Grigoriev, V.I. Porembskiy, S.V. Korobtsev, V.N. Fateev, F. Auprêtre, P. Millet, *Int. J. Hydrogen Energy* **36**, 2721–2728 (2011).

# SCIENTIFIC ACHIEVEMENTS 2015

FUEL CELLS & ELECTROLYSIS –

MATERIALS

## Open circuit voltage hold test of radiation grafted membranes

A. Albert, T.J. Schmidt, T. Lochner, L. Gubler

phone: +41 56 310 4539, e-mail: albert.albert@psi.ch

Radiation grafted membranes have been investigated as alternative for Nafion® membranes in fuel cell and electrolyser application, since they show lower area resistance, better gas barrier, and mechanical properties [1]. One of the important aspects for the lifetime of a fuel cell or electrolyser system is the stability of the membranes. In order to investigate the membrane's stability, accelerated stress tests (AST) are often applied. They are based on the known membrane degradation mechanisms.

One of the main degradation phenomena observed in the fuel cell is the attack by radicals which are formed in the presence of H<sub>2</sub>, O<sub>2</sub> and the Pt catalyst. The OCV hold-test is an established AST protocol in fuel cell research to assess membrane stability. At OCV, the formation of radicals which can attack the membrane, is maximised. Although it is still unclear whether radical formation also occurs in the electrolyser, OCV hold tests can be used to give an indication of membrane oxidative stability. This AST will be used in this work to assess the stability of the membranes intended for electrolysers.

The stability of radiation grafted membranes with styrene (St),  $\alpha$  methylstyrene (AMS), acrylonitrile (AN) and 1,3 diisopropenylbenzene (DiPB) combinations is investigated (Figure 1). These membranes are intended for the electrolyser application and synthesised from 50  $\mu$ m ETFE base film. The OCV hold tests are performed for 120 hours. The extent of degradation is investigated by comparing the area resistance and hydrogen crossover value of the membranes before and after the AST.

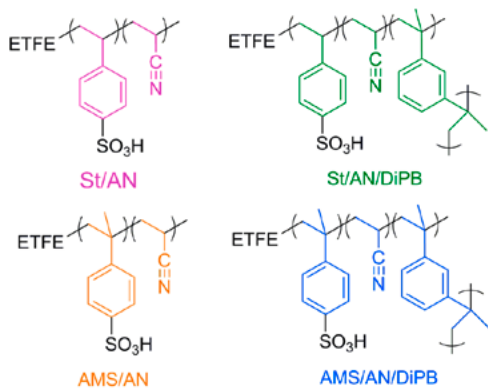


Figure 1. Chemical structure of radiation grafted membranes.

### Experimental

The detailed synthesis of the St/AN, St/AN/DiPB, AMS/AN, AMS/AN/DiPB radiation grafted membranes is described elsewhere [1], as well as the experimental details for the OCV hold test [2].

### Results

The values of hydrogen crossover and area resistance of the radiation grafted membranes before and after the OCV hold test are shown in Figure 2. Before the OCV hold test, all the radiation grafted membranes have lower hydrogen crossover

and area resistance than Nafion® 115 and 117 membranes, which are state of the art membranes for the electrolyser application. After 120 hours on test, the St/AN membrane exhibited a much higher hydrogen crossover value. Meanwhile, the other radiation grafted membranes do not show any significant change. The area resistance values of the uncrosslinked radiation grafted membranes increase around 30 mOhm-cm<sup>2</sup> for both St/AN and AMS/AN, and the crosslinked membranes 70 mOhm-cm<sup>2</sup> for St/AN/DiPB and 60 mOhm-cm<sup>2</sup> for AMS/AN/DiPB. The greater increase of area resistance of the crosslinked membranes may be due to degradation. However, it cannot be directly concluded that the crosslinked membranes are less stable than the uncrosslinked membranes, since the St/AN has much higher hydrogen crossover after the test. It is also shown that the membranes based on AMS monomer are more stable in the peroxide-rich environment than the membranes based on St monomer. Therefore, the most stable membrane is AMS/AN, followed by AMS/AN/DiPB, St/AN/DiPB, and St/AN according to this study.

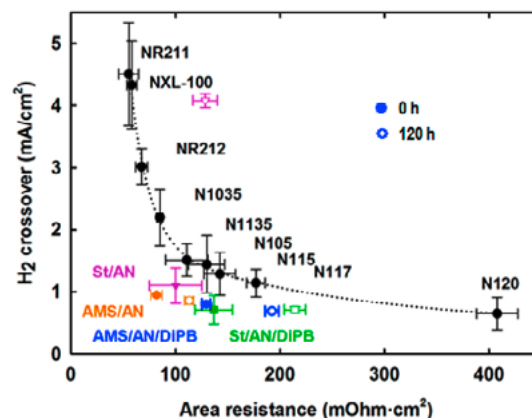


Figure 2. Hydrogen crossover and area resistance values of radiation grafted membranes before and after 120 hours OCV hold test.

### Conclusion

OCV hold tests are used to investigate the oxidative stability of radiation grafted membranes. AMS based membranes, AMS/AN and AMS/AN/DiPB, are more stable than St based membranes, St/AN and St/AN/DiPB.

### Acknowledgement

The research leading to these results has received funding from the European Union's Seventh Framework Programme (FP7/2007–2013) for the Fuel Cells and Hydrogen Joint Technology Initiative under grant agreement n°303484 (NOVEL).

### References

- [1] A. Albert, A.O. Barnett, M.S. Thomassen, T.J. Schmidt, L. Gubler, *ACS Appl. Mater. Interf.* **7**, 22203–22212 (2015).
- [2] A. Albert, T.J. Schmidt, L. Gubler, *PSI Electrochemistry – Annual Report 2014*, 28–29, DOI: 10.3929/ethz-a-007047464 (2014).

## ETFE based e-beam grafted membranes for fuel cells with GMA comonomer

V. Sproll, T.J. Schmidt, L. Gubler

phone: +41 56 310 2673, e-mail: lorenz.gubler@psi.ch

Radiation grafting is a promising and versatile way to produce membranes with tailored characteristics to meet the demands of different applications. Especially in the field of fuel cell membranes, radiation grafted membranes can offer an alternative to perfluorosulfonic acid membranes, such as Nafion® (DuPont), which are currently used as proton conducting membrane (PEM) in polymer electrolyte fuel cells (PEFCs) [1]. The synthesis of the membranes comprises two different steps, the electron beam irradiation of the base film and the modification comprising the grafting of the activated film using selected monomers and subsequent sulfonation. This renders radiation grafting a highly flexible and cost efficient method to combine a wide range of commercially available base films with an easy functionalization by different monomers. Among the large number of base film materials, the partially fluorinated ETFE proved to be a promising candidate for the development of new PEMs [1]. In combination with sulfonated styrene derivatives a competitive fuel cell performance and stability can be achieved. The latter was further improved by the addition of different comonomers to increase, for example, the gas barrier properties of the membrane [1]. One weakness of those membranes still remaining is their behavior at reduced relative humidities (RH) where the proton conductivity decreases significantly. In order to improve this performance loss, one approach is the incorporation of hydrophilic groups leading to enhanced water uptake properties of the membrane. This work presents the copolymerization of styrene (S) and glycidylmethacrylate (GMA), which is used in its hydrolyzed version (diol) as contact lens material and other biomedical applications, due to its large water sorption [2, 3]. After a sulfonation step, the styrene is transformed to styrene sulfonic acid, which provides the proton conductivity. The grafting reaction is briefly summarized in Scheme 1.

### Experimental

The membrane synthesis was conducted similar to what has been reported in our earlier work (deposited dose 5 kGy, reaction temperature 60 °C, monomer concentration 25 vol%) [4]. Three different ratios of S and GMA were used in the grafting solution (styrene molar fraction  $X_S = 0.7, 0.5$  and  $0.4$ ) to obtain different ratios in the grafted film/membrane. The reaction time was varied to determine the grafting kinetics. All films and membranes were characterized gravimetrically and with FTIR spectroscopy. For quantitative compositional analysis by transmission FTIR spectroscopy calibration curves for both homografted films (ETFE-g-PS and ETFE-g-PGMA) were established. The through-plane proton conductivity as a function

of the RH was measured with the 740 Membrane Test System from Scribner Associates Inc. (North Carolina, USA) at a temperature of 80 °C. For further details see reference [5].

### Results

For a reliable and reproducible synthesis of a PEM by radiation grafting, it is essential to know the grafting kinetics of the particular combination of base film and monomers. The grafting kinetics are used to determine the reaction conditions to produce defined grafting levels. Therefore, different mole fractions of S and GMA ( $X_S = 0.7, 0.5$  and  $0.4$ ) in the reaction mixture were used and films with varying grafting level were synthesized. The obtained kinetics are shown in Figure 1.

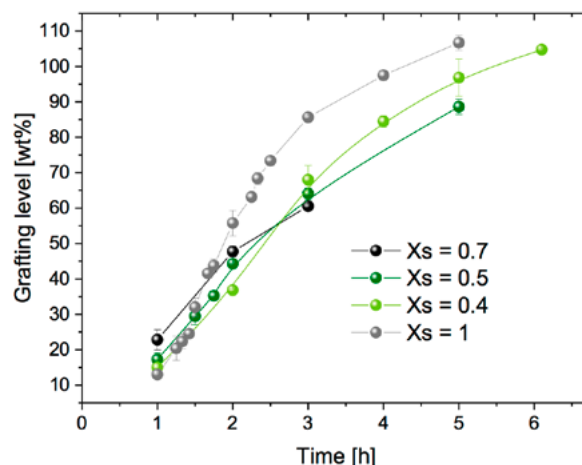
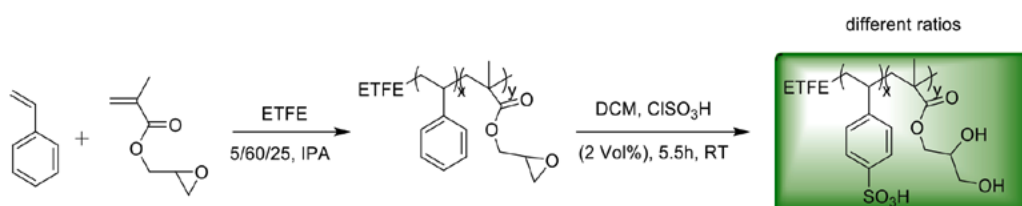


**Figure 1.** Grafting kinetics of ETFE-g-P(S-co-GMA) with different molar ratios of styrene and GMA ( $X_S$ : styrene mole fraction,  $X_{GMA} = 1 - X_S$ ) in the grafting mixture.

The analysis of the resulting dependency of the grafting level on the reaction time shows slight differences. The higher the content of S the faster the initial polymerization. But after this rapid onset the reaction slows down and the reaction mixtures with a higher content of GMA yield a higher grafting level than the one with an  $X_S$  of 0.7 despite their slower initial grafting kinetics.

The functionalization reactions are carried out after the incorporation of the monomers as grafted polymer chains into the base film. This functionalization comprises in the present synthesis two modifications, the sulfonation of the styrene moiety



**Scheme 1.** Reaction procedure for the grafting of S and GMA onto ETFE, followed by sulfonation / hydrolysis.

and the hydrolysis of the GMA group (Scheme 1). Both reactions are carried out simultaneously during the sulfonation with chlorosulfonic acid and subsequent hydrolysis in water.

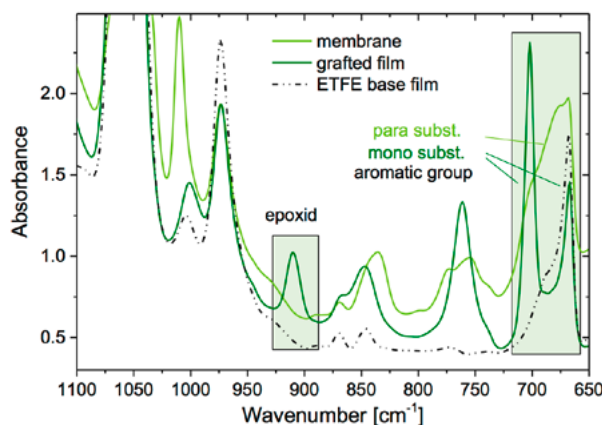


**Figure 2.** IR-spectra of the ETFE base film, grafted film (dark green) and the hydrolyzed membrane (light green).

Complete hydrolysis can be verified via IR-spectroscopy. The oxirane vibration band at  $\sim 900\text{ cm}^{-1}$ , which is clearly visible in the spectrum of the grafted film, completely vanished in the IR-spectrum of the hydrolyzed membrane (marked with «epoxid» in Figure 2). In addition, the sulfonation of the styrene moiety can be confirmed by the characteristic change in the range from  $650\text{ to }720\text{ cm}^{-1}$ , indicating a para-substituted aromatic group (marked in Figure 2).

In order to investigate the influence of the incorporated hydrolyzed GMA, the proton conductivity of the different membranes were measured. The hydrolyzed GMA should increase the water content, especially at low RH and therefore overcome or at least improve the performance of the membrane in this region compared to membranes containing pure sulfonated styrene. The proton conductivity was recorded as a function of RH (Figure 3).

In contrast to the expected trend, the analysis shows that with an increasing fraction of GMA in the membrane, the corresponding proton conductivity decreases over the entire range of RH. Figure 3 also shows the ion exchange capacity (IEC, number of sulfonic acid groups per dry polymer mass) of each membrane produced with the different composition of grafts. Similar to pure styrene grafted membranes, an increased IEC shifts the conductivity curves of the membrane corresponding to a specific composition to higher values. Still, the trend remains: the higher the content of incorporated GMA, the steeper the conductivity decreases towards lower RH.

For similar initial (at 95% RH) conductivities the comonomer systems need a much higher IEC than the all styrene system (compare e.g.  $X_s = 0.7$ ). This indicates that although the water content in a membrane should be a crucial parameter when it comes to proton conductivity in the low RH regime, other effects seem to be dominating. It seems as if the incorporation of GMA has kind of a «diluting effect» that hinders proton conductivity as it was also observed for other comonomers as acrylonitrile.

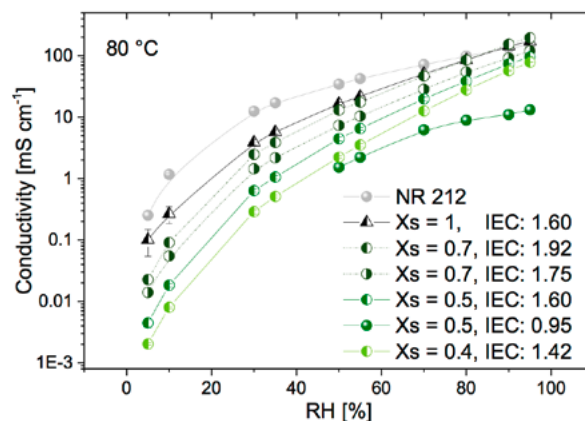


**Figure 3.** Through-plane proton conductivity in dependence of RH for various grafted membranes. The data for Nafion is given as a reference.

Therefore, the introduction of hydrophilic groups to radiation grafted membranes should either be based on much smaller comonomers or ideally on monomers bearing both the strongly acidic and water-uptake enhancing moiety.

## Acknowledgement

Funding by PSI within the framework of the «CROSS Departmental Initiative» is gratefully acknowledged.

## References

- [1] L. Gubler, *Adv. Energy Mater.* **4** (3), 1300827 (2014).
- [2] G. Gates, J.P. Harmon, J. Ors, P. Benz, *Polymer* **44**, 215 (2003).
- [3] H. Mori, A. Hirao, S. Nakahama, *Macromolecules* **27**, 4093 (1994).
- [4] H. Ben youcef, S. Alkan-Gürsel, A. Buisson, L. Gubler, A. Wokaun, *Fuel Cells* **10** (3), 401–410 (2010).
- [5] V. Sproll, T.J. Schmidt, L. Gubler, *Polym. Int.*, in press (2015).
- [6] K. Jetsrisuparb, S. Balog, C. Bas, L. Perrin, A. Wokaun, L. Gubler, *Eur. Polym. J.* **53**, 75–89 (2014).

## Ionic conductivity of radiation grafted membranes doped with phosphoric acid

T. Rojek, T.J. Schmidt, L. Gubler

phone: +41 56 310 4188, e-mail: tomasz.rojek@psi.ch

High-temperature polymer electrolyte fuel cells (HT-PEFCs) offer certain advantages over low-temperature polymer electrolyte fuel cells such as reduced carbon monoxide poisoning of the catalyst allowing the use of the hydrogen-rich fuel stream directly from the reformer [1] and no need for external humidification.

Membranes typically utilised in the HT-PEFC are based on polybenzimidazole polymers (PBIs) doped with phosphoric acid (PA). High loadings of PA allow these materials to exhibit high proton conductivity at temperatures above the boiling point of water. At the same time PA present in the membrane is susceptible to redistribution [2] and evaporation [3] during fuel cell operation.

Our approach is to use radiation grafting of monomers containing nitrogen with a lone electron pair as a method to obtain membranes for the HT-PEFC. The synthesis route used in this study is presented in Figure 1.

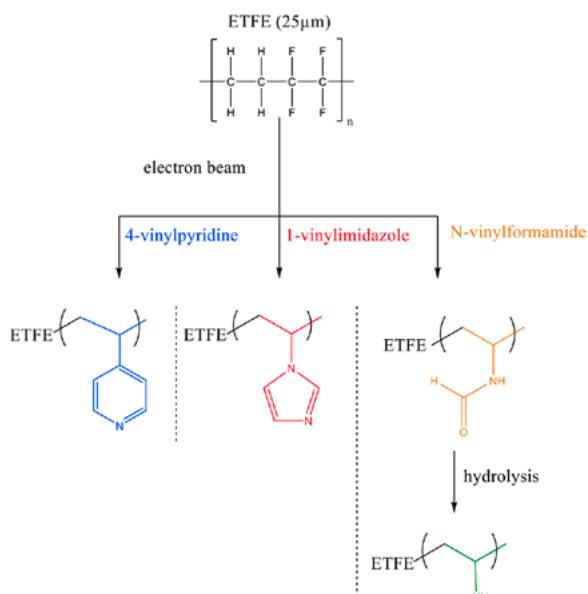


Figure 1. Synthesis route based on radiation grafting.

### Experimental

The synthesis of radiation grafted membranes was conducted by immersing pre-irradiated (100 kGy, electron beam in air) poly(ethylene-co-tetrafluoroethylene) films (Dupont, 25  $\mu\text{m}$  thickness) in a reaction mixture according to Table 1. For all types of membrane the reaction was performed at 60  $^{\circ}\text{C}$ .

Membrane	Monomer	Solvent	Monomer (%vol)
P(ETFE)-g-P(4VP)	4-vinyl pyridine	Isopropanol	50
P(ETFE)-g-P(1VIm)	1-vinyl imidazole	Water	95
P(ETFE)-g-P(NVAm)	N-vinyl formamide	Water	40

Table 1. Grafting reaction parameters.

The grafting parameters were optimised for each of the monomers in order to achieve grafting levels (GL) yielding a density of nitrogen sites with a lone electron pair (N-site density) of approx. 5–6 mmol/g, calculated as:

$$GL = \frac{m_{\text{grafted}} - m_{\text{basefilm}}}{m_{\text{basefilm}}} \cdot 100\% \quad (1)$$

$$N\text{-site density} = \frac{\frac{m_{\text{grafted}} - m_{\text{basefilm}}}{M_w}}{m_{\text{basefilm}}} \quad (2)$$

Where  $m$  is the mass of the corresponding film and  $M_w$  is the molar mass of the monomer.

Conversion of formamide (NVF) functional groups into amine functional groups (NVAm) was done by alkaline hydrolysis. The grafted films were immersed in 2 M NaOH at 80  $^{\circ}\text{C}$  for up to 16 h.

Introduction of the phosphoric acid into the grafted membranes was done by immersing the grafted films in 85 % phosphoric acid at room temperature for 5 days. The acid uptake was determined by means of ion chromatography (Metrohm 882 Compact IC Plus) after leaching it out from the membranes.

Area resistance was determined using a four-probe conductivity head (Scribner Associates) placed in a custom built cell with controlled temperature and relative humidity.

### Results

Incorporation of the desired functional groups during the grafting was confirmed by FT-IR spectroscopy (Figure 2).

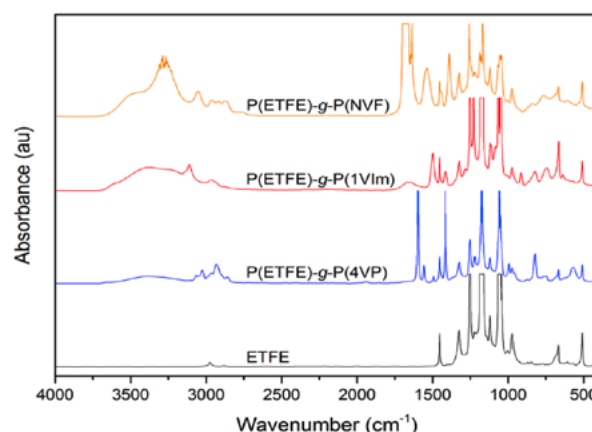
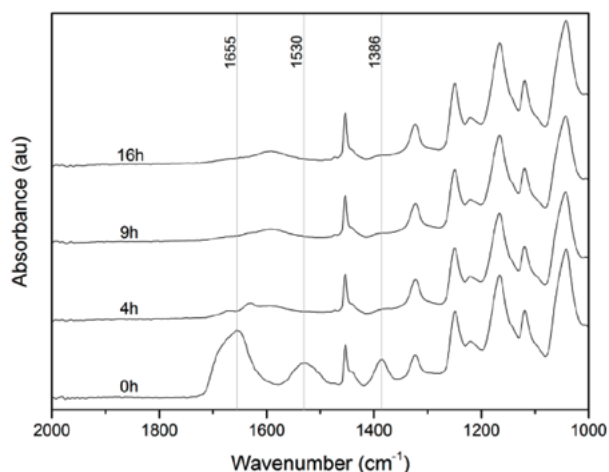


Figure 2. FT-IR spectra of radiation grafted films.

Conversion of grafted NVF into NVAm was monitored as a function of time. As Figure 3 demonstrates, maximum conversion was reached after approx. 9 h, as indicated by the disappearance of peaks at 1655, 1530 and 1386  $\text{cm}^{-1}$  (C=O stretch, N-H bend, and C-H bend, respectively) and appearance of a characteristic peak at 1590  $\text{cm}^{-1}$  ( $\text{NH}_2$  bend.).



**Figure 3.** FT-IR spectra of P(ETFE)-g-P(NVF) upon hydrolysis as a function of time.

By using nitrogen-containing monomers it was possible to obtain membranes with high grafting levels and therefore high nitrogen site densities. The presence of nitrogen sites with lone electron pair resulted in uptake of phosphoric acid by grafted membranes (Table 2).

Membrane	GL (wt%)	N-site density (mmol/g)	Acid uptake (mol/mol N)	Acid content (wt%)
P(ETFE)-g-P(4VP)	144	5.62	3.5 ± 0.2	65 ± 1
P(ETFE)-g-P(1VIm)	91	5.05	3.8 ± 0.1	65 ± 1
P(ETFE)-g-P(NVAm)	83	6.31	1.8 ± 0.1	52 ± 1

**Table 2.** Properties of grafted membranes.

In Figure 4 the area resistance of acid doped membranes is presented. The lowest area resistance can be observed for the P(ETFE)-g-P(4VP) membrane followed by P(ETFE)-g-P(1VIm) and P(ETFE)-g-P(NVAm). This trend corresponds with the acid content trend – membranes with higher acid content exhibit lower area resistance. This is to be expected as the proton conduction mechanism can be attributed to the phosphoric acid itself.

The area resistance of the membranes decreases with increasing temperature up to 160 °C, which is a typical operating temperature for a HT-PEFC.

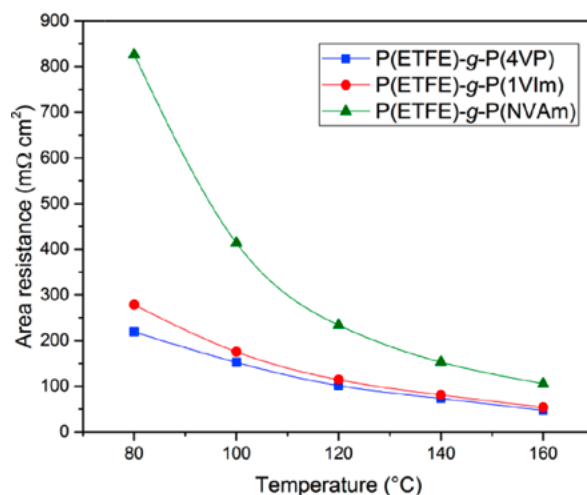


**Figure 4.** Area resistance at 5% relative humidity.

## Conclusion and Outlook

High grafting levels of selected monomers were achieved resulting in membranes having nitrogen site densities of ca. 5–6 mmol/g. All three types of membrane were successfully doped with phosphoric acid and thus can function as proton conductors at temperatures up to 160 °C. As a next step other parameters of the membranes vital for the HT-PEFC application, such as mechanical properties, stability, and more detailed interaction with phosphoric acid, will be addressed.

## Acknowledgement

The authors gratefully acknowledge the Swiss National Science Foundation for the financial support (grant no. 156604).

## References

- [1] D.C. Seel, B.C. Benicewicz, L. Xiao, T.J. Schmidt, in *Handbook of Fuel Cells – Fundamentals, Technology and Applications* **5**(19), John Wiley & Sons (2009).
- [2] S.H. Eberhardt, M. Toulec, F. Marone, M. Stampanoni, F.N. Büchi, T.J. Schmidt, *J. Electrochem. Soc.* **162**(3), F310–F316 (2015).
- [3] S.H. Eberhardt, T. Lochner, F.N. Büchi, T.J. Schmidt, *J. Electrochem. Soc.* **162**(12), F1367–F1372 (2015).

## Tuning the wettability of gas diffusion layers

A. Forner-Cuenca, V. Manzi-Orezzoli, L. Gubler, T.J. Schmidt, P. Boillat

phone: +41 56 310 5125, e-mail: antoni.forner@psi.ch

The so-called gas diffusion layers (GDLs) are highly porous carbon substrates which need to provide several functions in fuel cells: heat and electrical conduction protects the mechanical integrity of the membrane, gas diffusion and water permeation. The transport of gases towards the catalysts layers and liquid water leaving the cell happen in opposite direction.

Current state of the art materials do not provide an optimized balance between diffusivity and permeability. Recently, we have developed a method to produce GDLs with structured wettability [1]. Generally speaking, the method consists of locally modifying the coating chemistry in order to create hydrophilic regions. The hydrophilic patterns provide preferential channels for liquid water to leave the cell, leaving low-resistance pathways for the gases to reach the catalyst layer.

Recently, we have demonstrated the success of the modified GDL to have water filled hydrophilic channels at low capillary pressure, while much higher pressures were required in order to fill hydrophobic regions [2]. However, limited details were provided concerning the synthetic conditions which allow hydrophilizing.

The main advantage of grafting polymerization is the potential of tuning the final contact angle. The choice of experimental conditions (dose, monomer concentration, temperature, time, etc.) defines the final property of the substrate. In this work, special attention is paid to the wettability. The untreated polymer coating, fluoroethylene propylene (FEP), is hydrophobic. In order to find synthetic conditions to lower the contact angle in a flat system, FEP films were initially used.

The use of two grafting monomers is herein reported. The first, acrylic acid (AA) has been widely studied in radiation grafting literature, both referring to surface (plasma) [3] and bulk (electron beam) [4] modifications. The second, n-vinylformamide (NVF) has been studied mainly for surface applications [5], in which very hydrophilic surfaces were achieved. Initially, a kinetic study was performed on the films with both monomers.

After that, promising conditions were applied to the grafting in porous GDLs. The actual GDL consists of carbon fibers which are partially coated with FEP. The understanding of wettability in this system is more complicated for two reasons: the intrinsic rough nature of the substrate material and its heterogeneity. However, a first insight into the wettability of the treated GDL is obtained.

### Experimental

In order to simplify the wettability studies, FEP flat films (25  $\mu\text{m}$  thickness) were used as a model system. They were acquired from DuPont (Teflon® FEP Gauge 100).

For the synthesis in GDLs, Toray TPG-H 060 (190  $\mu\text{m}$  thickness) carbon paper was purchased from Fuel Cell Earth and in-house coated using a «dip coating» method with FEP dispersion (to different coating loads, Table 1). The details of the coating procedure are given elsewhere [2].

All FEP films and GDLs were electron beamed at Leoni Studer (Däniken, Switzerland) using a linear accelerator with 2.1 MeV energy and 50 kGy.

AA (Sigma Aldrich) was used after dilution in  $\text{H}_2\text{O}$  to 15 %wt, NVF (Sigma Aldrich) was diluted at 80 %wt in water. For the reaction in FEP films, cylindrical glass reactors were used (approximately 60 mL volume) at atmospheric pressure.  $\text{N}_2$  was flushed during 60 min for allowing deoxygenating the grafting solution. The AA reactions were carried out at 60 °C while the NVF at 70 °C.

In the case of the reactions carried out in porous media, the complete wetting of the materials by the monomer solution is crucial. Therefore, for the case of water solution of AA, a specially designed reactor was used. The reactor is a steel body (around 45 mL volume) and permits the application of vacuum and oxygen-free atmosphere. The underpressure removed the air trapped in the porosity and allows the solution to penetrate the internal pores. The different reactions carried out are summarized in Table 1.

Material	Coating load (%)	Monomer	Conc. (%wt in $\text{H}_2\text{O}$ )	Time (min)
FEP film	NA	AA	15	10, 30, 50, 70
FEP film	NA	NVF	80	10, 30, 50, 70
Toray paper	0, 5, 15, 30, 50, 70	AA	15	60
Toray paper	0, 5, 15, 30, 50, 70	NVF	80	60
Toray paper	30	AA	15	5, 15, 30, 45, 60, 120
Toray paper	30	NVF	80	5, 15, 30, 45, 60, 120

**Table 1.** Experimental conditions used for the synthesis in FEP films and Toray paper GDLs.

The degree of grafting (DG) is defined as the percent of mass increase due to grafting and was calculated as  $(m_f - m_0)/m_0 \cdot 100$ , where  $m_0$  is the mass of the original film and  $m_f$  the mass after grafting, cleaning and drying.

The contact angles (CA) were measured using an in-house developed contact angle goniometer. A volume of 2  $\mu\text{L}$  was used and, at least, 4 measurements per sample were performed. In the case of external contact angles measured on rough GDLs, videos were taken in order to record the imbibition dynamics (when happened).

### Results

The first results refer to the grafting reaction carried out in the model system of flat FEP films. As seen in Figure 1, the polyacrylic acid polymerizes very fast, having around 125% DG after only 30 minutes. The measured contact angles show a gradual decrease towards a minimum value of around 50°.

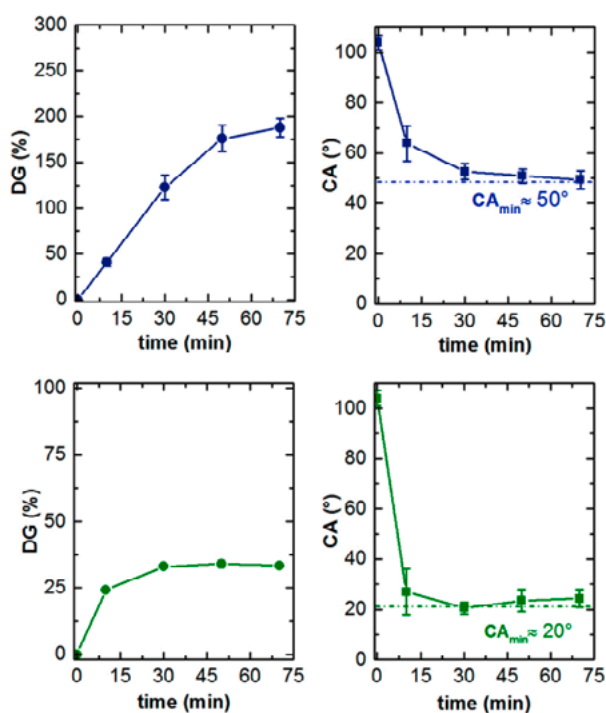


**Figure 1.** Grafting kinetics of FEP-g-pAA system (top row) and FEP-g-pNVF system (bottom row). On the left column, the degree of grafting is plotted against the reaction time. On the right column, the contact angle of water is plotted against the reaction time.

The kinetics of NVF shows a different trend. After a short time of around 30 minutes, the degree of grafting reaches a plateau around 38%. The contact angle reaches its minimum value (20°) after about 10 minutes. It is worth mentioning that around 5 minutes are needed in order to heat up the reactor to its final temperature, meaning that the kinetics of the NVF grafting is possibly faster than we can measure with this setup.

The knowledge obtained from the studies on flat films was afterwards transferred to GDLs. The effect of reaction time in the external wettability is plotted in Figure 2. The GDLs with 30% coating load treated with AA exhibited hydrophobic contact angles in every case, even those at higher reaction times. Interestingly, those treated with NVF produced surfaces which spontaneously wicked water after only 30 min of reaction time.

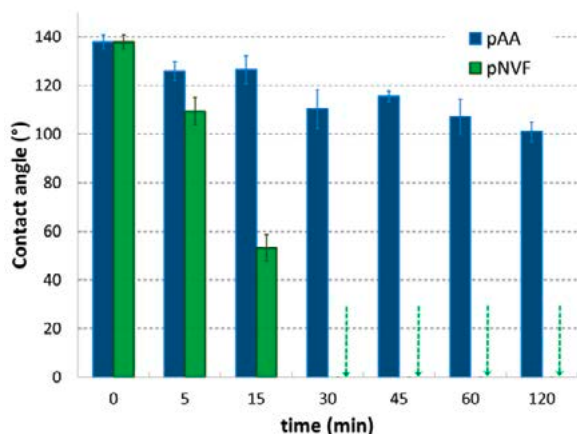


**Figure 2.** External contact angle of water plotted as a function of reaction time. The AA treated GDLs are represented in blue. NVF treated in green. The coating load was 30%wt FEP in every case. The dotted arrow represents completely sucked droplets.

The influence of coating load is presented in Figure 3. Within the GDL-g-pAA system, a coating load of at least 50% is needed in order to spontaneously imbibe the water. At lower coating loads, water droplets are held by the porous surfaces. The NVF treated behaves differently. Only 15%wt of FEP coating is needed in order to provide a spontaneously absorbing surface. The differences observed can be explained attending to the mixed wettability present in the GDL. The remaining uncoated carbon fibers provide internal surfaces with contact angles of around 80° [6].

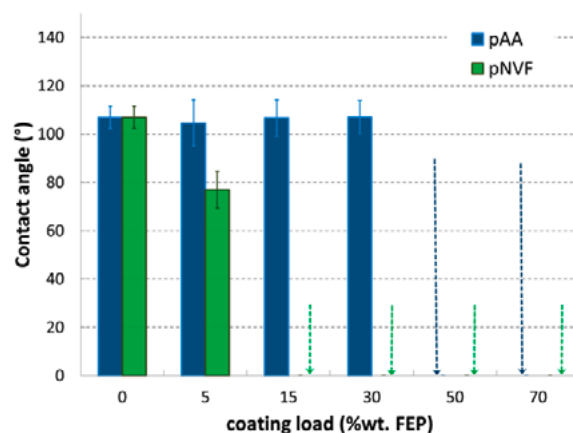


**Figure 3.** External contact angle of water plotted as a function of coating load. The AA treated GDLs are represented in blue. NVF treated in green. The reaction was 60 minutes in every case. The dotted arrow represents completely sucked droplets. AA treated showed much slower imbibition dynamics than those treated with NVF.

Interestingly, we observed different water imbibition dynamics when placing water droplets on the modified surfaces. For those materials that showed spontaneous water wicking (represented as dotted arrows) a clear tendency was observed when comparing the same chemistry and grafting time but different coating loads.

## Acknowledgement

Funding from the Swiss National Science Foundation (project n° 143432) is gratefully acknowledged.

## References

- [1] P. Boillat, A. Forner-Cuenca, L. Gubler, C. Padeste, F.N. Büchi, European Patent Application EP14184065 (2014).
- [2] A. Forner-Cuenca, J. Biesdorf, L. Gubler, P.M. Kristiansen, T.J. Schmidt, P. Boillat, *Adv. Mater.* **27** (41), 6317–6322 (2015).
- [3] M. Okubo, M. Tahara, N. Saeki, T. Yamamoto, *Thin Solid Films* **516** (19), 6592–6597 (2008).
- [4] B.D. Gupta, A. Chapiro, *Eur. Polym. J.* **25** (11), 1145–1148 (1989).
- [5] S. Neuhaus, C. Padeste, N.D. Spencer, *Plasma Process. Polym.* **8** (6), 512–522 (2011).
- [6] D.L. Wood III, R.L. Borup, *Polymer Electrolyte Fuel Cell Durability*, Springer New York, chapter 8, 159–195 (2009).

# SCIENTIFIC ACHIEVEMENTS 2015

BATTERIES –

MATERIALS

## Synthesis and characterization of carbon with tuneable porosity

S. Trabesinger

phone: +41 56 310 5775, e-mail: sigita.trabesinger@psi.ch

Elemental carbon has been for a long time one of the most important inorganic materials. In electrochemistry, carbon is extensively used due to its high conductivity and low weight, and each electrochemical application exploits carbon properties, specifically attuned, like high surface area in supercapacitors, porosity as support for catalysts in fuel cells, high conductivity in batteries and others [1]. With new emerging chemistries in the battery field new sets of carbon properties are required to satisfy new upcoming challenges. High conductivity is not enough, as properties, such as tailored surface area, bespoke porosity, high purity and corrosive resistance, are becoming of high importance. In Li–S system challenges are associated with the insulating nature of sulphur and solubility of Li and S reaction products (long-chain polysulphides) in electrolyte [2]. For this purpose, hierarchical carbon, besides traditionally required high conductivity and high surface area, is expected to simplify and enhance homogeneous sulphur distribution within the carbon matrix and to be able to contain soluble polysulphides within the positive electrode due to optimized pore-size distribution. The goal of this work is to initiate bespoke carbon materials design to obtain bespoke carbons to address the challenges of emerging new battery chemistries, such as the Li–S electrochemical system. Special attention is paid to pore tuneability and electrochemical performance.

The hierarchical porous carbons (HPCs) were synthesized employing resorcinol-formaldehyde polymer (RFP) chemistry, which is based on polymer chain network formation. Polymer foam is formed using an oil-in-water soft matter template and able to form an open-cell hierarchical carbon foam using inexpensive and easily removable templating materials [2]. The material is templated by using two immiscible phases under high speed mixing: a silicone oil and water containing resorcinol-formaldehyde precursor. The latter enables mesoporosity tuning by changing synthetic conditions; while former, by changing viscosity of the oil, tunes macroporosity.

### Experimental

Carbon foam is made by a number of simple steps: a) blending the oil and aqueous phase; b) thermally curing the precursor solution; c) removing the oil phase via solvent extraction; d) exchanging water for organic solvent; e) drying the monolith; f) carbonizing the sample.

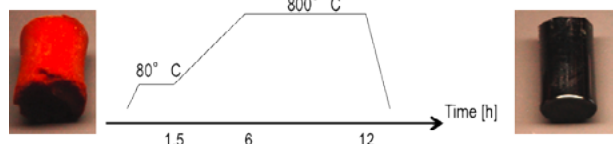


**Figure 1.** Image of a synthesized porous carbon precursor, carbonization conditions and resulting HPC monolith after carbonization.

To synthesize the carbon precursor foam, a mixture of resorcinol (2.912 g, 0.0264 mol) and formaldehyde (1.588 g, 0.0529 mol) was used with sodium carbonate (0.018 g,

0.1698 mmol) as a basic catalyst in water. All used ingredients were stirred until dissolved and then left for 1 hour at room temperature to start the formation of the polymer. Afterwards silicone oil with two different viscosities was added to the RFP-mixture and then rigorously stirred to create a gel, which was then poured into the jars, sealed and kept at 85 °C for 72 h. At the end of this process an orange HPC precursor, see Figure 1, was obtained using different oil viscosity and containing different percentage of organics, see Table 1. Before proceeding with carbonization, the orange precursor foam was purified. First, to remove the silicone oil, the precursor was washed with chloroform. Afterwards, to ensure the replacement of water inside the pores, the carbon foam was washed with acetone. The carbonization was performed with the temperature profile shown in Figure 1 under a constant nitrogen-flow, resulting in a, shrunk, black carbon monolith, see Figure 1.

Sample	Organic content, %	Oil Viscosity, cst	S <sub>BET</sub> , m <sup>2</sup> /g	V <sub>Tot</sub> , cm <sup>3</sup> /g
03_100	30	100	671	1.22
03_1000	30	1000	716	0.97
04_100	40	100	852	1.11
04_1000	40	1000	655	0.87

**Table 1.** Composite synthesis parameters and resulting surface area and pore volume after carbonization.

For testing the HPCs in Li–S cells, sulphur electrodes were prepared by mixing components such that standard [4] final component ratios are as follows: 60% sulphur, 30% carbon (HPC), 10% polyethylene oxide (PEO, M=4'000'000 g/mol). Components were mixed using turbo stirring and then doctor-bladed on a carbon pre-coated Al current collector. Electrolyte was 1 M LiTFSI in DME:Diox (2:1, where LiTFSI is lithium bis(trifluoromethane sulfone)imide, DME is dimethoxyethane, and Diox is 1,3-dioxolane. Cells were assembled in an argon-filled glove box, using celgard 2400 separator and metallic lithium as counter electrode. Galvanostatic cycling was performed in the voltage window 1.8–2.7 V vs. Li at C/5 rate, where C-rate is defined as 1C=1678 mA/g.

### Results

HPCs from RFP precursors made with four different compositions, see Table 1, were evaluated. Light microscopy analysis showed well preserved hierarchical porosity with well-expressed spherical macropores up to few hundreds of micrometres in diameter, see Figure 2.

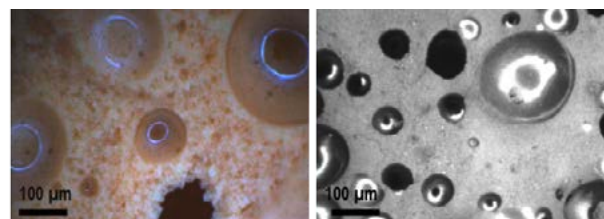


**Figure 2.** Light microscopy images of a synthesized porous carbon precursor (left) and resulting HPC (right) after carbonization.

Morphology evaluation by scanning electron microscopy (SEM) clearly revealed differences dependant on the precursor synthesis conditions: lower organic content in the precursor resulted in the porous carbon with thinner inter-pore walls while more viscous oil resulted in finer pores and smaller particles under the same grinding conditions, see Figure 3. Thickest walls were obtained with lowest viscosity oil and highest organic content. Clear qualitative differences in macropore sizes were observed during SEM analysis.

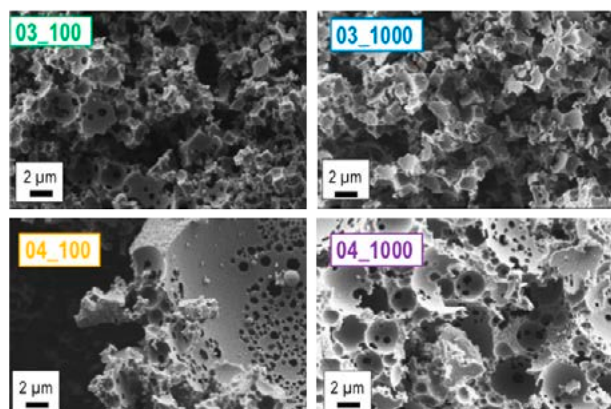


**Figure 3.** SEM micrographs of HPC synthesized from precursors with different starting compositions.

From nitrogen sorption study it was found that specific surface areas of HPCs were rather high, in the range of 600–900 m<sup>2</sup>/g, with correspondingly high pore volumes, in the range of 0.9–1.2 cm<sup>3</sup>/g, see Table 1. Pore size distribution derived from recorded full isotherms by utilizing the NLDFT module of Quantacrome Autosorb software showed clear differences in wider mesopore region (above 50 Å) and identical pore structure in lower pore size region, see Figure 4, showing that chosen variable parameters, oil viscosity and amount of organic content, do not influence pore sizes below 50 Å.

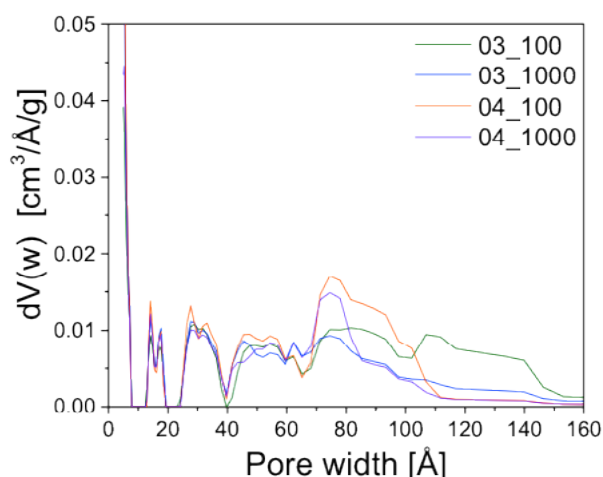


**Figure 4.** Pore size distribution of HPC synthesized from precursors with different starting compositions.

Finally the synthesized HPCs were used as a conductive matrix for the positive electrodes in the Li–S cells. The electrochemical performance of HPC–S composite electrodes was tested and galvanostatic cycling results are presented in Figure 5. All the HPCs resulted in similar and satisfactory coulombic efficiency of ~90% even without use of any of electrolyte additives. The most stable cycling performance was identified for HPC-03\_100, having the highest pore volume and one of the

lowest surface areas with broad pore size distribution. This sample as well exhibited thin inter-pore walls due to low organic phase content and no very large macropores, such as observed for the sample HPC-04\_100, see Figure 3. The specific charge when using HPC-03\_100 as a conductive matrix was rather high for the sulphur containing electrode prepared by simple component mixture and stable at ~800 mAh/g. Other HPCs showed quite poor cycling stability, which can be correlated to the lack of pores above 100 Å, which can be then assumed to improve the tortuosity of the electrode as the rest of PSD is similar or identical among the synthesized HPCs.

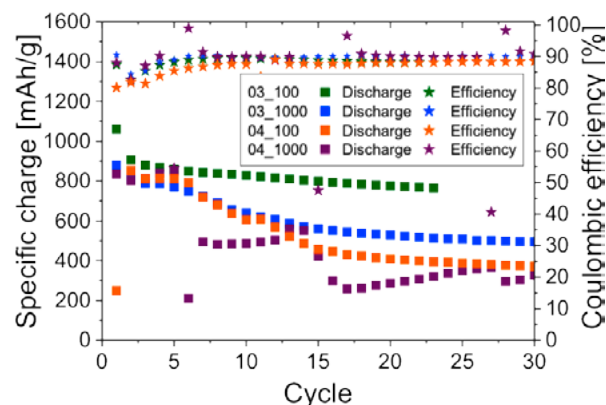


**Figure 5.** Electrochemical performance of Li–S cells with cathodes based on different HPCs.

## Conclusions

A number of HPCs from precursors with varied organic content and oil viscosity was successfully synthesized. The changes in the carbon precursor synthesis via the oil viscosity and the amount of organic phase influenced the morphology and porosity of the resulting HPCs. However, only the wider pores above 50 Å can be adjusted varying these two parameters. For control of smaller pores other variables need to be considered, such as carbon precursor, synthesis temperature, etc.

The electrochemical study of HPC-based sulfur positive electrodes confirmed HPC suitability for use in Li–S cells as the results showed reasonable specific charge and satisfactory coulombic efficiency. The comparison of the electrochemical performance of HPC based positive electrodes also indicated that the presence of pores above 100 Å is responsible for the better cycling stability and specific charge retention.

## Acknowledgement

M. Tornow is acknowledged for the experimental work within the semester project.

BASF SE is acknowledged for financial support within the «BASF Scientific Network for Electrochemistry and Batteries».

## References

- [1] P. Novák, D. Goers, M.E. Spahr, Carbon Materials in Lithium-Ion Batteries, in: F. Béguin, E. Frackowiak (Eds.) Carbon Materials for Electrochemical Energy Storage Systems, CRC Press – Taylor and Francis Group, Boca Raton-New York, 263–328 (2010).
- [2] S. Urbonaite, T. Poux, P. Novák, *Adv. Energy Mater.* **5**, 1500118 (2015).
- [3] A.F. Gross, A.P. Nowak, *Langmuir* **26**, 11378–11383 (2010).
- [4] S. Urbonaite, P. Novák, *J. Power Sources* **249**, 497–502 (2014).

## Poly(ethylene oxide)-coated double-layer separator for lithium-sulfur battery

J. M. Conder, C. Hänsel, S. Trabesinger, P. Novák, L. Gubler

phone: +41 56 310 2120, e-mail: joanna.conder@psi.ch

Although the lithium–sulfur (Li–S) battery has been studied for more than two decades, its commercialization is still hampered by short cycle life, low charging efficiency and high self-discharge rate. All these problems arise mainly from the so-called polysulfide shuttle [1]. Thus far to tackle this disadvantage, much effort has been devoted to the sulfur electrode engineering and to the confinement of the sulfur in various conductive carbon matrices. The recent development in highly conducting nanocarbon materials brought a great progress in the design of the sulfur electrode and thus significantly improved the performance of the Li–S cells [2]. «The battery is [however] more than just a collection of materials: It is a system» said Yet-Ming Chiang [3]. It means that components other than the sulfur electrode have to be also designed in order to further reduce the parasitic reactions. In the previous report [4] we presented an asymmetric porous separator based on polypropylene (PP) and styrene sulfonate, and its promising polysulfide rejection ability. In this work, we focus on another polymer candidate poly(ethylene oxide) (PEO), coated on one side of the commercial PP separator. We characterize this double-layer separator by means of attenuated total reflectance Fourier transform infrared spectroscopy (ATR–FTIR) and scanning electron microscopy (SEM), and explore its effect on electrochemical performance of the Li–S cells.

### Experimental

The appropriate amount of PEO powder (MW: 400 000, Fluka) was dissolved in anhydrous acetonitrile (ACN, Sigma Aldrich, ACS reagent > 99.5) to obtain a 2 %wt solution. The solution was then stirred at a constant rate for at least two days. Using a doctor blade, the resulting PEO/ACN solution was coated onto Celgard 2400 (Celgard) base film and dried in air. Prior to battery testing, all coated films were characterized by ATR–FTIR spectroscopy and SEM imaging, and their thicknesses were measured.

Subsequently, test cells were assembled by placing the separator (PEO-coated film) between the sulfur electrode and the lithium counter electrode. The sulfur electrodes were prepared as described in [5]. Prior to assembly, each PEO-coated film was soaked in 100  $\mu\text{l}$  of organic liquid electrolyte (BASF): 1 M LiTFSI (lithium bis(trifluoromethane) sulfonimide) in a 2:1 volume mixture of DME (dimethoxyethane) and Diox (1,3-dioxolane). It was then introduced to the cell with the coated side facing the sulfur electrode. Additional 30  $\mu\text{l}$  of electrolyte were added on top of the separator to ensure sufficient wetting. Celgard 2400 was used as reference separator. It was not soaked in advance but directly wetted by 50  $\mu\text{l}$  of electrolyte during cell assembly instead. All cells were galvanostatically cycled at C/5 and C/20 rate at room temperature in the potential range of 1.5 and 3.0 V vs. Li<sup>+</sup>/Li. 1C is defined as  $j = 1672 \text{ mA g}^{-1}$  of S.

### Results

As can be seen in Figure 1, the formation of a PEO layer leads to changes in: the surface chemistry (a), the thickness (b), and the morphology of the Celgard separator (c, d). On the coated side, among the new peaks corresponding to PEO, a triplet corresponding to C–O–C stretching is observed at 1145, 1095 and 1059  $\text{cm}^{-1}$ , with the maximum intensity at 1095  $\text{cm}^{-1}$  [6]. On the non-coated side, none of these peaks is present in the spectra indicating that indeed coating is asymmetric. This is in good agreement with the SEM observations. Introducing PEO onto the surface of Celgard leads to the formation of a flower-like irregular polymer layer completely covering the surface of the separator (c). The non-coated side preserves the original structure of Celgard with regular arrays of pores (d).

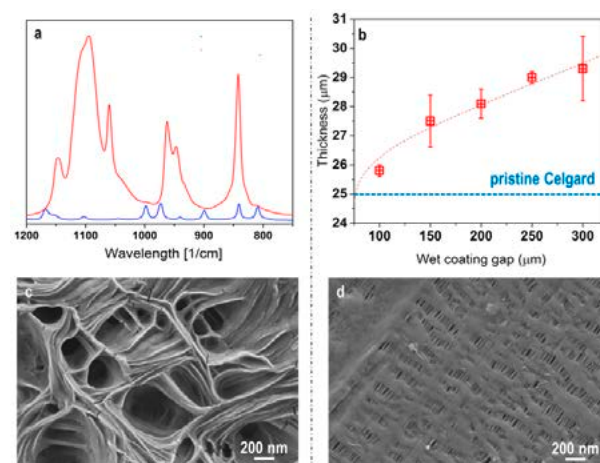


**Figure 1.** (a) ATR–FTIR spectra of the PEO-coated (—) and non-coated side (—) of Celgard. (b) Thickness of the coated films (—) as a function of a wet coating gap. SEM micrographs of (c) the coated and (d) non-coated side of Celgard.

Subsequently, the double-layer separators with two distinct thicknesses of 0.8 and 3.5  $\mu\text{m}$  were tested in Li–S cells. The results are summarized in Figure 2. Overall, the use of the coated separators did not lead to a tremendous increase in the practical specific charge, neither at C/5 (a) nor at C/20 rate (c). Though there was no significant increase in the polarization of the cells assembled with these separators (b). When a separator with a 3.5  $\mu\text{m}$  PEO layer was used, the average specific charge at C/5 was ca. 110  $\text{mAh g}^{-1}$  lower compared to the reference cell. To the contrary, at C/20 the average values were ca. 200  $\text{mAh g}^{-1}$  higher than that of the reference cell. Most importantly, in all cases, where the double-layer separator was used, the coulombic efficiency was higher than 90% indicating that the polysulfide shuttle was significantly reduced.

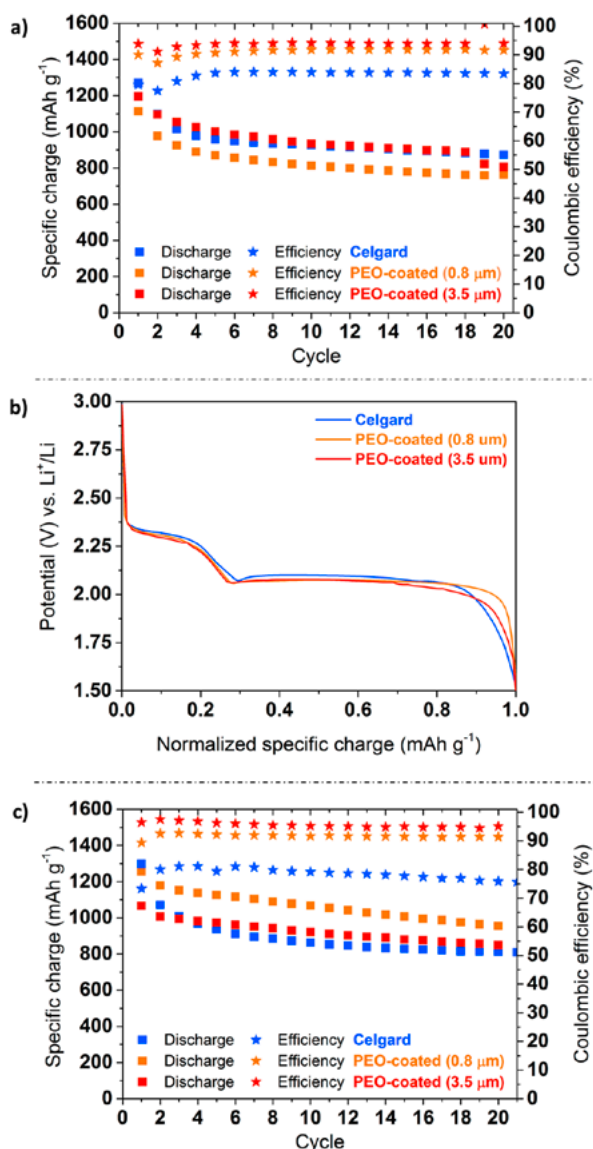


**Figure 2.** Electrochemical performance of the Li-S cells with reference Celgard and PEO-coated separators with two different coating thicknesses at (a) C/5 and (c) C/20 rate. (b) Corresponding normalized galvanostatic curves for the 10<sup>th</sup> lithiation at C/5.

Mikhaylik et al. [7] have demonstrated that a gel polymer electrolyte (GPE) sandwiched between the separator and the Li anode can tightly glue the two together and thus significantly improve the Li deposition morphology. Therefore, especially during long-term cycling, better capacity retention can be achieved when the coating layer faces the Li anode. Encouraged by this approach we also tested the coated separators in a way that the PEO layer was facing the Li anode.

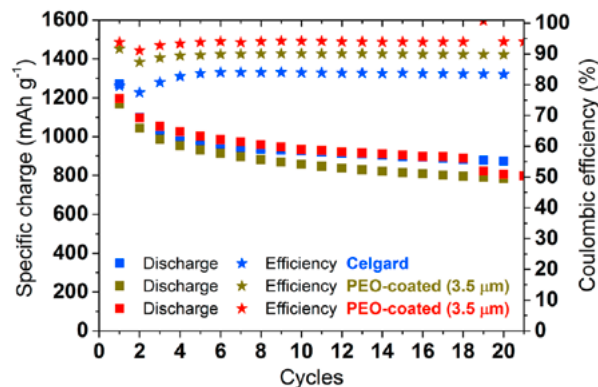


**Figure 3.** Electrochemical performance of the Li-S cells at C/5 rate with pristine Celgard and PEO-coated separators, where the coating faces to either the sulfur (—) or the lithium electrode (—).

As can be seen in Figure 3, the orientation of the PEO layer did not significantly influence the specific charge of the cells and its retention at least within first 20 cycles. The cell where the PEO layer was facing the Li electrode had a similar 90% efficiency as the one with the layer facing towards the sulfur electrode.

## Conclusions

The use of PEO-coated double-layer Celgard separator in Li-S cells resulted in improved coulombic efficiency as compared to the reference cell with Celgard. The presence of coating did not lead to an increase in the overpotential indicating no change in the internal resistance of the cell. We also demonstrated that the placement (lithium side or sulfur side) of the PEO layer had a limited impact on the electrochemical performance of the Li-S cell, as similar results were obtained in both configurations.

## Acknowledgement

The authors thank the Swiss National Science Foundation (project no 200021\_144292) for financial support.

## References

- [1] M. Barqhamadi, A.S. Best, A.I. Bhatt, A.F. Hollenkamp, M. Musameh, R.J. Rees, T. R  ther, *Energ. Environ. Sci.* **7**, 3902–3920 (2014).
- [2] J.-Q. Huang, Q. Zhang, F. Wei, *Energy Storage Materials* **1**, 127–145 (2015).
- [3] P. Patel, *ASC Cent. Sci.* **1** (4), 161–162 (2015).
- [4] J.M. Conder, L. Gubler, P. Nov  k, S. Urbonaite, *PSI Electrochemistry Laboratory – Annual Report 2014*, 40–41, DOI: 10.3929/ethz-a-007047464 (2014).
- [5] S. Urbonaite, P. Nov  k, *J. Power Sources* **249**, 495–502 (2014).
- [6] N. Gondaliya, D.K. Kanchan, P. Sharma, P. Joge, *Mater. Sci. Appl.* **2**, 1639–1643 (2011).
- [7] Y. Mikhaylik, I. Kovalev, R. Schock, K. Kumaresan, J. Xu, J. Af-finito, *ECS Trans.* **25** (35), 23–34 (2010).

## Polysulfides confined!

### New design of the separator for enhanced lithium sulfur cell performance.

J. M. Conder, L. Gubler, P. Novák, S. Trabesinger

phone: +41 56 310 2120, e-mail: joanna.conder@psi.ch

The functionalization of a porous separator for the lithium-sulfur (Li-S) battery could significantly inhibit the diffusion of polysulfides and thus improve the cycling stability of the battery. Recently, we designed and synthesized an asymmetric porous polypropylene-based separator (PP-g-PLiSS) with  $S_n^{2-}$  ( $n=5-8$ ) anion barrier functionality [1, 2] (Figure 1). Polysulfide diffusion tests coupled with preliminary galvanostatic cycling results showed that already the separator with 5 %wt grafts is able to suppress the diffusion of  $S_n^{2-}$  species to a significant extent compared to the reference Celgard separator, resulting in higher coulombic efficiency. Herein, we summarize our electrochemical testing results and discuss the influence of the graft level of PP-g-PLiSS separators on the performance of Li-S cells.

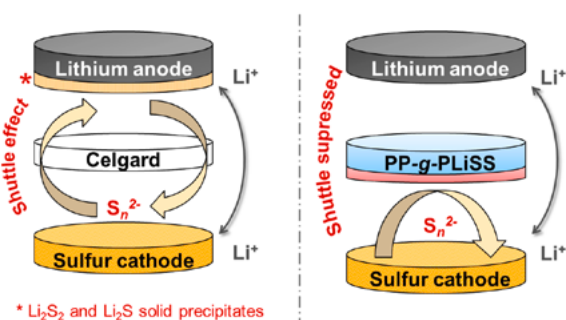


**Figure 1.** Schematic configuration of the Li-S cell assembly without (left) and with (right) the asymmetric porous separator with  $S_n^{2-}$  anion barrier functionality shown [1].

## Experimental

Asymmetric PP-g-PLiSS separators were prepared by one-step plasma-induced graft copolymerization as described in [1]. PP-g-PLiSS with different graft levels, namely 5, 8, 20 and 30 % were chosen for electrochemical performance screening. Celgard was used as a pristine reference separator. Sulfur electrodes with an average loading of  $2.0 \pm 0.5$  mgS cm<sup>-2</sup> were prepared according to [3]. Test cells were assembled by placing the separator between the sulfur composite electrode and the metallic lithium counter electrode, and introducing the electrolyte: 1 M of LiTFSI (lithium bis(trifluoromethane sulfonyl) imide) in DME (dimethoxyethane) : Diox (1,3-dioxolane) (2 : 1). Galvanostatic cycling was performed at C/20 rate between 1.5 and 3.0 V vs. Li<sup>+</sup>/Li. The C-rate is defined as  $j = 1672$  mA g<sup>-1</sup> of S.

## Results

As can be seen in Figure 2, the use of the 5 % grafted separator did not bring significant improvement in practical specific charge. The initial discharge capacity was similar to that of the reference cell (1020 mAh g<sup>-1</sup> and 950 mAh g<sup>-1</sup>, respectively). Presumably, the amount of  $SO_3^-$  groups at or near the surface of the separator was not yet sufficient to effectively suppress the polysulfide shuttle, even though the efficiency improved from 80 % (for Celgard) to 90 %.

Increasing the graft level to 8 % resulted in a high initial discharge capacity of ca. 1300 mAh g<sup>-1</sup>. It faded slightly within the first few cycles and stabilized at around 910 mAh g<sup>-1</sup> after 30 cycles. The use of separators with higher graft levels of 20 and 30 % did not further increase the capacity of Li-S cells. It did, however, enhance the coulombic efficiency, drawing it close to 100 % in the case of the 30 % grafted separator.

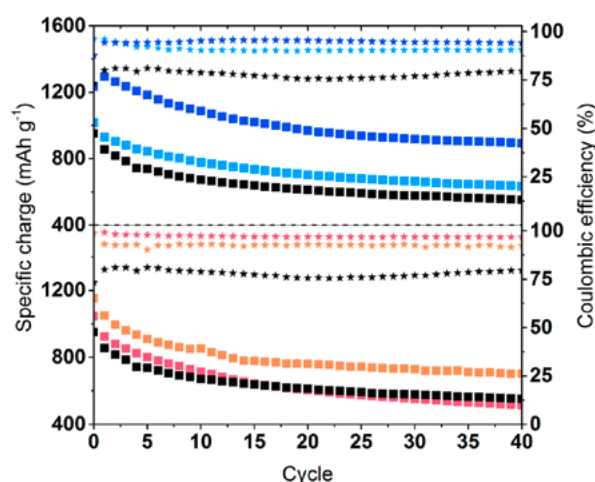


**Figure 2.** The discharge capacity (squares) and the coulombic efficiency (asterisks) of the Li-S cells tested with Celgard (—) and PP-g-PLiSS separators with 5 (—), 8 (—), 20 (—) and 30 % (—) graft level.

## Conclusions

The electrochemical testing results showed that the use of asymmetric PP-g-PLiSS separators greatly enhances the coulombic efficiency as compared to the pristine Celgard separator. The practical specific charge depends on the graft level of the separator. The highest capacity was achieved with the 8 % grafted separator. Presumably, it is a good compromise between the ratio of  $SO_3^-$  groups that reject the polysulfides and the thickness of grafted layer on the separator, which enables Li-ion transfer through this asymmetric separator.

## Acknowledgement

The authors thank the Swiss National Science Foundation (project no 200021\_144292) for financial support.

## References

- [1] J. Conder, S. Urbonaitė, D. Streich, P. Novák, L. Gubler, *RSC Adv.* **5**, 79654–79660 (2015).
- [2] J.M. Conder, L. Gubler, P. Novák, S. Urbonaitė, *PSI Electrochemistry Laboratory – Annual Report 2014*, 40–41, DOI: 10.3929/ethz-a-007047464 (2014).
- [3] S. Urbonaitė, P. Novák, *J. Power Sources* **249**, 495–502 (2014).

## Mitigation of the voltage fade of high-energy lithium nickel-manganese-cobalt oxides (HE-NCM) as cathodes for lithium-ion batteries

J. Billaud, S. Sallard, J.-Y. Shin, F. Chesneau, C. Villevieille

phone: +41 56 310 5303, e-mail: juliette.billaud@psi.ch

Lithium-ion batteries are currently the most advanced devices for portable energy storage and they are making their way into the electric vehicle market. Various materials are nowadays used as positive electrodes, such as  $\text{LiCoO}_2$  and  $\text{LiFePO}_4$ . However, their low energy density (below 200 Wh/kg) limits their applications for the hybrid vehicles market. Two strategies can be investigated in order to increase the energy density of Li-ion batteries: increase the operating voltage and/or increase the specific charge. Only one family of materials combines so far both approaches: the high energy lithium-rich nickel-manganese-cobalt oxides also named HE-NCM, operating at voltage higher than 4.5 V vs.  $\text{Li}^+/\text{Li}$  with a specific charge higher than 250 mAh/g, corresponding to an energy density of 900 Wh/kg. Unfortunately, this family suffers some major drawbacks: cation migration (Ni, Mn) polluting the counter electrode, as well as voltage fade upon cycling, both phenomenon leading to a capacity fading [1, 2]. Some attempts have been performed by various groups, such as coatings or metal substitutions, in order to prevent structural changes following Mn activation at the first charge and thus Mn migration between slabs and interslabs. We developed an original and unique approach to overcome the voltage fade by modifying by soft chemistry commercial powders.

In this work we propose to modify commercial powders by a two-steps synthesis: 1) an acid treatment followed by 2) a cation treatment. This method is expected to: 1) remove lithium from the structure and 2) replace the voids by the cation of choice (Al in this study).

Although this technique is easy to proceed and expecting to lead to stabilisation of the electrochemical properties, the morphology of the particles can be damaged and there is only little or no control on the amount of the dopants.

### Experimental

Commercial HE-NCM powders were subjected to two different treatments: a) an acid treatment (powders were stirred in  $\text{HNO}_3$  0.1 M for 4 hours at room temperature) and b) a cation exchange (powders were stirred and heated up to 60 °C in  $\text{AlNO}_3$  1 M for 4 to 24 hours. Powders were then filtered and vacuum dried at 180 °C. Powders were stored in an argon-filled glovebox prior to further handling.

Electrochemical tests were performed in half-cells using Li metal as a counter electrode and 1 M  $\text{LiPF}_6$  in ethylene carbonate/dimethylcarbonate (1 : 1 weight ratio) as electrolyte.

X-ray powder diffraction (XRD) was recorded at the MS-powder beamline at SLS with a wavelength of 0.7762 Å.

Scanning Electron Microscopy (SEM) was performed on a Zeiss Ultra55 SmartSEM electron microscope.

### Results

In this work we will focus on studying the influence of the introduction of Al in HE-NCM structure, keeping the acid treat-

ment time identical (4 hours). X-ray diffraction was performed on the reference sample, the 4 h (acid) / 4 h (exchange) sample as well as the 4 h / 24 h sample. X-ray diffractograms are displayed in Figure 1.

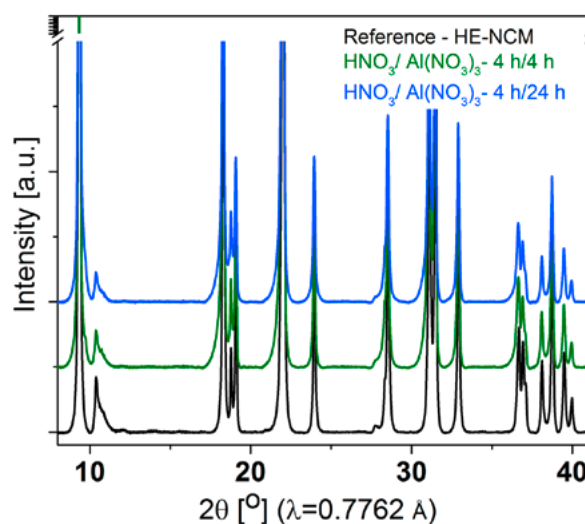


**Figure 1.** XRD powder pattern of different HE-NCM after various acid treatment / exchange times.

Figure 1 indicates that the structure is maintained independently of the treatment applied. Since XRD cannot help to determine the amount of Al introduced in the structure, inductively coupled plasma spectroscopy was performed on the samples (see Table 1).

$\text{HNO}_3\text{-AlNO}_3$ (hrs)	Li	Mn	Ni	Co	Al	O
Reference	1.33	0.60	0.21	0.12	n/a	n/a
4-4	0.91	0.58	0.20	0.11	0.017	n/a
4-24	0.64	0.55	0.18	0.11	0.025	

**Table 1.** ICP results for the different samples.

It appears from Table 1 that the lithium is extracted from the structure due to the acid treatment and as expected, the longer the acid treatment, the bigger is the amount of lithium extracted, explaining the increase in Al content. Oxygen seems to be extracted at the same time, which is confirmed by the electrochemical data displayed later. So far, the transition metals (Ni, Mn, Co) don't seem to be affected from these treatments.

Scanning electron microscopy images were obtained in order to compare the morphology of the samples. It appears from Figure 2 that the morphology of the samples is modified by the treatments employed: the longer the exchange post treatment, the more the morphology is damaged, some particles being destroyed (Figure 2c). The overall morphology (rounded shape particles) however is maintained and the particle size is kept constant (ca. 2–10 μm).

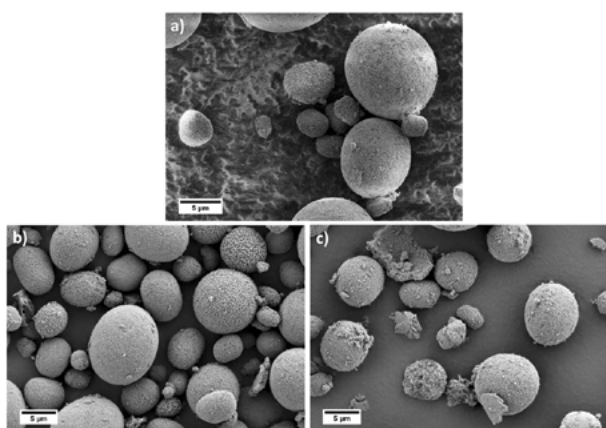


**Figure 2.** SEM images of a) HE-NCM reference sample, b) 4 h/4 h sample, c) 4 h/24 h sample.

Electrochemical tests show that the specific charge is largely decreased by the applied treatment: the longer the Al treatment, the lower the specific charge (see Figure 3).

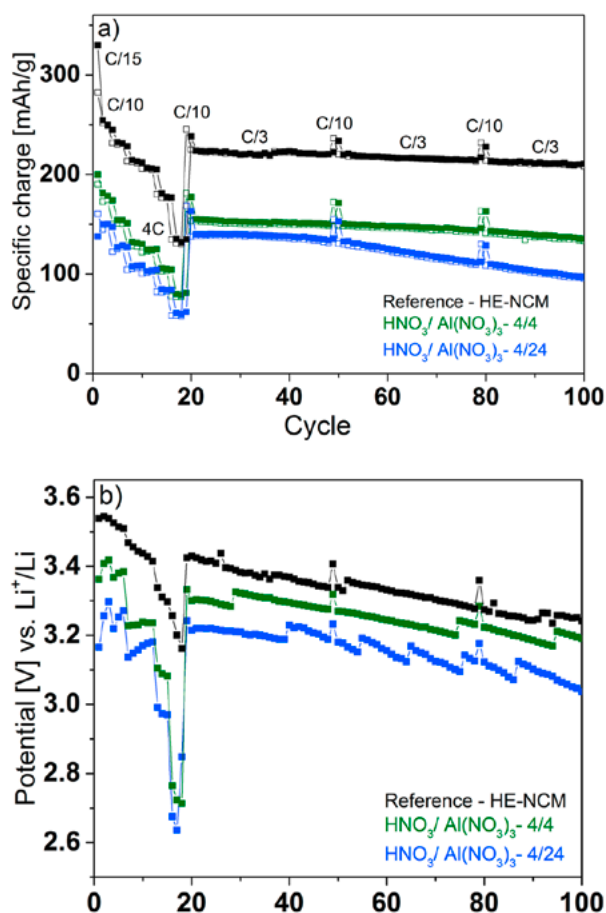


**Figure 3.** a) Evolution of the specific charge as a function of cycle number for the different HE-NCM samples. Cycling rates are indicated on the figure. b) Evolution of the potential at half discharge for the same compounds.

As can be seen from Figure 3, the initial specific charge drops with increasing the time of the treatment applied (from above 300 mAh/g for the reference to ca. 150–200 mAh/g for the treated samples after the first cycle at a C/15 cycling rate). This can be explained by the depletion of Li, as previously observed with ICP results: less Li ions in the structure leads to lower specific charge. It is also likely that the  $\text{Li}_2\text{MnO}_3$  domains are not

activated at the first cycle, explaining further the low specific charges obtained for the exchange samples. The 4 h/4 h and 4 h/24 h samples exhibit relatively similar specific charges (less than 10% difference at the 20<sup>th</sup> cycle), despite the longer Al exchange times of the 4 h/24 h sample. Moreover, the 4 h/4 h sample exhibits after 100 cycles a behaviour similar to the reference (fairly stable specific charge after 100 cycles). Short Al exchange times (less than 24 hours) are then essential in order to maintain good capacity retention.

Although the Al exchange treatment is undesirably affecting the specific charge, the potential at half discharge is stabilised for the 4 h/4 h sample with a slope of 1.76% compared to a slope of 2.24% for the reference sample and 1.94% for the 4 h/24 h sample (see Figure 3b).

The galvanostatic curve at the first cycle (Figure 4) indicates that there is no activation of the  $\text{Li}_2\text{MnO}_3$  since no potential plateau is visible at 4.5 V vs.  $\text{Li}^+/\text{Li}$ . This result is in agreement with the ICP since oxygen was found to be lacking after different post treatments.

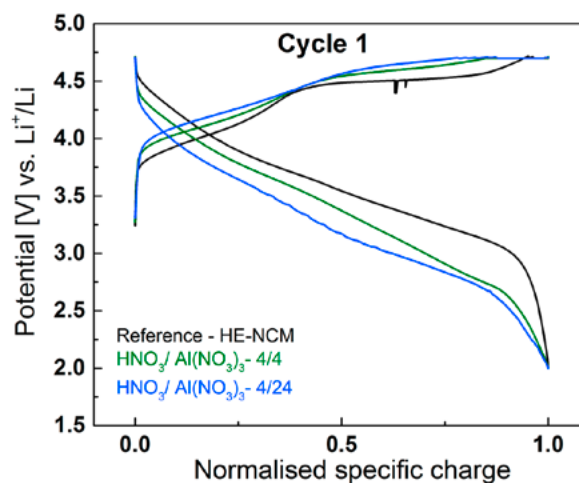


**Figure 4.** Evolution of the normalised specific charge as a function of the potential for the 1<sup>st</sup> cycle.

## Conclusion

We have successfully minimised the voltage fade of HE-NCM compounds by the means of various post-treatments. However, the specific charge of these compounds remains too low for practical applications. Therefore the amount of Al dopant (and thus the time of the cation treatment) will be decreased in order to maintain a lower voltage fade while having higher specific charge.

## Acknowledgement

The authors would like to express their gratitude to Dr. Nicola Casati from the MS-powder beamline at SLS for experimental support. BASF SE is acknowledged for the financial support. Prof. Dr. Petr Novák is acknowledged for fruitful discussions.

## References

- [1] A.R. Armstrong, N. Dupre, A.J. Paterson, C.P. Grey, P.G. Bruce, *Chem. Mater.* **16**, 3106–3118 (2014).
- [2] J.R. Croy, K.G. Gallagher, M. Balasubramanian, Z. Chen, Y. Ren, D. Kim, S.-H. Kang, D.W. Dees, M.M. Thackeray, *J. Phys. Chem. C* **117**, 6525–6536 (2013).

## Comparative study of Ni<sub>2</sub>SnP as negative electrode for Na-ion and Li-ion batteries

C. Marino, C. Villevieille

phone: +41 56 310 5304, e-mail: cyril.marino@psi.ch

Due to the relatively low amount of lithium resources, lithium-ion batteries (LiB) will not sustain the increasing demand of energy storage for the next decades. Sodium-ion batteries (NaB) could be an alternative and the first prototypes in full cells are promising since they can deliver 90 Wh/kg for over 200 cycles [1]. Even if the working principle of these two systems is similar, the chemistry induced by lithium is different to the one of sodium. Consequently, all the acquired knowledge through the LiB research cannot be applied to NaB, as it was demonstrated in our lab [2]. Conversion reactions have demonstrated good results in LiB and are highly attractive for negative electrode in NaB due to their high theoretical energy densities especially that graphite cannot be used in NaB [3]. In this work, we compare the electrochemical performances of Ni<sub>2</sub>SnP, versus lithium and versus sodium as negative electrode.

### Experimental

Ni<sub>2</sub>SnP materials were synthesized using two different routes. The first one was performed using ball-milling where the precursors (Ni, Sn, P) were mixed in stoichiometric amount during 16 hours at 800 rpm. The obtained material is hereafter called BM. The second one was obtained using solid-state synthesis at high temperature. A sealed quartz tube under vacuum containing the precursors was placed in a muffle oven and heated up to 800 °C during 7 days. The obtained material is hereafter denoted as TS. Electrodes were prepared by casting a mixture of 70 %wt active material, 9 %wt carbon black superC65 (CB, Imerys), 9 %wt vapor grown carbon fibers (VGCF, Showa Denko) and 12 %wt carboxymethylcellulose (CMC) mixed in deionized water onto copper foil. After a first drying at ambient temperature, electrodes were punched and dried at 120 °C under vacuum for 1 h 30'. Electrochemical cells were assembled in an argon glove box with lithium metal or sodium metal as counter electrode. 1 M LiPF<sub>6</sub> in EC/DMC or 1 M NaClO<sub>4</sub> in PC was used as electrolyte. Cells were galvanostatically cycled at 25 °C with C/20 rate.

### Results

The XRD patterns and SEM pictures of the two Ni<sub>2</sub>SnP materials are shown in Figure 1. The SEM pictures reveal crystalline samples with big particles size for the TS materials, as expected for solid-state synthesis. In both case, the Bragg peaks can be mainly assigned to the orthorhombic phase Ni<sub>2</sub>SnP (space group Pnma, ICSD n°06-1097). Some impurities such as Sn for TS and an unknown phase for BM can be detected. Broader diffraction peaks are obtained for BM due to the large particle size distribution usually generated by ball-milling.

The electrochemical performance of both materials in both systems (Li and Na) can be seen in Figure 2. Versus Li, BM displays the best electrochemical performances with a reversible specific charge of 680 mAh/g kept for 20 cycles. The specific charge of TS reaches only 450 mAh/g after 20 cycles. A potentiostatic step at the end of lithiation does not significantly improve the performance. This fading can be explained by the size of the particles bigger in TS than in BM, generating

more volume change during cycling thus causing the disconnection of particles from the conductive network of the electrode. Versus Na, a similar trend can be noticed. However, only 125 mAh/g is sustained for 45 cycles. Contrary to the Li system, a rapid fading in specific charge is observed during the first 10 cycles.

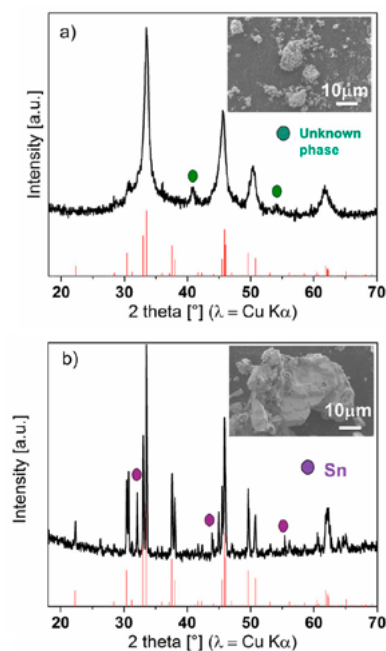


Figure 1. XRD patterns and SEM pictures of a) BM and b) TS.

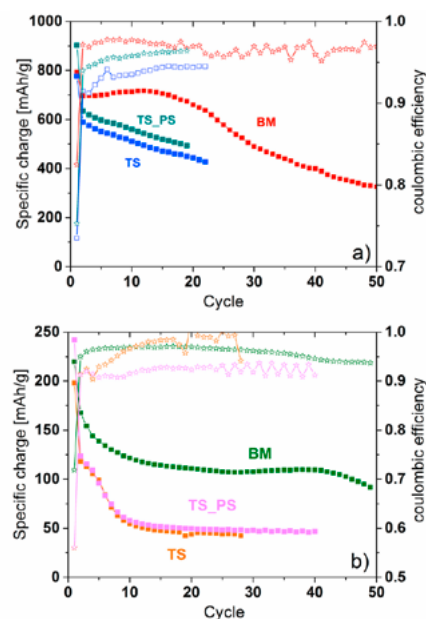
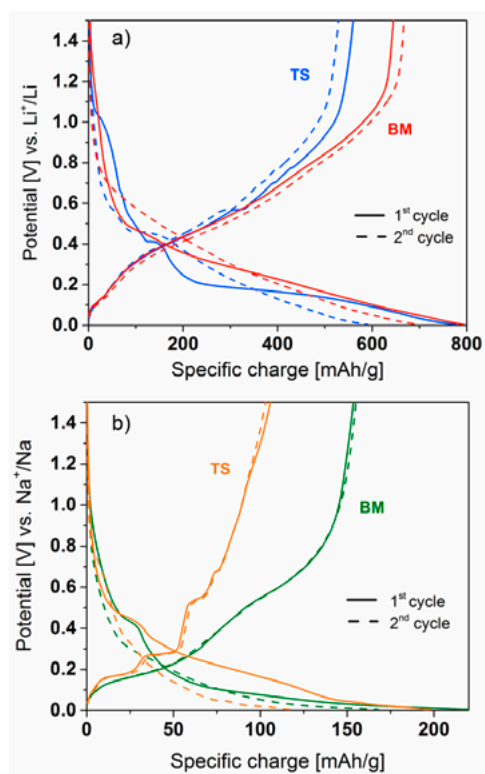


Figure 2. Electrochemical performance of BM and TS versus Li (a) and versus Na (b). The abbreviation PS means that the 1<sup>st</sup> cycle was performed using a potentiostatic step at 5 mV of 30 h.

The galvanostatic curves of the 1<sup>st</sup> and 2<sup>nd</sup> cycle are plotted in Figure 3. The 1<sup>st</sup> lithiation is slightly different between BM and TS most probably due to the impurities contained in TS. For further lithiation and delithiation the results are similar and only a difference in polarization can be observed.

Versus Na, different behaviours are found depending on the synthesis condition. A high polarization is seen for the 1<sup>st</sup> sodiation of BM, most probably due to the small particles size generating more SEI. The desodiation process of TS is different with the appearance of three potential plateaus which could be assigned to the desodiation of Sn. Only two potential plateaus are visible for the desodiation of BM.



**Figure 3.** Galvanostatic curves of the 1<sup>st</sup> and 2<sup>nd</sup> cycles for BM and TS versus Li (a) and versus Na (b).

Operando XRD experiments on the 1<sup>st</sup> cycle were carried out (Figure 4) using a homemade *in situ* cell [4]. For BM, the peaks assigned to Ni<sub>2</sub>SnP vanished upon lithiation to the benefit of two broad peaks. Those peaks are attributed to the formation of either Li<sub>4.4</sub>Sn [5] or Li<sub>7</sub>Sn<sub>2</sub>. On delithiation, these peaks disappear, however no other peak can be detected even at the end of the 1<sup>st</sup> cycle. Regarding the operando measurement performed onto TS sample, we found out more detail about the delithiation mechanism. Both Li<sub>2</sub>Sn<sub>5</sub> and Sn phases are detected but their origins are not clear since they can belong to the reaction of the impurities. It is interesting to note in both cases that phosphorus seems to be inert during the electrochemical processes.

In the case of Na, BM peaks slightly decrease in intensity at the end of sodiation and during the potentiostatic step at 5 mV no other phase appears. Unfortunately, no other modification can be detected along desodiation. The same trend was found for TS sample. One explanation could be that the sodiation of BM is not complete due to the very low potential plateau for the conversion reaction. Even by applying a very long potentiostatic step at 5 mV did not help to reach more than 200 mAh/g instead of 677 mAh/g for the theoretical value.

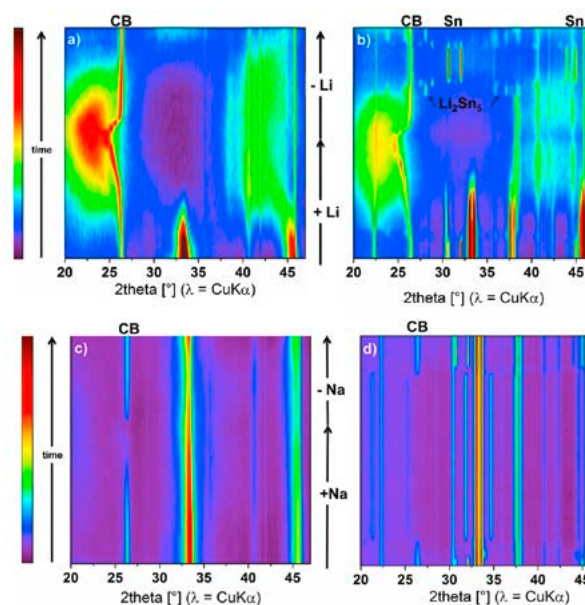


**Figure 4.** Operando XRD patterns evolution for the 1<sup>st</sup> cycle of a) BM vs. Li, b) TS vs. Li, c) BM vs. Na and d) TS vs. Na.

## Conclusion

Ni<sub>2</sub>SnP was synthesized by two routes (ball milling and high temperature) in order to obtain two different particle size distributions. Cycled versus Li, BM is able to sustain a specific charge superior than 600 mAh/g for 20 cycles. The lithiation was studied by operando XRD and the formation of Li<sub>i</sub>Sn phases was confirmed. Cycled versus Na, the mechanism is unclear since the potential plateau assigned to the reaction of Ni<sub>2</sub>SnP with Na is close to the sodium plating. Additional experiments like X-ray absorption at the Ni K-edge or <sup>31</sup>P NMR could help to assess better the reaction mechanism.

## Acknowledgement

This work was performed within the Swiss Competence Center of Energy Research Heat and Storage (SCCER) framework.

## References

- [1] J.-M. Tarascon, C. Masquelier, L. Croguennec, S. Patoux, CNRS press «a promising new prototype of battery», 27 Nov. 2015.
- [2] L. Vogt, M. El-Kazzi, E.-J. Berg, S.-P. Villar, P. Novák, C. Villevieille, *Chem Mater.* **27** (4), 1210 (2015).
- [3] F. Klein, B. Jache, A. Bhide, P. Adelhelm, *Phys. Chem. Chem. Phys.* **15**, 15876 (2013).
- [4] P. Bleith, H. Kaiser, P. Novák, C. Villevieille, *Electrochim. Acta* **176**, 18 (2015).
- [5] O. Mao, R. Dunlap, J. Dahn, *J. Electrochem. Soc.* **146** (2), 405 (1999).

## CuSbS<sub>2</sub> vs. Sb<sub>2</sub>S<sub>3</sub> as negative electrode for Li-ion and Na-ion batteries

C. Marino, C. Villevieille

phone: +41 56 310 5304, e-mail: cyril.marino@psi.ch

To date, graphite is the most used negative electrode in commercial lithium-ion batteries due to its stability, cost and relatively good specific charge (372 mAh/g). In the case of sodium-ion batteries, graphite cannot be used due to intrinsic parameters and thus hard carbon is used instead [1]. In order to improve the energy density of the batteries, conversion materials are showing promising results with theoretical specific charge higher than 500 mAh/g in Li or Na system [2]. We already studied a new type of material, MSnS<sub>2</sub> (M=Fe, Cu), as suitable negative electrode for both lithium-ion and lithium-sulphur batteries. A specific charge greater than 500 mAh/g for the lithium-ion system was obtained after 400 cycles [3]. In this work, we follow the same strategy by developing new anode types based on antimony, Sb<sub>2</sub>S<sub>3</sub> and CuSbS<sub>2</sub>. We investigate their electrochemical properties in Li and Na-ion batteries.

### Experimental

Both materials were synthesized by ball-milling from stoichiometric amount of Cu, Sb and S powders. Electrodes were prepared by casting a mixture of 70 %wt active material, 9 %wt carbon black superC65 (CB, Imerys), 9 %wt vapor grown carbon fibers (VGCF, Showa Denko) and 12 %wt carboxymethylcellulose (Na-CMC) in deionized water onto copper foil. After a first drying at ambient temperature, electrodes were punched and dried at 120 °C under vacuum for 1 h 30'. Electrochemical cells were assembled in an argon glove box with lithium metal or sodium metal as counter electrode. 1 M LiPF<sub>6</sub> in EC/DMC or 1 M NaClO<sub>4</sub> in PC was used as electrolyte. Cells were cycled in galvanostatic mode at 25 °C at C/3 rate.

### Results

The XRD pattern and SEM picture of the two synthesized materials are shown in Figure 1. For both materials, the SEM pictures revealed micrometer particles range up to 3 μm. The Bragg peaks of the synthesized CuSbS<sub>2</sub> match the ones of the orthorhombic CuSbS<sub>2</sub> phase (space group Pnma, ICSD card n° 85-0133). In the diffractogram of Sb<sub>2</sub>S<sub>3</sub>, the peaks can be assigned to the orthorhombic Sb<sub>2</sub>S<sub>3</sub> phase (space group Pnma, ICSD card n° 30-0779) but some impurities mainly Sb can be detected.

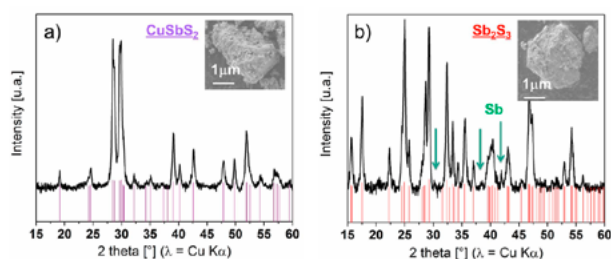


**Figure 1.** XRD patterns and SEM pictures of a) CuSbS<sub>2</sub> and b) Sb<sub>2</sub>S<sub>3</sub>.

The electrochemical performance of both materials can be seen in Figure 2. In all cases, the specific charge obtained during the first cycle is quite high due to the electrolyte decomposition. Versus Li, CuSbS<sub>2</sub> displays the best performance with a reversible specific charge of 900 mAh/g kept for 10 cycles whereas only 750 mAh/g is obtained for Sb<sub>2</sub>S<sub>3</sub>. However, after 10 cycles, the specific charge of CuSbS<sub>2</sub> drastically decreases to reach 400 mAh/g at the 30<sup>th</sup> cycle. Interestingly, the specific charge of Sb<sub>2</sub>S<sub>3</sub> is constantly decreasing but still higher than 450 mAh/g at the 30<sup>th</sup> cycle. The better specific charge obtained by CuSbS<sub>2</sub> could be related to the presence of Cu. However, during cycling and due to volume change of the materials upon lithiation/delithiation and the probable Cu extrusion, both could lead to a fast fading in case of Cu cannot be recombined. Versus Na, a similar trend can be observed with a reversible and stable specific charge for CuSbS<sub>2</sub> at 730 mAh/g for 7 cycles compared to 600 mAh/g for Sb<sub>2</sub>S<sub>3</sub>. However, after 10 cycles, the specific charge of Sb<sub>2</sub>S<sub>3</sub> drops down quickly to a value lower than 100 mAh/g. In the case of CuSbS<sub>2</sub>, the fading proceeds in two steps. The first one happens at the 8<sup>th</sup> cycle where the specific charge of 450 mAh/g is held until the 19<sup>th</sup> cycle then a second drop is observed leading to specific charge below 100 Ah/g after 30 cycles.

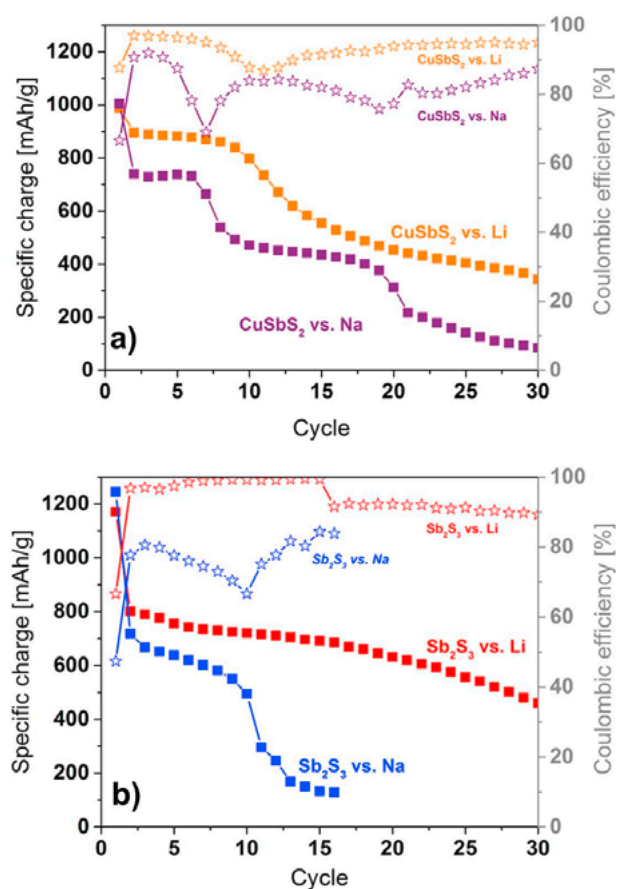


**Figure 2.** Electrochemical performance of a) CuSbS<sub>2</sub> and b) Sb<sub>2</sub>S<sub>3</sub> versus both Li and Na.

The galvanostatic curves for the 1<sup>st</sup> and 2<sup>nd</sup> cycles are shown in Figure 3. For  $\text{Sb}_2\text{S}_3$  (Figure 3a and 3b), two potential plateaus can be seen at 1.5 V and 0.8 V versus Li and at 1 V and 0.5 V versus Na during the 1<sup>st</sup> lithiation/sodiation. For the 1<sup>st</sup> delithiation/desodiation, two plateaus can also be observed at 0.9 V and 1.8 V versus Li and 0.6 V and 1.2 V versus Na. According to Park et al. [4], in  $\text{Sb}_2\text{S}_3$ ,  $\text{Li}_x\text{S}$  is formed first then Sb is reacting giving  $\text{Li}_3\text{Sb}$ . On delithiation,  $\text{Sb}_2\text{S}_3$  is reformed but the recombination is only partial. For the 2<sup>nd</sup> lithiation, the potential plateau at 1.5 V, assigned to the conversion of  $\text{Sb}_2\text{S}_3$  in  $\text{Li}_x\text{S}$  and Sb, is mostly vanished whereas, for the 2<sup>nd</sup> sodiation, the 1<sup>st</sup> plateau at 1 V is still visible. Interestingly, the recombination of  $\text{Sb}_2\text{S}_3$  seems to perform better in Na system.

For  $\text{CuSbS}_2$  (Figure 3c and 3d), four potential plateaus at 1.7 V, 1.5 V, 0.75 V and 0.1 V are distinguished during the 1<sup>st</sup> lithiation whereas, for the 1<sup>st</sup> sodiation, only three at 1.3 V, 0.9 V and 0.5 V are visible. Based on literature [5], the potential plateau at 0.1 V upon lithiation could be related to the formation of a polymeric film on the surface of metallic nanoparticles in Li system. The 1<sup>st</sup> delithiation and desodiation curves are composed of two potential plateaus at 0.9 V and 1.9 V and at 0.7 V and 1.4 V, respectively, for Li and Na systems. A partial reformation of  $\text{CuSbS}_2$  could explain the absence of a 3<sup>rd</sup> potential plateau upon delithiation/desodiation. For the 2<sup>nd</sup> lithiation, additionally to the plateaus at 0.75 V and 0.1 V seen in the 1<sup>st</sup> cycle, a new potential plateau between 1.8 V and 1.5 V is observed most probably related to the reaction of  $\text{Li}_x\text{S}$ . In the 2<sup>nd</sup> sodiation curve, a new potential plateau is observed at 1.5 V in addition to the two plateaus at 0.9 V and 0.5 V. Probably, the reformed phase upon the 1<sup>st</sup> delithiation/desodiation is slightly different to the  $\text{CuSbS}_2$  pristine.

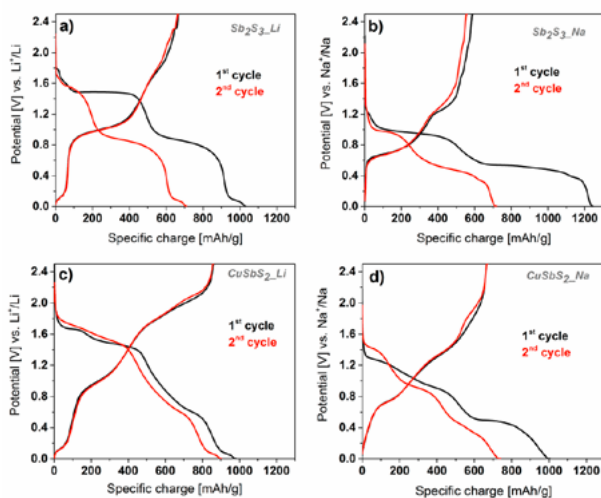


**Figure 3.** Galvanostatic curves of the 1<sup>st</sup> and 2<sup>nd</sup> cycles for  $\text{Sb}_2\text{S}_3$  versus Li (a) and  $\text{Sb}_2\text{S}_3$  versus Na (b),  $\text{CuSbS}_2$  versus Li (c),  $\text{CuSbS}_2$  versus Na (d).

To get better insight into the reaction mechanisms of  $\text{CuSbS}_2$ , X-ray absorption spectroscopy was performed at key potentials as seen in Figure 4. Both full lithiation and full sodiation provide similar X-ray absorption spectra with the experimental proof of Cu extrusion [6]. The extrusion of Cu metal at the end of sodiation/lithiation would confirm the conversion reaction mechanism of  $\text{CuSbS}_2$ . At the end of delithiation/desodiation, the spectra look similar to the pristine  $\text{CuSbS}_2$  spectrum. Only a slight difference can be noticed directly after the edge. Based on literature work [7], it can be assumed that a structure close to  $\text{CuSbS}_2$  pristine is reformed at the end of delithiation/desodiation.

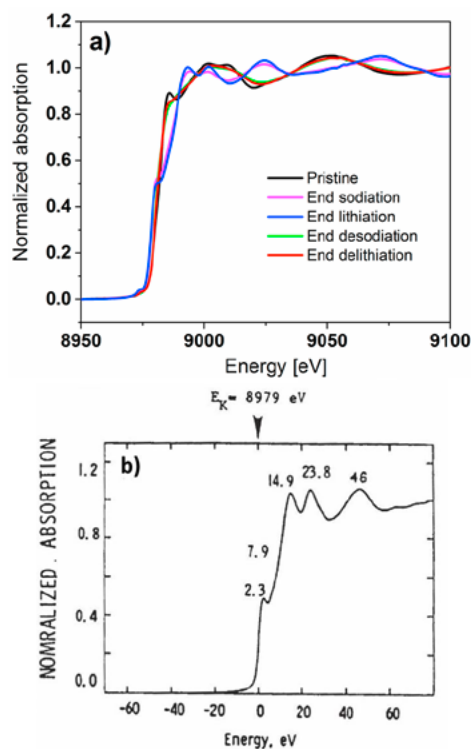


**Figure 4.** Comparison of XANES Spectra of lithiated and sodiated phases of  $\text{CuSbS}_2$  (a) and XANES spectra of Cu metal foil (b) extracted from [6].

## Conclusion

$\text{CuSbS}_2$  and  $\text{Sb}_2\text{S}_3$  were successfully synthesized by ball milling.  $\text{CuSbS}_2$  presents the best electrochemical performances whatever the system Li or Na. X-ray absorption experiments show that  $\text{CuSbS}_2$  undertakes a conversion reaction mechanism with the extrusion of Cu metal at the end of lithiation/sodiation. For  $\text{Sb}_2\text{S}_3$  the electrochemical performances are less good due to the difficulties to recombine the starting phase which is more pronounced versus Li.

## Acknowledgement

The authors thank M. Nachtegaal and the SuperXAS beamline at SLS for XAS experiments. This work was performed within the Swiss Competence Center for Heat and Electricity Storage framework.

## References

- [1] N. Yabuuchi, K. Kubota, M. Dahbi, S. Komaba, *Chem. Rev.* **114**, 11636 (2014).
- [2] F. Klein, B. Jache, A. Bhide, P. Adelhelm, *Phys. Chem. Chem. Phys.* **15**, 15876 (2013).
- [3] C. Villevieille, P. Novák, *J. Electroch. Soc.* **162**, A284–A287 (2015).
- [4] C. Park, Y. Hwa, N. Sung, H. Sohn, *J. Mater. Chem.* **20**, 1097 (2010).
- [5] G. Gachot, S. Grugeon, M. Armand, S. Pilard, P. Guenot, J.-M. Tarascon, S. Laruelle, *J. Power Sources* **178**, 409 (2008).
- [6] «Reference X-Ray spectra of metal foils», EXAFS materials, pdf available on <http://www.camd.lsu.edu/>.
- [7] C. Marino, B. Fraisse, M. Womes, C. Villevieille, L. Monconduit, L. Stievano, *J. Phys. Chem. C* **118**(48), 27772 (2014).

## Cr-Nasicon $\text{Li}_3\text{Cr}_2(\text{PO}_4)_3/\text{C}$ as a new cathode material with two redox couples

M. Reichardt, C. Villevieille, P. Novák, S. Sallard

phone: +41 56 310 5850, e-mail: martin.reichardt@psi.ch

Li-ion batteries are nowadays widely used for the energy supply of mobile electronic devices like smartphones or notebooks. However, to massively extend the electric cars market, the energy density of the batteries needs to be increased, in order to reach similar range and price compared to cars with combustion engines.

In commercial Li-ion batteries, positive electrodes such as  $\text{LiFePO}_4$  or  $\text{LiCoO}_2$  are based on only one electron exchange reaction per metal atom. This results in a limited specific charge which has a direct influence on the energy density of the battery.

Chromium possesses the advantage of having stable oxidation states from 2+ to 6+. Thus, it is in theory possible to overcome the one-electron limitation and to obtain high specific charge with Cr-based polyanion materials  $\text{Li}_x\text{CrX}$  (X as anionic part).

The material  $\text{LiCrP}_2\text{O}_7$  has been chosen as a proof of concept, since the synthesis [1] and crystal structure [2] are already described in the literature. The supposed  $\text{Cr}^{3+/2+}$  redox couple could be experimentally confirmed by our team already but no proof was found for the  $\text{Cr}^{4+}$  oxidation state [3].

Thus, our investigations were pursued with  $\text{Li}_3\text{Cr}_2(\text{PO}_4)_3$  and carbon coated (noted  $\text{Li}_3\text{Cr}_2(\text{PO}_4)_3/\text{C}$ ) material where the synthesis and crystal structure and, more recently, preliminary results of electrochemical cycling showed activity for the  $\text{Cr}^{4+}/\text{Cr}^{3+}$  redox couple [4]. The objective is to obtain a model cathode material to validate the concept of multiple redox couples based on chromium.

### Experimental

$\text{Li}_3\text{Cr}_2(\text{PO}_4)_3/\text{C}$  materials were synthesized by two different syntheses routes:

- Sol-gel synthesis, based on acetate precursors and citric acid as gelating agent (carbon coated).
- Solid state synthesis with carbon coating.

$\text{Li}(\text{CH}_3\text{COO})\cdot 2\text{H}_2\text{O}$ ,  $\text{Cr}_3(\text{CH}_3\text{COO})_7(\text{OH})_2$ ,  $\text{NH}_4\text{H}_2\text{PO}_4$  and citric acid (carbon source for the C-coating) in molar ratio 3.6:1:6, dissolved in demineralized water, were used as precursors for the sol-gel synthesis. The solution was heated up to 160 °C for 12 h. The material was then calcined in two steps, at 300 °C for 6 h under air and then under argon at 800 °C for 5 h. After each step, the material was ground carefully to homogenize the powder. Before the electrodes' preparation, all the synthesized materials were ball-milled at 300 rpm in order to reduce the particle size.

X-ray diffraction (XRD) experiments were performed with a PANalytical Empyrean diffractometer using Cu-K $\alpha$  radiation. Neutron powder diffraction (NPD) of pristine samples was conducted at HRPT, SINQ at the Paul Scherrer Institute. Electrodes for cyclic voltammetry and galvanostatic cycling were prepared using 80 %wt  $\text{Li}_3\text{Cr}_2(\text{PO}_4)_3/\text{C}$ , 10 %wt SuperC65 (Imerys)

and 10 %wt PVDF (Solvay) dissolved into NMP used as solvent. All measurements were performed using LP30 electrolyte (1 M  $\text{LiPF}_6$  in EC:DMC 1:1 wt.). The separator was from glass fibres or Celgard. Along this report, all the potentials will be given versus the  $\text{Li}^+/\text{Li}$  reference.

### Results

The structure of the home-made  $\text{Li}_3\text{Cr}_2(\text{PO}_4)_3/\text{C}$  (synthesized by sol-gel method) was investigated using neutron powder diffraction (NPD). The refinement of the NPD pattern (Figure 1) confirms the formation of the mono-clinic  $\text{Li}_3\text{Cr}_2(\text{PO}_4)_3$  phase ( $\text{P}2_1/\text{c}$ ) from the sol-gel route, since no other phases seem to be detected. For the refinement, the reference (ICSD n°. 96-2970) by Sun et al. [5] was used.

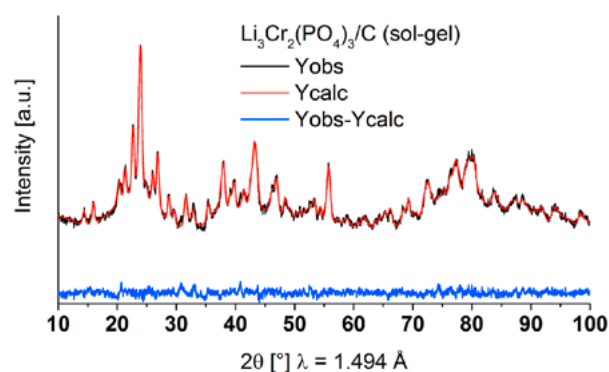


**Figure 1.** Refinement of the neutron powder diffraction data of  $\text{Li}_3\text{Cr}_2(\text{PO}_4)_3/\text{C}$  (sol-gel route) compared to reference [5].

The XRD pattern (Figure 2) of the sol-gel material shows broader peaks and high background. This is an indication that the material has a lower crystallinity (compared to solid-state synthesis materials). Even if less crystalline, no impurities could be detected in the sol-gel material.

### Electrochemistry

Both  $\text{Li}_3\text{Cr}_2(\text{PO}_4)_3/\text{C}$  obtained from the two different synthetic routes present similar electrochemical activities in the potential range 1.5–2.5 V (Figure 3) region attributed to the redox couple  $\text{Cr}^{3+}/\text{Cr}^{2+}$  [6]. Interestingly, two reduction peaks (1.60 and 1.90 V) and two oxidation peaks (1.85 and 2.30 V) are observed, suggesting two different electrochemical reactions or pathways. It is attributed to the two different chromium positions in the structure giving consequently different redox activities.

For the potential superior to 3.5 V, a difference is visible between the CVs of the two  $\text{Li}_3\text{Cr}_2(\text{PO}_4)_3/\text{C}$ . The one obtained from the solid state route shows oxidation peaks at ~4.5 and 4.83 V and reduction peaks at 4.73 and ~4.0 V. The peaks at potential  $\geq 4.0$  V are attributed to the redox couple  $\text{Cr}^{4+}/\text{Cr}^{3+}$ ,

in agreement with the DFT calculations performed by Hautier et al. [6]. The fact to see two peaks is most probably related to the crystal structure. Indeed, the chromium atoms are occupying different positions and thus one can imagine different energies and kinetics for each Cr, leading to different electrochemical potentials.

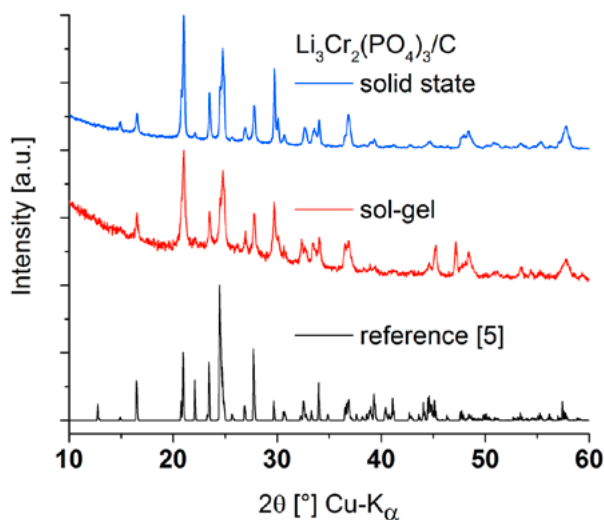


**Figure 2.** XRD patterns of the  $\text{Li}_3\text{Cr}_2(\text{PO}_4)_3/\text{C}$  materials with reference from Sun et al. [5].

For the sol-gel material, the oxidation peak at 4.83 V in the cyclic voltammogram is also present, but with a lower specific current. More important to notice, no significant reduction peak can be seen for the sol-gel material in the cyclic voltammogram. The difference of the electrochemical properties for the  $\text{Li}_3\text{Cr}_2(\text{PO}_4)_3/\text{C}$  obtained from the two different synthetic routes is attributed to the different particle size [7].

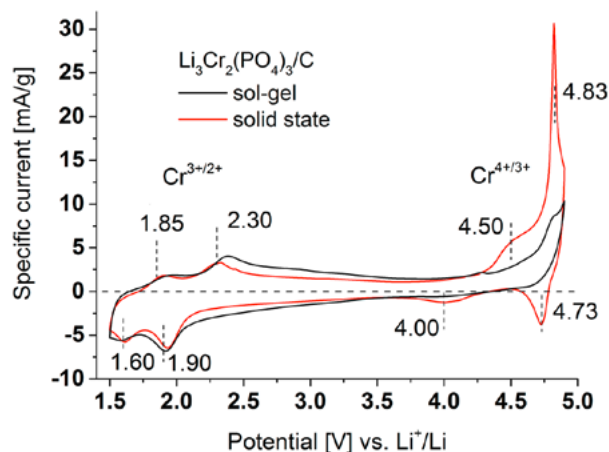


**Figure 3.** Cyclic voltammetry of  $\text{Li}_3\text{Cr}_2(\text{PO}_4)_3/\text{C}$  with two different synthesis routes, sol-gel and solid state carbon coated, 0.02 mV/s scanrate.

The evolution of the specific charge during cycling for the  $\text{Li}_3\text{Cr}_2(\text{PO}_4)_3/\text{C}$  materials is shown in Figure 4. The highest specific charge,  $\sim 141$  mAh/g, is reached with the sol-gel  $\text{Li}_3\text{Cr}_2(\text{PO}_4)_3/\text{C}$  in combination with a Celgard separator, followed by the same material,  $\sim 124$  mAh/g, but with a glass fibres separator. Both present a similar fading during ageing with a loss of  $\sim 20$  mAh/g from the 10<sup>th</sup> to the 80<sup>th</sup> cycle. The solid state carbon coated and  $\text{Li}_3\text{Cr}_2(\text{PO}_4)_3/\text{C}$  presents a specific

charge around 80–105 mAh/g in the first cycle, depending on the amount of citric acid introduced during the synthesis to generate a carbon coating. This carbon coating has a strong influence on the specific charge and especially on the ageing of the solid state material (Figure 4). Thick carbon coating (twice amount of citric acid in the synthesis) limits the specific charge fading to  $\sim 20$  mAh/g from the 10<sup>th</sup> to the 100<sup>th</sup> cycle while for thinner coating, the fading is four times more pronounced.

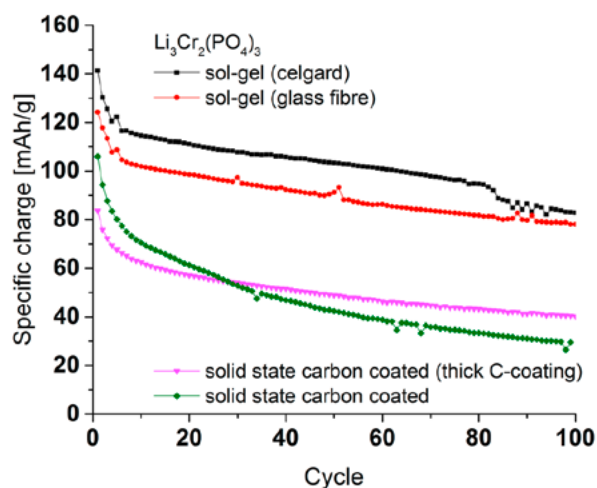


**Figure 4.** Comparison of the specific charge evolution of the different  $\text{Li}_3\text{Cr}_2(\text{PO}_4)_3/\text{C}$  materials. Cycling conditions: 13 mA/g in the potential range 1.5–4.9 V vs.  $\text{Li}^+/\text{Li}$ .

## Conclusion

The  $\text{Li}_3\text{Cr}_2(\text{PO}_4)_3/\text{C}$  material was synthesized via sol-gel and solid-state routes. The highest specific charge of roughly 140 mAh/g is obtained with the sol-gel route thanks to the carbon coating and smaller particles improving most probably the conductivity and lithium pathways. Interestingly, the carbon coated materials obtained by solid state route present two electrochemically active redox couple attributed to  $\text{Cr}^{4+}/\text{Cr}^{3+}$  and  $\text{Cr}^{3+}/\text{Cr}^{2+}$ . These results prove the concept of multiple redox couples as cathode materials for Li-ion batteries.

## References

- [1] Gangulibabu, D. Bhuvaneshwari, N. Kalaiselvi, *Appl. Phys. A* **96**, 489–493 (2009).
- [2] L.S. Ivashkevich, K.A. Selevich, A.I. Lesnikovich, A.F. Selevich, *Acta Crystallogr. Sect. E* **63**, i70–i72 (2007).
- [3] M. Reichardt, S. Sallard, P. Novák, C. Villevieille, *Acta Crystallogr. Sect. B* **71**, 661–667 (2015).
- [4] M. Herklotz, F. Scheiba, R. Glaum, E. Mosymow, S. Oswald, J. Eckert, H. Ehrenberg, *Electrochim. Acta* **139**, 356–364 (2014).
- [5] J. Sun, P. Kim, H. Yun, *Acta Crystallogr. Sect. E* **69**, i72 (2013).
- [6] G. Hautier, A. Jain, T. Mueller, C. Moore, S.P. Ong, G. Ceder, *Chem. Mater.* **25**, 2064–2074 (2013).
- [7] C. Wurm, M. Morcrette, G. Rousse, L. Dupont, C. Masquelier, *Chem. Mater.* **14**, 2701–2710 (2002).

## LiFe<sub>x</sub>Mn<sub>1-x</sub> methylene diphosphonate (x = 0, 0.2, 0.5, 0.8, 1.0): mixed transition metal diphosphonate positive electrode materials for Li-ion batteries.

S. Schmidt, C. Villeveille, P. Novák, S. Sallard

phone: +41 56 310 5762, e-mail: sebastian.schmidt@psi.ch

Nowadays, research on positive electrode materials for Li-ion batteries still mainly focuses on solely inorganic materials such as transition metal oxides or phosphates [1]. The range of accessible materials however is limited, as only a small range of transition metal ions have the properties for positive electrode materials. Due to the versatility of organic molecules, the introduction of organics into such structures opens a wide range of different new materials with tunable properties. Even though organic-inorganic hybrid positive electrode materials have been introduced by Férey et al. already in 2007 [2], still only few examples have been reported in the literature. The majority is based on carboxylate ligands, whose metal-O-bonds are suspected to be the cause for the instability at lithiation degrees higher than 0.5 Li per formula unit for the case of a Fe-benzylidicarbonyl-MOF [3]. Diphosphonates are an interesting alternative, as they are known to be versatile molecules to introduce organics into inorganic structures [4], and to form M-O-P bonds known to be stable.

In a previous work, we prepared lithium iron methylene diphosphonate to prove the concept of diphosphonates as positive electrode materials in Li-ion batteries [5]. Its structure was determined by neutron and X-ray powder diffraction (XRD) patterns. The redox activity of Fe in the material was proven by *operando* X-ray absorption. We decided to investigate lithium manganese methylene diphosphonate to verify the applicability to other 3d transition metals and whether Mn-based hybrid material can provide a different operating voltage. Additionally, mixed lithium Fe<sub>x</sub>Mn<sub>1-x</sub> methylene diphosphonates were prepared to investigate the possibility to obtain increased operating potential and improved rate capability as it was demonstrated by Aurbach et al. for the case of LiFe<sub>0.2</sub>Mn<sub>0.8</sub>PO<sub>4</sub> [6].

### Experimental

Lithium Fe<sub>x</sub>Mn<sub>1-x</sub> methylene diphosphonate was prepared by a hydrothermal route from FeSO<sub>4</sub>, Mn(OAc)<sub>2</sub> and tetraethyl methylene diphosphonate, as established in ref. [5]. XRD was measured on a PANalytical Empyrean diffractometer using Cu-K $\alpha$  radiation ( $\lambda = 1.546 \text{ \AA}$ ). Galvanostatic cycling was performed in a half-cell system, using LP30 as electrolyte in a potential window of 1.5 V – 4.5 V vs. Li<sup>+</sup>/Li at a rate of 5 mA/g. The working electrodes were prepared by doctor-blading a slurry based on 50 %wt active material, 40 %wt Super C65 carbon black used as conductive additive and 10 %wt PVdF binder on Al foil.

### Results

From XRD, all synthesized Fe<sub>x</sub>Mn<sub>1-x</sub> methylene diphosphonates crystallized in a single phase with a monoclinic space group as lithium iron methylene diphosphonate (C 2/c) [5]. With increasing Mn-content, all the peaks shift to lower angle affecting then the lattice parameters (Figure 1). The unit cell parameters obtained by LeBail refinement showed only a slight deviation from Vegard's law (Table 1). This indicates that the mixed materials can be described as a solid solution of the

two phases. This demonstrates that it is possible to synthesize mixed phases of transition metal diphosphonate.

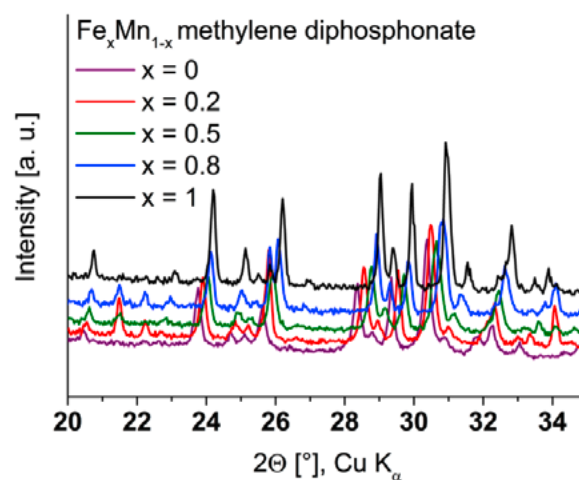


Figure 1. X-ray diffraction patterns of lithium Fe<sub>x</sub>Mn<sub>1-x</sub> methylene diphosphonates (x = 0, 0.2, 0.5, 0.8, 1.0).

	x = 1	x = 0.8	x = 0.5	x = 0.2	x = 0
a [Å]	18.809(1)	18.946(1)	18.994(2)	19.082(2)	19.151(2)
b [Å]	8.3260(3)	8.3191(12)	8.3769(8)	8.4517(7)	8.500(1)
c [Å]	8.9604(3)	8.9764(16)	8.9952(9)	9.0078(9)	9.040(1)

Table 1. Unit cell parameters of lithium Fe<sub>x</sub>Mn<sub>1-x</sub> methylene diphosphonate obtained from LeBail refinement.

Galvanostatic cycling showed that all materials exhibit a similar potential vs. specific charge profile (Figure 2). Lithium Mn methylene diphosphonate is cycling reversibly. Surprisingly though, it does not show a higher reduction potential than Fe methylene diphosphonate, but superior specific charge (Figure 3). Unfortunately, the mixed materials are all inferior in terms of specific charge, and present no increased potential in comparison to Fe. At 50:50 mixture, the obtained specific charge is lowest, so the «mismatch» in metals seems to play a role in the decreased specific charge. An interesting effect of the mixed materials is the lower irreversibility of the first oxidation. The coulombic efficiency increases for x = 0.2 and x = 0.8 for 6% and 7% respectively. For x = 0.5, the same coulombic efficiency as for the Fe-only material was obtained. This leads to the assumption that by adding a lower amount of the additional metal (e.g. 2% or 5% instead of 20%) the coulombic efficiency could be improved at a lower relative loss of specific charge.

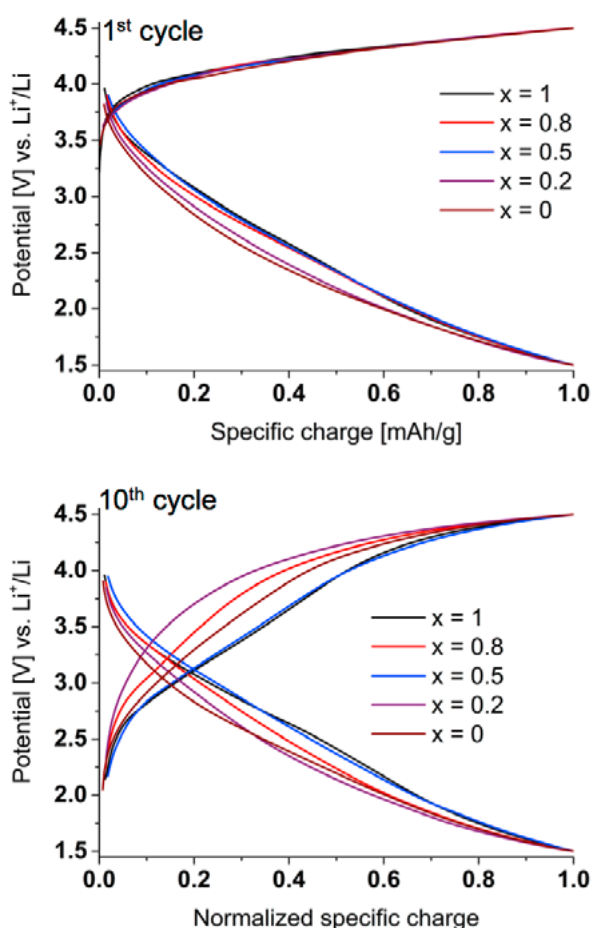


Figure 2. Normalized galvanostatic cycling curves of the lithium  $\text{Fe}_x\text{Mn}_{1-x}$  methylene diphosphonates of the first cycle (top) and the 10<sup>th</sup> cycle (bottom).

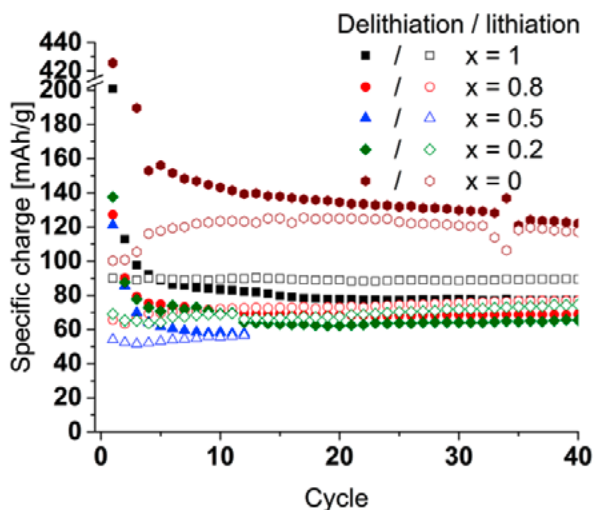


Figure 3. Comparison of the specific charge vs. cycle number of the lithium  $\text{Fe}_x\text{Mn}_{1-x}$  methylene diphosphonates.

## Conclusions

Lithium  $\text{Fe}_x\text{Mn}_{1-x}$  methylene diphosphonates were successfully synthesized using the previously established method [5]. For lithium Mn methylene diphosphonate, a higher specific charge than for the Fe-one was obtained. Unfortunately, the mixed materials performed less effectively than the materials containing Fe or Mn only, the observed reduction of irreversibility opens the possibility of further improvements.

## Acknowledgement

The authors would like to express their sincere gratitude to the Swiss National Science Foundation (SNF) for funding (project 200021\_146224).

## References

- [1] M. Hu, X. Pang, Z. Zhou, *J. Power Sources* **237**, 229–242 (2013).
- [2] G. Férey, F. Millange, M. Morcrette, C. Serre, M.-L. Doublet, J.-M. Grenèche, J.-M. Tarascon, *Angew. Chem. Int. Ed.* **46**, 3259–3263 (2007).
- [3] C. Combelles, M. Ben Yahia, L. Pedesseau, M.L. Doublet, *J. Power Sources* **196**, 3426–3432 (2011).
- [4] P.H. Mutin, C. Delenne, D. Medoukali, R. Corriu, A. Vioux, *MRS Online Proceedings Library* **519**, 345–350 (1998).
- [5] S. Schmidt, D. Sheptyakov, J.-C. Jumas, M. Medarde, P. Benedek, P. Novák, S. Sallard, C. Villevieille, *Chem. Mater.* **27** (23), 7889–7895, doi: 10.1021/acs.chemmater.5b02595 (2015).
- [6] S.K. Martha, J. Grinblat, O. Haik, E. Zinigrad, T. Drezen, J.H. Miners, I. Exnar, A. Kay, B. Markovsky, D. Aurbach, *Angew. Chem. Int. Ed.* **48**, 8559–8563 (2009).

## Effect of carbon additive on the cycling stability of the Li–S electrodes with high sulfur loading

T. Poux, P. Novák, S. Trabesinger

phone: +41 56 310 3792, e-mail: tiphaine.poux@psi.ch

Due to the abundance of sulfur, its low toxicity, and its high theoretical specific charge (1672 mAh/g<sub>s</sub>), the lithium–sulfur (Li–S) battery is one of the promising electrochemical systems for next-generation energy-storage applications. However, the commercialization of Li–S cells is hampered by numerous challenges, such as the insulating nature of sulfur and of its discharge product Li<sub>2</sub>S, hindering active material utilization, and the so-called polysulfide shuttle, leading to a loss of active material and a low coulombic efficiency. Significant improvements on the electrode and cell levels were made in the past few years [1], minimizing these limitations and leading to a growing interest in Li–S battery commercialization.

In order to achieve high energy density and to be therefore suitable for practical applications, high sulfur loading is required in Li–S positive electrodes. However, attempts to do so often result in poor electrochemical performance [2–5]. In this work the effect of the carbon additive nature on the cycling behavior of highly loaded sulfur electrodes was investigated.

### Experimental

Sulfur composite electrodes were prepared by mixing 60 wt sulfur, 30 wt carbon additive and 10 wt polyethylene oxide (PEO) binder by turbo stirring, using acetonitrile as a solvent. The carbon additive was either (i) 30 wt Super P carbon black; (ii) 30 wt KS6 graphite; or (iii) 25 wt Super P + 5 wt carbon fibers. The resulting slurry was doctor-bladed on a carbon-coated aluminum foil. After drying at room temperature for 24 h, the electrodes were punched out to form 13-mm-diameter discs, and then transferred into an argon-filled glove box. The sulfur loading was ~3.3 mg per electrode (~2.5 mg<sub>s</sub> cm<sup>-2</sup>).

Sulfur electrodes were assembled into coin-type cells, using Celgard 2400 as a separator and metallic lithium as the counter electrode. The cells were filled with 50 μL of electrolyte containing 1 M lithium bis(trifluoromethane sulfone)imide (LiTFSI) in dimethoxyethane (DME):1,3-dioxolane (Diox) (2:1), the electrolyte-to-sulfur ratio being then 15:1 (mL:g<sub>s</sub>). The cells were galvanostatically cycled between 1.8 and 2.7 V vs Li<sup>+</sup>/Li at C/5 rate (1C rate is defined as I = 1672 mA g<sub>s</sub><sup>-1</sup>) using an Astrol battery cycler. The specific charge is denoted per mass of sulfur, and, for clarity, only the specific charge on the discharge (reduction of the sulfur) is shown.

### Results

The sulfur electrodes were first characterized by scanning electron microscopy (SEM). As observed in Figure 1, the carbon additive has a strong impact on the morphology of these electrodes. The substitution of only 5 wt of Super P by carbon fibers leads to a much more open structure, which may allow a better access of electrolyte into the depth of the electrode. When Super P is replaced by KS6 graphite, small carbon particles are replaced by large graphite flakes, which are expected to improve the mechanical integrity of thick electrodes [4].

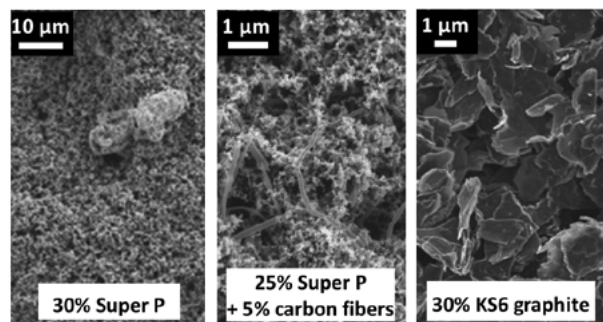


Figure 1. SEM images of electrodes containing 60% sulfur, 30% carbon (indicated in the figure) and 10% PEO binder.

The electrochemical behavior of these sulfur electrodes was then investigated by galvanostatic cycling. When the carbon additive is Super P only, the specific charge is 500 mAh/g<sub>s</sub> after 50 cycles (Figure 2 & 3). For electrodes with lower loading, cycled in similar conditions, 600 mAh/g<sub>s</sub> was still reached after 50 cycles [6]. Thus, the loading increase clearly leads to lower sulfur utilization in the electrode.

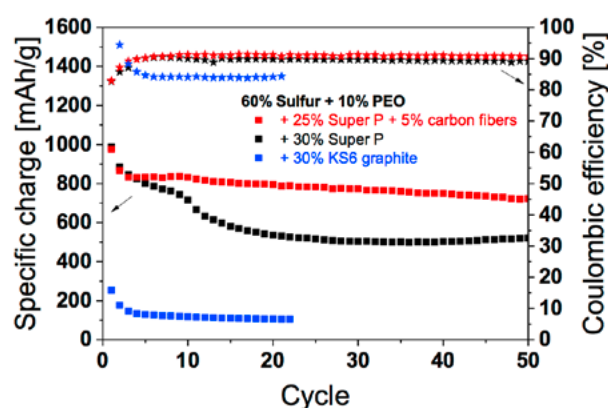


Figure 2. Specific charge (squares) and coulombic efficiency (stars) of sulfur electrodes with various carbon additives: Super P and carbon fibers (red), Super P (black) and KS6 graphite (blue).

The mechanical integrity of thick electrodes might be compromised while cycling, resulting in sulfur being disconnected from conductive network and thus in lower specific charge. However, the replacement of Super P by KS6 graphite, which is supposed to solve this challenge [4], leads to even worse performance. Indeed, less than 200 mAh/g<sub>s</sub> is delivered after the second cycle and the coulombic efficiency is lower than with Super P (Figure 2). It is observed from the galvanostatic profiles (Figure 4) that only the upper discharge plateau is present in the studied potential range, due to the overpotential of the lower plateau being too high. This may be caused by the low surface area of graphite, and after first layers of S or Li<sub>2</sub>S deposition, the low conductivity in the electrode which hinders sulfur utilization in the absence of carbon black additive.

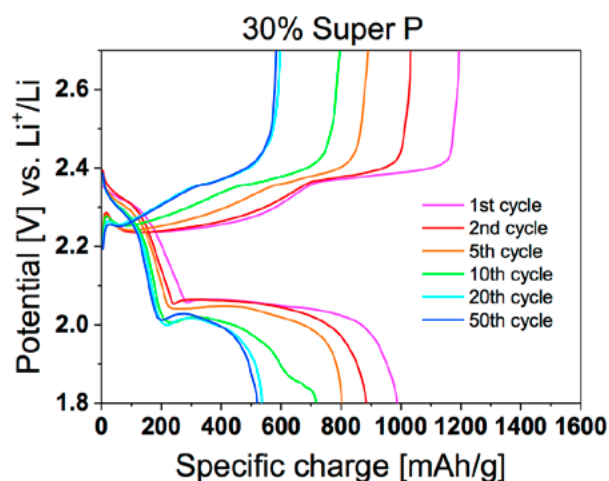


Figure 3. Galvanostatic profiles of a Li-S cell with Super P as carbon additive.

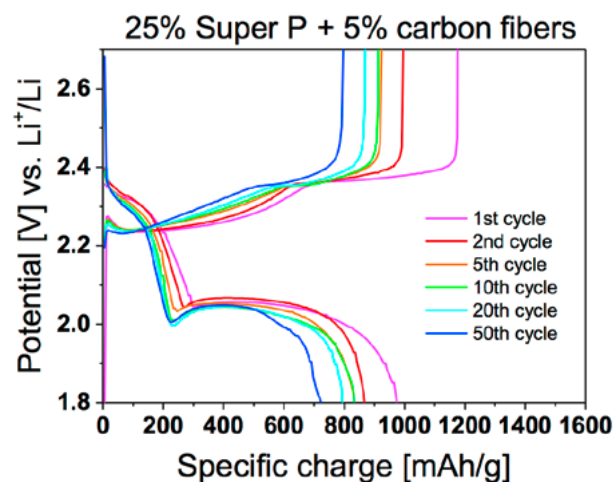


Figure 5. Galvanostatic profiles of a Li-S cell with Super P and carbon fibers as carbon additive.

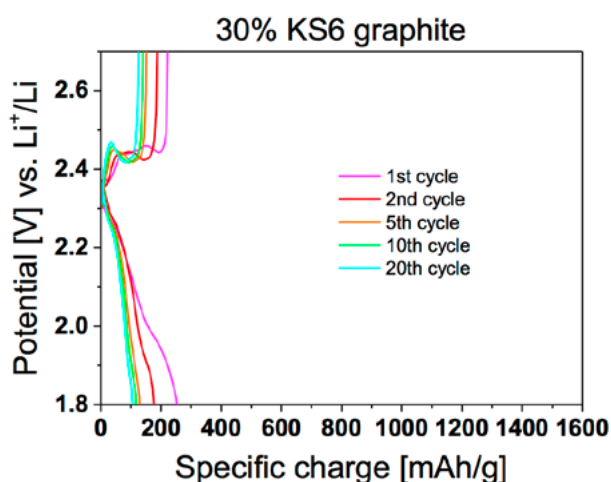


Figure 4. Galvanostatic profiles of a Li-S cell with KS6 graphite as carbon additive.

Another possible cause of the low sulfur utilization may be the difficult access of the electrolyte into the depth of the thick electrode. From the SEM images (Figure 1), the addition of a small amount of carbon fibers is expected to improve the electrolyte pathway. As observed in Figure 2, the presence of carbon fibers indeed leads to higher specific charge for long-term cycling, as well as slightly higher coulombic efficiency. From the galvanostatic profiles, it is observed that the length and potential of the voltage plateaus are better maintained while cycling with (Figure 5) than without carbon fibers (Figure 3). In particular, the lower plateau – reduction of long-chain to short-chain polysulfides – is longer with carbon fibers. This may indicate that, in addition to the easier electrolyte access, this type of carbon matrix allows a better trap of the soluble long-chain polysulfides for further conversion.

In conclusion, this study shows that the nature of the carbon additive has strong impact on the cycle life of thick sulfur electrodes and should therefore be carefully chosen for further development of highly loaded electrodes for high energy density applications.

#### Acknowledgement

BASF SE is acknowledged for financial support within the <BASF Scientific Network on Electrochemistry and Batteries>.

#### References

- [1] S. Urbonaite, T. Poux, P. Novák, *Adv. Energy Mater.* **5**(16), 1500118 (2015).
- [2] S.-E. Cheon, K.-S. Ko, J.-H. Cho, S.-W. Kim, E.-Y. Chin, H.-T. Kim, *J. Electrochem. Soc.* **150**(6), A800–A805 (2003).
- [3] S.-H. Kang, X. Zhao, J. Manuel, H.-J. Ahn, K.-W. Kim, K.-K. Cho, J.-H. Ahn, *Phys. Status Solidi A* **211**(8), 1895–1899 (2014).
- [4] N. Ding, S.W. Chien, T.S.A. Hor, Z. Liu, Y. Zong, *J. Power Sources* **269**, 111–116 (2014).
- [5] S.S. Zhang, *Energies* **5**(12), 5190–5197 (2012).
- [6] S. Urbonaite, P. Novák, *J. Power Sources* **249**, 497–502 (2014).

# SCIENTIFIC ACHIEVEMENTS 2015

BATTERIES –

DIAGNOSTICS

## H<sub>2</sub> and POF<sub>3</sub> gases as markers for the formation of ROH species in carbonate electrolytes

A. Guéguen, D. Streich, M.L. He, P. Novák, E.J. Berg

phone: +41 56 310 2176, e-mail: aurelie.queguen@psi.ch

Carbonate-based electrolytes with LiPF<sub>6</sub> salt are widely used nowadays in Li-ion batteries. So far such electrolytes offer the best compromise regarding the electrolyte requirements. Carbonate solvents start to oxidize at potentials > 4.1 V [1]. Li-rich nickel-cobalt-manganese oxide, hereafter called HE-NCM, is a promising cathode material for the next Li-ion batteries generation because of its high specific charge (250 mAh g<sup>-1</sup>) and large potential window (2.0–4.7 V). The high cut-off potential of the cell enhances electrolyte degradation and thus alters its electrochemical performance. In a previous study (Annual Report 2014, p. 60) we were able to follow the evolution of POF<sub>3</sub> and H<sub>2</sub> in HE-NCM half-cells using Online Electrochemical Mass Spectrometry (OEMS). POF<sub>3</sub> evolves upon reactions between PF<sub>5</sub> gas resulting from LiPF<sub>6</sub> thermal instability and ROH species produced during charge from carbonate solvent decomposition. Reduction of ROH species at potential ~ 2 V will release H<sub>2</sub>. Such gases can therefore be used as indirect markers to follow the formation of ROH species. In the present report we investigate the role of some cell components, namely the separator and conductive carbon on POF<sub>3</sub> and H<sub>2</sub> evolution in order to evaluate their influence on electrolyte degradation.

### Experimental

The electrodes were prepared by coating thin glass-fiber (GF) (Sigma-Aldrich) sheets or Celgard® 2400 polypropylene (PP) sheets with a mixture of 79 %wt conductive carbon Super C65 (Imerys Graphite & Carbon) and 21 %wt PVdF (polyvinylidene fluoride) dispersed in N-methylpyrrolidone (NMP, Sigma-Aldrich). The NMP was evaporated under vacuum at 80 °C for 8 hours. Electrodes were subsequently punched (18 mm diameter) and dried at 120 or 80 °C overnight before being introduced into an argon-filled glove-box.

The OEMS experiments were performed in a home-designed electrochemical cell (Annual Report 2012, p. 47). Cyclic voltammograms (CV) were collected for cells composed of Super C65 positive electrodes and Li metal negative electrode between 2.0 and 4.7 V (all potentials in the report are given vs. Li<sup>+</sup>/Li) with a voltage sweep rate of 0.075 mV/s to mimic the galvanostatic tests run for HE-NCM electrodes. The electrolyte was 1 M LiPF<sub>6</sub> in EC:DEC (3:7). Separators were the same material as that used to coat the electrodes. Calibration gases were used to quantify precisely amounts of O<sub>2</sub> and CO<sub>2</sub> evolved. No calibration gas was used for POF<sub>3</sub> and H<sub>2</sub>, thus the evolution rates reported here are approximate but comparable between the experiments.

### Results

The top part of Figure 1 shows the CV data collected for Super C65 electrodes coated on GF and PP. The resulting current recorded in the case of GF for the 1<sup>st</sup> scan is significantly higher than that of PP. This indicates that more electrochemical reactions are taking place when GF is used and that GF itself is involved in such reactions. The presence of surface groups such as hydroxides and the higher surface area of GF can explain its

increased reactivity. The influence of the separator and coating support is also visible in the gas evolution. Higher CO<sub>2</sub>, POF<sub>3</sub> and H<sub>2</sub> evolution rates are observed in the case of GF. Work by Metzger et al. highlighted the implication of conductive carbon on CO<sub>2</sub> release during ethylene carbonate oxidation [2]. In the case of Super C65 coated on GF, the approximate highest POF<sub>3</sub> evolution rate is ~7.6 μmol min<sup>-1</sup> g<sup>-1</sup> active material. This evolution rate is much higher than that obtained previously for HE-NCM coated on GF (~0.05 μmol min<sup>-1</sup> g<sup>-1</sup> active material) (Annual Report 2014, p. 60). The same remark can be done for H<sub>2</sub> gas. This suggests that conductive carbon Super C65 is also involved in side-reactions producing ROH species which can further react with PF<sub>5</sub> to release POF<sub>3</sub>.

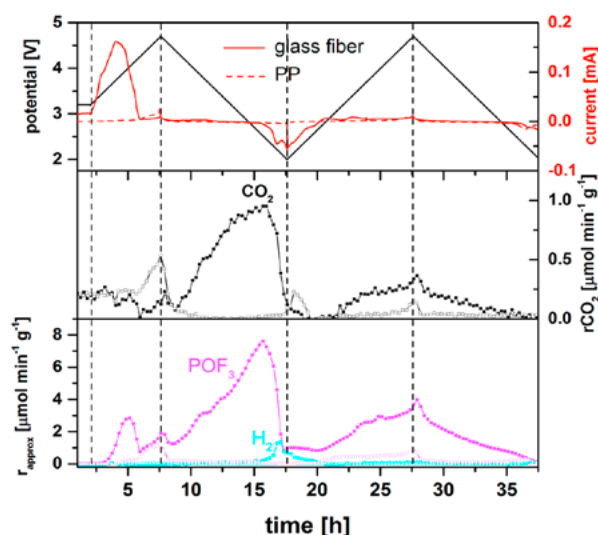


**Figure 1.** Cyclic voltammograms and corresponding O<sub>2</sub>, CO<sub>2</sub>, POF<sub>3</sub> and H<sub>2</sub> evolution rates for conductive carbon Super C65 cycled vs. Li metal using glass-fiber (solid symbols) or polypropylene (open symbols) separator.

### Conclusions

Following POF<sub>3</sub> and H<sub>2</sub> evolution using OEMS provides useful information regarding LiPF<sub>6</sub> degradation and ROH side-products formed upon carbonate decomposition. «Inactive» cell components such as separator or conductive carbon were shown to take part in such side-reactions, thus increasing POF<sub>3</sub> amount evolved and enhancing electrolyte degradation. Careful attention must be paid when optimizing cell engineering like the choice of separator for example.

### Acknowledgement

The authors thank BASF SE for financial support.

### References

- [1] K. Xu, *Chem. Rev.* **104**, 4303–4417 (2004).
- [2] M. Metzger, C. Marino, J. Sicklinger, D. Haering, H.A. Gasteiger, *J. Electrochem. Soc.* **162** (7), A1123–A1134 (2015).

## Contribution of 5 V cathodes to the surface layer formation at the anodes in Li-ion batteries

D. Leanza, P. Novák, M. El Kazzi

phone: +41 56 310 2797, e-mail: daniela.leanza@psi.ch

One of the most controversial issues investigated in the Li-ion battery community involves the study of the interfacial (electrolyte/electrode) processes occurring upon cycling on the surface of the electrodes. Understanding the surface chemistry of these materials and the associated effects on the electrochemical performance is a pivotal assessment for the long-term behavior of such systems [1]. In particular, this interface strongly relies on the stability of the liquid carbonate-based electrolytes commonly employed in Li-ion batteries. Indeed, as is reported in Figure 1, operating at potential higher than 4.1 V or lower to 0.8 V vs.  $\text{Li}^+/\text{Li}$ , respectively, is well known to induce partial oxidation and reduction of the electrolyte (salts and solvents) [2].

However, after cycling a 5 V cathode as  $\text{Li}_{1-x}(\text{Ni}_a\text{Mn}_b\text{Co}_c)\text{O}_2$  (HE-NMC) between 2.5–5.1 V vs.  $\text{Li}^+/\text{Li}$  (system I) at C/5 cycling rate, a very thin surface layer formation is reported at the end of the first charge. In fact the C1s XPS\* core level in Figure 2, do not show a considerable variation between the pristine electrode and the first charge, despite the shift to lower binding energies of some peaks (e.g. PVDF in blue). Notwithstanding the cathode is cycled beyond the thermodynamic stability of the organic electrolyte, the surface film formation is in the order of few nanometers, suggesting that the decomposition products formed at high potential ( $>4.1$  V vs.  $\text{Li}^+/\text{Li}$ ) do not deposit on the cathode surface, but rather a dissolution in the electrolyte is favored.

Conversely, when  $\text{LiFePO}_4$  (LFP) is cycled between 3–4 V vs.  $\text{Li}^+/\text{Li}$  (system II) at C/5, a negligible surface layer is formed after the first charge. Examining the C1s core level we can notice that there are no strong differences between the pristine electrode and the first charge, indicating that almost no surface layer is covering the positive electrode. This result is not surprising since LFP is cycled along its plateau at potential of 3.45 V vs.  $\text{Li}^+/\text{Li}$ , where no electrolyte oxidation is expected.

Finally when graphite is cycled between 5 mV–1.5 V vs.  $\text{Li}^+/\text{Li}$  at C/5, a thick surface layer ( $\sim 8$  nm) is covering the negative electrode at the end of the first charge. In the XPS C1s core level the signal at 284.2 eV assigned to the C–C bond in the graphite almost disappeared in the cycled electrode and the spectra are mainly dominated by the breakdown species of the electrolyte, as it is evidenced by the components between 288–292 eV, as a result of the reduction processes of the electrolyte components aforementioned.

In this context, the following report deals with the investigation of the impact and contribution of a 5 V Li-ion cathode material on/to the formation and growth of the surface layer on the negative electrode. Particular emphasis will be dedicated on the correlation between the oxidation processes taking place at the cathode and the surface layer formation on the anode side. To better conduct this study, post mortem XPS measurements are performed first on a model system (III)  $\text{LiFePO}_4$  vs.  $\text{Li}_4\text{Ti}_5\text{O}_{12}$  (LTO) cycled in the potential cut-off limits of 3.45 V – 1.55 V vs.  $\text{Li}^+/\text{Li}$  respectively. This cell should work indeed in a «safe potential window» where the carbonate-based electrolyte is expected to be stable and both the electrodes

are surface-layer free. The results will be compared with full cell (V) HE-NMC vs. LTO and pristine electrodes. Thanks to this step-by-step procedure any dissolution of the decomposed electrolyte species or diffusion/migration to the negative electrode can be easily discriminated.

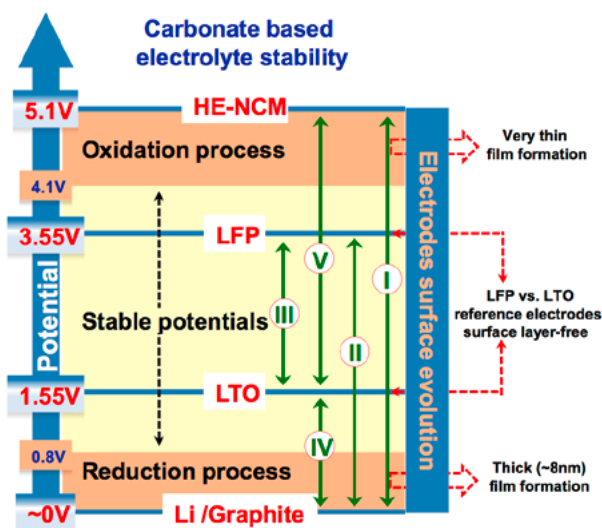


Figure 1. Stability of carbonate-based electrolyte at different operating potentials and the correspondent influence on the surface layer formation on positive (HE-NMC, LFP) and negative (LTO, graphite) electrodes.

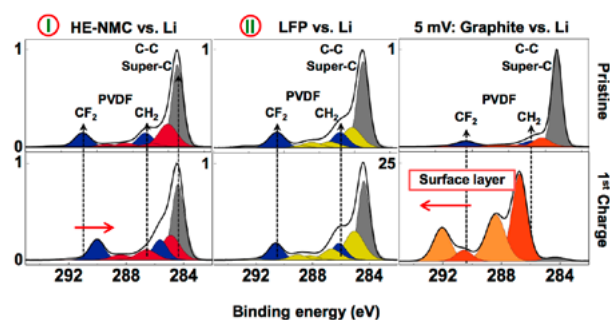


Figure 2. C1s XPS core levels acquired on HE-NMC, LFP and graphite half-cells on pristine electrodes and after the first charge.

### Experimental

Electrodes were prepared by casting a mixture of active material, binder (PVDF) and Super C carbon (Imerys), in a ratio of 80:10:10 for  $\text{Li}_4\text{Ti}_5\text{O}_{12}$  (Clariant) and  $\text{LiFePO}_4$  (Clariant) and 90:6:4 for HE-NMC, all suspended in N-methyl-2-pyrrolidone (Fluka) and then spread onto an aluminum foil current collector. The cells were assembled in an argon-filled glove box, using both glass fiber and Celgard as separators and LC30 as electrolyte (1 M  $\text{LiClO}_4$  solution in a mixture of 1:1 w/w of ethylene carbonate (EC) and dimethyl carbonate (DMC).

\* XPS: X-ray photoemission spectroscopy

Electrochemical cycling was carried out galvanostatically at room temperature along the recalculated potential 3.45–1.55 V vs. Li<sup>+</sup>/Li for the reference cell LFP vs. LTO (III), and 2.5–5.1 V vs. Li<sup>+</sup>/Li for the system HE-NMC vs. LTO (V). During this study just the first charge will be presented using C/5 rate cycling for all the cells.

## Results

The C1s, F1s and Ti2p XPS core levels reported in Figure 3 are only acquired on LTO electrodes. The peaks recorded on every sample have been normalized with the intensity of their respective C1s component at 284.2 eV (grey), attributed to the C–C bond of the conductive carbon (Super C). This normalization enables to track the relative amount of the different elements together with the evolution and growth of the surface layer upon cycling on top of the different particles.

In the pristine LTO, XPS C1s core level shows two carbon species related to the PVDF components (blue) at 286.5 eV (CH<sub>2</sub>) and at 290.9 eV (CF<sub>2</sub>). Additional minor peaks (red) are detected at 285.5 eV (hydrocarbons), 287.2 eV (carbonyl –C=O) and 288.9 eV (carboxyl O–C=O), believed to come from surface carbon oxidized species. The F1s core level shows similarly the CF<sub>2</sub> component (blue) of PVDF at 688.3 eV and LiF species (in orange) at 685.3 eV, due to the binder reaction with Li. Finally Ti2p core level shows spin-orbit peaks at 459 eV (Ti2p<sub>3/2</sub>) and at 465.2 eV (Ti2p<sub>1/2</sub>) in good agreement with the Ti<sup>4+</sup> ions in the LTO structure.

After cycling LTO vs. LFP we observe slight changes due to the increase of the component at 285.5 eV related to C–H/C–O species in the C1s core level. In the same time, F1s and Ti2p core levels show the presence of additional peaks shifted to lower binding energies attributed to LiF formation and Ti reduction from Ti<sup>4+</sup> → Ti<sup>3+</sup> respectively. On the contrary, the C–C signal and F1s do not exhibit considerable attenuation compared to the pristine electrode. However, the intensity evolution between the Super C component at 284.2 eV of the conductive carbon and the Ti2p originated from LTO particles show an obvious decrease of the latter signal. This observation is confirmed by the increase of the intensity ratio  $I_{(C-C)}/I_{(Ti2p)}$  calculated between the signals generated from the Super C and the active material (LTO), respectively, as is presented in Figure 4a, high-lighting the preferential growth of a thin surface layer on top of LTO rather than on carbon particles or the binder. The absence of any surface layer on carbon and PVDF is also evidenced by the ratio of the corresponding peaks at 284.2 eV and 688.5 eV, which remains in the same range as in the pristine electrode, as presented in Figure 4b. As a consequence we can assume that no reduction of electrolyte occurred in the potential window used, as expected. However, the changes observed on LTO surface can be explained assuming that, during charging, the desolvation of Li-ions leads to adsorbed EC/DMC species which deposit on top of the LTO surface after Li<sup>+</sup> intercalation in the anode structure. However the thickness of the surface layer is negligible and remains in the range of few monolayers.

On the contrary, the surface of LTO cycled vs. HE-NMC shows a noticeable modification after the first charge. The decomposition products of the electrolyte species shown in C1s core level between 285.6–292.5 eV rise abruptly and seem to cover the surface of the negative electrode homogeneously, since the signals from the Super C (284.2 eV) and LTO (459.6 eV) are attenuated accordingly (Figure 4). Based on the previous

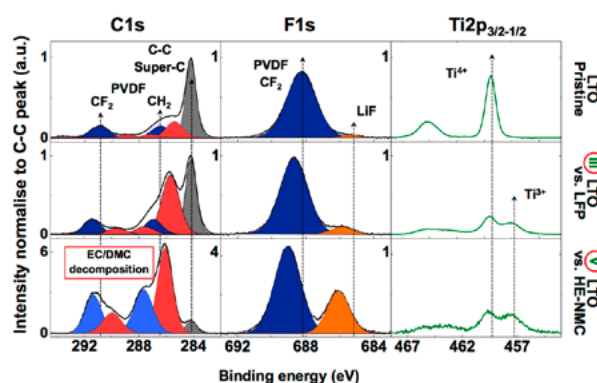


**Figure 3.** Surface layer evolution on LTO: C1s, F1s, Ti2p XPS core levels carried on LTO pristine and cycled vs. LFP and vs. HE-NMC. Intensity normalized to the signal of C–C at 284.2 eV.

observations, it is clear that the surface layer developed on this electrode derives from the migration/diffusion species formed at high potential HE-NMC interfaces, which later deposit on the surface of the negative electrode.

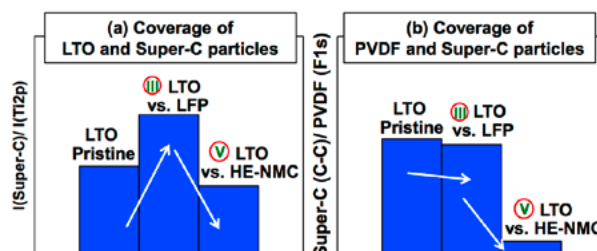


**Figure 4.** (a) Intensity ratio between the signals of Super C (284.2 eV) and LTO (459 eV) on the left and (b) between Super C (284.2 eV) and PVDF (688 eV) on the right, to follow the surface layer formation on different particles.

## Conclusion

During this study we evidenced the correlation between the surface layer formed at high potential on the cathode and the surface chemistry developed on the negative electrode. This remarkable result proves that the oxidation process which occurs at potential higher than 4.1 V vs. Li<sup>+</sup>/Li leads to the formation of breakdown organic/inorganic species which do not deposit on the surface of the positive material. Indeed they are first dissolved in the electrolyte and later diffuse/migrate to the anode, contributing to the growth of a surface layer. Similarly, XPS results indicate that the LTO is developing a thin surface layer when cycled vs. LFP. However in this case the coverage is involving only the surface of the active material (LTO) and it is believed not to be related to a reduction process, but rather to adsorbed EC/DMC molecules originating from the Li<sup>+</sup> desolvation after being inserted in the anode structure.

## References

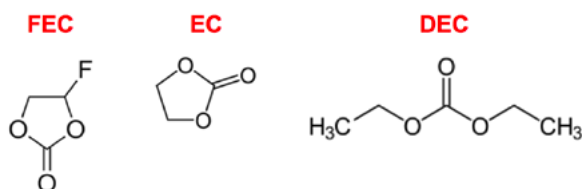
- [1] T. Joshi, K. Eom, G. Yushin, T.F. Fuller, *J. Electrochem. Soc.* **161**, A1915–A1921 (2014).
- [2] L. Baggetto, D. Mohanty, R.A. Meisner, C.A. Bridges, C. Daniel, D.L. Wood lii, N.J. Dudney, G.M. Veith, *RSC Adv.* **4**, 23364–23371 (2014).

## Impact of FEC on HE-NCM half- and full-cells investigated by online electrochemical mass spectrometry

D. Streich, A. Guéguen, P. Novák, E.J. Berg

phone: +41 56 310 4396, e-mail: daniel.streich@psi.ch

Fluoroethylene carbonate (FEC) has been reported to have beneficial effects on the cycling behavior of lithium-ion batteries [1]. Unfortunately, the knowledge about how these effects are brought about remains scarce. In order to shed light on the reactivity of FEC in HE-NCM/Li half-cells and HE-NCM/graphite full-cells, we compared the gas evolution in EC:DEC and FEC:DEC based 1 M LiPF<sub>6</sub> electrolytes during the first two galvanostatic charge/discharge cycles. Online electrochemical mass spectrometry (OEMS) was employed to obtain quantitative information about reactions at the electrode/electrolyte interface based on the detection of gaseous decomposition products formed during electrochemical cycling [2].



Scheme 1. Investigated solvents and co-solvents.

### Results and discussion

Figure 1 shows OEMS results for HE-NCM/graphite full-cells with EC:DEC (top) and FEC:DEC (bottom) based electrolytes in direct comparison with the sums of the corresponding HE-NCM/Li and graphite/Li half-cell gas evolution traces. The C<sub>2</sub>H<sub>4</sub> and CO<sub>2</sub> evolutions occurring very early during the first charge (Time < 5 h) are due to reductive EC and FEC decomposition, respectively, as verified by OEMS measurements of graphite/Li half-cells (data not shown). An early CO<sub>2</sub> formation rate maximum at ca. 4.2 V vs. Li<sup>+</sup>/Li is accompanied by the onset of slow O<sub>2</sub> release due to Li<sub>2</sub>MnO<sub>3</sub> activation [3]. The major part of the O<sub>2</sub> originating from Li<sub>2</sub>MnO<sub>3</sub> activation is, however, released along with a second CO<sub>2</sub> evolution at the end of the first charge. The fact that the early CO<sub>2</sub> formation process and O<sub>2</sub> release cease to occur after the first charge/discharge cycle provides indirect evidence for the formation of reactive oxygen species during Li<sub>2</sub>MnO<sub>3</sub> activation. The first oxidative CO<sub>2</sub> formation process (time < 10 h) is considerably diminished in the «full-cell» compared to the «sum of half-cells» traces in EC:DEC (Figure 1, top) but not in FEC:DEC (Figure 1, bottom, inset). Our hypothesis is that substantial amounts of CO<sub>2</sub> formed at the HE-NCM electrode become reduced at the graphite electrode because SEI formation has not yet reached completion in the EC:DEC electrolyte at this stage of the first charge.

### Conclusions

Reactive oxygen species are formed on HE-NCM throughout Li<sub>2</sub>MnO<sub>3</sub> domain activation without any obvious dependence on whether EC or FEC is used as co-solvent. In contrast, substantial differences in the reductive decomposition of FEC compared to EC have major effects on follow-up reactions such as CO<sub>2</sub> consumption at the graphite electrode. These reactivity differences are likely to originate from co-solvent dependent differences in SEI formation kinetics and/or composition.

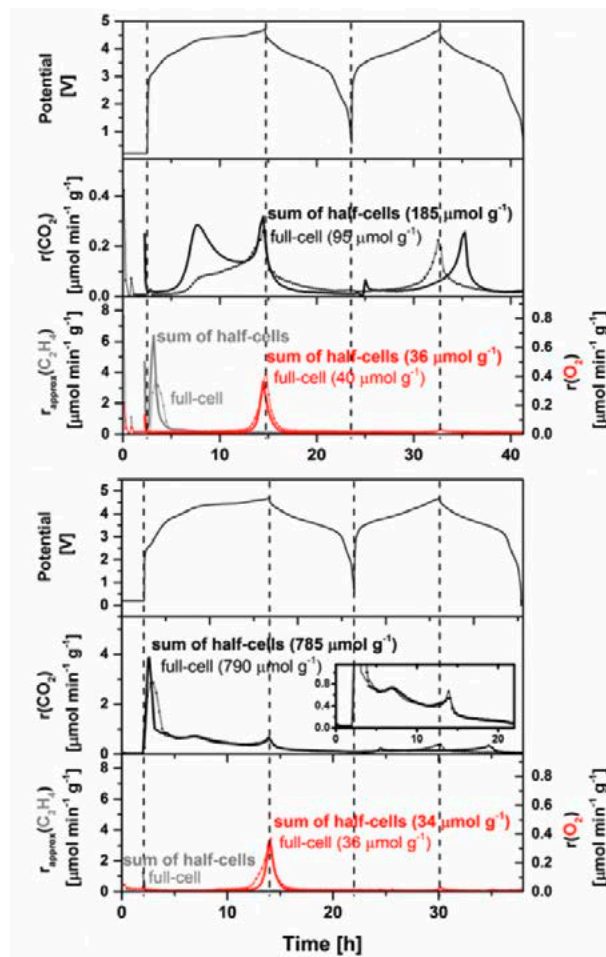


Figure 1. Galvanostatic OEMS. (top) HE-NCM/graphite full-cell in 1 M LiPF<sub>6</sub> 3:7 (w/w) EC:DEC, (bottom) HE-NCM/graphite full-cell in 1 M LiPF<sub>6</sub> 3:7 (w/w) FEC:DEC (inset: magnified view of the HE-NCM related CO<sub>2</sub> formation during the first charge).

The quantities in parentheses refer to the integrated gas amounts normalized with respect to the mass of the active material, respectively. The solid lines are the sums of the gas evolution traces observed in the corresponding HE-NCM/Li and graphite/Li half-cells. Shifts between the full-cell and the sum-of-half-cell traces are due to slight deviations in electrochemical cycling behavior of the respective cells. Dashed vertical lines are included as guides to the eye and mark the beginnings of new electrochemical cycling stages.

### References

- [1] V. Etacheri, O. Haik, Y. Goffer, G.A. Roberts, I.C. Stefan, R. Fasching, D. Aurbach, *Langmuir* **28**(1), 965–976 (2012).
- [2] E.J. Berg, P. Novák, in: *ECL Annual Report 2012, Paul Scherrer Institut, Villigen, Switzerland*, pp. 47, (2012).
- [3] M.M. Thackeray, S.H. Kang, C.S. Johnson, J.T. Vaughey, R. Benedek, S.A. Hackney, *J. Mater. Chem.* **17**, 3112–3125 (2007).

## XPS surface analysis of silicon thin films as model anode for Li-ion batteries

G. Ferraresi, L. Czornomaz<sup>1</sup>, P. Novák, C. Villevieille, M. El Kazzi

phone: +41 56 310 4542, e-mail: giulio.ferraresi@psi.ch

Silicon is considered to be the most promising negative electrode to replace graphite in Li-ion batteries thanks to its abundance and its high specific charge [1]. The main drawback of silicon is the enormous volume expansion and shrinkage during lithiation/delithiation (ca. 300%). Scaling down to nanoscale silicon limits the volume expansion and improves the stability during cycling [2].

In this work we use thin films of silicon as model material to follow the reaction at the interface taking into account that no binder and no conductive additives are present [3]. We investigate the surface evolution of silicon thin films during the first charge/discharge using X-ray photoelectron spectroscopy (XPS) to follow the evolution of the Li-Si alloy formation and the evolution of the solid electrolyte interphase (SEI) layer which rises from the electrolyte decomposition.

### Experimental

30 nm amorphous phosphorous-doped silicon thin films were deposited by plasma-enhanced chemical vapour deposition on copper foils (used as current collector). Galvanostatic cycling was performed using Celgard soaked with LP30 electrolyte (EC:DMC solvent (1:1) + 1 M LiPF<sub>6</sub> salt) in the potential range 5 mV–1.5 V vs. Li<sup>+</sup>/Li at 1C rate (one hour to fully charge). For XPS analyses, electrodes were cycled to the desired potential. Post mortem samples were then removed from the electrochemical cell, carefully rinsed with DMC solvent and transferred from the glovebox to the XPS spectrometer under Ar atmosphere. All the potentials along this manuscript will be given in respect to the reference Li<sup>+</sup>/Li.

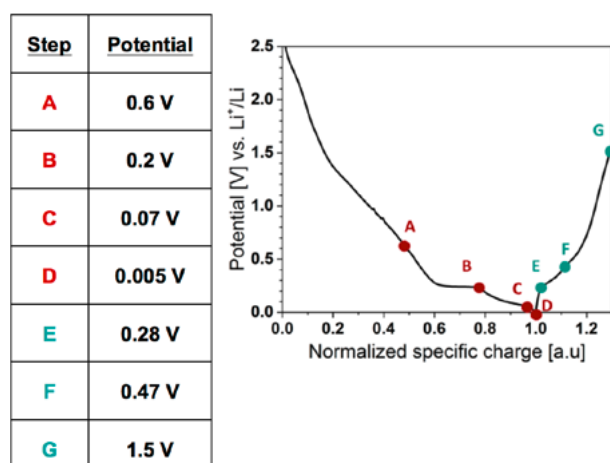


**Figure 1 (right).** Galvanostatic cycle of silicon thin films in LP30 electrolyte cycled at 1C rate.

**Table 1 (left).** Selected potentials for ex situ XPS analyses during charge (A–D) and discharge (E–G).

### Results

The recorded XPS spectra of Si2p core level in Figure 2 show at 0.6 V (A) the presence of two main peaks at 98.9 and 103.7 eV associated to Si<sup>0</sup> (Si-Si) and Si<sup>4+</sup> (SiO<sub>2</sub>) bonds, respectively. At this stage the two peaks do not show any shift in binding energy compared to the pristine sample (not shown here) suggesting no reaction of the active material, as expected. Once the potential reached 0.2 V (B), we observe a shift of both peaks to lower binding energy due to reaction of Li with Si (97.1 eV) and the formation of Li-silicate (101.6 eV). Pursuing the lithiation, a more pronounced shift to lower energy is observed for Li-Si alloy peak until the cut-off potential (5 mV), whereas the peak related to Li-silicate stays at 101.6 eV. During delithiation (E–G), the reaction mechanism is reversible with the delithiation of the Li-Si alloy (shift backwards) until reaching cut-off voltage at 1.5 V. So far the analyses of the Si2p show the alloying of Li-Si but did not give direct information about possible SEI at the surface of the samples.

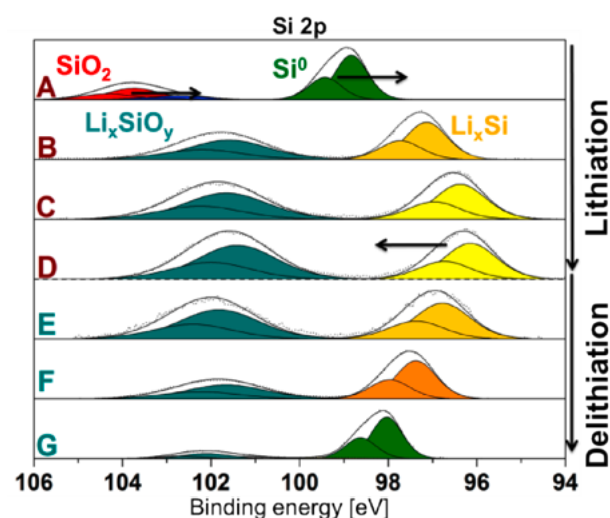


**Figure 2.** XPS spectra of Si2p core level during first lithiation (A–D) and delithiation (E–G).

Thus, the SEI formation and evolution was followed and characterised using O1s, C1s and Li1s core levels as reported in Figure 3 and Figure 4 for lithiation and delithiation, respectively.

During lithiation, we notice that most of the changes take place at 0.2 V (B) whereas at higher potential (A) the peaks are similar to the pristine sample (not shown here).

- The O1s peak (Si-O binding energy) shifts to lower binding energy during lithiation associated with Li-silicate formation (Figure 3, B), as was observed on Si2p peak. At this potential (B) there is the appearance of two extra peaks correlated to the formation of C-O-Li and RO-CO<sub>2</sub>Li species belonging to the SEI layer [4–5].
- For the Li1s level, we observe the appearance of a new component at 53.85 eV related to Li-Si alloy which shifts

to lower binding energy during lithiation, as reported earlier.

- The C1s peak reveals a main contribution (red peak) from adventitious carbon and also the presence of carbonates and carbonyl species attributed to SEI layer.

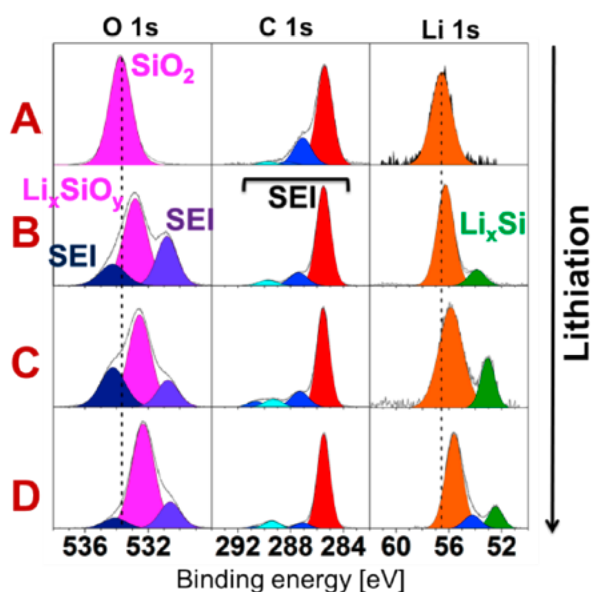


Figure 3. XPS spectra of the O1s, C1s and Li1s peaks during first lithiation recorded at key potentials.

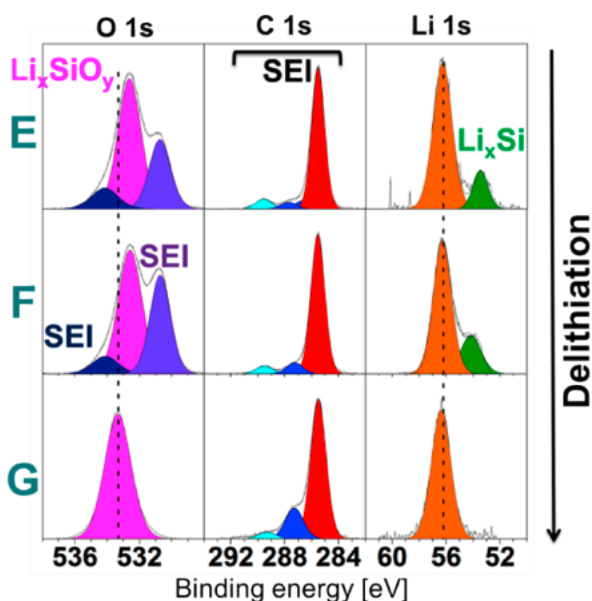


Figure 4. XPS spectra of the O1s, C1s and Li1s peaks during first delithiation recorded at key potentials.

During delithiation (Figure 4):

- O1s peaks attributed to O–C and O=C disappear once reaching 1.5 V.
- Li1s core level: the peak related to Li–Si alloy (green peak) shifts back to higher binding energy and then disappears at the end of delithiation suggesting the complete delithiation of silicon.
- The C1s core level shows again the presence of C–C, C–O and C=O bonds attributed to the SEI layer.

Another interesting feature to consider is the evolution of the area under the peak reported in Figure 5. We compare the Si2p area to the C1s area to get insight into the SEI mechanisms. During lithiation (A–D) the overall Si2p/C1s ratio decreases because of a continuous building up of the SEI layer which leads to the attenuation of the Si2p signal and the increase of the C1s signal. The tendency observed during lithiation is reversible during delithiation step (E–G) with a decrease of the SEI layer.

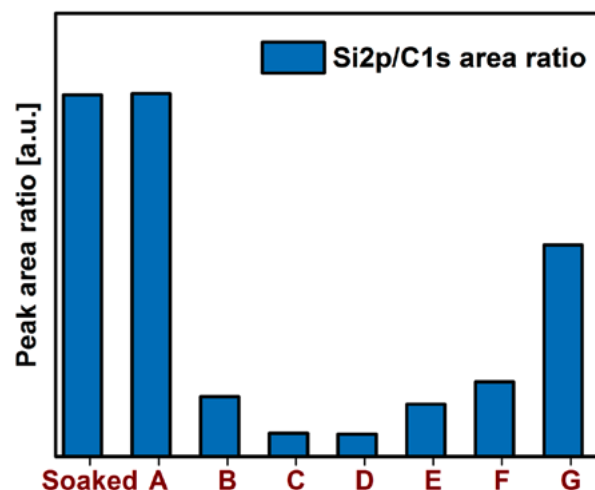


Figure 5. Peak area ratio between Si2p and C1s levels along first cycle.

## Conclusions

Performing a surface analysis on Si thin film during lithiation/delithiation with X-ray photoelectron spectroscopy on Si2p, C1s, Li1s and O1s core levels we were able to monitor the surface evolution, elucidating the SEI growth mechanism and the Li–Si alloy formation. SiO<sub>2</sub> is irreversibly oxidised at 0.2 V vs. Li<sup>+</sup>/Li whereas the Si is reversibly lithiated/delithiated. The SEI layer indicates a dynamic effect starting to grow at 0.2 V until the end of lithiation and, on delithiation, the thickness decreases until it is completely removed from the surface at 1.5 V.

## Acknowledgement

The authors are grateful to CCEM-SLIB and Swiss electric for financial support.

## References

- [1] J.O. Besenhard, J. Yang, M. Winter, *J. Power Sources* **68**, 87 (1997).
- [2] S. Bourderau, S. Brousse, T. Schleich, *J. Power Sources* **81**, 233–236 (1999).
- [3] B. Philippe, R. Dedryvère, J. Allouche, F. Lindgren, M. Gorgoi, H. Rensmo, D. Gonbeau, K. Edström, *Chem. Mater.* **24** (6), 1107–1115 (2012).
- [4] A.M. Andersson, K. Edström, *J. Electrochem. Soc.* **148** (10), A1100–A1109 (2001).
- [5] K. Kanamura, H. Tamura, S. Shiraishi, Z. Takehara, *J. Electroanal. Chem.* **394**, 49 (1995).

## Ageing phenomena in high-voltage aqueous supercapacitors investigated by *in situ* gas analysis

M. He, K. Fic<sup>1</sup>, E. Frąckowiak<sup>1</sup>, P. Novák, E.J. Berg  
phone: +41 56 310 5032, e-mail: minglong.he@psi.ch

High-voltage aqueous electrolyte based electrical double layer capacitors (EDLC,  $U > 1.23$  V) attract significant attention for next-generation high power, low cost and environmentally friendly energy storage applications [1]. Cell ageing is however markedly pronounced at elevated voltages and results in accelerated overall performance fade and increased safety concerns. The aim of the present study is the identification of the onset potentials and governing mechanisms of performance limiting side-reactions in a high-voltage aqueous EDLC by performing both *in situ* cell pressure analysis as well as *online* electrochemical mass spectrometry (OEMS).

### Experimental

Self-standing circular carbon electrodes were punched (14 mm for pressure cell, 18 mm for OEMS cell) from the activated carbon fabric (ACC 507-20, Kynol, Germany). 1 mol/L  $\text{Li}_2\text{SO}_4$  aqueous electrolyte was prepared by dissolving analytical quality  $\text{Li}_2\text{SO}_4$  salt (> 99.99%, Sigma-Aldrich, Switzerland) into distilled water. Both the *in situ* pressure and OEMS cells were assembled in a symmetric electrode configuration containing two activated carbon electrodes ( $m_c = 18$  mg for pressure cell,  $m_c = 30$  mg for OEMS cell, mass discrepancy < 0.3 mg), a glass fiber separator (18 mm for pressure cell, 28 mm for OEMS cell; GF/A, Whatman, Switzerland) and fixed amount of electrolyte (200  $\mu\text{L}$  for pressure cell, 250  $\mu\text{L}$  for OEMS cell). The electrolyte had pH 10.2. Cyclic voltammetry was consecutively performed in a cell voltage window of 0–1, 0–1.2, 0–1.4, 0–1.6, 0–1.8 and 0–2 V (3 repeated cycles for each window) at scan rates of 1 and 0.1 mV/s. All potential values in this work were referred to standard hydrogen electrode (SHE) unless noted otherwise.

### Results

Figure 1 shows the cyclic voltammograms (CV, 1 mV/s) of the symmetric activated carbon EDLC cell containing 1 mol/L  $\text{Li}_2\text{SO}_4$  electrolyte. Up to 1 V, the main electrochemical response is the typical rectangular double-layer profile with a specific capacitance of  $\sim 106$  F/g. However, a minor amount of faradaic current is discernible, e.g. possibly deriving from the oxidation and reduction of carbon surface groups [2, 3]. The stepwise voltage increase up to 2 V significantly intensifies the faradaic currents, being rather a response for water decomposition. However, these faradaic current contributions decrease with cycles in the same voltage range, indicating a gradual change of the activated carbon functionalities [4].

The inset of Figure 1 shows the positive and negative electrode potentials (labelled as  $E^+$  and  $E^-$ , respectively) for a given voltage applied over the symmetric EDLC cell as given by the reference electrode. The thermodynamic potential limits (represented by horizontal dashed lines) of oxygen evolution reaction (OER) and hydrogen evolution reaction (HER) calculated according to Nernst equation are 0.63 V ( $E_{\text{OER}} = 1.23 - 0.059 \cdot \text{pH}$ ) and -0.60 V ( $E_{\text{HER}} = -0.059 \cdot \text{pH}$ ), respectively. The positive electrode reaches the thermodynamic OER potential limit when a 1.3 V cell voltage is applied. The practical HER potential is

believed to shift towards more negative values due to hydrogen electro sorption on activated carbon surface and a local pH value increase [5].

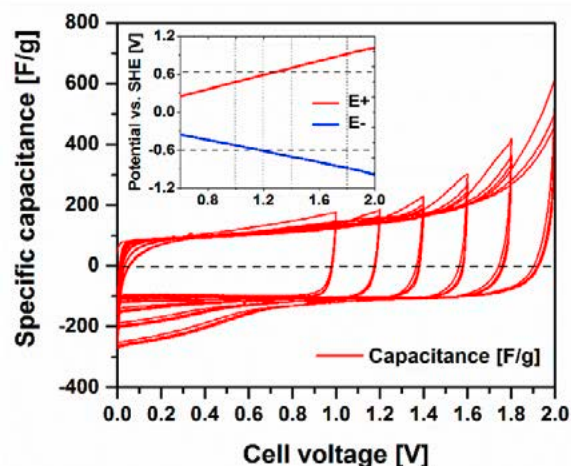


**Figure 1.** Cyclic voltammetry (1 mV/s) of the activated carbon based symmetric EDLC cell (1 mol/L  $\text{Li}_2\text{SO}_4$ ) with step-wise increasing cell voltage limits. Inset shows the positive ( $E^+$ ) and negative ( $E^-$ ) electrode potentials as a function of cell voltage.

Figure 2a shows voltage, specific current, and internal pressure profiles as well as the specific pressure increase rates of the symmetric EDLC cell during cyclic voltammetry at 0.1 mV/s scan rate. On a short term, cell pressure fluctuations are observed during cycling, which largely are believed to arise from partly reversible gas evolution and consumption processes. The influence of side-reactions is evidenced by comparing the internal cell pressure  $P$  (blue solid line in Figure 2a) after the complete CV experiments: a total increase of  $\Delta P \sim 95$  mbar. The splitted  $dP/dt$  peaks (indexed as 1 and 2 in the 0–2 V range) indicate the presence of at least two different processes of gas evolution at  $U < 1.6$  V and  $U > 1.6$  V, respectively.

Figure 2b shows the OEMS profile during cyclic voltammetry (0.1 mV/s) of the symmetric EDLC cell.  $\text{H}_2$  evolution is detected in the cell voltage ranges of 0–1.8 V and 0–2 V, as the negative electrode potential is beyond the thermodynamic limit of HER (-0.6 V, Figure 1). Even though the positive electrode is polarized beyond the potential onset of OER (0.63 V, Figure 1) at cell voltages  $U > 1.2$  V, no  $\text{O}_2$  evolution was observed at any potential. The ion-current signals of CO and  $\text{CO}_2$  appearing on  $m/z = 28$  and 44, respectively, present nearly identical evolution profiles when the symmetric EDLC cell is cycled. The peak intensities of CO/ $\text{CO}_2$  in each CV cycle are detected at the maximum applied voltages. The evolution at relatively low cell voltages  $U < 1.2$  V is assigned to the decomposition of carbon surface functionalities, which are supported by the gradually decreasing signal intensities until the cell voltage reaches 1.8 V. In agreement with the specific  $dP/dt$  pattern in Figure 2a, two  $\text{CO}_2$  evolution peaks in voltage range of 0–2 V can be clearly distinguished. The first  $\text{CO}_2$  evolution peak ( $0 < U < 1.6$  V) corresponds to the decomposition of carbon surface groups while carbon corrosion is believed to account for the second

CO<sub>2</sub> evolution peak at cell voltages higher than 1.6 V. The ion-current intensity related to CO ( $m/z=28$ ) increases to a larger extent at  $U > 1.6$  V than for CO<sub>2</sub>, indicating that CO gas evolution is higher during the carbon corrosion process.

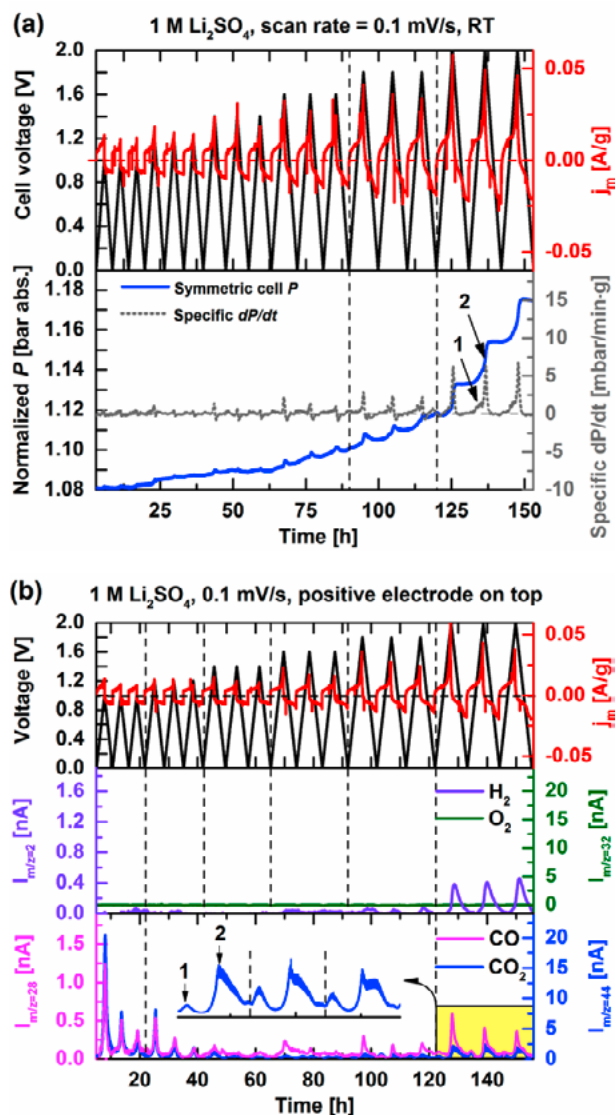


**Figure 2.** (a) Cell voltage, specific current  $j_m$ , internal pressure  $P$ , and calculated specific pressure increase rate  $dP/dt$  profiles during CV at 0.1 mV/s. (b) Cell voltage, current and H<sub>2</sub>, O<sub>2</sub>, CO, and CO<sub>2</sub> mass signal intensities during CV at 0.1 mV/s.

## Conclusions

*In situ* pressure cell and OEMS analysis provide complementary data on gas evolution in EDLC cells. The type, onset, and quantity of gas evolution are correlated with the potential of the activated carbon electrodes. H<sub>2</sub>, CO and CO<sub>2</sub> are the detected volatile species, and the involved reaction processes may presumably be classified into four general categories:

1. Carbon surface functional group decomposition.
2. Water splitting (HER and OER).
3. Carbon corrosion.
4. Chemical/electrochemical gas consumption.

In summary, short-term cycling leads to breathing-like and partly reversible cell pressure fluctuation, which is due to

reversible gas formation/consumption reactions, while long-term cycling causes the continuous cell pressure increase. Although these side-reactions provide additional pseudo-capacitance at higher voltages, both the long-term performance and the safety are compromised due to irreversible formation of volatile side-reaction products.

## Acknowledgement

Financial support from the Polish-Swiss Research Programme (INGEC PSPB-107/2010) is gratefully acknowledged.

## References

- [1] K. Fic, G. Lota, M. Meller, E. Frackowiak, *Energy Environ. Sci.* **5**, 5842–5850 (2012).
- [2] C. Moreno-Castilla, M.V. López-Ramón, F. Carrasco-Marín, *Carbon* **38**, 1995–2001 (2000).
- [3] B. Avsarala, R. Moore, P. Haldar, *Electrochim. Acta* **55**, 4765–4771 (2010).
- [4] P. Ratajczak, K. Jurewicz, F. Béguin, *J. Appl. Electrochem.* **44**, 475–480 (2014).
- [5] Q. Gao, L. Demarconnay, E. Raymundo-Pinero, F. Béguin, *Energy Environ. Sci.* **5**, 9611–9617 (2012).

## Transition metal dissolution in the $\text{Li}_{1+x}(\text{Ni}_a\text{Co}_b\text{Mn}_{1-a-b})_{1-x}\text{O}_2/\text{graphite}$ full-cell

H.-J. Peng, C. Villevieille, S. Trabesinger, H. Wolf<sup>1</sup>, K. Leitner<sup>1</sup>, P. Novák

phone: +41 56 310 5737, e-mail: hai-jung.peng@psi.ch

Lithium-manganese-rich cathode materials with layered structure ( $\text{Li}_{1-x}(\text{Ni}_a\text{Co}_b\text{Mn}_{1-b-c})_{1-x}\text{O}_2$ , called hereafter HE-NCM), have attracted much attention in the passing decade due to their high energy density, good thermal stability, and potentially low cost. [1] However, the practical application of this class of materials is hindered by the well-known voltage fade and rapid specific charge decay during prolonged cycling, especially in full-cell configuration. The latter has been proposed to occur due to the dissolution of transition-metal (TM) ions, which then transport to the anode and can catalyse further electrolyte reduction at the anode-electrolyte interface [2, 3]. So far most of the studies concerning TM dissolution focus on the influence of high working potential. In this study, the effect of cycling rate was investigated (C/2 and C/10). The influence of TM dissolution on the electrochemical performance of HE-NCM vs. graphite full-cell was evaluated.

### Experimental

Both the HE-NCM ( $\text{Li}_{1.17}(\text{Ni}_{0.22}\text{Co}_{0.12}\text{Mn}_{0.66})_{0.83}\text{O}_2$ ) cathode and graphite anode used in this study were provided by BASF SE. The cathodes consisted of 88% of HE-NCM (BASF SE, Germany), 7% of PVDF binder (Kynar HSV 900, Arkema, France), and 5% of conductive additives (2.5% of Super P and 2.5% of TIM-REX KS6, Imerys, Switzerland). Full-cells were assembled using pouch-type cells with a cathode of  $25\text{ cm}^2$  and two pieces of Celgard® 2500 polypropylene separator. LP57 electrolyte, containing 1 M  $\text{LiPF}_6$  in the solvent mixture of EC:EMC = 3:7 (%wt), was purchased from BASF SE, Germany.

To activate HE-NCM and to ensure a good passivation of the graphite anode, the cells were cycled galvanostatically at C/15 and C/10 rates during the first and second cycle, respectively, between 1.0 and 4.8 V. Subsequently, the cells were cycled either at C/10 or C/2 rate within the same potential window. For the cells cycled at C/2 rate, a potentiostatic step was added at the end of each charge with the following two end-conditions: current (I) = the current applied for C/10-rate cycling and time (T) = 30 mins. The C rates were calculated based on the nominal specific charge of HE-NCM, and 1C corresponds to a specific current of 250 mA/g.

After different predefined cycle numbers, cells were disassembled in an argon-filled glovebox for analysis. The graphite anode and the separator facing it were rinsed with 4 ml of DMC to remove the residual salt. The quantity of Li, Ni, Co, and Mn deposited on the anode were analysed with inductively coupled plasma optical emission spectrometry (ICP-OES).

### Results

Figure 1 shows the specific charge of the last discharge of cells used for the TM dissolution analysis. The values are an average of the 2 nominally identical cells, and the error bars show the deviation between two of them. It can be clearly seen that the electrochemical performance of the cells is well reproducible. Better specific charge retention is observed for the cells cycled

at higher rate. The specific charge of the cells cycled at C/10 rate decays roughly twice as fast as those cycled at C/2 rate. The average amount of Li detected on the graphite anode after 100 cycles at C/2 rate and 50 cycles at C/10 rate corresponds to a loss in specific charge of 137 mAh/g and 136 mAh/g, respectively (Table 1). These values agree well with the actual loss of specific charge calculated from the electrochemical cycling data. This indicates that the specific charge decay of the HE-NCM vs. graphite full-cell is mainly caused by the excessive Li consumption at the anode-electrolyte interface instead of the formation of inaccessible Li sites within HE-NCM after prolonged cycling, in agreement with the study of Li et al. [2]

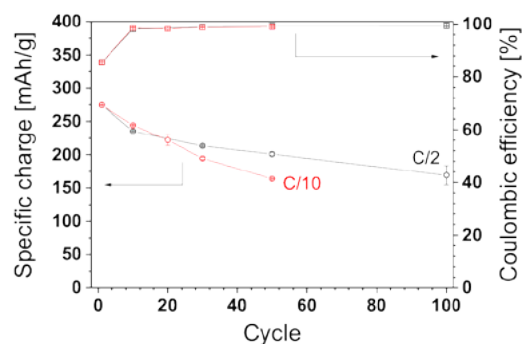


**Figure 1.** Average specific charge obtained after specified cycle number at C/2 (black) or C/10 (red) rates.

The weight percent of the Ni, Co, and Mn dissolved from HE-NCM cathodes is shown in Figure 2. The given values are normalized to the mass of HE-NCM in the cathode. Generally, the deposition of TM on the graphite increases with cycle number. As can be derived from the tangent of the dissolution curves in Figure 2, Ni, Co, and Mn all show the highest dissolution rate at the beginning of the cycling. A clear slowdown is then observed during prolonged cycles. After first cycle at C/15 rate, Ni is the only transition metal detected on the anode. Whether Mn and Co are dissolved could not be assessed, because the amount was below the detection limit. After 10 cycles, the total dissolution of Mn dominates, followed by Ni and Co. The above described trends apply to both C/2 and C/10 rates.

Despite the overall similar trends observed for cells cycled at C/2 and C/10 rates, the dissolution of individual TM is higher in the cells cycled with faster rate. If one simply correlates the amount of lithium consumed at the graphite anode to that of TM after different cycle numbers using only one cycling rate, one may conclude the following: the increasing lithium consumption at the anode-electrolyte interface with cycle number, and thus the specific charge decay, directly depends on the increased amount of TM deposited on the graphite. However, a different conclusion is drawn by comparing the data of two different cycling rates. While poorer specific charge retention and more lithium consumption at the anode is observed in cells cycled at C/10 rate, the amount of TM detected on the corresponding anode is less than in the cells cycled at C/2 rate. With a similar specific charge after 50 cycles at C/10 rate and 100 cycles at C/2 rate, the amount of TM accumulated on the

anode is doubled in the cells cycled at C/2 rate. Therefore, TM dissolution and its deposition on the anode is not the main reason that causes the depletion of accessible Li in the HE-NCM-graphite full-cell system.

Cycle rate	Cycle number	Average loss of Li <sup>1</sup> [mAh/g]	Average loss of specific charge <sup>2</sup> [mAh/g]
C/2	50	106	85
C/2	100	137	119
C/10	50	136	120

<sup>1</sup> The amount of Li deposited on the anode is analysed by ICP-OES. The value is then converted to the amount of specific charge.

<sup>2</sup> The values are calculated from the electrochemical cycling data.

**Table 1.** The average loss of Li as compared to the average loss of specific charge after specific cycles.

Within roughly the same cycling time of 400 h, the overall TM dissolution sums up to 4.5 atom% after 100 cycles at C/2 rate, while only 1.3 atom% is detected in cells cycled at C/10 rate for 20 cycles. This provides a hint that the total amount of time that HE-NCM is exposed to high potential does not have significant influence on the overall TM dissolution. It seems that the repeated lithium insertion and extraction plays a more important role in determining the extent of TM dissolution.

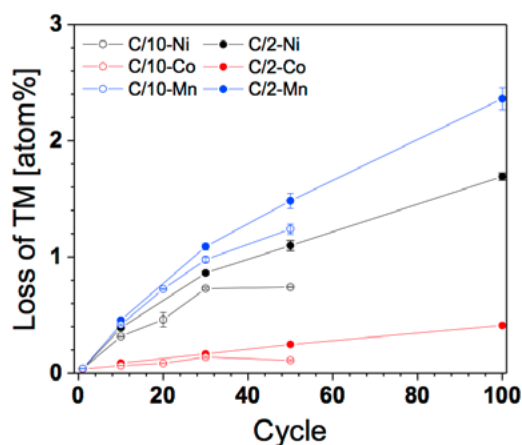


**Figure 2.** The average amount of Ni, Co, and Mn detected on the graphite anode after the given cycle number at C/2 and C/10 rates. The values presented here were calculated according to the following equation:  $\text{loss of Ni [atom\%]} = \text{number of dissolved Ni [mol]} / \text{total number of TM in the pristine cathode [mol]}$ .

The concentration gradient of each TM (Mn > Ni > Co) at the cathode/electrolyte interface is expected to be one of the driving forces causing deviations between the dissolution rates of different TMs. To facilitate the comparison, Figure 3 shows the recalculated data from Figure 2 by dividing the amount of the specific TM detected on the anode by the amount of the same TM in the pristine HE-NCM cathode. Unexpectedly, while Co and Mn share similar loss after 100 cycles at C/2 rate (~3.5 atom%), the loss of Ni is more than twice higher (~7.9 atom%). Higher Ni dissolution can also be seen at C/10 rate. Therefore, the concentration gradient cannot fully explain the dissolution of different TMs, as Mn is the dominant TM within HE-NCM pristine material. The origin of the dissolution of each specific TM is not yet very well understood and several suggestions are presented in the literature. While Hunter, for the LiMnO<sub>2</sub> system, proposed that the disproportionation reaction of LiMnO<sub>2</sub> in acidic environment results in Mn dissolution, Tang et al. suggested a mechanism based on surface structural transformation from LiMnO<sub>2</sub> to Mn<sub>3</sub>O<sub>4</sub>, where Mn is

in the oxidation state prone to dissolution [4, 5]. The study of Yan et al. on Li<sub>1.2</sub>Ni<sub>0.2</sub>Mn<sub>0.6</sub>O<sub>2</sub> also identified a lithiated form of M<sub>3</sub>O<sub>4</sub> phase (M stands for transition metal ion) [6]. In the same report, a gradual Ni migration to the surface was proposed. The detected Ni-poor structure at the outer most surface may provide a hint that Ni dissolves easier in liquid electrolyte than other TMs. We are conducting further investigation to find the origin of preferential dissolution of Ni.

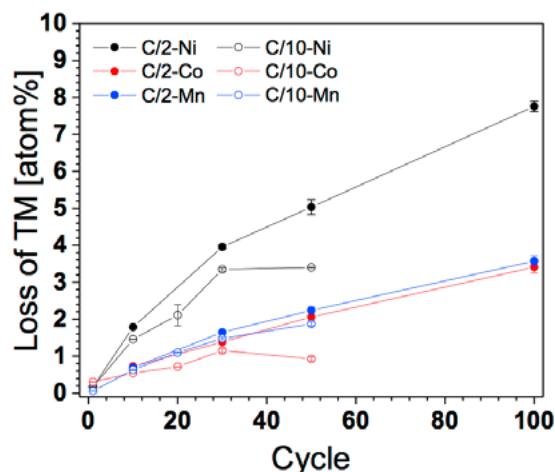


**Figure 3.** The average loss of Ni, Co, and Mn detected on the graphite anode after the given cycle number at C/2 and C/10 rates. The values presented here were calculated according to the following equation:  $\text{loss of Ni [atom\%]} = \text{number of dissolved Ni [mol]} / \text{total number of Ni in the pristine cathode [mol]}$ .

## Conclusion

In this study, the poorer specific charge retention of HE-NCM vs. graphite full-cell using low cycling rates was identified to be a direct consequence of excess lithium consumption at the anode-electrolyte interface. Opposed to the common believe that TMs deposited on graphite catalyse further electrolyte reduction, we propose that TM does not play the major role in depleting rechargeable lithium from the cathode. Although the exact dissolution mechanism is not yet well understood, Ni was found to have the highest dissolution rate as compared to Mn and Co. In addition, rather than the total time that HE-NCM is exposed to high potential, the repeated lithium insertion and extraction from HE-NCM seems to be an important factor that influences the overall TM dissolution in HE-NCM vs. graphite full-cell.

## Acknowledgement

The authors are grateful for the financial support from BASF SE.

## References

- [1] M.M. Thackeray, C.S. Johnson, J.T. Vaughey, N. Li, S.A. Hackney, *J. Mater. Chem.* **15**, 2257–2267 (2005).
- [2] Y. Li, M. Bettge, B. Polzin, Y. Zhu, M. Balasubramanian, D.P. Abraham, *J. Electrochem. Soc.* **160**, A3006 (2013).
- [3] S. Komaba, N. Kumagai, Y. Kataoka, *Electrochim. Acta.* **47**, 1229 (2002).
- [4] J.C. Hunter, *J. Solide State. Chem.* **39**, 142 (1981).
- [5] D. Tang, Y. Sun, Z. Yang, L. Ben, L. Gu, X. Huang, *Chem. Mater.* **26**, 3535 (2014).
- [6] P. Yan, A. Nie, J. Zheng, Y. Zhou, D. Lu, X. Zhang, R. Xu, I. Belharouak, X. Zu, J. Xiao, K. Amine, J. Liu, F. Gao, R. Shahbazian-Yassar, J.-G. Zhang, C.-M. Wang, *Nano Lett.* **15**, 514 (2015).

## Improved cylindrical cell for operando neutron powder diffraction of $\text{LiNi}_{0.5}\text{Mn}_{1.5}\text{O}_4$ vs. graphite

L. Boulet-Roblin, D. Sheptyakov<sup>1</sup>, P. Borel<sup>2</sup>, C. Tessier<sup>2</sup>, C. Villevieille

phone: +41 56 310 2115, e-mail: lucien.boulet@psi.ch

Li-ion batteries are based on (de)lithiation of electroactive materials upon cycling and therefore, structural changes occur. It is crucial to fully understand such reactions in order to prevent possible damaging effects of electrode materials and to avoid for example any degradation or failure of a battery during cycling. Disordered  $\text{LiNi}_{0.5}\text{Mn}_{1.5}\text{O}_4$  (d-LNMO) spinel is a promising cathode material with an average potential of 4.7 V vs.  $\text{Li}^+/\text{Li}$ . However, its structural changes during (de)lithiation are not yet fully understood. Neutron powder diffraction (NPD) is a technique of choice to investigate structural changes, especially for light elements like lithium. Developing a cell dedicated to operando neutron measurements is challenging in regard to the large amount of electroactive materials needed and/or the incoherent neutron scattering with hydrogen, highly contributing to the background [1].

Previously, we developed a cylindrical commercial-like cell suitable for operando NPD at HRPT beamline (SINQ) using d-LNMO as positive electrode and standard graphite as counter electrode [2]. Although this cell has the desired electrochemistry with gram of materials, the signal-to-noise ratio of the neutron patterns was not satisfying for Rietveld refinement. To achieve this goal, we report here an optimal design of the cell: i) the commercial casing made of iron is replaced by an aluminum one to reduce the number of phases in the patterns, ii) three times more active material is present in the cell, iii) an alumina/polymer composite separator is used instead of polypropylene separator to reduce the hydrogen content and, finally iv) a lithium reference electrode is added to precisely follow the two active materials electrodes separately.

### Experimental

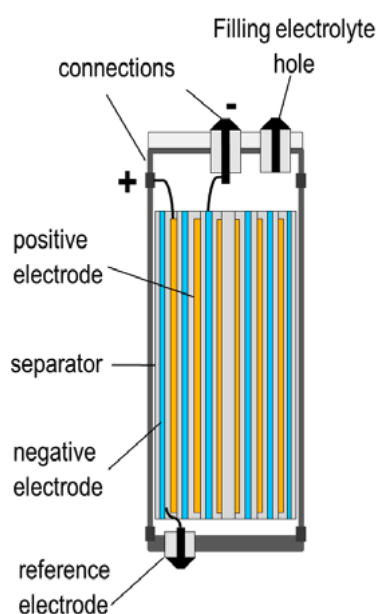


**Figure 1.** Scheme of the improved cylindrical cell used for the operando NPD.

Figure 1 represents the improved design of the cylindrical cell. The positive electrode was prepared by casting a mixture of 92 %wt d-LNMO (provided by SAFT), 4 %wt Super P carbon and 4 %wt PVDF binder suspended in N-methyl-2-pyrrolidinone onto an aluminum foil used as current collector. The casted slurry was dried at 80 °C under vacuum overnight. The negative electrode, based on a mixture of graphite (provided by SAFT) and Na-CMC binder, was casted onto a copper foil used as current collector. The cylindrical cell made of aluminum is filled with the two electrodes separated by a composite alumina/PP separator. A tiny lithium reference electrode is placed in between the two electrodes. Prior to cycling, the cell is filled with deuterated LP30 electrolyte (ethylene carbonate (EC):dimethyl carbonate (DMC) (1:1 w/w) and 1 M  $\text{LiPF}_6$ ). The cycling of the cells was carried out galvanostatically between 3.5 V and ca. 4.9 V at different C-rates, assuming theoretical specific charges of 147 mAh/g for d-LNMO. An open circuit voltage (OCV) of one hour was added at the end of (dis)charge. The NPD measurements were performed at HRPT beamline (SINQ), with a wavelength of 1.494 Å and high intensity settings.

### Results

Figure 2 shows the difference between the NPD patterns of the previous design and the new one. The new design (red curve) has a better signal-to-noise ratio than the previous one. Moreover, the casing made of aluminum helps by removing the large signals from iron casing as the one at 155°. This new design allows to measure NPD patterns in 2 min with enough quality to follow operando the lattice parameter of graphite and d-LNMO.

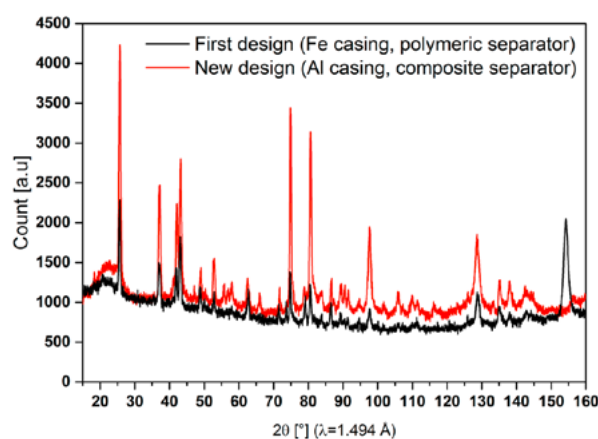


**Figure 2.** NPD patterns of d-LNMO vs. graphite recorded in modified cylindrical cell: i) first design and ii) new design after 40 and 15 min of acquisition, respectively.

Figure 3 shows the evolution of the galvanostatic profile of the three electrode couples at C/20 rate. The lithium reference electrode helps to follow separately the potential of d-LNMO

and graphite electrodes. Due to its localization in the cylindrical cell, the lithium reference can only «see» a small area of both electrodes. Nevertheless, those potentials are similar to the ones obtained in half-cell configuration (metallic lithium as counter electrode) [3]. For sake of clarity, only potential vs.  $\text{Li}^+/\text{Li}$  will afterwards be plotted and discussed.

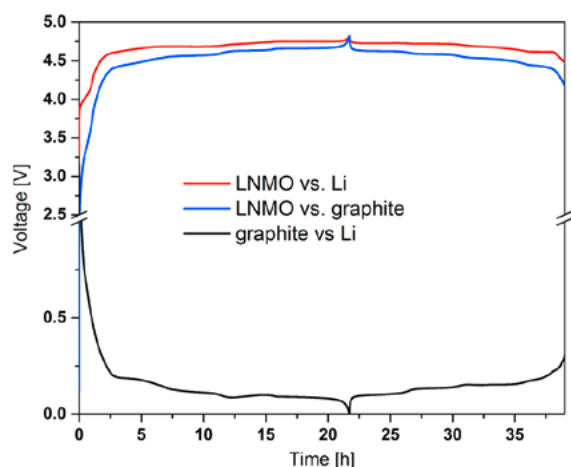


**Figure 3.** Galvanostatic profile at C/20 rate of LNMO vs. graphite, LNMO vs. Li ref. and graphite vs. Li ref. electrodes.

Figure 4 is the contour plot of the most intense LNMO reflection (222) during the first cycle at C/20 rate. Upon delithiation, a solid-solution reaction between  $\text{Li}_1\text{NMO}$  and  $\text{Li}_{0.5}\text{NMO}$  phases is observed while  $\text{Ni}^{2+}$  is oxidized to  $\text{Ni}^{3+}$  (up to 4.7 V). Then, a two-phase reaction occurs between  $\text{Li}_{0.5}\text{NMO}$  and  $\text{Li}_\epsilon\text{NMO}$  following  $\text{Ni}^{3+}$  to  $\text{Ni}^{4+}$  oxidation state, marked by the second plateau above 4.7 V. Those structural changes produce shrinkage of the LNMO unit cell and are reversibly observed during lithiation. However, the initial position of the (222) peak is not recovered and attributed to a lack of lithium.

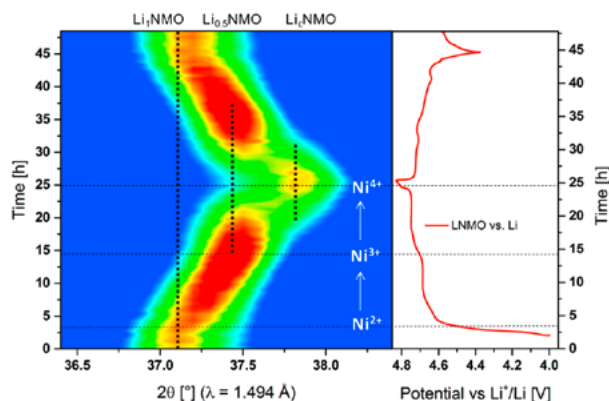


**Figure 4.** Contour plot representation obtained from operando NPD patterns of the first cycle of d-LNMO (222 peak).

Figure 5 depicts the evolution of (002) graphite reflection. During the (de)lithiation graphite undergoes several phase transitions, called «stages» [4]. For example stage 3 and 2 correspond to one interslab filled with lithium every three and two graphene sheets, respectively. It can be seen that pristine graphite,  $\text{LiC}_{12}$  (stage 2) and  $\text{LiC}_6$  (stage 1) phases are the main phases measured during the first lithiation. As expected,  $\text{LiC}_{12}$  reflection does not fully disappear at the end of lithiation (~24 h) indicating that not all graphite is fully lithiated, which is consistent with the balancing of the cell. Interesting features are recorded between graphite and  $\text{LiC}_{12}$  lithiation with five

different steps (represented by horizontal dash lines in Figure 5) which could not be observed with previous cylindrical cell design. No structural changes are recorded before step 1 (above 0.4 V), thus the electrochemistry is attributed to the built-up of a solid electrolyte interphase (SEI) which consumes lithium [4]. This lithium loss is correlated to the non-fully lithiated LNMO after the first cycle as previously discussed. From steps 1 to 2 (0.4 to 0.2 V), a solid-solution is observed and is attributed to the transition 1L to 4L stages. With steps 2 and 3 (0.2 and 0.16 V), the phase transition from stage 4L to 3L is seen, however it is unclear if it is a pure solid-solution or two-phase reaction. The next transition is a solid-solution reaction between stage 3L to 2L (step 3 and 4 with 0.16 V and 0.13 V, respectively). The transition of stage 2L to 2 is happening between step 4 and 5 (0.13 V and 0.1 V, respectively). All phase transitions were found reversible during further discharge.

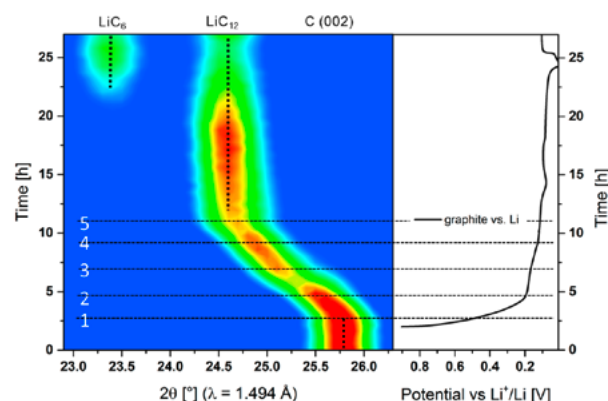


**Figure 5.** Contour plot representation obtained from operando NPD patterns of the first cycle of graphite (002 peak).

## Conclusion

Thanks to the reference electrode and improved signal-to-noise ratio, a better attribution of the structural changes of LNMO or graphite electrodes upon cycling is possible and for the first time stage 4L, 3L and 2L were distinctly observed.

Given the ability of this cell to register neutron patterns in short time with a good quality, this design can be used to probe fast and slow rates.

## Acknowledgement

The authors are grateful to SAFT for the financial support. This work is partly based on experiments performed at the Swiss spallation neutron source SINQ, Paul Scherrer Institute, Villigen, Switzerland.

## References

- [1] M. Roberts, J.J. Biendicho, S. Hull, P. Beran, T. Gustafsson, G. Svensson, K. Edström, *J. Power Sources* **226** (3), 249–255 (2013).
- [2] L. Boulet-Roblin, P. Borel, D. Sheptyakov, C. Tessier, P. Novák, C. Villevieille, *PSI Electrochemistry Laboratory – Annual Report 2014*, 55–56 (2014).
- [3] J.H. Kim, N.P.W. Pieczonka, Z. Li, Y. Wu, S. Harris, B.R. Powell, *Electrochim. Acta* **90**, 556–562 (2013).
- [4] B.M. Winter, J.O. Besenhard, M.E. Spahr, P. Novák, *Adv. Mater.* **10** (10), 725–763 (1998).

## Combining operando X-ray diffraction and operando Raman spectroscopy to understand the reaction mechanisms of $\text{LiNi}_{0.5}\text{Mn}_{1.5}\text{O}_4$ in Li-ion batteries

L. Boulet-Roblin, D. Streich, P. Borel<sup>1</sup>, C. Tessier<sup>1</sup>, C. Villeveille

phone: +41 56 310 2115, e-mail: lucien.boulet@psi.ch

To answer the challenges of clean energy storage especially for mobility, Li-ion battery technology is one of the most promising solutions. However, Li-ion batteries suffer from low energy density to offer reasonable autonomy range and to compete with the actual cars' fuel engines. Disordered  $\text{LiNi}_{0.5}\text{Mn}_{1.5}\text{O}_4$  spinel (named hereafter d-LNMO) electroactive material has an impressive energy density (ca. 650 Wh/kg) surpassing the commercial cathodes thanks to its high working voltage of ca. 4.7 V vs.  $\text{Li}^+/\text{Li}$  [1]. However, side reactions such as transition metal dissolution and electrolyte decomposition occur at these high potentials. To understand the underlying problem of stability, Raman spectroscopy was selected to study the «near-surface» region (~30 to ~300 nm) [2].

Raman spectroscopy has been used to characterize pristine d-LNMO but difficulties are encountered to properly assign the obtained vibration modes. Typically, one assumes that  $[\text{NiO}_6]$  and  $[\text{MnO}_6]$  octahedral are spectroscopically discernible and give rise to different vibration signals (at ca. 505  $\text{cm}^{-1}$  and ca. 645  $\text{cm}^{-1}$ , respectively [3]). This concept is based on the appearance of a peak at 505  $\text{cm}^{-1}$  when a part of Mn is replaced by Ni in  $\text{LiMn}_2\text{O}_4$ . However, no proof has yet been proposed to support this assumption.

In order to properly assign the Raman spectra and to use an original approach to determine the oxidation state of transition metal of d-LNMO during (de)lithiation, we combined operando X-ray diffraction (XRD) and operando Raman measurements.

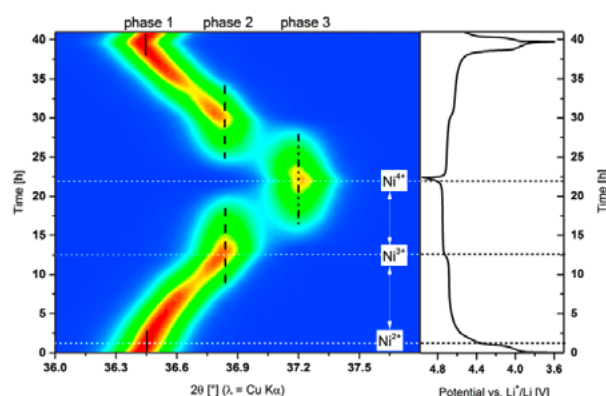
### Experimental

Self-standing electrodes were prepared by casting a mixture of 70 %wt d-LNMO (provided by SAFT), 10 %wt Super P carbon and 20 %wt PVDF binder suspended in acetone/ethanol solution. The casted slurry was dried at 80 °C under vacuum overnight. All the cells were assembled in an argon-filled glove box. Metallic lithium foil was used as counter electrode and a glass fiber sheet soaked with LP30 electrolyte (EC:DMC 1:1 %wt 1 M  $\text{LiPF}_6$ ) as separator. The operando cells [4, 5] were cycled galvanostatically between 3.5–4.9 V vs.  $\text{Li}^+/\text{Li}$  at C/20 rate (based on a theoretical specific charge of 147 mAh/g) at room temperature using Bat-small from Astrol Electronics AG. All the potentials are given compared to the reference  $\text{Li}^+/\text{Li}$ .

XRD measurements were performed using a PANalytical Empyrean diffractometer with Cu-K $\alpha$  radiation. The Raman spectra were acquired by using a Labram HR800 Raman microscope (Horiba-Jobin Yvon), equipped with a He-Ne laser (632.8 nm) and a 50x objective. The electronic conductivity of chemically delithiated d-LNMO powder with  $\text{NO}_2\text{BF}_4$  oxidizing agent was measured by 4-wire impedance spectroscopy.

### Results

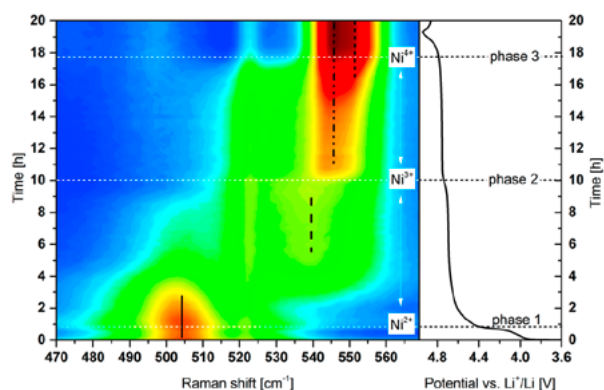
Figure 1 shows the contour plot representation of the operando XRD patterns of the d-LNMO electrode and its galvanostatic curve. During cycling, two main potential plateaus are observed and ascribed to  $\text{Ni}^{2+} \leftrightarrow \text{Ni}^{3+}$  (~4.68 V) and  $\text{Ni}^{3+} \leftrightarrow \text{Ni}^{4+}$  (~4.74 V) [6]. It can be seen that from OCV to ~4.7 V, a solid-solution reaction occurs with a shift of the peak position to higher angles (phase 1) and after ca. 9 h, a new peak appears (~36.85°) belonging to the phase 2. This phenomenon is followed by a two-phase reaction occurring during the last potential plateau (up to ~4.7 V) with the appearance of a new peak at ~37.3° (phase 3). On lithiation, we observe the reversibility of the reaction mechanisms. Phases 1, 2 and 3 belong to Fd-3m space group and have lattice parameters of ca. 8.17 Å, 8.08 Å and 8.00 Å, respectively.



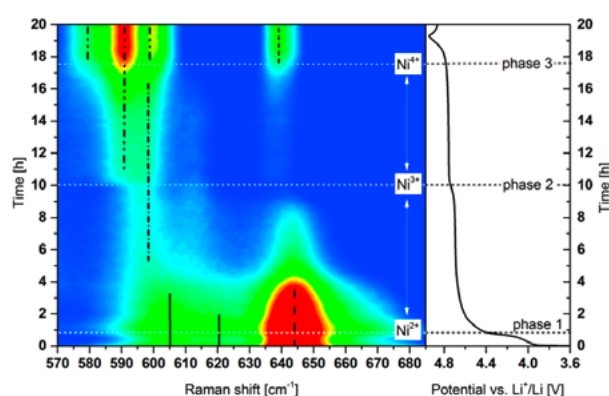
**Figure 1.** Contour plot representation obtained from operando XRD of the first cycle of d-LNMO electrode.

Figure 2 shows the evolution of Raman spectra [470–570  $\text{cm}^{-1}$ ] of d-LNMO during cycling against metallic lithium. The signal at ca. 522  $\text{cm}^{-1}$  corresponds to the electrolyte. The peak at 505  $\text{cm}^{-1}$  has been previously assigned to Ni-O vibration modes of d-LNMO. It can be seen that this peak disappears while  $\text{Ni}^{2+}$  is oxidised to  $\text{Ni}^{3+}$ . In the meantime, another broad peak appears at ca. 536  $\text{cm}^{-1}$ , which could be attributed to  $\text{Ni}^{3+}$ -O vibrations as Delichère et al. reported with  $\text{LiNiO}_2$  material [7]. This broad peak shifts to 545  $\text{cm}^{-1}$  and gets very intense as soon as  $\text{Ni}^{3+}$  starts to be oxidised into  $\text{Ni}^{4+}$  (after ~10 h). Thus, those Raman signatures can be ascribed to the three cubic phases and correlated to the Ni oxidation state.

Unfortunately, the peak which was assigned to Mn-O vibrations [3] at 645  $\text{cm}^{-1}$  evolves as well during cycling. Indeed, it can be seen in Figure 3 that this peak disappears while  $\text{Ni}^{2+}$  is oxidised into  $\text{Ni}^{3+}$ . For phase 2, only a weak peak is detected at ca. 595  $\text{cm}^{-1}$  in the interval 570–690  $\text{cm}^{-1}$ . However, a set of three peaks appears around 590  $\text{cm}^{-1}$  and another one at 640  $\text{cm}^{-1}$  when the  $\text{Ni}^{3+}$  changes to  $\text{Ni}^{4+}$ . A similar Raman signature was observed with the  $\text{LiMn}_2\text{O}_4$  spinel when fully delithiated [8] however without the intense peak at ca. 545  $\text{cm}^{-1}$  (Figure 2).



**Figure 2.** Contour plot representation obtained from operando Raman spectra [470–570  $\text{cm}^{-1}$ ] during the first charge of d-LNMO electrode.



**Figure 3.** Contour plot representation obtained from operando Raman spectra [570–690  $\text{cm}^{-1}$ ] during the first charge of d-LNMO electrode.

The Raman signals were found to be reversible during lithiation of d-LNMO.

The fluctuations of Raman peak intensities during the charging process can be related to a change in electronic conductivity of the d-LNMO. According to the theory, if the electronic conductivity of a material increases, the intensity of its Raman signals is expected to decrease, proportionally [2]. To verify this, conductivity measurements of chemically delithiated d-LNMO powders were performed (Table 1). One can see that the electronic conductivity progressively increases from the pristine to the half-delithiated sample ( $1 \times 10^{-7}$  to  $2 \times 10^{-5} \text{ S cm}^{-1}$ ) and afterwards decreases again when most of the lithium is removed from the d-LNMO ( $2 \times 10^{-5}$  to  $7 \times 10^{-6} \text{ S cm}^{-1}$ ).

These variations of conductivity are in accordance with the intensity trend observed in the Raman spectra during cycling.

Sample	$\text{Li}_7\text{NMO}$	$\text{Li}_{0.5}\text{NMO}$	$\text{Li}_0\text{NMO}$
Electronic conductivity [ $\text{S.cm}^{-1}$ ]	$1 \times 10^{-7}$	$2 \times 10^{-5}$	$7 \times 10^{-6}$

**Table 1.** Relative electronic conductivity of chemically delithiated  $\text{Li}_x\text{NMO}$  powder.

## Conclusions

Thanks to the combination of operando XRD and Raman measurements, the Raman signatures were linked to the three phases of LNMO occurring during (de)lithiation. By correlation, the Ni oxidation state of LNMO can be followed via Raman spectroscopy. However, a clear distinction between Ni-O and Mn-O vibrations cannot be made. Indeed, the shrinkage of the lattice parameter during delithiation affects Ni-O and Mn-O bonds and the changes in electronic conductivity of LNMO make it difficult to follow the putative Mn-O vibration mode. Therefore, theoretical calculations are needed to ensure the true nature of the underlying vibrations.

## Acknowledgement

The authors are grateful to SAFT for the financial support.

## References

- [1] D. Liu, W. Zhu, J. Trottier, C. Gagnon, F. Barry, A. Guerfi, A. Mauger, H. Groult, C.M. Julien, J.B. Goodenough, K. Zaghib, *RSC Adv.* **4** (1), 154 (2014).
- [2] R. Baddour-Hadjean, J.-P. Pereira-Ramos, *Chem. Rev.* **110**, 1278–1319 (2010).
- [3] D.H. Park, S.T. Lim, S.-J. Hwang, J.-H. Choy, J.H. Choi, J. Choo, *J. Power Sources* **159** (2), 1346–1352 (2006).
- [4] P. Bleith, H. Kaiser, P. Novák, C. Villevieille, *Electrochim. Acta* **176**, 18–21 (2015).
- [5] P. Lanz, C. Villevieille, P. Novák, *Electrochim. Acta* **130**, 206–212 (2014).
- [6] R. Qiao, L.A. Wray, J.-H. Kim, N.P.W. Pieczonka, S.J. Harris, W. Yang, *J. Phys. Chem. C* (2015).
- [7] P. Delichère, *J. Electrochem. Soc.* **135**, 1856, (1988).
- [8] W. Huang, R. Frech, *J. Power Sources* **81–82**, 616–620, (1999).

## A bulk investigation of $\text{CoSn}_2$ and $\text{FeSn}_2$ as anodes for Na-ion batteries

L.O. Vogt, C. Villevieille

phone: +41 56 310 5738, e-mail: leonie.vogt@psi.ch

Stationary energy storage is gaining importance, as the world moves towards relying on renewable but intermittent energy sources. Cost is the most prevalent factor for such stationary energy storage applications and in light of this, research on Na-ion batteries has been growing [1]. Unlike lithium, sodium is extremely abundant all across the world and its production is consequently cheap. However, no suitable anode materials have yet been found for sodium ion batteries and research into this area is imperative to allow commercialisation.

Elements such as P, Sb and Sn have been shown to react reversibly with sodium; however, their reactions are accompanied by large volume changes which lead to fast fading of the performance [2, 3]. By alloying these active elements to transition metals that don't react with sodium, this effect can be mitigated [4]. Here we explore the family  $\text{MSn}_2$  (with  $M = \text{Co}$  and  $\text{Fe}$ ) as promising sodium-ion battery anode materials. The two alloys have the same structure, yet they show different electrochemistry with  $\text{FeSn}_2$  always outperforming  $\text{CoSn}_2$ . We explore the reaction mechanism of the two alloys through the use of operando XRD measurements.

### Experimental

XRD measurements were performed at room temperature with a PANalytical Empyrean diffractometer using Cu-K $\alpha$  radiation. Operando measurements were performed in a home-made cell described elsewhere [5]. One pattern was recorded every hour. A self-standing electrode was used in the setup composed of 70 %wt active material, 12 %wt CMC binder (Alfa Aesar) and 9 %wt Super P $^{\circ}$  carbon (Imerys) and 9 %wt vapour grown carbon fibers (ShowaDenko). The electrode was cast from a water suspension onto Copper foil and then dried in air. Heating under vacuum for 1 hour at 120  $^{\circ}\text{C}$  causes the electrode to detach from the copper foil to give a self-standing film. The latter was cycled against sodium metal at a C/100 rate or slower in the electrolyte  $\text{NaClO}_4$  in PC; 250  $\mu\text{L}$  of electrolyte were used to soak the glass fiber separator in the cell. A potentiostatic step was applied after each galvanostatic step for varying lengths of time.

### Results

By using operando XRD it was possible to track the phase changes occurring within the material during cycling. To ensure the reaction reached completion the electrochemical sodiation of  $\text{FeSn}_2$  included intermediate potentiostatic steps applied at defined potentials (Figure 1, right). During these intermediate potentiostatic steps the current always drops off very fast, indicating that the reactions occurring at those potentials are close to being complete. The evolution of the operando XRD indicates that no intermediate states are formed during the first six potentiostatic steps. In contrast, for the last potentiostatic step at 5 mV, the current decreases very slowly and even after 80 hours in the potentiostatic step it is only at half of the original galvanostatic current applied, indicating that the reaction is not yet complete.

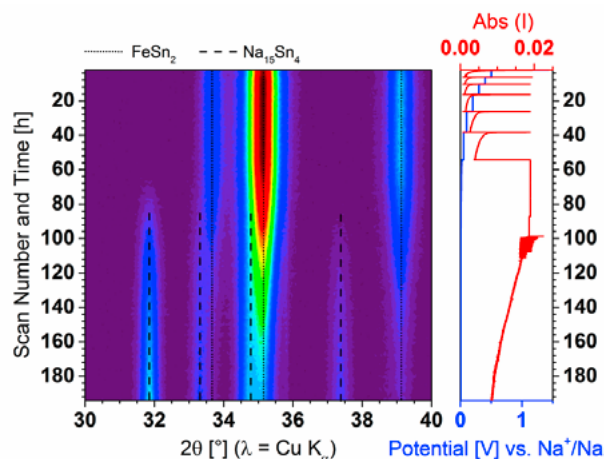


Figure 1. Contour plot of operando XRD and electrochemistry of a  $\text{FeSn}_2$  cell during the first sodiation of the material.

Despite nearly four days of potentiostatic step at 5 mV not all the pristine  $\text{FeSn}_2$  material reacted with the two largest peaks at  $35.2^{\circ}$  and  $39.2^{\circ}$  in Figure 1 still being visible at full sodiation (186<sup>th</sup> hr), though they are much diminished in intensity. Unlike in the Sn system, no crystalline intermediate phases appear (we cannot exclude amorphous intermediate phases) [6]. The diminishing of the pristine  $\text{FeSn}_2$  phase is, however, accompanied by the appearance of the most sodiated Na-Sn phase known to exist,  $\text{Na}_{15}\text{Sn}_4$ . However, no peaks corresponding to iron were observed, which in theory should have been extruded for the conversion reaction of  $\text{FeSn}_2$  into  $\text{Na}_{15}\text{Sn}_4$  and  $\text{Fe}^{\circ}$ . We hypothesize that the iron cannot be observed via XRD as it gets extruded as nanoparticles dispersed throughout the electrode and thus no long range order is detectable by XRD [7, 8].

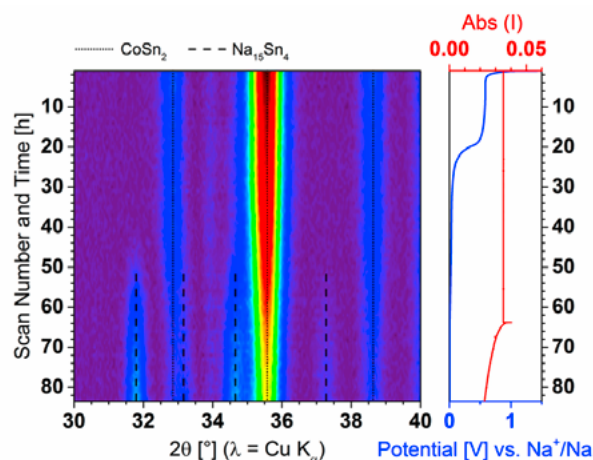
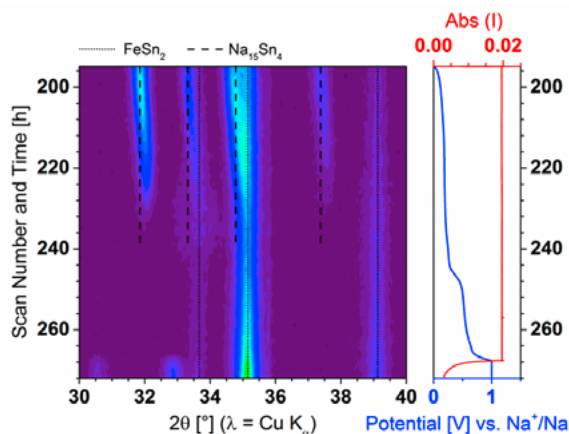


Figure 2. Contour plot of operando XRD and electrochemistry of a  $\text{CoSn}_2$  cell during the first sodiation of the material.

A similar picture is seen for the sodiation of  $\text{CoSn}_2$  (Figure 2). Even at full sodiation (82<sup>nd</sup> hr)  $\text{CoSn}_2$  peaks are clearly visible at  $31.9^{\circ}$ ,  $35.6^{\circ}$  and  $38.7^{\circ}$ . The  $\text{Na}_{15}\text{Sn}_4$  phase appears and grows

from the 50<sup>th</sup> hour onwards, on the low potential plateau just above 5 mV. The current reaches half of its original galvanostatic value after 20 hours in the potentiostatic step at 5 mV, indicating that the reaction was still ongoing.

The desodiation of the two systems FeSn<sub>2</sub> and CoSn<sub>2</sub> are shown in Figure 3 and 4, respectively. The electrochemistry shows two distinct potential plateaus between 5 mV and 1 V for both systems. In contrast to the potentiostatic step during sodiation, during desodiation the current in the potentiostatic step falls rapidly in both systems indicating that the desodiation reaction is complete at this point.



**Figure 3.** Contour plot of operando XRD and electrochemistry of a FeSn<sub>2</sub> cell during the first desodiation of the material.

The lower potential plateau in the electrochemistry can be linked to the extraction of sodium from the Na<sub>15</sub>Sn<sub>4</sub> phase. For both the FeSn<sub>2</sub> and CoSn<sub>2</sub> system, a shift in the peaks attributed to Na<sub>15</sub>Sn<sub>4</sub> to higher angles is observed before their disappearance in the second half of the lower potential plateau (Figure 3 and Figure 4). This shift to higher angles means that the lattice parameter of the structure is shrinking as sodium is extracted from the system and a new intermediate phase with the nominal composition Na<sub>15-x</sub>Sn<sub>4-y</sub> forms. An alternative possibility is that some iron/cobalt is inserted back into the structure at this point. Interestingly, this Na<sub>15-x</sub>Sn<sub>4-y</sub> intermediate did not appear on sodiation and it has to our knowledge not been documented in literature. Its formation seems favorable in the MSn<sub>2</sub> system on desodiation. After a shift of about 0.3° the Na<sub>15-x</sub>Sn<sub>4-y</sub> Bragg peaks disappear, indicating the disappearance of the structure.

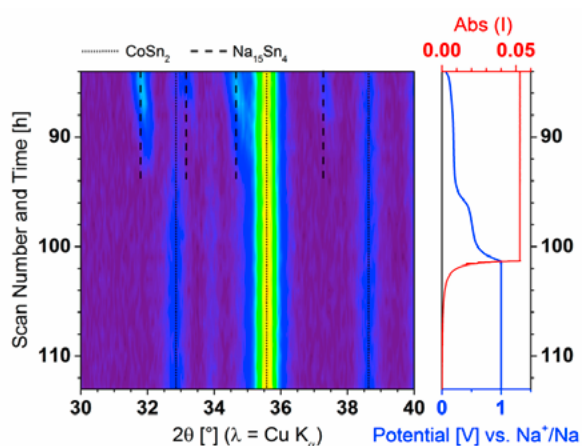


**Figure 4.** Contour plot of operando XRD and electrochemistry of a CoSn<sub>2</sub> cell during the first desodiation of the material.

Though the second potential plateau is visible in both systems, the reaction occurring here is substantially different for FeSn<sub>2</sub> compared to CoSn<sub>2</sub> as uncovered by the operando XRD. While a clear back reaction to form FeSn<sub>2</sub> is visible in the system containing iron (Figure 3, 240<sup>th</sup>–266<sup>th</sup> hour), no such reaction is visible in the system containing cobalt (Figure 4, no changes from 94<sup>th</sup>–113<sup>th</sup> hour). The FeSn<sub>2</sub> system thus undergoes partial reformation to the starting phase. Electrochemically FeSn<sub>2</sub> always outperforms CoSn<sub>2</sub>. We believe that the partial reformation of the original structure is one factor contributing to the better performance of FeSn<sub>2</sub>.

## Conclusion and Outlook

The operando XRD results are in line with the cycling of the MSn<sub>2</sub> materials. Electrochemically FeSn<sub>2</sub> always outperforms CoSn<sub>2</sub> in terms of specific charge; visualized in the *in situ* experiment described here where more FeSn<sub>2</sub> reacted to Na<sub>15</sub>Sn<sub>4</sub> than CoSn<sub>2</sub> to Na<sub>15</sub>Sn<sub>4</sub>. Additionally on desodiation FeSn<sub>2</sub> shows some reformation of the starting phase, a feature completely absent for the CoSn<sub>2</sub> system. It is likely that this difference also contributes to the better electrochemical performance of the FeSn<sub>2</sub> system. Refinements of intermediates and further operando tests during later stages of cycling are planned to confirm these initial results.

## Acknowledgement

The authors would like to thank Prof. Dr. Petr Novák for fruitful discussions. Additionally, the Swiss National Science Foundation is thanked for financial support (Project 200021\_156597). This work was performed within the Swiss Competence Center of Energy Research (SCCER) Heat and Storage framework.

## References

- [1] N. Yabuuchi, K. Kubota, M. Dahbi, S. Komaba, *Chem. Rev.* **114**, 11636 (2014).
- [2] L.D. Ellis, T.D. Hatchard, M.N. Obrovac, *J. Electrochem. Soc.* **159**, A1801 (2012).
- [3] A. Darwiche, C. Marino, M.T. Sougrati, B. Fraise, L. Stievano, L. Monconduit, *J. Am. Chem. Soc.* **134**, 20805 (2012).
- [4] M.R. Palacin, *Chem. Soc. Rev.* **38**, 2565 (2009).
- [5] P. Bleith, H. Kaiser, P. Novák, C. Villevieille, *Electrochim. Acta* **176**, 18 (2015).
- [6] L.O. Vogt, M. El Kazzi, E. Jämstorp Berg, S. Pérez Villar, P. Novák, C. Villevieille, *Chem. Mater.* **27**, 1210 (2015).
- [7] J.L. Gomez-Camer, C. Villevieille, P. Novak, *J. Mater. Chem. A* **1**, 13011 (2013).
- [8] C. Marino, B. Fraise, M. Womes, C. Villevieille, L. Monconduit, L. Stievano, *J. Phys. Chem. C* **118**, 27772 (2014).

## PEEM spectroscopy: a promising technique to study the surface of commercial-like battery electrodes at the nanoscale

D. Leanza, C.A.F. Vaz, P. Novák, M. El Kazzi

phone: +41 56 310 5149, e-mail: mario.el-kazzi@psi.ch

The continuous need for increasing the electrochemical performance and safety of Li-ion batteries require an incessant development of characterization techniques to provide better insights into the physics and chemistry of the various parts of the battery and particularly of the working electrodes. Both the bulk and the surface structure modification of the electrodes need to be investigated upon cycling due to their direct impact on battery behaviour.

In the last few years, the expansion of post mortem and operando techniques has helped tremendously to gain fundamental understanding of the structural and chemical evolution of the bulk of electrode materials. However, the processes taking place at the surface and at the electrolyte/electrode interface remain elusive, even though they have been extensively studied in the last 30 years [1]. Indeed the complex chemistry and morphology of Li-ion battery electrodes make the detailed comprehension of the surface electrochemical reaction mechanism very challenging. These complexities result from various parameters:

- (I) The extreme roughness, inhomogeneity and porosity of the surface which is composed of a mixture of active particles, conductive carbon and organic binder (Figure 1).
- (II) The nature of the electrolyte/electrode interface developed during lithiation/delithiation process leads to the formation of organic and inorganic species with some preferential growth on the different particles of the surface.
- (III) The evolution of the surface reconstruction layers of high voltage cathode materials, regardless the bulk structure, drives the leaching of the transition metals and their dissolution in the electrolyte. [2]

In this context, it is of utmost importance to exploit new characterization techniques that are able to provide surface chemical information at the nanoscale level on the different particles constituting the electrode, while preserving their working environment (as in commercial-like cycled electrodes).

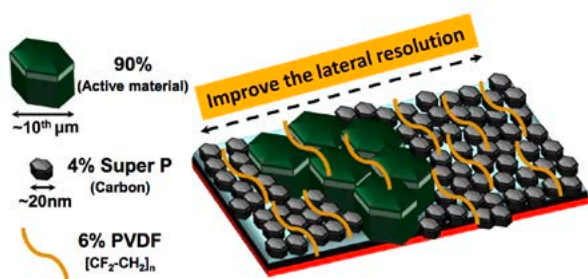


**Figure 1.** Sketch representing the surface composition and morphology of Li-ion battery electrodes.

In the following report we explore for the first time the potential and feasibility of X-ray PhotoEmission Electron Microscopy (PEEM) to investigate commercial-like battery electrodes and to study individually, at the nanoscale level, the surface layer

chemistry evolution on the active materials and on the conductive carbon.

X-ray PEEM is a synchrotron-based soft X-ray microscopy which was first developed in the 1930s and since then has become a well-established imaging technique with the development of third generation X-ray synchrotron sources. In a standard experiment the secondary electrons emitted from the sample surface upon absorption of photons are collected to obtain a magnified image of the material. Simultaneously, synchrotron X-rays provide a direct chemical contrast by using the elemental selectivity of the X-ray absorption edges.

The lateral resolution in XPEEM is in the range of 50–70 nm but can detect signals from particles as small as 10 nm with a depth analysis in the order of 3 nm. All these characteristics make XPEEM comparable and complementary to traditional surface techniques such as XPS, RAMAN, SEM and FTIR with the unique advantage of enabling one to obtain chemical information thanks to its ability to provide spatially-resolved X-ray absorption spectra at the nanometer scale. Besides the analysis of the oxidation states of the transition metals, the PEEM technique provides valuable information to study the evolution of the surface layer originated upon cycling from the electrolyte decomposition following the C K-edge variation.

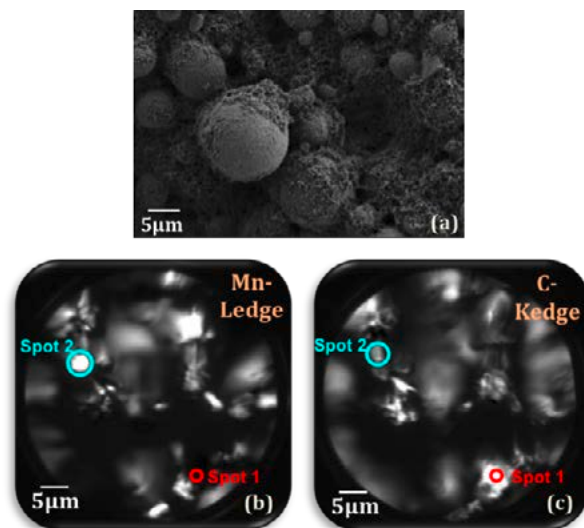
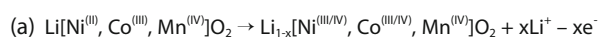


**Figure 2.** (a) SEM image showing the surface morphology of a HE-NCM electrode composed of 90% active material, 4% conductive carbon and 6% PVDF organic binder. Element-specific PEEM contrast images performed on HE-NCM pristine electrode by acquiring the (a) Mn-L, (b) C-K edges using a field of view of 45  $\mu\text{m}$  revealing the distribution of the HE-NCM and carbon particles.

The feasibility of realizing XPEEM measurements on electrodes for Li-ion batteries was tested on SIM beamline at the Swiss Light Source (SLS). XPEEM images of pristine HE-NCM electrode with 90% of HE-NCM active material, 4% conductive carbon and 6% PVDF are presented in Figure 2 (b, c). Element-

specific XPEEM contrast images at the Mn-L edge (641.6 eV) and C-K edge (285.6 eV) and below the absorption edge at (637 eV) and (280 eV) respectively, were recorded sequentially. Dividing the images enhances the elemental contrast and reduces topographic contrast and illumination inhomogeneities, as shown in Figure 2. Thanks to the element-specific contrast images we are able to identify HE-NCM and carbon particles at the surface. The white spots on the Mn-L edge contrast image correspond to HE-NCM particles (Figure 2b) while on the C-K edge contrast image they are associated with the carbon particles (Figure 2c). The X-ray absorption spectra (XAS) at the Mn-L edge and C-K edge collected on carbon particles (spot 1 in Figure 2) show a weak peak in the noise level for Mn-L edge confirming the absence of HE-NCM particles (Figure 3a), while a strong peak of the unoccupied  $\pi^*$  state of the conductive carbon (C=C) is detected (Figure 3b). The opposite behavior is observed on spot 2 (HE-NCM particles) in Figure 2, where the XAS spectra show strong peaks at the Ni-L, Co-L and Mn-L edges and a weak unoccupied  $\pi^*$  state peak of the carbon (C=C) on the C-K edge confirming the absence of carbon particles on this spot.

The oxidation states of the transition metals on spot 2 (HE-NCM) presented in Figure 4 are determined to be +2, +3 and +4 as is expected on pristine electrodes, based on the reaction equations:



However, on the C-K edge spectra (Figure 4b) we observe the presence of the unoccupied  $\pi^*$  state of the conductive carbon (C=C) together with hydrocarbon at  $\sim 285.7$  eV in addition of two peaks located at 288.7 eV and 290.6 eV associated with Li alkyl carbonate and  $\text{Li}_2\text{CO}_3$  present on the surface of the HE-NCM.

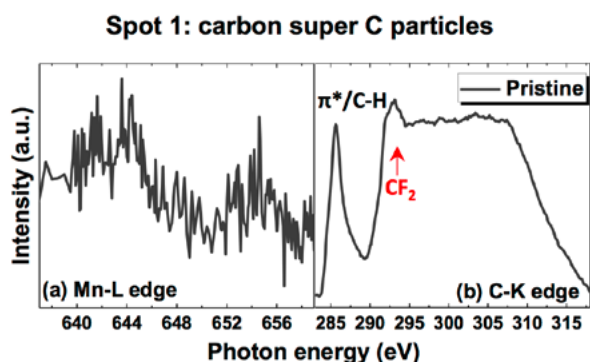


**Figure 3.** XAS measurements at Mn-L and C-K edges recorded on carbon super C particles (spot 1 of Figure 1 b, c).

The same XAS spectra were acquired on one single HE-NCM particle of an electrode cycled up to 3.55 V vs. LTO and compared to the pristine one (Figure 4). The Ni, Co and Mn undergo significant changes upon cycling. In particular Ni L3-edge exhibits an increase of the shoulder at higher energy, whereas the Mn L3-edge shows a variation towards lower energy. Surprisingly, the Co L3-edge presents simultaneous changes at low and high energy. Shape and energy shift variations in the absorption edge towards lower or higher energy are correlated to the reductive or oxidative states, respectively. The increase of the oxidation state of the Ni and Co is anticipated based on equation (a) since the measurements are performed

on an electrode in a fully charged state. However after full delithiation of HE-NCM, the presence of Co and Mn in a lower oxidation state (+3/+2) compared to the pristine is not expected. This result provides evidence that the surface of the HE-NCM undergoes a structural reconstruction with reduced layers associated with the collapse and rearrangement of local crystal structures.

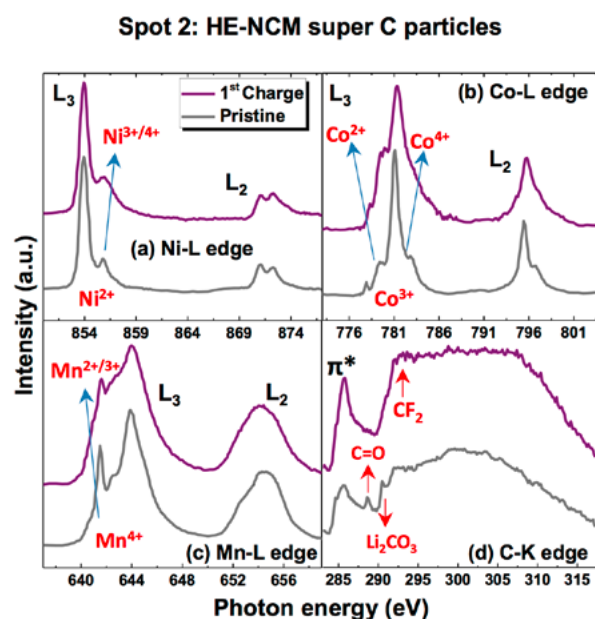


**Figure 4.** XAS measurements at the Ni-, Co-, Mn-L edges and C-K edge acquired on one single HE-NCM pristine particle and after 1<sup>st</sup> charge vs. LTO at 3.55 V.

## Conclusion

These innovative and successful results confirm the feasibility of XPEEM measurements and the possibility of collecting, at the micro- and nanometer scale, chemical information related to isolated active or carbon particles on the surface of the commercial-like electrode for Li-ion battery. It should be noted that it is the first time that we are able to highlight the presence of Li carbonate and Li alkyl carbonate species on the surface of isolated NCM particles, without interference from the carbon and PVDF signals. Moreover, monitoring the evolution of the oxidation states of the transition metals within the range of 2 nm depth, places the PEEM as a unique technique to follow the surface local rearrangement of the structure together with surface evolution due to electrolyte oxidation/reduction.

## References

- [1] S. Malmgren, K. Ciosek, M. Hahlin, T. Gustafsson, M. Gorgoi, H. Rensmo, K. Edström, *Electrochim. Acta* **97**, 23–32 (2013).
- [2] F. Lin, I.M. Markus, D. Nordlund, T.-C. Weng, M.D. Asta, H.L. Xin, M.M. Doeff, *Nat. Commun.* **5**, 1–8 (2014).

\* HE-NCM is a Li-rich material considered as a mixture of  $\text{Li}_2\text{MnO}_3$  and  $\text{Li}[\text{Ni}, \text{Co}, \text{Mn}]\text{O}_2$ .

## Microstrain and its impact on the electrochemical performance of $\text{LiNi}_{0.80}\text{Co}_{0.15}\text{Al}_{0.05}\text{O}_2$

R. Robert, P. Novák

phone: +41 56 310 5426, e-mail: rosa.robert@psi.ch

In the layered transition metal oxide cathode materials such as the  $\text{LiNi}_{0.80}\text{Co}_{0.15}\text{Al}_{0.05}\text{O}_2$  (NCA) and the  $\text{Li}_{1+a}(\text{Ni}_x\text{Mn}_y\text{Co}_z)_{1-a}\text{O}_2$  (NMC), an increase of the working potential window increases considerably the initial specific charge [1], i.e. for the NCA, an increase of the operating upper cut off potential to 4.9 V can provide an additional  $\sim 40$  mAh/g of specific charge on the first charge [2], which in turn improves the specific energy of the cathode. However, an important drawback caused working at high potential is the structural instability of the cathode materials, i.e., they suffer from loss of oxygen, transition metal dissolution and irreversible structural transitions, which contributes to their degradation.

This study aims to provide new insights into the degradation mechanism of the NCA material by means of the evaluation of microstrain generated in the layered oxide lattice during several electrochemical (over-)charge and discharge cycles. Its influence on cycling performance is presented.

### Experimental

The positive electrode and coin-cell assembly was prepared as described elsewhere [2]. Cells were galvanostatically tested between 3.0 V and different upper cut off potentials (4.3, 4.6, and 4.9 V vs.  $\text{Li}^+/\text{Li}$ ), at a specific current of 10 mA/g, using an Astrol (Switzerland) standard battery cyler.

Structural evaluations were performed on powder X-ray diffraction patterns taken *ex situ* at the Materials Science Beamline of the Swiss Light Source. Measurement conditions and structural characterization are described in detail in [2]. Microstructural information was obtained by powder XRD data analysis, described elsewhere [2] and references therein, using the Rietveld refinement method. The apparent strains were calculated for each reflection according to:

$$\langle \varepsilon \rangle = \frac{\eta}{4} = \frac{1}{2} \beta_{\text{strain}}$$

### Results

The X-ray powder diffraction profiles of NCA electrodes at different lithium deintercalation levels reveal anisotropic *hkl*-dependent peak-broadening effects. The peak-broadening, expressed as the integral breadth  $\beta$  (defined as peak area/peak maximum) of a reflection is plotted vs. the diffraction angle  $\Theta$  in Figure 1. The largest strain broadening occurs in the (00 $l$ ) lines as more lithium is removed from the NCA lattice. This is a result of the increase of lattice imperfection such as vacancies, site-disorder, and composition variation [2].

Table 1 shows the average value of the microstrain and the specific charge values on discharge. The strain generated during charge is considerable large reaching a 4.5 times larger value at 4.6 V compared to its initial value. This microstrain does not completely recover to the pristine material value after full discharge.  $\langle \varepsilon \rangle$  is increased by  $\sim 6\%$  after the first charge-(4.6 V)-discharge cycle and to  $\sim 7\%$  after the second

charge-discharge cycle. These observations correlate very well with the continuous decay of the cycling performance from cycle 1 to cycle 10 of the cell cycled between 3.0 and 4.6 V. While the rapid increase of microstrain from cycle 1 to cycle 10 for the cell cycled between 3.0 and 4.9 V, meaning that after the first cycle  $\langle \varepsilon \rangle$  increases by  $\sim 8\%$  and after the second cycle  $\langle \varepsilon \rangle$  increases by  $\sim 11\%$ , leads to a stronger fading of the specific charge.

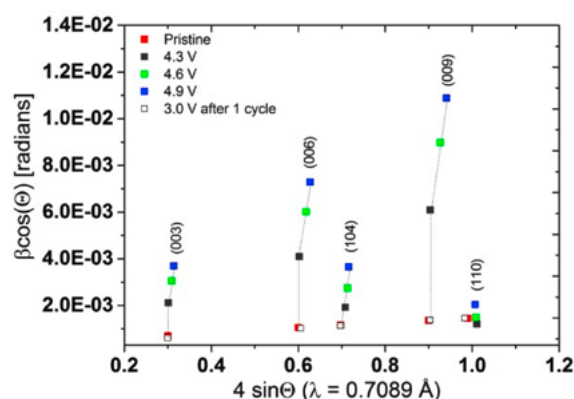


**Figure 1.** Integral breadth  $\beta$  vs.  $4\sin\Theta$  plot of NCA, for selected reflections, of the pristine material and samples charged to 4.3 V, 4.6 V, and 4.9 V, and discharged to 3.0 V after a full charge-(4.6 V)-discharge cycle (vs.  $\text{Li}^+/\text{Li}$ ).

$\langle \varepsilon \rangle \cdot 10^{-4}$	Pristine	4.3 V	4.6 V	4.9 V
	11.6868	43.2331	53.1638	-
	<b>4.6-3.0 V</b>	<b>4.6-3.0-4.6-3.0 V</b>	<b>4.9-3.0 V</b>	<b>4.9-3.0-4.9-3.0 V</b>
	12.4074	12.5669	12.6328	13.0115
Specific charge [mAh/g]		<b>4.3 V</b>	<b>4.6 V</b>	<b>4.9 V</b>
After 1 cycle	-	195.91	212.48	208.35
After 10 cycles	-	194.24	206.21	160.90

**Table 1.** Microstrain values on charge and discharge extracted from Rietveld refinements fits and specific charge on discharge for NCA charged to 4.3/4.6/4.9 V.

From this study we conclude that, besides the electrolyte decomposition and irreversible structural changes among other factors, the observed microstrain generated during each charge has also a deleterious impact on the cycle performance of this material when charged to very positive cut off potentials.

### References

- [1] R. Robert, C. Villevieille, P. Novák, *J. Mater. Chem. A* **2**, 8589 (2014).
- [2] R. Robert, P. Novák, *J. Electrochem. Soc.* **162** (9), A1823–A1828 (2015).
- [3] R. Robert, Ch. Bünzli, E.J. Berg, P. Novák, *Chem. Mater.* **27**, 526–536 (2015).

## Impact of operating conditions on the cycling performance of all-vanadium redox flow batteries

O. Nibel, T.J. Schmidt, L. Gubler

phone: +41 56 310 2326, e-mail: olga.nibel@psi.ch

The growing need for energy as well as the CO<sub>2</sub> emission and associated global warming require clean and renewable energy sources, such as sun and wind power. Since those renewable energy sources are intermittent, the development of adequate energy storage systems is essential. Redox flow batteries are considered as one of the attractive options for energy storage from renewable sources and can be used in applications ranging from kW to MW and even GW power scale. The all-vanadium redox flow battery (VRB) is the most advanced technology. VRBs use the same element (vanadium) in both half cells, which prevents irreversible cross-contamination of electrolytes. The VRB consists of a stack of cells where redox reactions occur, two tanks in which electrolytes are stored and of pumps and piping for electrolyte circulation. The single redox flow cell in a VRB contains an ion exchange membrane (IEM), electrolyte distributors, electrodes and current collector plates [1].

The overall performance of the redox flow cell strongly depends on the properties of the used membrane [2], electrodes [3] and electrolytes [4] and can be enhanced by choosing the most advanced materials or by modifying these materials. In addition, the operating conditions can affect the VRB cell performance. The objective of this study is to investigate the impact of the operating temperature and flow rate on the performance of all-vanadium redox flow cells.

### Materials and Methods

A redox flow test system Model 857 from Scribner was used. 3 sheets of SGL 10 AA carbon paper (from Ion-Power, 350 μm thick) with an area of 25 cm<sup>2</sup> were used in each half-cell. They were compressed to 90% of their original thickness.

The redox flow battery was charged and discharged at a constant current density of 40 mA/cm<sup>2</sup> using 1.7 V as upper and 0.8 V as lower voltage limit. 70 mL of 0.75 M V<sup>2+</sup>/V<sup>3+</sup> and VO<sup>2+</sup>/VO<sub>2</sub><sup>+</sup> solutions in 2 M H<sub>2</sub>SO<sub>4</sub> were used as negative and positive electrolyte, respectively.

The ohmic resistance of the single redox flow cell was measured at fully charged state at different temperatures by means of electrochemical impedance spectroscopy. An AC amplitude of 10 mV and frequency range from 100'000 to 0.1 Hz was used. Subsequently, the ohmic resistance of the redox flow cell could be determined at high frequencies from the x-intercept in the Nyquist plot representation.

### Results and Discussion

As demonstrated in Figure 1, the influence of the flow rate on the performance of the redox flow cell was investigated by charging and discharging the redox flow battery at three different flow rates, namely 15 mL/min, 30 mL/min and 60 mL/min.

The change of the operating flow rate from 15 to 60 mL/min resulted in a significant increase of discharging capacity from 0.64 Ah to 1.11 Ah. The theoretical capacity for the 70 mL of

solution on either side is 1.41 Ah. Also coulombic efficiency and voltage efficiency improved from 70.6% to 99.5% and from 67.1% to 73.7%, respectively. The overall energy efficiency increased from 47.4% to 73.3% by applying higher flow rates.

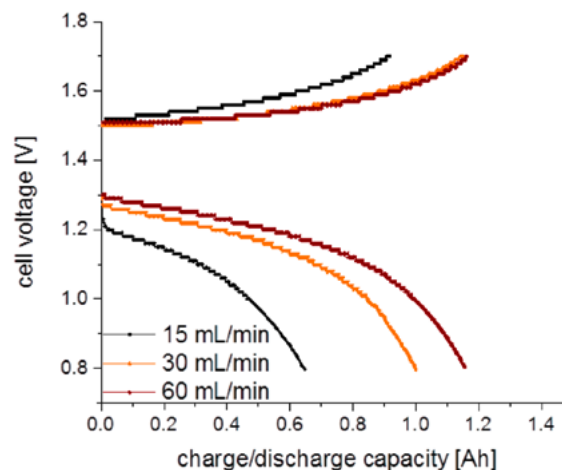


**Figure 1.** Charge-discharge curves measured at different flow rates. The redox flow battery with Nafion® 117 as separator was charged and discharged at a constant current density of 40 mA/cm<sup>2</sup> using 1.7 V as upper and 0.8 V as lower voltage limit. 70 mL of 0.75 M vanadium solutions in 2 M H<sub>2</sub>SO<sub>4</sub> were used as negative and positive electrolyte, respectively.

In addition, the influence of the operating temperature on the performance of the redox flow battery was studied. For this purpose, the ohmic resistance of the redox flow cell and charge-discharge curves were measured at different temperatures ranging from 35 °C to 50 °C. The area resistance of the redox flow cell with Nafion® 117 as separator decreased at higher temperatures from 0.46 to 0.45 Ohm cm<sup>2</sup>.

Figure 2 shows the results obtained from charging and discharging the redox flow battery at different temperatures. For this study the redox flow cell was operated with two different ion exchange membranes. Not only Nafion® 117 was used as separator but also a bifunctional radiation grafted membrane containing protogenic sulfonic acid and amidoxime groups.

It was shown that the presence of the amidoxime groups in the membranes leads to a significant decrease of the vanadium crossover without significantly affecting the current density. The bifunctional ion-conducting membranes with reduced vanadium permeability were prepared by radiation-induced graft copolymerization of styrene and acrylonitrile into ETFE films of 25 μm thickness. Subsequently, grafted films were functionalized with desired functional groups [5]. For the present study, membranes with a graft level of 34% and a styrene molar fraction of 0.4 in the grafts have been chosen. The graft level was adjusted by the reaction time whereas the composition of the grafts was tuned by varying the monomer ratio in the grafting solution.

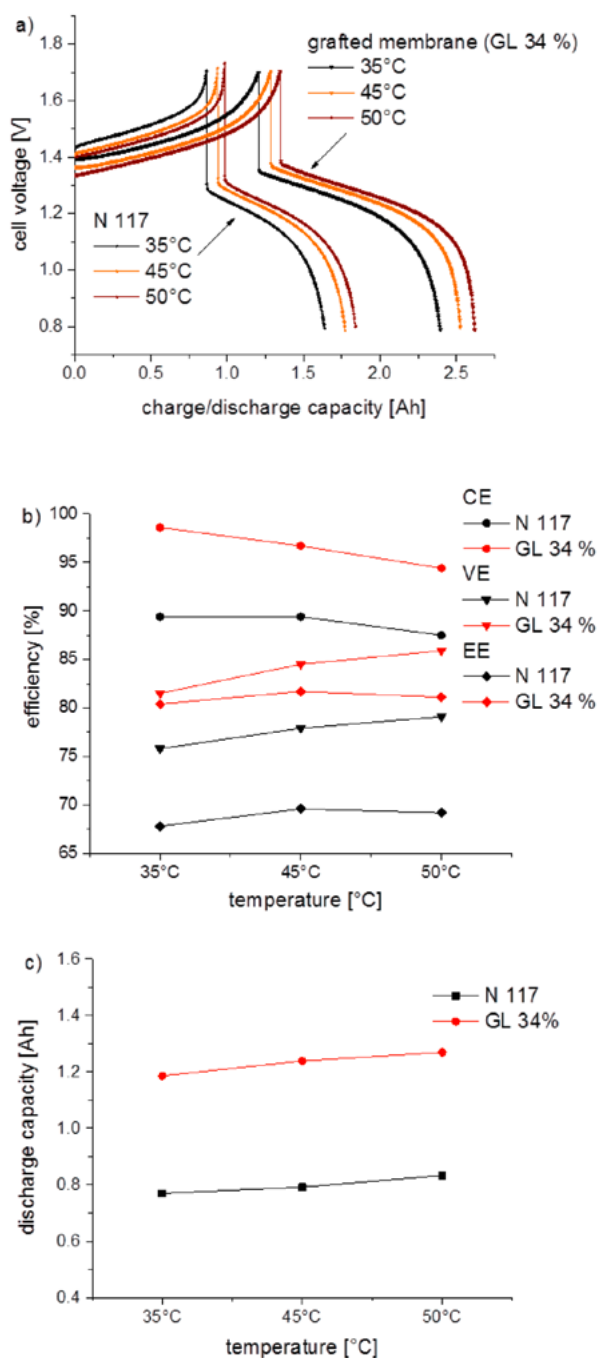


**Figure 2.** Charge/discharge cycling of the redox flow battery at a constant flow rate of 30 mL/min and a current density of 40 mA/cm<sup>2</sup> using 1.7 V as upper and 0.8 V as lower limit. 70 mL of 0.75 M vanadium solutions in 2 M H<sub>2</sub>SO<sub>4</sub> were used as negative and positive electrolyte, respectively. Nafion® 117 (N 117) or a radiation grafted membrane (GL 34%) was used as separator.

a) Charge-discharge curves measured at different temperatures.

b) Coulombic (CE), voltage (VE) and energy efficiency (EE) at different temperatures.

c) Discharge capacity at different temperatures (theoretical discharge capacity = 1.41 Ah).

Independent of the used membrane an increase in charging/discharging capacity could be observed at higher temperatures, whereas the cell with the radiation grafted membrane instead of Nafion® 117 showed superior cycling performance. Moreover, at higher temperatures discharging voltage increased while charging voltage decreased resulting in higher

overall voltage efficiency. Again the redox flow cell with a radiation grafted membrane showed higher voltage efficiency compared to the cell with Nafion® 117. However, not only positive but also negative effects could be observed by using higher operating temperatures. For instance, a decline in coulombic efficiency could be detected in case of redox flow cells with both membranes, whereas the redox flow battery with a radiation grafted membrane showed higher coulombic efficiency. Among the investigated temperatures, the redox flow cells with both membranes exhibited the highest energy efficiency at the operation temperature of 45 °C.

## Conclusion

It was shown that the cycling performance of the redox flow battery strongly depends on its operating conditions. Charge-discharge curves were measured at temperatures ranging from 35 °C to 50 °C. Two different membranes were used for this investigation, namely Nafion® 117 and a radiation grafted membrane containing protogenic sulfonic acid and amidoxime groups, which were shown to act as a vanadium barrier.

The same trends were observed in case of redox flow cells with different ion exchange membranes. At higher temperatures charging/discharging capacity and voltage efficiency improved, whereas the coulombic efficiency decreased. The energy efficiency of redox flow cells with both membranes increased by changing the operating temperature from 35 °C to 45 °C and decreased again at 50 °C. The redox cell with the radiation grafted membrane instead of Nafion® 117 always showed superior cycling performance.

In addition, the influence of the flow rate on the cycling performance was studied. The use of higher flow rates resulted in higher charging/discharging capacity. Also coulombic efficiency and voltage efficiency improved leading to higher overall energy efficiency.

## Acknowledgement

Funding by the Swiss National Science Foundation (Sinergia, project CRSII2\_147661) is gratefully acknowledged.

## References

- [1] G. Kear, A.A. Shah, F.C. Walsh, *Int. J. Energ. Res.* **36**, 1105–1120 (2012).
- [2] H. Prifti, A. Parasuraman, S. Winardi, T.M. Lim, M. Skyllas-Kazacos, *Membranes* **2**, 275–306 (2012).
- [3] K.J. Kim, M.-S. Park, Y.-J. Kim, J.H. Kim, S.X. Dou, M. Skyllas-Kazacos, *J. Mater. Chem.* **3**, 16913–16933 (2015).
- [4] L. Li, S. Kim, W. Wang, M. Vijayakumar, Z. Nie, B. Chen, J. Zhang, G. Xia, J. Hu, G. Graff, J. Liu, Z. Yang, *Adv. Energy Mater.* **1**, 394–400 (2011).
- [5] L. Gubler, O. Nibel, L. Bonorand, Patent Application No. EP 2015P01713, Paul Scherrer Institut, 2015.

# SCIENTIFIC ACHIEVEMENTS 2015

## ELECTROCATALYSIS & INTERFACES

## Activity and stability of high surface area IrO<sub>2</sub>

D. Abbott, D. Lebedev<sup>1</sup>, E. Fabbri, C. Copéret<sup>1</sup>, T.J. Schmidt

phone: +41 56 310 4323, e-mail: daniel.abbott@psi.ch

The development of cost-effective PEM electrolyzers is key to the implementation of a hydrogen-based infrastructure. The electrochemical conversion of water to hydrogen using excess energy generated from intermittent renewable sources, such as wind and solar, provides a rather attractive means of reducing society's dependency on fossil fuels [1]. Stored hydrogen can later be reclaimed using fuel cells to power anything from personal electronic devices to vehicles, while producing only water as a byproduct.

The cathodic generation of hydrogen from water splitting is known to be extremely facile on Pt-based catalysts. The simultaneous oxygen evolution reaction (OER) occurring at the anode, however, is limited by sluggish kinetics and requires a significant overpotential to achieve modest current densities. In addition, the harsh acidic environment and high anodic operating potentials limit the choice of stable electrocatalyst materials to those of the noble metal oxides. Reduction of the noble metal loading at the anode and enhancing catalyst stability for OER in PEM electrolyzers remain a challenge. The current approach considers reducing the catalyst particle size, increasing the electrochemically active surface area, and substituting the noble metals with inexpensive alternatives.

The research reported herein is focused on expanding the fundamental understanding of particle size effects. By decreasing the catalyst particle size one effectively increases the electrochemically active surface area, which generally corresponds to an overall increase in the electrochemical activity per gram of material. Therefore a synthetic protocol was developed, yielding a series of high surface area (HSA) IrO<sub>2</sub> catalyst materials, via a modified Adams Fusion Method. All materials were evaluated using a combination of N<sub>2</sub> adsorption, XRD, HRTEM, electrochemical methods, and XAS analysis.

### Experimental

Particle surface area and morphology are first evaluated using N<sub>2</sub> adsorption/desorption and HRTEM, respectively. The electrochemical activity and stability are then measured in a standard 3-electrode cell using the rotating disk electrode (RDE) methodology. Chronoamperometric measurements are used to record the steady-state polarization of each catalyst within the range of 1.0 to 1.6 V vs. RHE in 0.1 M HClO<sub>4</sub>. The current was recorded after allowing two minutes for stabilization. Accelerated catalyst stability tests are then performed by stepping the potential between 1.0 and 1.6 V and holding at 10 second intervals for 500 cycles.

### Results

The catalyst activities reported in Figure 1 are based upon the potential required to reach 10 A g<sup>-1</sup> of current density. The observed trend clearly shows the increasing electrochemical OER activity (lower overpotential required to reach the target current density) with increasing BET surface area. Although the BET surface area is not a direct measure of the available cata-

lytically active surface sites, it is evident that the electrochemical surface area increases monotonously with the measured increase in BET surface area.

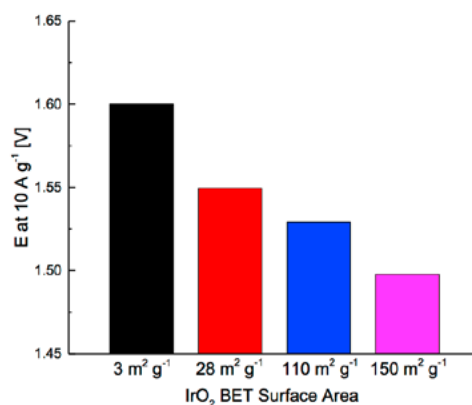


Figure 1. Activity of IrO<sub>2</sub> in 0.1 M HClO<sub>4</sub> based on steady-state chronoamperometric measurements.

The stability of the IrO<sub>2</sub> catalysts was measured over the course of 500 potential cycles. As can be seen in Figure 2, there is no direct correlation between the catalyst stability and the BET surface area when considering the range of uncertainty for each sample. Further insight will be gained from HRTEM images that depict the distinct morphology of each catalyst sample, which may play an important role in the apparent catalyst stability. In addition, *in situ* X-ray absorption (XAS) measurements will be used to help elucidate the development of the electronic surface structure as the particle size and cathode polarization are varied.

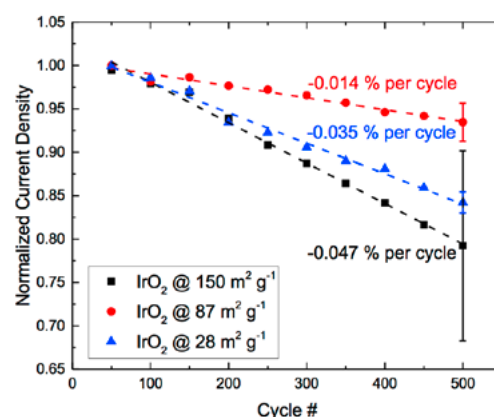


Figure 2. Stability of HSA IrO<sub>2</sub> measured in 0.1 M HClO<sub>4</sub>.

### Acknowledgement

The authors gratefully acknowledge the financial support from CCEM, CTI & SCCER Heat and Electricity Storage.

### References

- [1] M. Carmo, D.L. Fritz, J. Mergel, D. Stolten, *Int. J. Hydrogen Energy*, **38**, 4901–4934 (2013).

<sup>1</sup> ETH Zürich, Department of Chemistry and Applied Biosciences

## Oxygen evolution reaction on $\text{Ba}_{0.5}\text{Sr}_{0.5}\text{Co}_{0.8}\text{Fe}_{0.2}\text{O}_{3-\delta}$ perovskite

E. Fabbri, X. Cheng, M. Nachtegaal, T.J. Schmidt  
 phone: +41 56 310 2795, e-mail: emiliana.fabbri@psi.ch

Alkaline water electrolyzers (AWEs) are electrochemical energy conversion devices able to produce  $\text{H}_2$  and  $\text{O}_2$  from external energy sources with relatively high efficiency [1]. The potential of AWEs can be particularly exploited within an energy economy based on renewable energies, which have an intermittent nature and, thus, require excellent storage capabilities. This can be offered by AWEs, since the excess of energy can be efficiently converted in  $\text{H}_2$  (and  $\text{O}_2$ ), and stored for long time. One of the limitations of AWEs is the high overpotential associated with the oxygen evolution reaction (OER) that takes place at the anode side of AWEs.

Perovskite oxides have recently shown outstanding activities for the OER in alkaline environment [1]. Particularly, composite electrodes made of perovskites and carbon have shown the most promising OER performance compared to electrodes made of only perovskite powder [2, 3]. By using X-ray absorption near edge structure spectroscopy (XANES) we show here that changes in the local electronic structure of the perovskite are induced by processing the perovskite with carbon black, affecting the OER activity of the electrode. This finding provides a novel understanding of perovskite/carbon composite electrodes, addressing new perspectives for tailoring more active perovskite-based OER catalysts.  $\text{Ba}_{0.5}\text{Sr}_{0.5}\text{Co}_{0.8}\text{Fe}_{0.2}\text{O}_{3-\delta}$  (BSCF) is the selected catalyst for this study, since this perovskite has shown promising OER activity in combination with carbon but not as a single perovskite catalyst.

### Experimental

BSCF powders were synthesized using a modified sol–gel process [3]. The electrodes were prepared as reported in ref [3]. The electrochemical measurements were performed in 0.1 M KOH in a homemade Teflon cell using a hydrogen reference electrode (RHE) and a gold counter electrode. The OER activity was determined by chronoamperometry measurements holding each potential for 30 s in  $\text{O}_2$ -saturated electrolyte and 1600 rpm. Prior to the OER measurements, 15 reverse scan sweeps between 1 and 1.7 V (RHE) at  $10 \text{ mVs}^{-1}$  in  $\text{O}_2$ -saturated electrolyte were performed. All reported potentials are ohmic drop corrected.

### Results

Figure 1a shows the Tafel plots for BSCF single material electrode and BSCF/Acetylene black (AB) composite electrode. BSCF/AB displays a significant higher OER activity than BSCF. Considering the potential reached at  $10 \text{ A/g}_{\text{metal}}$ , BSCF/AB displays a potential of  $1.55 \pm 0.012 \text{ V}$ , which is about 100 mV lower than that of BSCF.

XANES spectra at the Sr, Fe, Co K-edges and Ba L1 edge were recorded for the BSCF and the BSCF/AB electrode, prepared in the same way as for the electrochemical. While identical spectra were recorded for the Sr, Fe, and Ba absorption edges [3], a clear shift in the Co K-edge toward lower energies was observed for BSCF/AB compared to BSCF, as shown in Figure 1b. Co K-edge spectra were also recorded for reference samples such as  $\text{Co}_3\text{O}_4$  and CoO, showing that while the Co K-edge of

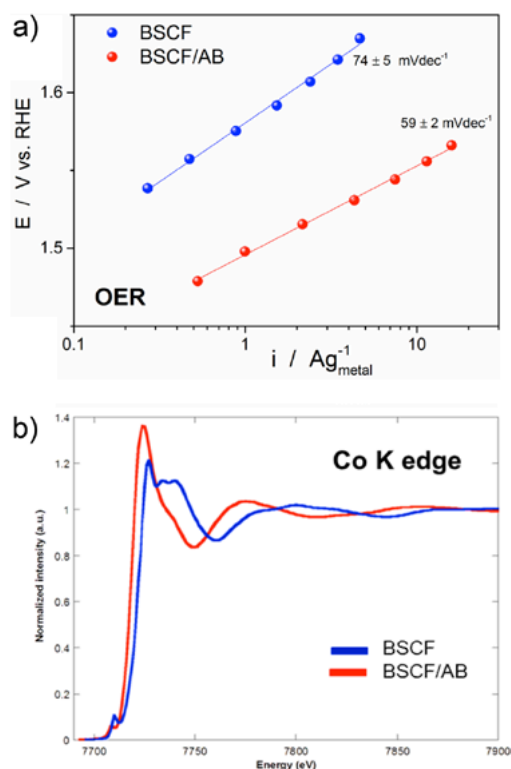


**Figure 1.** Tafel plots for BSCF and BSCF/AB electrodes recorded by chronoamperometric measurements (a). XANES spectra at Co K edge for BSCF and BSCF/AB electrode, prepared as for the electrochemical measurements (b). Figures reproduced by permission of John Wiley & Sons, Ltd., from ref. [3].

BSCF corresponds to that of  $\text{Co}_3\text{O}_4$ , BSCF/AB displays an adsorption edge much closer to that of CoO [3]. These results indicate that the mean oxidation state of the Co cations is lower in BSCF/AB than in BSCF electrode, unravelling for the first time that a direct interaction between the BSCF catalyst and the carbon occurs, which can account for the improved OER activity of the composite electrodes compared to single perovskite catalysts.

### Acknowledgement

The authors gratefully acknowledge the Ambizione Program of the Swiss National Science Foundation for financial contributions and the Swiss Light Source for providing beamtime at the SuperXAS beamline.

### References

- [1] E. Fabbri, A. Haberer, K. Waltar, R. Kötter, T.J. Schmidt, *Catal. Sci. Technol.* **4**, 3800–3821 (2014).
- [2] R. Mohamed, X. Cheng, E. Fabbri, P. Levecque, R. Kötter, O. Conrad, T.J. Schmidt, *J. Electrochem. Soc.* **162**, F579–F586 (2015).
- [3] E. Fabbri, M. Nachtegaal, X. Cheng, T.J. Schmidt, *Adv. Energy Mater.* **5** (5), 1402033 (2015).

## Compared stability of carbon-supported Pt-nanoparticles vs. unsupported Pt-aerogels for O<sub>2</sub>-reduction in PEFCs

J. Herranz, W. Liu<sup>1</sup>, S. Henning, A. Eychmüller<sup>1</sup>, T.J. Schmidt

phone: +41 56 310 5562, e-mail: juan.herranz@psi.ch

State-of-the-art electrocatalysts for the O<sub>2</sub>-reduction reaction (ORR) taking place inside polymer electrolyte fuel cells (PEFCs) consist of Pt-nanoparticles (NPs) supported on a high-surface area carbon black (Pt/C). This carbon support grants the large extents of Pt-nanoparticle dispersion (with surface areas of up to  $\approx 100 \text{ m}_{\text{metal}}^2 \cdot \text{g}_{\text{metal}}^{-1}$ ) and reactant/product-transport required to achieve optimum PEFC performance, but also suffers from severe corrosion during the potential cycles intrinsic to the device's operation [1]. One approach to overcome this issue relies on the development of unsupported electrocatalysts that can be prepared, e.g., by following a NP-destabilization and gelation procedure that yields so-called aerogels with high degrees of nanoparticle dispersion [2, 3]. In an effort to verify the validity of this strategy, in this work we have used rotating disk electrode (RDE) voltammetry to compare the stability of a Pt-aerogel with that of a commercial Pt/C-catalyst. As it will be shown in the following, the use of potential cycling protocols that mimic the start/stop cycles in a PEFC [4] did not yield the expected stability advantage of the aerogel over the carbon-supported material. We speculate that this result arises from the greater extent of Pt-dissolution undergone by the aerogel, in terms motivated by the  $\approx 20$ -fold thinner catalytic layer compared to the Pt/C-benchmark.

### Experimental

The Pt-aerogel was synthesized at TU-Dresden following procedures described elsewhere [2]. In brief, the volume of a 40 mM NaBH<sub>4</sub> solution needed for a final concentration of 0.3 mM was added to a 0.2 mM solution of K<sub>2</sub>PtCl<sub>4</sub>. After stirring for  $\approx 30$  min and leaving to set for  $\approx 17$  days, a hydrogel was formed at the bottom of the flask. Following repeated washing with water, the supernatant was stepwise exchanged with acetone (over  $\approx 3$  days) and transferred into the chamber of a critical point dryer flushed with liquid CO<sub>2</sub>. After repeating the flushing procedure once and sealing the pressure chamber, the temperature was increased above the critical point of carbon dioxide ( $\approx 36$  °C) and the pressure built in the chamber ( $> 70$  bar) was slowly released, yielding highly porous aerogel monoliths. The 30 %wt Pt/C benchmark catalyst was provided by E-TEK.

Catalyst inks for electrochemical characterization using the thin film rotating disc electrode (TF-RDE) voltammetry technique [5, 6] were prepared by mixing a known mass of catalyst with ultrapure water (18.2 M $\Omega$ -cm, ELGA PureLab) and isopropanol (Chromasolv<sup>®</sup> grade, Sigma Aldrich). Following sonication, the volume of ink required for a Pt-loading of  $30 \mu\text{g}_{\text{Pt}} \cdot \text{cm}_{\text{geom}}^{-2}$  was pipetted atop a mirror-polished, 5 mm glassy carbon disc embedded in an interchangeable rotating ring-disc electrode (Pine Research Instrumentation). The latter was then screwed onto a PEEK shaft mounted in a rotator (Pine Research Instrumentation) and subsequently immersed in the electrochemical glass cell in which all the measurements were performed. The latter had been previously filled with 0.1 M HClO<sub>4</sub> (prepared from high purity, 60 % HClO<sub>4</sub> – Kanto Chemical co., Inc.) and included a (shielded) gold mesh and a reversible hydrogen electrode (RHE) as the counter

and reference electrodes, respectively. All subsequent cyclic voltammograms (CVs), polarization curves and electrochemical impedance spectra were acquired using a Biologic VSP-300 potentiostat.

### Results

As revealed by transmission electron microscopy (TEM, not shown), the Pt-aerogel consists of a tridimensional network of interconnected nanoparticles with an average diameter of  $4 \pm 1$  nm, along with larger, randomly distributed particles of size  $> 10$  nm. As a result of this structure, the aerogel's electrochemical surface area (ECSA, derived from the hydrogen underpotential deposition charge estimated by cyclic voltammetry) is  $\approx 30 \text{ m}_{\text{metal}}^2 \cdot \text{g}_{\text{metal}}^{-1}$ , similar to that of the Pt/C-benchmark.

The stability of these materials within a potential cycling protocol that mimics the start/stop events concomitant to PEFC-operation was determined by recording up to 2'000 cycles between 0.5 and 1.5 VRHE (at  $50 \text{ mV} \cdot \text{s}^{-1}$  and with the electrode rotating at 100 rpm). Periodically along these cycles, the catalysts' ECSA and ORR-activity were assessed by recording CVs (at  $20 \text{ mV} \cdot \text{s}^{-1}$ ) or polarization curves (at  $5 \text{ mV} \cdot \text{s}^{-1}$  and 1'600 rpm) in N<sub>2</sub>- or O<sub>2</sub>-saturated electrolyte, respectively. The results of these tests are displayed in Figure 1, whereby both catalysts are shown to undergo a similar loss of Pt-area upon potential cycling (cf. Figure 1a).

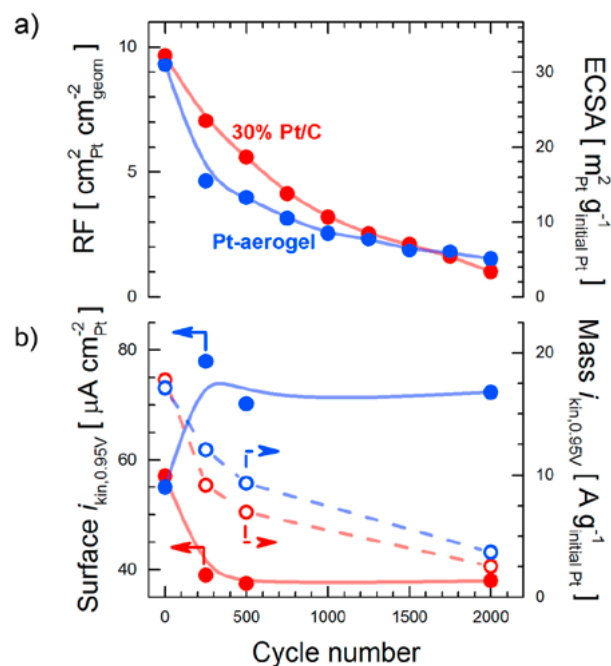


**Figure 1.** Evolution of the roughness factor (RF) or ECSA (on the basis of the initial Pt-loading) (a), and of the surface- or mass-normalized ORR-activity (b) during the start/stop protocol (E-cycling between 0.5 and 1.5 VRHE at  $50 \text{ mV} \cdot \text{s}^{-1}$ , 100 rpm).

<sup>1</sup> Technische Universität Dresden, Dresden, Germany

On the other hand, Figure 1b reveals that, even if the mass-normalized ORR-activity of both catalysts also decreased similarly upon cycling, the surface-specific activity of the aerogel increased within the first  $\approx 500$  cycles, while that of Pt/C decreased. Considering that this surface normalized ORR-activity is inversely proportional to the ECSA [1, 7], this behaviour points at different mechanisms of Pt-loss upon potential cycling.

In an attempt to clarify this behaviour, the durability tests also included periodical CO-stripping measurements that can provide qualitative information concerning the catalysts' particle size, since carbon monoxide gets preferentially oxidized (i.e., at lower potentials) on larger particles [8]. With this consideration in mind, the CO-stripping results in Figure 2a would indicate that smaller NPs are the main contributor to Pt-loss in the Pt/C-benchmark; in the case of the aerogel (cf. Figure 2b), however, all NP-sizes appear to be affected by Pt-dissolution and detachment in a resembling extent. *Post-mortem* TEM analysis of these aged catalysts should help to verify the validity of this hypothetical explanation and draw a clearer link with the ORR-activity loss described above.

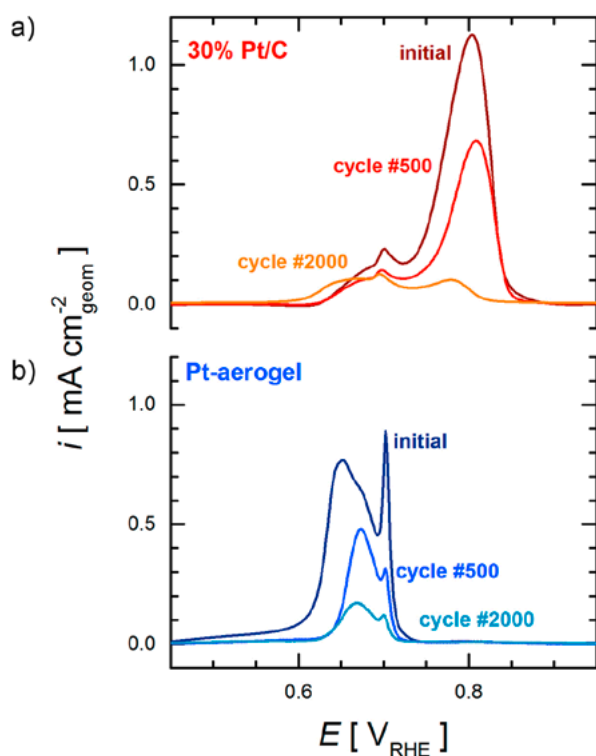


**Figure 2.** Evolution of the CO-stripping profiles (at  $20 \text{ mV s}^{-1}$ , background subtracted) of the Pt/C-benchmark and the Pt-aerogel (top and bottom panels, respectively) during the start/stop durability protocol.

Beyond these mechanistic considerations, the similarity between the durability trends displayed by both catalysts may appear as striking when considering the absence of a corrodible carbon support in the Pt-aerogel. Tentatively, we assign this apparent resemblance to the marked differences in the catalysts' film thicknesses; on the basis of the Pt-loading of  $30 \mu\text{g}_{\text{Pt}}\text{cm}^{-2}_{\text{geom}}$  in both RDE-tests, along with the catalysts' densities (i.e.,  $22 \text{ g cm}^{-3}$  for Pt-aerogel vs.  $2 \text{ g cm}^{-3}$  for Pt/C) and an assumed film porosity of 50% [5, 6], these can be estimated to  $\approx 0.03$  and  $\approx 0.7 \mu\text{m}$  for the Pt-aerogel and Pt/C, respectively. As a result, the Pt dissolving and/or detaching from the Pt-aerogel is significantly more likely to get lost in the

surrounding electrolyte than in the case of Pt/C, for which diffusion along the  $\approx 1 \mu\text{m}$  film can become relevant [7, 8]. As discussed above, though, the validity of this explanation should be verified with complementary, *post-mortem* analysis of the electrode films using TEM, along with quantification of the Pt-concentration in the electrolyte during the cycling protocol.

## Conclusions and Outlook

The durability of Pt-aerogel and Pt/C ORR-catalysts with similar ECSAs was assessed following an RDE-based potential cycling protocol that mimics start/stop PEFC events. The somehow unexpected similarity between the stability trends displayed by both materials is tentatively assigned to differences in the catalyst layer thicknesses, which negatively impacts the durability of the Pt-aerogel. Beyond the verification of this hypothesis using *post-mortem* TEM, more meaningful durability tests in an actual PEFC need to be performed in order to assess the viability of these materials for their envisaged application.

## Acknowledgement

Financial support from SNF (20001E\_151122/1) and DFG (EY 16/18-1) is greatly acknowledged.

## References

- [1] A. Rabis, P. Rodríguez, T.J. Schmidt, *ACS Catal.* **2**, 864 (2012).
- [2] W. Liu, P. Rodríguez, L. Borchardt, A. Foelske, J. Yuan, A.-K. Herrmann, D. Geiger, Z. Zheng, S. Kaskel, N. Gaponik, R. Kötz, T.J. Schmidt, A. Eychmüller, *Angew. Chem. Int. Ed.* **52**, 9849 (2013).
- [3] W. Liu, A.-K. Herrmann, N.C. Bigall, P. Rodríguez, D. Wen, M. Özaslan, T.J. Schmidt, N. Gaponik, A. Eychmüller, *Acc. Chem. Res.* **48**, 154 (2015).
- [4] C.A. Reiser, L.J. Bregoli, T.W. Patterson, J.S. Yi, J.D. Yang, M.L. Perry, T.D. Jarvi, *Electrochem. Solid-State Lett.* **8**, A273 (2005).
- [5] T.J. Schmidt, H.A. Gasteiger, G.D. Stab, P.M. Urban, D.M. Kolb, R.J. Behm, *J. Electrochem. Soc.* **145**, 2354 (1998).
- [6] U.A. Paulus, T.J. Schmidt, H.A. Gasteiger, R.J. Behm, *J. Electroanal. Chem.* **495**, 134 (2001).
- [7] E. Fabbri, S. Taylor, A. Rabis, P. Leveque, O. Conrad, R. Kötz, T.J. Schmidt, *ChemCatChem* **6**, 1410 (2014).
- [8] F. Maillard, S. Pronkin, E.R. Savinova, in *Handbook of Fuel Cells: Fundamentals, Technology and Applications* **5**, W. Vielstich, H.A. Gasteiger, H. Yokokawa, Editors, p. 91, John Wiley & Sons, New York (2009).

## Pt coverage of model catalysts: active vs inactive area and its consequences on ORR limiting currents in a flow cell

N. Poyatos Salguero, S.A. Tschupp, S.E. Temmel, T.J. Schmidt

phone: +41 56 310 4580, e-mail: noemi.poyatos@psi.ch

Currently, efficient state-of-the-art fuel cell catalysts are platinum-based materials, which are too expensive to be commercialized. Therefore, for the purpose of establishing competitive electrochemical energy conversion systems, a lot of effort has been invested in developing catalysts with high activity and stability and improved electrochemical performance [1]. In order to establish design principles for more efficient electrocatalysts, fundamental understanding of the key parameters governing electrochemical reactions is required. These are most often easier to study on simple model catalysts than in the full scale system.

One of the most important parameters in heterogeneous catalysis, especially in electrocatalysis, is the accessible surface area of the catalyst or electrode, which will determine the catalyst activity [2]. Electrochemical reactions are based on the charge transfer at the electrode-electrolyte interface. So the reaction rate, and consequently the electric current, is proportional to the electrode's accessible surface area. As soon as the applied potential is high enough to obtain the maximum reaction rate, the process is limited by mass-transfer. The limit is indicated by a current plateau (the limiting current) on a current versus applied potential (I-V) plot. The value of the limiting current  $I_{lim}$  can be determined by this general equation [3]:

$$I_{lim} = n F A \frac{D}{\delta} c_{bulk} \quad (\text{Equation 1})$$

$n$  describes the number of electrons transferred,  $F$  the Faraday constant in  $\text{C mol}^{-1}$ ,  $A$  the geometric area of the electrode exposed to electrolyte in  $\text{cm}^2$ ,  $c_{bulk}$  the bulk concentration of the reactants in  $\text{mol cm}^{-3}$ ,  $\delta$  the thickness of the Nernst diffusion boundary layer in cm and  $D$  the diffusion coefficient of the reacting species in  $\text{cm}^2 \text{s}^{-1}$ .

However, the geometric area  $A$  exposed to electrolyte is a controversial parameter that should be well-defined depending on the electrode performance. Since it is not always possible to design model catalysts with homogeneous surface, the presence of surface inhomogeneities due to nanoparticles, not active materials parts, holes, kinks, and terraces can result in an electrode accessible surface area that is larger or smaller than the geometric one. In these cases, a comparison of the  $I_{lim}$ , and in turn, of the kinetic activity between such electrodes might not be straightforward.

The samples used as electrodes in this study are titanium (Ti) thin films samples covered by platinum (Pt) squares of different sizes resulting in different coverages of the Ti with Pt. Here the geometric area does not correspond to the accessible surface area as Ti is not active towards the reaction that has been studied. The main purpose of the present work is to gain further understanding of the relation between Pt coverage and its limiting current in a wall-jet flow cell. Despite the fact that mass transfer limiting currents can be observed in most electrochemical reactions, we focus on oxygen reduction reaction (ORR).

### Experimental

Electrodes were made by a lift-off process. First,  $10 \times 10 \text{ mm}^2$  silicon (Si) chips were coated with an e-beam evaporated Ti layer of 50 nm thickness. Then, by UV lithography, patterns consisting of 52 square holes were transferred from a photo-mask to a photoresist film on the chips. In the second step, a 2 nm Ti/20 nm Pt bilayer was deposited again by electron beam evaporation. Finally, the photoresist was removed by acetone. By variation of the squares' side lengths  $L$  (370, 430 and 530  $\mu\text{m}$ ), different Pt coverages from 40% to 100% were obtained. The distance between the centres of squares is 600  $\mu\text{m}$ . The different sizes of the Pt-squares were verified by microscope as shown in Figure 1b.

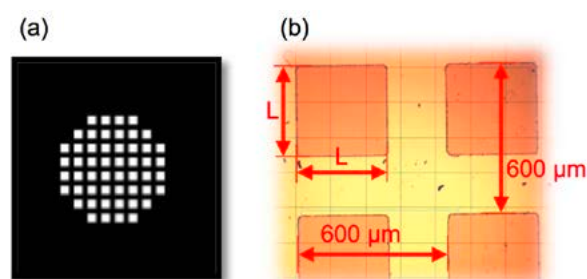


**Figure 1.** a) Mask pattern, where the color black corresponds to the Ti layer and white to Pt for the final samples. b) Microscope image at 5x magnification. Pt squares (orange) are shown on Ti background (yellow).  $L$  describes the side lengths used for each chip; here,  $L = 370 \mu\text{m}$ . Grid scale is  $140 \mu\text{m}$ . Period is  $600 \mu\text{m}$ .

An in-house designed flow cell utilizing a three-electrode setup was used to record the ORR polarization curves. A platinumized Pt wire served as counter electrode. A Hg/Hg<sub>2</sub>SO<sub>4</sub> (ALS Co., Ltd.) electrode was used as a reference. However, for convenience, all electrode potentials are reported with respect to the reversible hydrogen electrode (RHE). A solution of 0.5 M sulfuric acid was used as electrolyte.

The samples were soaked in 1 M sulfuric acid overnight before being tested. Before connecting the potentiostat, 50 mL of N<sub>2</sub>-saturated electrolyte was flushed through the assembled cell. Then the catalyst was cleaned by potential cycling between 0.05 and 1 V for 50 cycles (15 cycles at  $100 \text{ mV s}^{-1}$ , 35 cycles at  $50 \text{ mV s}^{-1}$ ). A cyclic voltammogram (CV) was then recorded at  $50 \text{ mV s}^{-1}$  to assess the cleanliness and the saturation of the cell. Subsequently, ORR polarization curves were recorded at room temperature in oxygen saturated electrolyte at flow rates varying from 0.1 to  $2 \text{ mL min}^{-1}$  at  $10 \text{ mV s}^{-1}$  and from 5 to  $7.5 \text{ mL min}^{-1}$  at  $50 \text{ mV s}^{-1}$ .

### Results

Polarization curves for various flow rates have been obtained for each electrode with different Pt surface coverage. In all cases, it can be clearly seen that flow rate dependent current plateaus are reached below 0.5 V indicating mass transfer limitation (Figure 2).

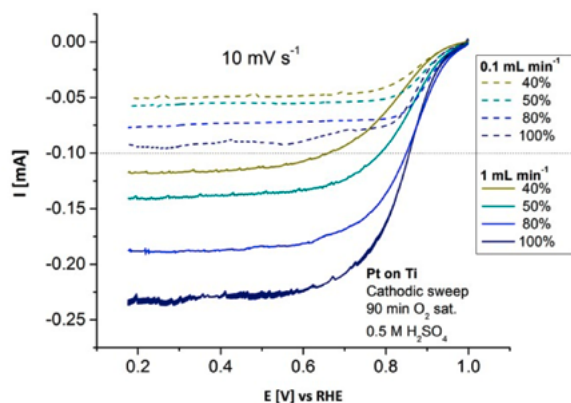


**Figure 2.** ORR polarization curves for different Pt coverages at two different flow rates ( $0.1 \text{ mL min}^{-1}$  and  $1 \text{ mL min}^{-1}$ ).

Limiting current density per geometric area ( $A_{\text{geo}}$ ) – including the inactive Ti – plotted versus the flow rate for different coverages is shown in Figure 3.

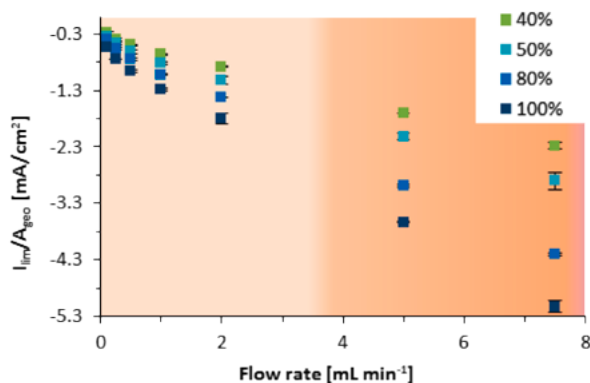


**Figure 3.** Limiting current density (per geometric area) as function of flow rate for several Pt coverage electrodes.

Per definition (Equation 1), the limiting current (density) depends on  $A_{\text{geo}}$  and not on the active catalyst area. Despite this fact, we observe a linear relation between the Pt coverage and  $I_{\text{lim}}/A_{\text{geo}}$  – the lower the Pt coverage, the smaller the limiting current.

It is, therefore, interesting to analyse the limiting current density as function of the active Pt surface area ( $A_{\text{calc}}$ ) – excluding the inactive Ti – for a constant flow rate of  $1 \text{ mL min}^{-1}$  (Figure 4).

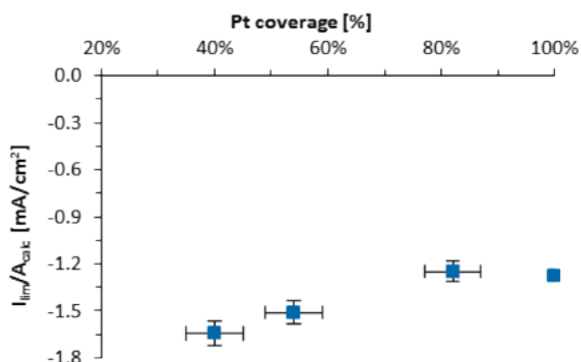


**Figure 4.** Limiting current density (per calculated Pt surface area) as a function of Pt coverage at constant flow rate ( $1 \text{ mL min}^{-1}$ ).

Theoretically, the values of the newly defined current density in this graph should be independent of Pt coverage, only related to the flow rate – a certain error remains though. We attribute the y-axis error bar to uncertainties in the determination of the covered area and accuracy of the electrochemical experiments (ORR polarization curves) regarding small coverage differences. Another reason might be the non-uniform current density distribution resulting from the wall-jet geometry of our measurement system.

## Conclusions

The dependence of the diffusion-limited current on the flow rate demonstrates the stability and good conductivity of the electrodes in the mass transport region.

The correlation between the limiting current density and Pt surface area indicates that surface area  $A$  as defined in Equation 1 for the limiting current  $I_{\text{lim}}$  should be treated carefully, especially for samples not covered homogeneously (e.g. model catalysts). We have shown that for these systems  $A$  cannot be treated as geometrical area (Figure 3). Using assumptions to evaluate the accessible area  $A$  improves the assessment (Figure 4). Consequently, in the next steps we aim to confirm this assumption by modelling and derive a correlation between  $I_{\text{lim}}$  and the flow rate for the future determination of the kinetic activity.

## Acknowledgement

We thank our colleagues of the Electrocatalysis and Interfaces group for productive discussions and technical assistance.

## References

- [1] A. Rabis, P. Rodriguez, T.J. Schmidt, *ACS Catal.* **2**, 864 (2012).
- [2] J.M. Smith, *Chemical Engineering Kinetics*, 3<sup>rd</sup> ed., McGraw-Hill, New York, 383 (1986).
- [3] A.R. Mount, in *Encyclopedia of Electrochemistry*, Wiley-VCH, Weinheim, 134 (2007).

## Oxide supported Pt catalyst for low temperature polymer electrolyte fuel cell application in MEAs: performance and stability

A. Pătru, E. Fabbri, A. Rabis, S. Temmel, R. Kötz, T.J. Schmidt

phone: +41 56 310 2318, e-mail: alexandra.patru@psi.ch

One of the major drawbacks for the fuel cell commercialisation is related to its components stability. The degradation of the cathode catalyst in low temperature polymer electrolyte fuel cells (PEFC) is a well known phenomenon especially when carbon support Pt catalyst is used. In order to increase the catalyst stability, alternative supports with improved stabilities and electronic conductivities are needed. Conductive metal oxides appear as good candidates for catalyst support use as they exhibit a high electrochemical stability and a high conductivity when used in their higher oxidation states [1].

Up to date, promising results are reported in the literature when new oxide support catalysts are used [2]. Most of the reported stability studies of these catalysts are realised at laboratory level, under conditions far from real operating ones (typically room temperature, variable stability protocols and non-optimised catalytic layer). Only few data are available regarding the stability of this catalyst generation in a PEFC under real working conditions.

In the present study the stability of a model oxide catalyst support (Pt/IrO<sub>2</sub>-TiO<sub>2</sub>) was followed in a fuel cell operation regime.

### Experimental

47 %wt Pt/C (EC10E50ETKK) and 8.9 %wt Pt/IrO<sub>2</sub>-TiO<sub>2</sub> catalysts were employed. For each catalyst different ink compositions were prepared and sprayed directly on a Nafion® XL 100 membrane until a loading of ~0.4 mg<sub>Pt</sub>/cm<sup>2</sup> was reached for the cathode side. For the anode side Pt/C catalyst was always used. The final membrane electrode assemblies (MEAs) were built by hot-pressing the prepared catalyst coated membrane (CCM) and two gas diffusion layers (Sigracet® 24 BC SGL Carbon) at 120 °C for 1 minute under a defined pressure of 0.1 MPa.

The MEAs were tested in a single test cell (29.16 cm<sup>2</sup> geometric area). Air was used as cathode reactant with  $\lambda_{\text{air}} = 2$  and pure hydrogen was used as anode reactant with  $\lambda_{\text{H}_2} = 2$ . The polarization curves were measured galvanostatically for a T = 80 °C cell temperature, full humidification and 1.5 bar<sub>abs</sub> pressure.

MEAs stability was tested using specific Accelerated Stress Test protocol (AST) developed by the US Department of Energy's (DOE) Fuel Cell program [3, 4]. For catalyst stability, i.e. platinum nanoparticles stability, a first AST protocol was applied. In a standard manner a triangular potential cycling at 50 mV/s between 0.6 and 1 V vs RHE (16 seconds per cycle) was applied to the cathode. For the evaluation of support stability another AST protocol (start-stop protocol) was used. The air electrode (cathode) potential was cycled between 1 and 1.5 V vs RHE at a scan rate of 500 mV/s (2 seconds per cycle). 10'000 cycles were recorded on a fresh MEA at 80 °C, 100% relative humidity (RH), atmospheric pressure, with pure hydrogen on the anode side (200 sccm) and nitrogen at the air side (75 sccm).

The *in situ* Pt electrochemical surface area (ECSA) was estimated by cyclic voltammetry when Pt/C was used as catalyst and by a modified CO stripping method when Pt/IrO<sub>2</sub>-TiO<sub>2</sub> was used [5].

### Results

The stability of the two catalysts was examined *in situ* with the two protocols described above. These protocols are simulating the catalyst behaviour during vehicle acceleration and deceleration and during vehicle start-up and shut-down, respectively, triggering platinum dissolution and support corrosion.

MEA	Pt loading, mg <sub>Pt</sub> /cm <sup>2</sup>	ECSA, m <sup>2</sup> <sub>Pt</sub> /g <sub>Pt</sub>	Voltage losses @ 0.8 A/cm <sup>2</sup>
Pt/C BOT	0.39	45	-
Pt/C EOT	0.39	17	100
Pt/IrO <sub>2</sub> -TiO <sub>2</sub> BOT	0.45	43	-
Pt/IrO <sub>2</sub> -TiO <sub>2</sub> EOT	0.45	-	100

**Table 1.** Catalyst characterization and catalytic performances of the CCMs based on Pt/C and Pt/TiO<sub>2</sub>-IrO<sub>2</sub> obtained at the beginning of test (BOT) and end of test (EOT) when AST protocol was applied.

Figure 1 shows the comparison of the fuel cell performances at the beginning and end of AST protocol for both catalysts. The initial performances are comparable in both cases. These results show that, when using a conductive oxide support with a good MEA design, similar performances can be reached. Moreover, the initial ECSA values were very close in both cases.

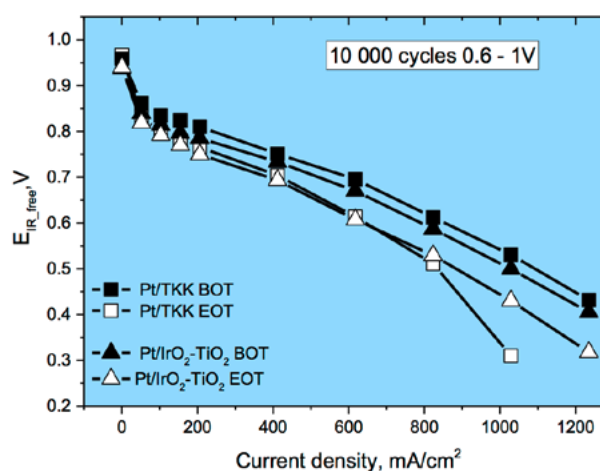


**Figure 1.** Comparison of H<sub>2</sub>-air polarization curves obtained with Pt/C and Pt/TiO<sub>2</sub>-IrO<sub>2</sub> catalyst at the beginning of test (BOT) and at the end of test (EOT) after exposure to catalyst accelerated stress protocol (10'000 cycles). T = 80 °C, p = 1.5 bar<sub>abs</sub>, 100% RH,  $\lambda_{\text{H}_2} = 2$ ,  $\lambda_{\text{air}} = 2$ .

The voltage loss at  $0.8 \text{ A/cm}^2$  gives a good estimation for the overall stability of the assembly, including information about the catalyst kinetics and the mass transport losses. These values are grouped in Table 1. The voltage losses at  $0.8 \text{ A/cm}^2$  are around 100 mV for both MEAs. The EOT data suggest that the corrosion resistance of platinum phase is not improved by the alternative support when compared to the carbon supported catalyst.

MEA	Pt loading, $\text{mg}_\text{Pt}/\text{cm}^2$	ECSA, $\text{m}^2_\text{Pt}/\text{g}_\text{Pt}$	Voltage losses @ $0.8 \text{ A/cm}^2$
Pt/C BOT	0.4	49	-
Pt/C EOT	0.4	8	670
Pt/IrO <sub>2</sub> -TiO <sub>2</sub> BOT	0.42	42	-
Pt/IrO <sub>2</sub> -TiO <sub>2</sub> EOT	0.42	-	25

**Table 2.** Catalyst characterization and catalytic performances of the CCMs based on Pt/C and Pt/TiO<sub>2</sub>-IrO<sub>2</sub> obtained at the beginning of test (BOT) and end of test (EOT) when start-stop protocol was applied.

Figure 2 shows the polarization curves obtained on MEAs based on the two catalysts studied here, before and after exposure to the start-stop protocol. The Pt/C-based MEA revealed a significant loss in performance, whereas the Pt/IrO<sub>2</sub>-TiO<sub>2</sub>-based MEA showed a minimal loss in performance after exposure to 10'000 cycles. The loss in cell voltage at  $0.8 \text{ A/cm}^2$  was only about 25 mV for Pt/IrO<sub>2</sub>-TiO<sub>2</sub>, whereas for Pt/C, the loss was too high to maintain operation at this current density (data shown in Table 2). These observations can be attributed to the excellent stability of IrO<sub>2</sub>-TiO<sub>2</sub> when used as catalyst support.

At the end of the start-stop protocol the significant losses of performance are accompanied by important losses of ECSA (84 % in the case of MEA based on Pt/C). In the case of Pt/IrO<sub>2</sub>-TiO<sub>2</sub> catalyst the quantitative losses of ECSA were impossible to estimate for reasons described elsewhere [6].

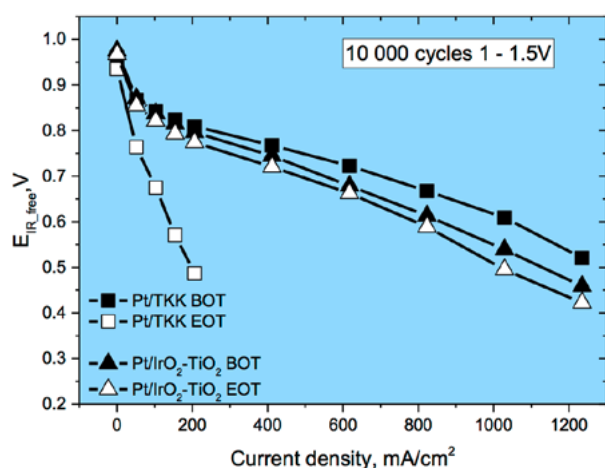


**Figure 2.** Comparison of H<sub>2</sub>-air polarization curves obtained with Pt/C and Pt/TiO<sub>2</sub>-IrO<sub>2</sub> catalyst at the beginning of test (BOT) and at the end of test (EOT) after exposure to start-stop protocol (10'000 cycles).  $T=80 \text{ }^\circ\text{C}$ ,  $p=1.5 \text{ bar}_{\text{abs}}$ ,  $100\% \text{ RH}$ ,  $\lambda_{\text{H}_2}=2$ ,  $\lambda_{\text{air}}=2$ .

## Conclusions

The electrochemical stability of a new catalyst generation, Pt supported on IrO<sub>2</sub>-TiO<sub>2</sub>, was investigated using *in situ* PEFC tests. It was shown that similar fuel cell performances can be achieved when using a conductive oxide catalyst support and a simple MEA optimization approach.

When the catalysts were subjected to the AST protocol in both cases, Pt/C and Pt/IrO<sub>2</sub>-TiO<sub>2</sub>, Pt dissolution and agglomeration showed a minimal impact on the fuel cell performances and the behavior of both tested MEAs were similar. This result suggests that the stability of the support is critical for PEFC operation compared to the stability of platinum nanoparticles. Consequently, the identification of a corrosion-resistant and inexpensive support is a key priority for the commercialization of fuel cells. All these pieces of information will be used as a starting point for the introduction of the next catalyst support generation based on SnO<sub>2</sub>.

## Acknowledgement

The authors thank Umicore AG&Co. KG and the Competence Center for Energy and Mobility (CCEM) of Switzerland for their financial support within the DuraCat project.

## References

- [1] E. Fabbri, A. Rabis, R. Kötz, T.J. Schmidt, *Phys. Chem. Chem. Phys.* **16**, 13672–13681 (2014).
- [2] Y. Takabatake, Z. Noda, S.M. Hayashi, K. Sasaki, *Int. J. Hydrogen Energ.* **39**, 5074–5082 (2014).
- [3] US DoE, *DoE Cell Component Stress Test Protocols for PEM Fuel Cells Report*, <http://energy.gov>.
- [4] R. Borup, et al., *Chem. Rev.* **107**(10), 3904–3951 (2007).
- [5] T. Binninger, E. Fabbri, R. Kötz, T.J. Schmidt, *J. Electrochem. Soc.* **161**, H121–H128 (2013).
- [6] A. Pătru, A. Rabis, S.E. Temmel, R. Kötz, T.J. Schmidt, *Catal. Today* **262**, 161–169 (2016), doi: 10.1016/j.cattod.2015.09.009.

## The non-uniformly accessible wall-jet electrode: a numerical study of the current distribution and its implications for inhomogeneously covered model electrodes

S.A. Tschupp, N. Poyatos Salguero, S.E. Temmel, T.J. Schmidt

phone: +41 56 310 2127, e-mail: simon.tschupp@psi.ch

To elucidate the role of particle size and interparticle distance in fundamental electrochemical reactions such as the hydrogen oxidation and oxygen reduction reactions (HOR, ORR) we fabricated Pt dot arrays using top-down nanofabrication methods. The advantage of these model systems over supported metal nanoparticles obtained by conventional chemical synthesis is the high degree of uniformity. Using achromatic Talbot lithography (ATL) at the XIL-II beamline of the Swiss Light Source (SLS), feature sizes down to 15 nm can be patterned on areas in the cm<sup>2</sup> range [1]. The transfer of the pattern into Pt by reactive ion etching has been described earlier [2].

The electrochemical performance of samples fabricated in this manner cannot be assessed using standard rotating disk electrode (RDE) techniques due to the samples' insulating backside and square shape. Therefore, we designed an electrochemical wall-jet flow cell where samples are sandwiched between two polyether etherketone (PEEK) blocks and the wetted area is defined by a Kalrez® O-ring. Samples are contacted outside of the O-ring from top and mass transport is controlled by applying a flow of electrolyte normal to the sample's surface utilizing a syringe pump. The small reaction volume defined by the O-ring does not allow the formation of a fully developed hydrodynamic flow profile of a wall-jet. According to literature [3], a mixture between wall-jet and channel flow is to be expected, with no analytical correlation between limiting current  $I_{lim}$  and flow rate  $V_{in}$  known.

In the present work we apply numerical methods to approximate the flow profiles in our electrochemical cell. By coupling these to the equations for the transport of reacting species, we obtain the current distribution on the electrode surface and present an approximate relation between  $I_{lim}$  and  $V_{in}$  for our system. We also demonstrate the dependency of  $I_{lim}$  on the xy coordinate, modelling similar electrode geometries as used in [4].

### Experimental

For the numerical study we assume a fully diffusion limited reaction, in an experimental setup most closely obtained by HOR on a metallic electrode in an acidic electrolyte:



Under the assumption that the number of protons produced in the reaction is negligibly small in comparison to the bulk acidic electrolyte, the proton concentration is constant. Therefore, we need to model the H<sub>2</sub> distribution only. Further, we assume that any H<sub>2</sub> molecule reaching the electrode reacts immediately, allowing us to forgo electrode reaction kinetics by instead setting the H<sub>2</sub> concentration to zero at the electrode. In a laboratory experiment this condition can be achieved by applying a potential such that the reaction rate is large in comparison to the diffusion of H<sub>2</sub>. Assuming a constant temperature and nearly constant concentration of the reacting species, the density of the electrolyte can be treated as a constant throughout the model. For this case, the fluid flow is described

by the incompressible Navier-Stokes equations:

$$\begin{aligned} (\mathbf{u} \cdot \nabla)\mathbf{u} - \nu\Delta\mathbf{u} + \Delta p &= 0 \\ \nabla \cdot \mathbf{u} &= 0, \end{aligned} \quad (\text{Equation 2})$$

where  $\mathbf{u}$  is the fluid velocity,  $\nu$  its kinematic viscosity and  $p$  the pressure. Through the use of a supporting electrolyte migration can be neglected, thus the transport of the reacting species is described as follows:

$$\begin{aligned} \nabla \cdot \mathbf{N} &= 0 \\ \mathbf{N} &= -D\nabla c + c\mathbf{u}. \end{aligned} \quad (\text{Equation 3})$$

Here  $\mathbf{N}$  is the molar species flux,  $D$  the diffusion coefficient,  $c$  the species concentration and  $\mathbf{u}$  the fluid velocity from Equation 2. The flux normal to the electrode surface  $\mathbf{N}$  combined with Faraday's law can be used to calculate the local current density  $j_{loc}$ :

$$j_{loc} = nF\mathbf{N}, \quad (\text{Equation 4})$$

where  $n$  is the number of transferred electrons and  $F$  is the Faraday constant.

The model geometry used in this study is shown in Figure 1a). A bottom view of the total reaction volume is shown in Figure 1b) with the O-ring sealing depicted as dashed circle and the modelled domain (a 90° circular arc due to geometrical symmetry) shown in blue. A further reduction was omitted taking into account the different outlet volumes for counter and reference electrodes. Grey squares indicate the partially covered model electrode used further below. The model was set up and calculated using the COMSOL Multiphysics software.

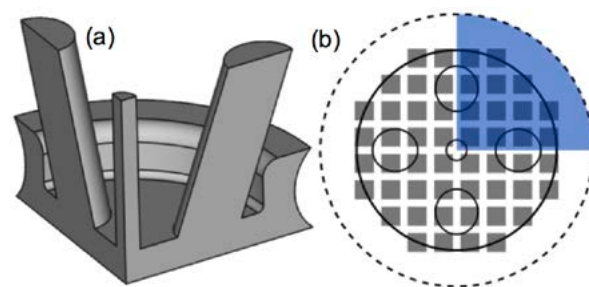


**Figure 1.** a) Schematic of the model geometry used in this study. The radius of the circular arc is 3.1 mm, the height in z direction is 3 mm. b) Bottom view of the reaction volume including 0.5 mm Ø inlet and 1 mm Ø outlets. The dashed circle ( $r=3.1$  mm) depicts to the O-ring sealing while the blue area corresponds to the modelled domain. The grey squares ( $s=430$  µm,  $p=600$  µm) represent one particular model electrode used in this study.

## Results

Figure 2 shows the integrated current across the electrode as obtained for different flow rates. A power fit was applied to find the relation  $I_{lim} \propto V_{in}^{4/5}$ .

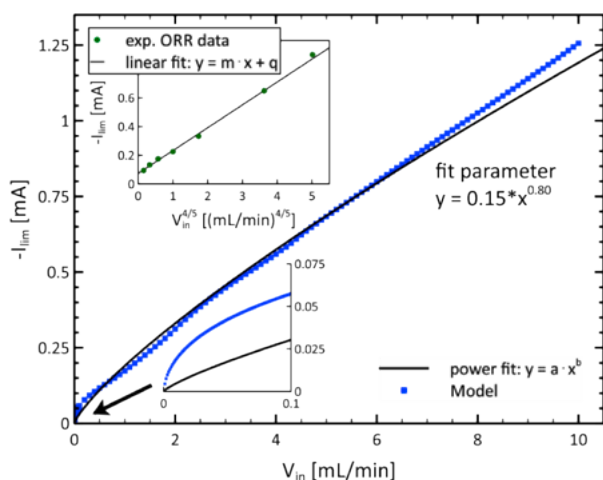


**Figure 2.**  $I_{lim}$  vs  $V_{in}$  plot showing a relation  $\propto V_{in}^{4/5}$ . The blue squares were obtained by integrating Equation 4 numerically across the electrode surface. The inset to the bottom left shows a magnification at low flow rates from 0.001 to 0.1 mL/min. The inset to the top shows ORR limiting currents obtained experimentally from [4] plotted against  $V_{in}^{4/5}$ ; the linear fit demonstrating a good agreement between model and experiment for the  $I_{lim}$  vs  $V_{in}$  relation.

Due to the non-uniform thickness of the Nernst diffusion boundary layer across the working electrode resulting from the wall-jet flow profile, we expect the limiting current to depend not only on the total Pt coverage as demonstrated earlier in this report [4] but also on the xy coordinate of the electrode. It is, therefore, necessary to optimize the sample geometry not only with regard to the fabrication at the XIL-II beamline (particle uniformity) but also with regard to the subsequent measurements (current uniformity).

For this numerical study we chose three different square sizes equally spaced at a 600  $\mu\text{m}$  period to obtain different electrode coverages. For all three square sizes, the active area was determined by a concentration-equals-zero boundary condition as outlined above: in one computation for the squares and in another for the gaps, resulting in six different electrode architectures in total, summarized in Figure 3.

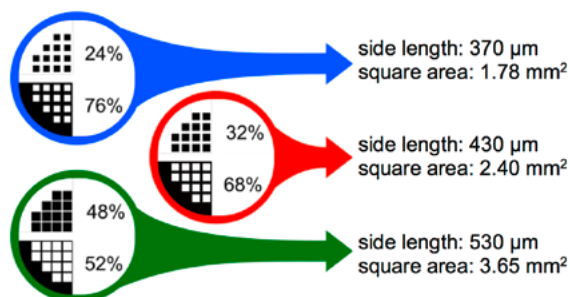


**Figure 3.** Schematic model boundary conditions: dark = active ( $c=0$  boundary), bright = inactive ( $c=\text{no flux}$  boundary), and the resulting coverage of the electrode. Total area is 7.56  $\text{mm}^2$ .

Figure 4 shows the limiting currents divided by the corresponding active area for all six electrodes plotted against the flow rate. This normalization of the modelled currents does result in equal current densities only for the geometries where the active area is formed by the background, not the squares. For the 530  $\mu\text{m}$  side length squares with almost equal coverage the limiting current densities are significantly different, demonstrating their xy dependency in our system.

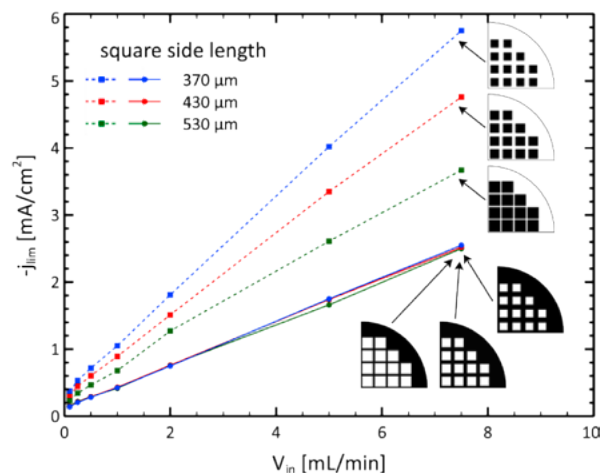


**Figure 4.** Limiting current density for six different electrode geometries obtained by numerical simulation plotted against flow rate. The boundary condition for every curve is shown as to the right analogous to the representation in Figure 3.

## Conclusions

By numerical methods we obtained a relation between the limiting current  $I_{lim}$  and the flow rate  $V_{in}$  for our electrochemical wall-jet electrode. Experimental data obtained from ORR lies in good agreement with the modelled relation. The model has yet to be compared to absolute values from HOR with regard to molecular diffusion coefficient and inlet concentration [5]. We showed that for field array electrodes the integrated limiting current density  $j_{lim}$  depends on the xy coordinates. Further studies aim to optimize the gap and placement of the fields.

## Acknowledgement

We would like to thank PSI Research Commission for financial support.

## References

- [1] W. Karim, S.A. Tschupp, M. Özasan, T.J. Schmidt, J. Gobrecht, J.A. van Bokhoven, Y. Ekinici, *Nanoscale* **7**, 7386–7393 (2015).
- [2] S.A. Tschupp, W. Karim, Y. Ekinici, T.J. Schmidt, *PSI Electrochemistry Laboratory – Annual Report 2014*, 92–93, DOI: 10.3929/ethz-a-007047464 (2014).
- [3] J. Fuhrmann, A. Linke, H. Langmach, H. Baltruschat, *Electrochim. Acta* **55**, 430–438 (2009).
- [4] N. Poyatos Salguero, S.A. Tschupp, S.E. Temmel, T.J. Schmidt, *PSI Electrochemistry Laboratory – Annual Report 2015*, 82–83, DOI: 10.3929/ethz-a-007047464 (2015).
- [5] J. Fuhrmann, H. Zhao, E. Holzbrecher, H. Langmach, M. Chojak, R. Halseid, Z. Jusys, J. Behm, *Phys. Chem. Chem. Phys.* **10**, 3784–3795 (2008).

## Carbon surface modification by introduction of oxygen defects – influence on vanadium (V) reduction activity

S.M. Taylor, A. Pătru, T.J. Schmidt

phone: +41 563104340, e-mail: susan.taylor@psi.ch

Research into redox flow cell technologies is on the rise, with the focus being placed on improving power density, efficiency and optimising overall cell performance [1, 2]. The electrode materials play a key role in improving the overall system performance. The best researched redox flow cell system is the all-vanadium system and will be the focus of this study. There is extensive literature detailing carbon based materials as one of the most suitable electrodes for this system [3, 4]. It has been observed by several studies that carbon surface modification with oxygen functional groups improves the activity and reversibility of the vanadium (V) reduction reaction. However, not all studies are in agreement regarding the reason for the observed improvement in activity [5, 6]. This lack of agreement in the literature calls for a more fundamental approach to understanding the role of the different properties of carbon itself, such as carbon microstructure and surface oxygen content on vanadium (V) reduction activity.

### Experimental

Pyrolytic graphite (PG) and glassy carbon (GC) disk electrodes (Pine instruments Co.) were used as a model catalyst system. The carbon surfaces were oxidised by potential holding at 1.95 V/RHE for 5 min followed by a reduction step at 0.3 V/RHE for 30 s in 2 M H<sub>2</sub>SO<sub>4</sub> [6]. Cyclic voltammetry (CV) was measured in a standard three electrode setup using a platinum-mesh counter electrode and a Hg/HgSO<sub>4</sub> reference electrode. The CVs were measured in 0.9 M V<sup>5+</sup>/2 M H<sub>2</sub>SO<sub>4</sub> with a scan rate of 50 mV/s. The V<sup>5+</sup> solution was obtained by the electrolysis of vanadyl (IV) sulphate (1 M VOSO<sub>4</sub> in 2 M H<sub>2</sub>SO<sub>4</sub>) using a Scribner® redox flow cell system. The final V<sup>5+</sup> concentration was determined by UV-visible spectroscopy. All CVs were corrected for ohmic resistance (iR-free) and reported against the reversible hydrogen electrode scale (RHE). X-ray photoelectron spectroscopy (XPS) was used to determine the oxygen content on the electrode surfaces. XPS measurements were performed using a VG ESCALAB 220iXL spectrometer (Thermo Fischer Scientific). Raman spectra were recorded with a Raman microscope (Labram HR800 Horiba-Jobin Yvon, Japan) equipped with a He-Ne laser (irradiation wavelength 632.8 nm) and laser power was 20 mW.

### Results

The Raman spectra for both the untreated and oxidized surface of PG and GC electrodes is shown in Figure 1. There are two main peaks of interest in the Raman spectra of carbon materials, namely the G-band at 1580 cm<sup>-1</sup> and the D-band at 1330 cm<sup>-1</sup>. Disorder/defect concentration in the crystal planes is generally reflected by the D-band. The ID/IG ratio is used as a characteristic descriptor to denote order or disorder in carbon materials. The ID/IG ratios of the carbon surfaces studied here are summarised in Table 1.

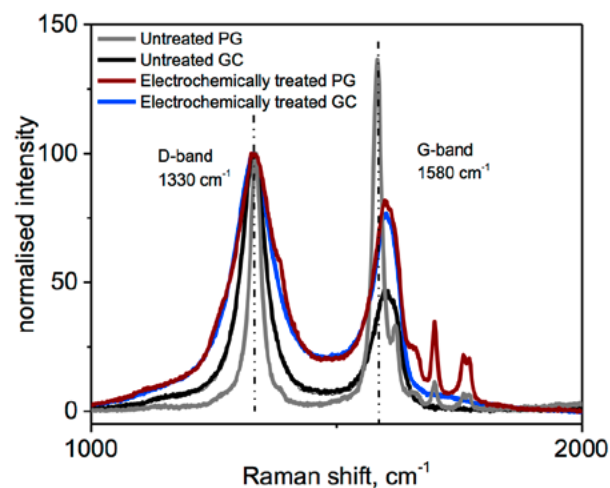


Figure 1. Raman spectra for untreated and electrochemically treated GC and PG electrodes normalised to the D-Band intensity.

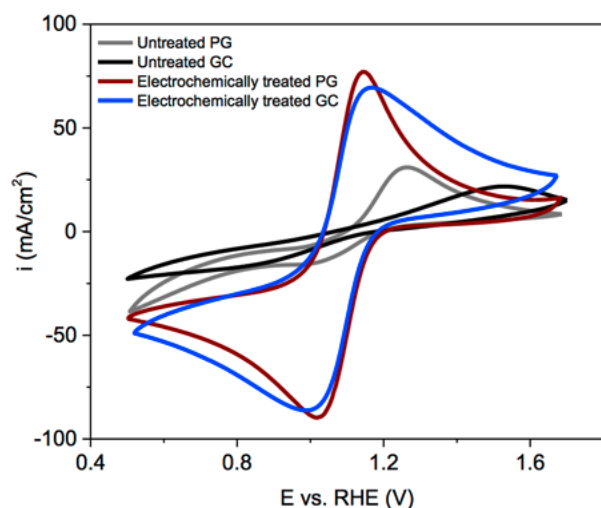
Electrode	%O	ID/IG
Untreated PG	14.7	0.74
Untreated GC	10.0	2.17
Electrochemically treated PG	21.2	1.26
Electrochemically treated GC	16.1	1.3

Table 1. Summary of oxygen content (%O) and ID/IG ratios for untreated and electrochemically treated GC and PG electrodes.

The PG shows a low ID/IG ratio which reflects a more ordered type of carbon surface. Once the surface is electrochemically oxidized, the ID/IG ratio increases and indicates a change in the carbon microstructure (towards a more disordered surface). The GC surface initially shows a high ID/IG ratio indicating an amorphous type structure [7]. Here again after the electrochemical oxidation the ID/IG ratio changes. In this case, the ID/IG ratio is lower than the initial and corresponds to a more ordered GC structure. After treatment the Raman spectra of the two electrodes are very similar, seen by similar ID/IG ratios.

The XPS analysis shows that the surface oxygen content (%O) increases after electrochemical treatment for both PG and GC electrodes. The total oxygen content is summarized in Table 1.

The effect of electrochemical oxidation of GC and PG electrodes on vanadium (V) reduction activity is illustrated by the CVs in Figure 2. The activities expressed as peak separations ( $\Delta E_p$ , mV) [8] are summarised in Table 2.



**Figure 2.** Cyclic voltammograms measured at 50 mV/s in  $0.9 \text{ M V}^{5+}/2 \text{ M H}_2\text{SO}_4$  for untreated and electrochemically treated GC and PG electrodes.

Carbon electrode	$\Delta E_p$ @ 50mV/s, mV
Untreated PG	710
Untreated GC	286
Electrochemically treated PG	153
Electrochemically treated GC	124

**Table 2.** Summary of activities ( $\Delta E_p$ ) for untreated and electrochemically treated GC and PG electrodes.

There is a significant improvement in activity (small  $\Delta E_p$ ) for both the electrochemically treated PG and GC electrodes relative to the untreated electrodes. The activity improvement could be assigned either to the increase in surface oxygen content observed by XPS or to the carbon microstructure modification seen by Raman spectroscopy. The surface oxygen content for GC and PG electrodes is significantly different: 16.1 and 21.2%, respectively. However, the resulting activities after electrochemical treatment are similar. This indicates that vanadium (V) reduction activity appears to be not fully sensitive to the total surface oxygen content for the electrodes studied here. The ID/IG ratios of both electrochemically oxidized carbon electrodes have similar values and the corresponding activities are also very close. Therefore, this is an indication that carbon microstructure could be an important parameter responsible for the improvement in activity seen here.

## Conclusions

It is difficult to isolate the role of either surface oxygen content or carbon microstructure on vanadium (V) reduction activity based on this study. However, some important observations have been made regarding electrochemical oxidation of different carbon materials. It can be concluded that electrochemical oxidation of two different carbon surfaces is accompanied by a carbon microstructural change observed by Raman spectroscopy, this observation is in line with previous studies [9]. Secondly, while the role of surface oxygen cannot be excluded, it appears that vanadium (V) reduction activity is not sensitive to the total amount of surface oxygen. Therefore, a study based on a non-oxidative treatment, resulting in carbon structural changes could shed significant light on the reasons behind the improved activity observed in this study.

## Acknowledgement

The authors thank The Swiss National Science Foundation (SNF) for their financial support within the REPCOOL Project (Grant No. 147 661).

## References

- [1] Q.H. Liu, G.M. Grim, A.B. Papandrew, A. Turhan, T.A. Zawodzinski, M.M. Mench, *J. Electrochem. Soc.* **159**(8), 1246–1252 (2012).
- [2] A.M. Pezeshki, J.T. Clement, G.M. Veith, T.A. Zawodzinski, M.M. Mench, *J. Power Sources* **294**, 333–338 (2015).
- [3] A. Parasuraman, T.M. Lim, C. Menictas, M. Skyllas-Kazacos, *Electrochim. Acta* **101**, 27–40 (2013).
- [4] M.H. Chakrabarti, N.P. Brandon, S.A. Hajimolana, F. Tariq, V. Yufit, M.A. Hashim, M.A. Hussain, C.T.J. Low, P.V. Aravind, *J. Power Sources* **253**, 150–166 (2014).
- [5] J. Melke, P. Jakes, J. Langner, L. Riekehr, U. Kunz, Z. Zhao-Karger, A. Nefedov, H. Sezen, C. Wöll, H. Ehrenberg, C. Roth, *Carbon* **78**, 220–230 (2014).
- [6] N. Pour, D.G. Kwabi, T. Carney, R.M. Darling, M.L. Perry, *J. Phys. Chem.* **119**(10), 1–19 (2015).
- [7] A.C. Ferrari, J. Robertson, *Phys. Rev. B* **61**(20), 95–107 (2000).
- [8] R.S. Nicholson, *Anal. Chem.* **37**(11), 1351–1355, (1965).
- [9] R. Bowling, R.T. Packard, R.L. Mccreery, *J. Am. Chem. Soc.* **111**, 683–688 (1989).

## Fundamental study towards the development of perovskite ( $\text{LaMO}_3$ ) oxygen evolution catalysts in alkaline environment

X. Cheng, Y. Yamashita, E. Fabbri, T.J. Schmidt

phone: +41 56 310 5937, e-mail: xi.cheng@psi.ch

Perovskite oxides ( $\text{ABO}_3$ ) have shown the potentials of being efficient oxygen-electrode catalysts in alkaline solutions [1]. However, it is a difficult task to find the most active oxides among the many different families of perovskites. A descriptor-based analysis can provide a promising approach to predict and identify the most active materials, since it correlates the prospective electrocatalytic activity to other, simpler properties. In our previous study, by selecting a paradigmatic test case (the  $\text{La}_{1-x}\text{Sr}_x\text{CoO}_3$  series of cobalt-based perovskites with varying lanthanum to strontium ratios) and complementing experiments with density-functional theory calculations, we showed that it is possible to reliably relate some simple physico-chemical materials properties including the electronic structure to the observed activity towards the oxygen evolution reaction [2]. To verify if we could spread this correlation over other series of perovskites, in the present work, we are proceeding a combined experimental and theoretical study on  $\text{LaMO}_3$  perovskites, with  $M = \text{Cr, Mn, Fe, Co, Ni}$ .

### Experimental

$\text{LaMO}_3$  powder was synthesized using a modified sol-gel process. In brief, stoichiometric quantities of commercial  $\text{La}_2\text{O}_3$  and nitrate salts of B-sites cations ( $M = \text{Cr, Mn, Fe, Co, Ni}$ ) precursors were dissolved in an aqueous solution of 0.2 M nitric acid. Citric acid was used as a chelating agent in a 2:1 ratio with respect to the total metal cations (for  $M = \text{Ni}$ , Citric acid and EDTA were used in a 2:1:1 ratio with respect to the total metal cations). After obtaining a transparent solution, the pH was adjusted between 9 and 10 by  $\text{NH}_4\text{OH}$  additions. The solution was then heated under stirring to evaporate water until it changed into a viscous gel and finally ignited to flame, resulting in ash. To obtain single phase oxide material, the  $\text{LaMO}_3$  powder was calcined in air (800–1000 °C for 2–5 h). The single phase material was confirmed by X-ray diffraction analysis. The specific surface area of the powder was determined by Brunauer-Emmett-Teller (BET) analysis. To measure the *ex situ* conductivity for each material, impedance spectroscopy measurements have been performed. The pure oxide powders were kept under a constant pressure of 0.6 MPa for 5 minutes and the electrical resistivity was evaluated by 4-wire impedance spectroscopy measurements at room temperature applying a bias of 100 mV in the frequency range between 1 MHz and 1 Hz.

Thin-film electrodes were prepared from an ink suspension consisting of 7.5 mg of the oxide powder, 2.5 ml isopropanol and 10  $\mu\text{l}$   $\text{Na}^+$ -exchanged Nafion as a binder. The sonicated ink (30 mins) was dropped and then dried on a rotating mirror polished glassy carbon electrode (0.196  $\text{cm}^2$ ). The oxygen evolution reaction (OER) was investigated by thin-film RDE measurements using a home-made Teflon cell with a Biologic VMP-300 potentiostat system. The working electrodes were immersed under potential control (1.0 V vs. RHE) in 0.1 M KOH electrolyte at room temperature and the measurements were performed using a hydrogen reference electrode (RHE) separated by a salt bridge with diffusion barrier and a gold counter electrode in a three electrode configuration. After 30 reverse

scan sweeps between 1–1.7 V (RHE) at 10  $\text{mV s}^{-1}$  and 1600 rpm in synthetic air-saturated electrolyte, chronoamperometry measurements holding each potential for 30 sec (synthetic air-saturated and 1600 rpm) were performed. The chronoamperometry measurements allow obtaining an almost steady-state current with no capacitive contribution which allows a more reliable analysis of the Tafel slope (Figure 1).

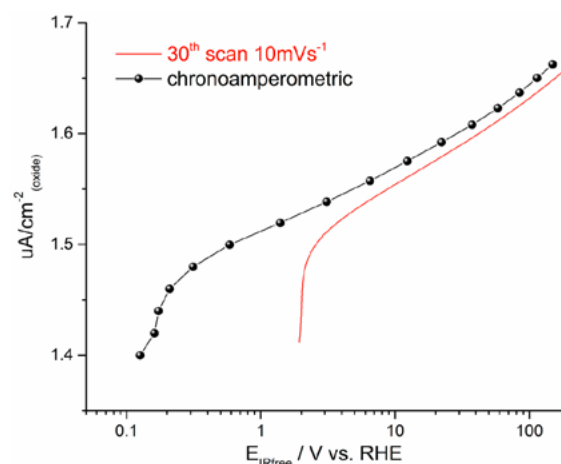


**Figure 1.** Tafel curves of a  $\text{LaNiO}_3$  electrode obtained by a cyclic voltammetry (30<sup>th</sup> cycle at 10  $\text{mV s}^{-1}$ ) and by a chronoamperometry (holding for each potential for 30 sec) measurements in synthetic air-saturated 0.1 M KOH electrolyte at 1600 rpm.

### Results

The X-ray diffraction (XRD) pattern of the  $\text{LaMO}_3$  powders shown in Figure 2 confirmed that single phase materials were achieved. The  $\text{LaCrO}_3$  and  $\text{LaFeO}_3$  show an orthorhombic structure; while for the other oxides a rhombohedral structure was obtained.

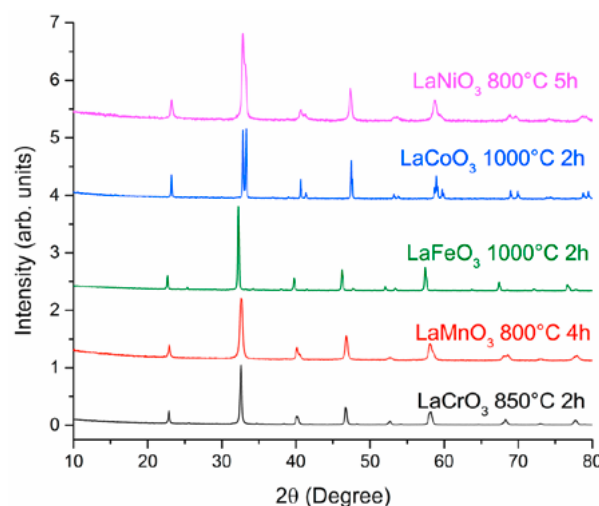


**Figure 2.** XRD spectra of  $\text{LaMO}_3$  powders as synthesized.

Table 1 shows the specific surface area of  $\text{LaMO}_3$  powders obtained by BET analysis. Surprisingly,  $\text{LaMnO}_3$  shows a high BET surface area of  $22 \text{ m}^2 \text{ g}^{-1}$ . The other oxides present a relatively low BET surface area, typical of perovskite oxides synthesized by sol-gel.[3]

Sample	$S_{\text{BET}}(\text{m}^2 \cdot \text{g}^{-1})$	Sample	$S_{\text{BET}}(\text{m}^2 \cdot \text{g}^{-1})$
$\text{LaCrO}_3$	9	$\text{LaCoO}_3$	4
$\text{LaMnO}_3$	22	$\text{LaNiO}_3$	7
$\text{LaFeO}_3$	4		

Table 1. BET surface area of  $\text{LaMO}_3$  powders.

The loading effect on each  $\text{LaMO}_3$  powder was studied to find the optimized oxide loading for the OER measurements. For  $\text{LaCrO}_3$ , the OER current increased in proportion to the increase of loading at  $77 \mu\text{g cm}^{-2}$ . For higher loading, the current decreased rapidly, indicating an important conductivity limitation for the  $\text{LaCrO}_3$  electrode. However, for  $\text{LaNiO}_3$  which present a much higher conductivity compared to  $\text{LaCrO}_3$ , the proportional increase in current could attain up to  $600 \mu\text{g cm}^{-2}$ . Therefore, the optimized oxide loadings for each  $\text{LaMO}_3$  were used in the subsequent OER measurements.

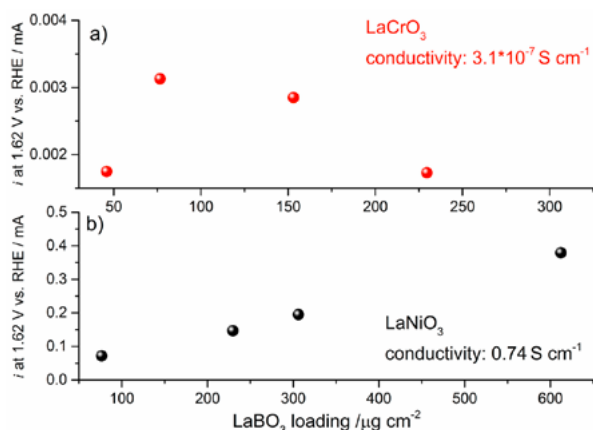


Figure 3. The OER current as a function of the  $\text{LaCrO}_3$  and  $\text{LaNiO}_3$  oxide loading at 1.62 V vs. RHE.

To compare the OER activity of different  $\text{LaMO}_3$  oxides, the steady-state current (noted from the chronoamperometry measurement at a potential of 1.62 V vs. RHE) normalized by the BET surface area of the perovskite oxide was taken as a parameter of OER activity. All the potentials were corrected for the ohmic-drop measured by impedance spectroscopy. Similar to our previous study [2], here we try to build a correlation between the OER activity and the *ex situ* electronic conductivity. For  $\text{La}_x\text{Sr}_{1-x}\text{CoO}_3$  oxide (Figure 4a), we could clearly observe a linear relationship between the OER activity and conductivity. For  $\text{LaMO}_3$  (Figure 4b), no clear correlation between OER activity and conductivity could be found, specifically  $\text{LaMnO}_3$  thoroughly deviates from a possible linear dependence.

The different behavior between  $\text{LaMO}_3$  and  $\text{La}_x\text{Sr}_{1-x}\text{CoO}_3$  oxides could be explained considering that for  $\text{La}_x\text{Sr}_{1-x}\text{CoO}_3$ , by only varying the A-site composition, we could progressively tune the physico-chemical materials properties (these properties were observed changing as a function of Sr fraction) allowing us building a 2-dimensional relationship between the OER activity and other physico-chemical properties. On the other hand, by varying the B-site, which is considered to be the active site for OER, the modification of physico-chemical properties

from one  $\text{LaMO}_3$  oxide to another might be more abrupt and complicate compared to  $\text{La}_x\text{Sr}_{1-x}\text{CoO}_3$ . Thus, a 2-dimensional correlation might not be suitable to describe the OER activity trend for  $\text{LaMO}_3$  oxides. Apart from the conductivity, there may be other properties which play a multi-effect on the OER activity. Our next step is to complete the characterization of  $\text{LaMO}_3$  with DFT calculation,  $\text{O}_2$ -ion mobility measurements and electrode/electrolyte interface determination, which could help us to build a multi-dimensional correlation between the OER activity and physico-chemical properties, with the further purpose of improving known materials or predicting new active materials.

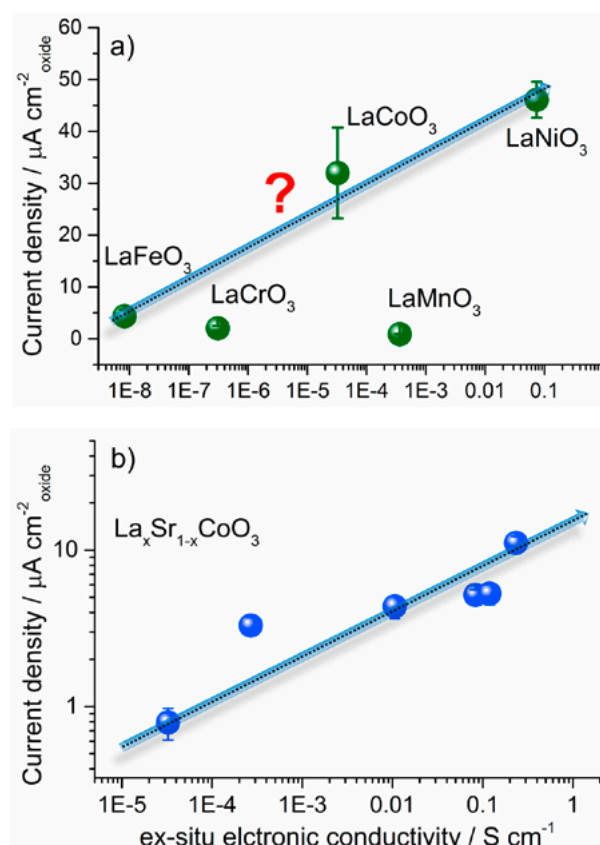


Figure 4. Current density (at 1.62 V vs. RHE for  $\text{LaMO}_3$  and at 1.53 V vs. RHE for  $\text{La}_x\text{Sr}_{1-x}\text{CoO}_3$ ) normalized by the BET surface area as a function of the *ex situ* electronic conductivity.

## Acknowledgement

The authors gratefully acknowledge the Swiss National Science Foundation through its Ambizione Program, the Swiss Competence Center for Energy Research (SCCER) Heat & Electricity Storage and the Commission for Technology and Innovation (CTI) Switzerland as well as the Swiss National Science Foundation within NCCR Marvel and Paul Scherrer Institute for financial contributions to this work.

## References

- [1] E. Fabbri, A. Habereder, K. Waltar, R. Kötzt, T.J. Schmidt, *Catal Sci Technol* **4**, 3800–3821 (2014).
- [2] X. Cheng, E. Fabbri, M. Nachttegaal, I.E. Castelli, M. El Kazzi, R. Haumont, N. Marzari, T.J. Schmidt, *Chem. Mater.* **27**, 7662–7672 (2015).
- [3] A. Lan, A.S. Mukasyan, *J. Phys. Chem. C* **111**, 9573–9582 (2007).

## Bimetallic Pt-Ni aerogels for electrocatalysis of the oxygen reduction

S. Henning, J. Herranz, L. Kühn<sup>1</sup>, A. Eychmüller<sup>1</sup>, T.J. Schmidt

phone: +41 56 310 2125, e-mail: sebastian.henning@psi.ch

State-of-the-art polymer electrolyte fuel cells (PEFCs) require large amounts of carbon-supported platinum nanoparticle (Pt/C) catalysts ( $\sim 0.4 \text{ mg}_{\text{Pt}}/\text{cm}^2_{\text{MEA}}$ ) to account for the large overpotential of the oxygen reduction reaction (ORR) [1]. One approach to reduce this excessive Pt-loading relies on increasing the catalysts' ORR activity, e.g. by alloying platinum with other metals like Ni, Cu and Co, to form materials which show up to one order of magnitude higher specific activity than commercial Pt/C catalysts [2]. On the other hand, these carbon-supported materials suffer from significant carbon- and Pt-corrosion during the normal operation of PEFCs, gradually compromising their reliability and profitability [3].

To partially overcome these stability issues, unsupported mono- and bimetallic electrocatalysts with very high surface areas ( $\sim 100 \text{ m}^2_{\text{metal}}/\text{g}_{\text{metal}}$ ) can be synthesized using a nanoparticle gel formation and destabilization process [4, 5]. On the basis of previous work with PtPd-alloy compositions [6], the concept of this new class of materials, often referred to as aerogels, has been extended to the combination of a noble and a non-noble metal. This approach could lead to a further reduction in noble metal content and costs. To assess this assumption, the ORR activity of bimetallic aerogels consisting of platinum and nickel was investigated in this study.

### Experimental

Bimetallic aerogels were synthesized at TU Dresden by a simple co-reduction process of  $\text{NiCl}_2 \cdot 6\text{H}_2\text{O}$  and  $\text{H}_2\text{PtCl}_6$  with  $\text{NaBH}_4$  in aqueous solution [6]. The resulting gels were dried supercritically in a critical point dryer operating with  $\text{CO}_2$  to obtain  $\text{Pt}_3\text{Ni}$  and  $\text{Pt}_{1.5}\text{Ni}$ .

The electrochemical measurements were performed in 0.1 M  $\text{HClO}_4$  solution in a house-made glass cell. A gold mesh and a reversible hydrogen electrode (RHE) served as counter and reference electrode, respectively. An interchangeable rotating ring-disc electrode (RRDE, Pine Research Instrumentation) with a 5 mm diameter glassy carbon (GC) disk insert was used as working electrode. The working electrode was attached to a PEEK shaft and rotator system (Pine Research Instrumentation). Current and potential were controlled with a Biologic VSP-300 potentiostat, in combination with EC-Lab V10.40 software.

To prepare thin catalyst films on the GC electrode, the aerogel powders were suspended in mixtures of ultrapure water and isopropanol. After sonication, fractions of the suspensions were pipetted on the GC electrode to obtain Pt loadings of  $30 \mu\text{g}_{\text{Pt}}/\text{cm}^2_{\text{electrode}}$  after drying.

### Results

Both synthesized aerogels consist of a 3D nanowire network of interconnected nanoparticles with an average diameter of  $\sim 5 \text{ nm}$  (see Figure 1 for results of  $\text{Pt}_3\text{Ni}$ , similar to those obtained for  $\text{Pt}_{1.5}\text{Ni}$ ). This average diameter is consistent with the surface areas of  $\sim 50 \text{ m}^2/\text{g}$  obtained by  $\text{N}_2$ -sorption porosimetry (not shown).

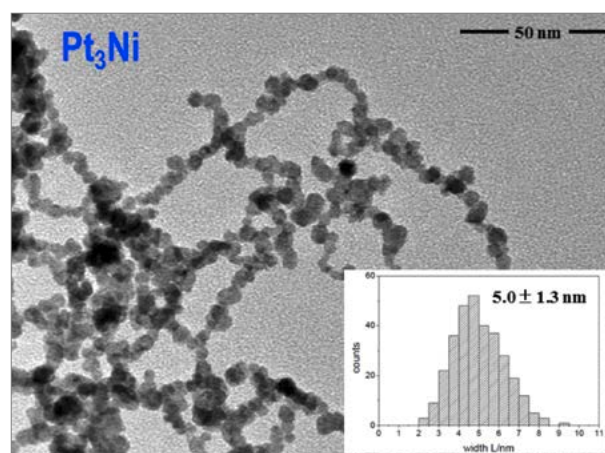


**Figure 1.** High resolution TEM image of  $\text{Pt}_3\text{Ni}$  aerogel and particle size distribution (inset).

The electrochemical surface area (ECSA) was determined by evaluating CO-stripping and hydrogen underpotential deposition ( $\text{H}_{\text{upd}}$ ) charges (see Figure 2). For  $\text{Pt}_3\text{Ni}$  and  $\text{Pt}_{1.5}\text{Ni}$ , this yields an average ECSA of  $\sim 29$  and  $27 \text{ m}^2/\text{g}$ , respectively. The difference in  $\text{N}_2$ -sorption surface area vs. ECSA is attributed to the presence of micropores (with diameters  $< 2 \text{ nm}$ ) that cannot be wetted by electrolyte.

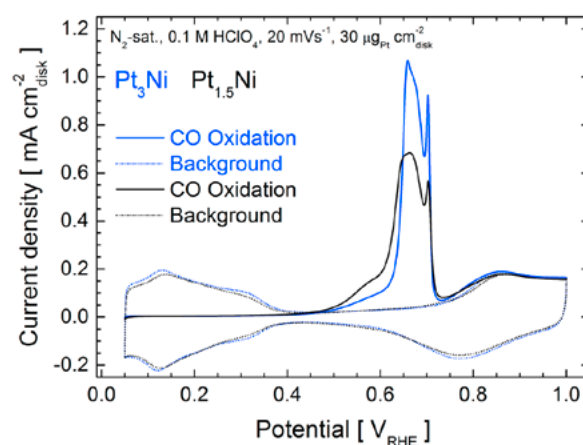


**Figure 2.** Electrochemical behaviour of  $\text{Pt}_3\text{Ni}$  and  $\text{Pt}_{1.5}\text{Ni}$  in  $\text{CO}$  and  $\text{N}_2$  saturated 0.1 M  $\text{HClO}_4$ .

Finally, the ORR activity was determined by recording potential sweeps between 0.05 and 1.1 VRHE at  $5 \text{ mVs}^{-1}$  in  $\text{O}_2$  saturated  $0.1 \text{ M HClO}_4$  at a rotation speed of 1600 rpm. Activity values were extracted at 0.95 VRHE from anodic sweeps after iR-correction of the potential. Results for  $\text{Pt}_3\text{Ni}$  and  $\text{Pt}_{1.5}\text{Ni}$  are summarized in Figure 3 and compared to those of monometallic Pt aerogel and commercial Pt/C (E-TEK Inc.) samples with similar ECSAs.

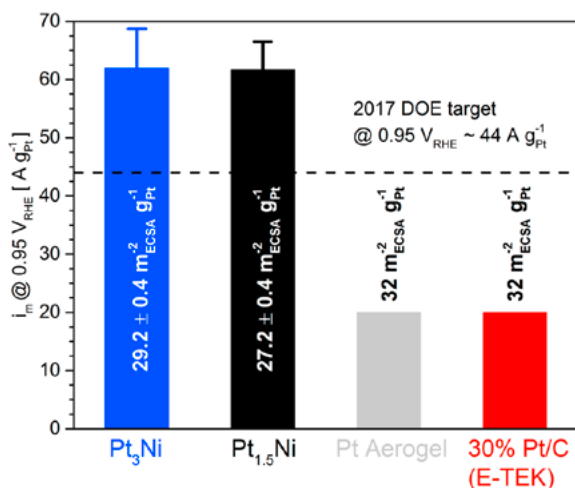


**Figure 3.** Comparison of ORR mass specific activities of Pt-Ni bimetallic aerogels with Pt aerogel and Pt/V. The dotted line represents the DOE ORR activity target 2017 estimated for a potential of 0.95 VRHE.

Both Pt-Ni aerogels show an ORR mass specific activity of  $\sim 60 \text{ A/g}_{Pt}$  at 0.95 VRHE, thus exceeding the US Department of Energy (DOE) ORR activity target 2017 ( $\sim 44 \text{ A/g}_{Pt}$ ) [7]. This represents an activity improvement by a factor of 3 vs. Pt aerogel and Pt/V catalysts (see Figure 3), caused by changes in electronic properties of the catalytically active Pt due to the alloying [7].

The similar activity for Pt-Ni bimetallic aerogels is attributed to the observation from XRD analysis that  $\text{Pt}_{1.5}\text{Ni}$  consists of two phases,  $\text{Pt}_3\text{Ni}$  alloy and excess Ni. Consequently, the non-alloyed Ni dissolves rapidly upon the beginning of the electrochemical measurement due to exposure to  $0.1 \text{ M HClO}_4$  and a material very similar to  $\text{Pt}_3\text{Ni}$  aerogel forms.

## Conclusions and Outlook

The investigated non-supported Pt-Ni alloys show a high ORR activity that is on par with 3M's latest Pt-Ni NSTF catalysts [8] and exceeds the DOE ORR activity target for 2017. Further experiments to explore the behaviour of these materials in PEFCs are necessary to assess the potential for application.

## Acknowledgement

Financial support from SNF (20001E\_151122/1) and DFG (EY 16/18-1) is greatly acknowledged.

## References

- [1] F.T. Wagner, B. Lakshmanan, M.F. Mathias, *J. Phys. Chem. Lett.* **1**, 2204 (2010).
- [2] C. Wang, M. Chi, D. Li, D. Strmcnik, D. van der Vliet, G. Wang, V. Komanicky, K.C. Chang, A.P. Paulikas, D. Tripkovic, J. Pearson, K.L. More, N.M. Markovic, V.R. Stamenkovic, *J. Am. Chem. Soc.* **133**, 14396 (2011).
- [3] A. Rabis, P. Rodriguez, T.J. Schmidt, *ACS Catal.* **2**, 864 (2012).
- [4] N.C. Bigall, A.K. Herrmann, M. Vogel, M. Rose, P. Simon, W. Carrillo-Cabrera, D. Dorfs, S. Kaskel, N. Gaponik, A. Eychmüller, *Angew. Chem. Int. Ed.* **48**, 9731 (2009).
- [5] A.-K. Herrmann, P. Formanek, L. Borchardt, M. Klose, L. Giebel, J. Eckert, S. Kaskel, N. Gaponik, A. Eychmüller, *Chem. Mater.* **26**, 1074 (2014).
- [6] W. Liu, P. Rodriguez, L. Borchardt, A. Foelske, J. Yuan, A.-K. Herrmann, D. Geiger, Z. Zheng, S. Kaskel, N. Gaponik, R. Kötz, T.J. Schmidt, A. Eychmüller, *Angew. Chem. Int. Ed.* **52**, 9849 (2013).
- [7] C. Chen, Y. Kang, Z. Huo, Z. Zhu, W. Huang, H.L. Xin, J.D. Snyder, D. Li, J.A. Herron, M. Mavrikakis, M. Chi, K.L. More, Y. Li, N.M. Markovic, G.A. Somorjai, P. Yang, V.R. Stamenkovic, *Science* **343**, 1339 (2014).
- [8] A.J. Steinbach, D. van der Vliet, A.E. Hester, J. Erlebacher, C. Duru, I. Davy, M. Kuznia, D.A. Cullen, *ECS Trans.* **69**, 291 (2015).

## Use and misuse of Pourbaix diagrams: Instability of metal oxide catalysts for oxygen evolution

T. Binninger, E. Fabbri, T.J. Schmidt

phone: +41 56 310 5728, e-mail: tobias.binninger@psi.ch

Whereas in heterogeneous catalysis systems the critical thermodynamic state variables are temperature  $T$  and pressure  $p$ , in an aqueous electrocatalytic system the electrolyte pH value and the electrode potential generally are the more relevant parameters defining the thermodynamic state of the system. Therefore, phase diagrams for materials in aqueous electrocatalysis are generally given in terms of pH value and potential  $E$  for fixed values of temperature and pressure. Such pH- $E$  diagrams are termed Pourbaix diagrams and play an important role in describing the thermodynamically stable phases of metals and metal oxides in contact with an electrolyte. One prominent example for the general application of Pourbaix diagrams is the search for stable catalysts for the oxygen evolution reaction (OER) in electrolysis [1]. However, recent experimental findings have revealed a wealth of corrosion phenomena for OER metal oxide catalysts even for systems like  $\text{IrO}_2$  that are expected to be thermodynamically stable under these conditions [2].

The key to the resolution of this apparent contradiction between theory and experiment, is the question whether the system pressure is a state variable independent from the pH value and the potential. In other words, can the pressure be considered to be at an arbitrarily fixed value for all points in a Pourbaix diagram? The answer to this question is «No»: Since Pourbaix diagrams consider the entire system at thermodynamic equilibrium, the partial pressures of hydrogen  $p_{\text{H}_2}$  and oxygen  $p_{\text{O}_2}$  must be equal to their equilibrium values, which are defined by the pH value and the potential  $E$  according to the Nernst equations,

$$E = E_{0,\text{H}_2} - \ln(10) (RT/F) \text{pH} - \ln(10) (RT/(2F)) \log_{10}(p_{\text{H}_2})$$

and

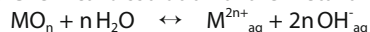
$$E = E_{0,\text{O}_2} - \ln(10) (RT/F) \text{pH} + \ln(10) (RT/(4F)) \log_{10}(p_{\text{O}_2})$$

where the pressures are given in bar,  $R$  is the gas constant, and  $F$  is the Faraday constant. Therefore, at each point of a Pourbaix diagram, different hydrogen and oxygen partial pressures – and thus also different overall system pressures – are implicitly assumed. Strictly speaking, for practical applications, where the system pressure is fixed at near ambient values, Pourbaix diagrams are valid only in the stability window of water, where the respective equilibrium hydrogen and oxygen partial pressures are smaller than the system pressure.

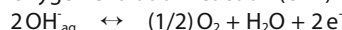
This is clearly not the case under OER conditions: Typical potentials for OER in electrolyzers at near-ambient temperatures are well above  $1.5 V_{\text{RHE}}$ . According to the Nernst equation, the respective equilibrium oxygen partial pressure at such potentials is extremely large, of the order of  $p_{\text{O}_2} = 1020$  bar. In technical electrolysis, the system pressure is generally in the range of 1–1000 bar. The huge difference to the equilibrium partial pressure is the thermodynamic driving force for the desired OER. However, at the same time this discrepancy between equilibrium oxygen partial pressure and system pressure also brings the metal oxide catalyst out of equilibrium. This can be understood by considering the three following processes for

an arbitrary metal oxide  $\text{MOn}$  [3]:

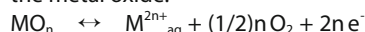
(1) Chemical dissolution of the metal oxide:



(2) Oxygen evolution reaction (OER) from electrolyte:



(3) Lattice oxygen evolution reaction (LOER) directly from the metal oxide:



These processes are written explicitly for alkaline conditions. However, all considerations equally well apply to acidic conditions. The three processes (1)–(3) are not independent from each other: Each process can be written as a sequence of the other two processes. For instance, the lattice oxygen evolution process (3) can also be written as a sequence of (1) the chemical dissolution of the metal oxide, followed by (2) the oxygen evolution from the electrolyte. As a consequence, also the equilibrium conditions are not independent – if two out of the three processes are in thermodynamic equilibrium, the equilibrium condition for the third process is automatically fulfilled [3]. It can therefore be concluded that, vice versa, if one process is brought out of equilibrium, the other two processes cannot remain in equilibrium at the same time. This subtle point has drastic consequences for the thermodynamic stability of OER metal oxide catalysts: During OER, the process (2) is clearly out of equilibrium with a thermodynamic driving force from left to right towards the molecular oxygen phase. As a consequence, even if process (1) remains in equilibrium, the lattice oxygen evolution reaction (3) is automatically brought out of equilibrium with a thermodynamic driving force favoring the right hand side of reaction (3). This LOER process could explain the experimentally observed corrosion phenomena even for metal oxide catalysts that are considered to be stable according to their respective Pourbaix diagrams. The discrepancy between the system pressure during electrolysis and the huge oxygen equilibrium partial pressure illustrates the force which drives the oxygen to evolve not only from the electrolyte, but also directly from the metal oxide lattice.

### Acknowledgement

Financial support from CCEM Switzerland, Umicore AG & Co KG, the SCCER Heat and Electricity Storage, and the Commission for Technology and Innovation Switzerland is greatly acknowledged.

### References

- [1] A. Minguzzi, F.-R.F. Fan, A. Vertova, S. Rondinini, A.J. Bard, *Chem. Sci.* **3**, 217–229 (2012).
- [2] S. Cherevko, T. Reier, A.R. Zeradjanin, Z. Pawolek, P. Strasser, K.J.J. Mayrhofer, *Electrochem. Commun.* **48**, 81–85 (2014).
- [3] T. Binninger, R. Mohamed, K. Waltar, E. Fabbri, P. Levecque, R. Kötz, T.J. Schmidt, *Sci. Rep.* **5**, 12167 (2015).

## Physical and electrochemical investigation of strained Pt model catalysts prepared by pulsed laser deposition

S.E. Temmel, D. Pergolesi, E. Fabbri, T. Lippert, T.J. Schmidt,  
phone: +41 56 310 2128, e-mail: sandra.temmel@psi.ch

One of the prime impediments towards a wide-ranged application of polymer electrolyte fuel cells (PEFCs) is the potential loss at the cathode side resulting from the slow kinetics of the oxygen reduction reaction (ORR). Over the last decade, many attempts have been made to improve the PEFC performance by altering the electrocatalytic activity of Pt, state-of-the-art catalyst for the ORR [1]. For instance, Strasser et al. [2] demonstrated that dealloyed Pt-Co core-shell nanoparticles exhibited a higher catalytic activity compared to bulk Pt-Co NPs. The increased activity was attributed to the compressed state of the Pt rich shell, resulting from the adaption of the Pt shell lattice to the smaller lattice of the underlying Pt-Co core. Nevertheless, in this work, contributions to the electrocatalytic activity from Co contaminations or the underlying conductive support cannot be completely elucidated. In this regard, a new approach for tailoring strained Pt model electrocatalysts was developed. Thin, epitaxial, strained pure Pt films were prepared on a non-conductive substrate using pulsed laser deposition (PLD) avoiding any alloy contaminations. By tuning the deposition parameters and varying the film thickness, epitaxial Pt films in differently strained states can be prepared. In an epitaxial film growth, the Pt film lattice adapts to the lattice constant of the substrate and the crystallographic orientation of the substrate surface determines that of the film. Strain refers to the change in lattice constant due to forced matching to the substrate's lattice and is given by  $\varepsilon = \frac{\Delta d}{d_{\text{bulk}}}$  and  $\Delta d = d_{\text{bulk}} - d_{\text{strain}}$  with  $d_{\text{bulk}}$  and  $d_{\text{strain}}$  being the lattice constant of the bulk and the strained Pt film, respectively.

The overall aim of the project is to study the influence of the strain-induced variations of Pt interatomic distances and/or surface crystallographic orientation on its electrocatalytic activity towards ORR. First results on as-deposited (111) Pt films regarding the strain-thickness correlation, the growth behaviour and surface morphology are presented. In addition, CO stripping experiments were used to probe the electrocatalytic properties of strained nearly relaxed Pt films.

### Experimental

Thin Pt films were grown on (111) single crystal SrTiO<sub>3</sub> (STO) substrates (CrysTec, thickness of 0.5 mm, one-sided epipolished, miscut angle <0.5°, 10×10 mm<sup>2</sup>) in O<sub>2</sub> atmosphere (1.5×10<sup>-2</sup> mbar) at 400 °C by PLD using a KrF excimer laser (248 nm, 10 Hz, 26 kV). The target (positioned at 5 cm normal to the substrate surface) was rastered by the laser beam (spot size = 1×10<sup>-2</sup> cm<sup>2</sup>, Fluence F = 1.5 J/cm<sup>2</sup>) under a 45° angle. The total number of pulses was varied from 10'000 to 50'000 depending on the final film thickness. Prior to deposition, the substrates were ultrasonically cleaned in ethanol, acetone and isopropanol for 10 min each. The film growth was monitored *in situ* via reflection high energy electron diffraction (RHEED).  $\theta$ -2 $\theta$  X-ray scans were carried out with a D500 diffractometer (Bruker, Germany) using Cu-K $\alpha$  radiation to examine the crystal structure and the out-of-plane strain of the Pt films. All measurements were performed at room temperature in the Bragg-Brentano diffraction geometry varying 2 $\theta$  from 35° to 50°. The film thickness was determined via X-ray reflectometry

(XRR) in a  $\Theta$ -2 $\theta$  scan. The morphology of the films was investigated with scanning electron microscopy (SEM-Zeiss Supra). Electrochemical measurements were performed in a three electrode setup in an in-house designed flow cell. A platinized Pt wire and a Hg/Hg<sub>2</sub>SO<sub>4</sub> electrode served as counter and reference electrode, respectively. CO stripping experiments were carried out at room temperature in 0.5 M sulfuric acid. To cover the Pt surface with CO molecules, the potential was held at 0.1 V vs RHE for 1 min while introducing CO. Subsequently, the electrolyte was saturated with nitrogen to remove the CO. The potential was then swept to 1 V at a scan rate of 10 mV s<sup>-1</sup> to oxidize the CO<sub>ads</sub>.

### Results

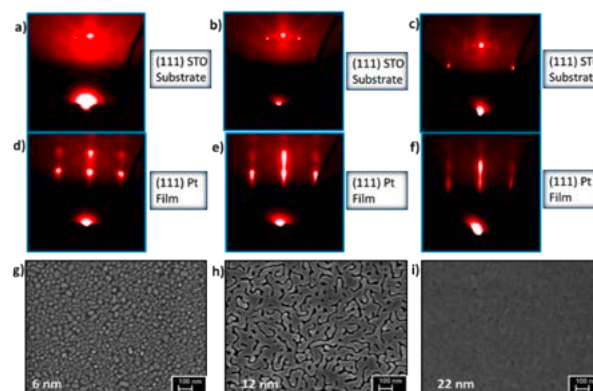


**Figure 1.** Top row: RHEED patterns of the substrate prior to deposition. Middle row: RHEED patterns of the final Pt films. Bottom row: SEM images of Pt films of varying thickness.

The growth of Pt films of three different thicknesses was followed *in situ* by RHEED. The RHEED pattern of the (111) STO substrate surface prior to deposition is depicted in Figure 1 (a–c). The Laue circle is clearly recognizable for each of them, proving the well-ordered crystalline structure of the surface. The RHEED patterns of the Pt film at the end of deposition vary significantly with the thickness (d–f). The spotty pattern of the 6 nm thick film indicates a 3-dimensional surface. With increasing thickness, the RHEED pattern becomes more streaky, suggesting a progressively smoother Pt film surface. These findings are in accordance with recorded SEM images shown in Figure 1 (g–i). Pt films thinner than 10 nm consist of separated islands, while only for larger thicknesses the islands merge providing a continuous electrical path over the surface of the film. A fully covered Pt film is only achieved at thickness > 20 nm with a corresponding RHEED pattern showing typical features of a more 2-dimensional surface. The observed growth mechanism is typical for films of noble metals and it is well-known in literature [3].

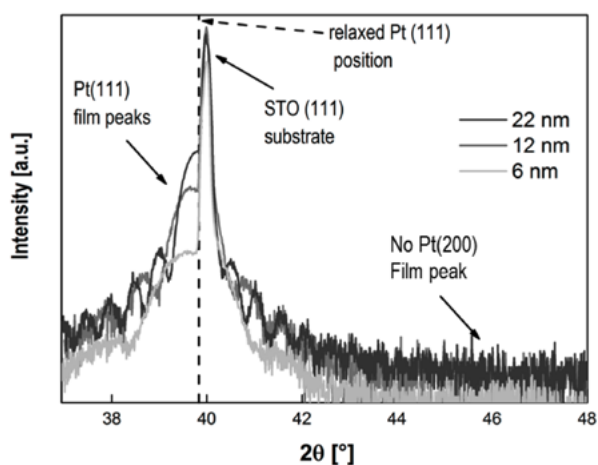


Figure 2. XRD pattern of thin Pt films of varying thickness.

The cubic perovskite structure of STO allows the epitaxially oriented cube-on-cube growth of Pt films. Due to the smaller lattice parameter of STO (3.905 Å) as compared to Pt (3.92 Å), the Pt film will grow compressively strained in-plane, whereas tensile strain is expected along the out-of-plane direction to preserve the unit cell volume. This behaviour can indeed be found in the  $\theta$ - $2\theta$  scans of the as-produced Pt films as shown in Figure 2. The Pt film reflexes for the 6 nm and 12 nm Pt films are clearly shifted to lower  $2\theta$  angles, indicating a tensile out-of-plane strain. In contrast, the Pt film reflex position of the thickest film (nearly) coincides with the angular position of a relaxed bulk Pt (111) position. Due to the absence of the (200) Pt peak, it can be concluded that all Pt films are purely (111) oriented.

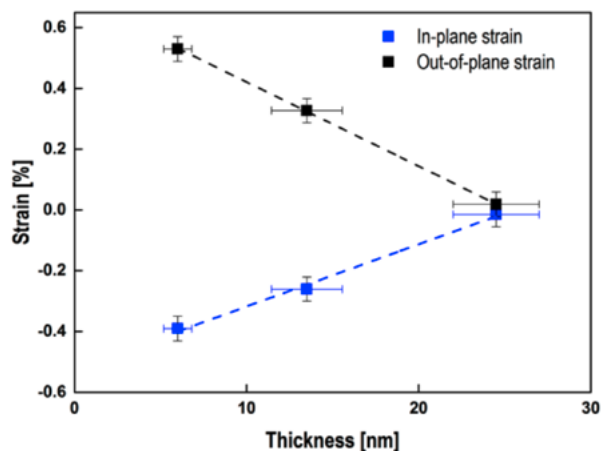


Figure 3. The out-of-plane strain and thereof calculated in-plane strain as a function of Pt film thickness.

The out-of-plane strain can be determined from the Pt film peak position in the  $\theta$ - $2\theta$  scan. Applying Equation 1, the in-plane strain can be calculated. Both strains are plotted over the thickness in Figure 3. It is clearly visible that the strain decreases with increasing film thickness, most probably due to strain relaxation by insertion of dislocations [4].

$$\varepsilon_{zz} = \frac{2\nu}{1-\nu} \varepsilon_{xx} \quad (\text{Equation 1})$$

As a proof-of-concept CO stripping experiments were carried out on the 12 nm strained Pt films (-0.27%) compared to the 22 nm nearly relaxed Pt films (-0.01%). The peak position was used to test the adsorption properties on the surface. As depicted in Figure 3, the main CO stripping peak shifts to more

positive potentials on the strained Pt surface. Similar behaviour was observed for strained Pt/W(111) films produced by molecular beam epitaxy [5]. The shift was attributed to a weaker adsorption of OH on the compressed Pt surface. On one side, since the same fabrication procedure was applied to all Pt films, we may assume that the roughness of the surface at atomic level is the same for the two films under investigation, as suggested by RHEED (Figure 1 e+f). On the other hand, to exclude completely any morphology-correlated effects, further investigations are necessary.

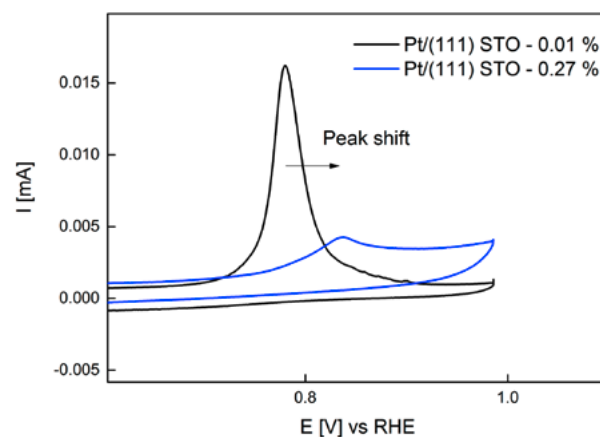


Figure 4. CO stripping experiments carried out on two differently strained Pt surfaces at  $10 \text{ mVs}^{-1}$  in  $0.5 \text{ M H}_2\text{SO}_4$ .

## Summary and Conclusion

Epitaxial (111)-oriented Pt films of varying strain were successfully fabricated by PLD. *In situ* monitoring of the film growth in addition to post-growth SEM analysis revealed a thickness-dependent morphology. The extent of strain is clearly correlated to the thickness. First electrochemical studies showed that strained Pt model catalysts exhibit a different electrocatalytic behaviour compared to fully relaxed Pt films. They hence represent promising candidates for future ORR investigations.

## Acknowledgement

Kindly acknowledged is financial support from Kabelwerke Brugg AG, FH Nordwestschweiz und PSI.

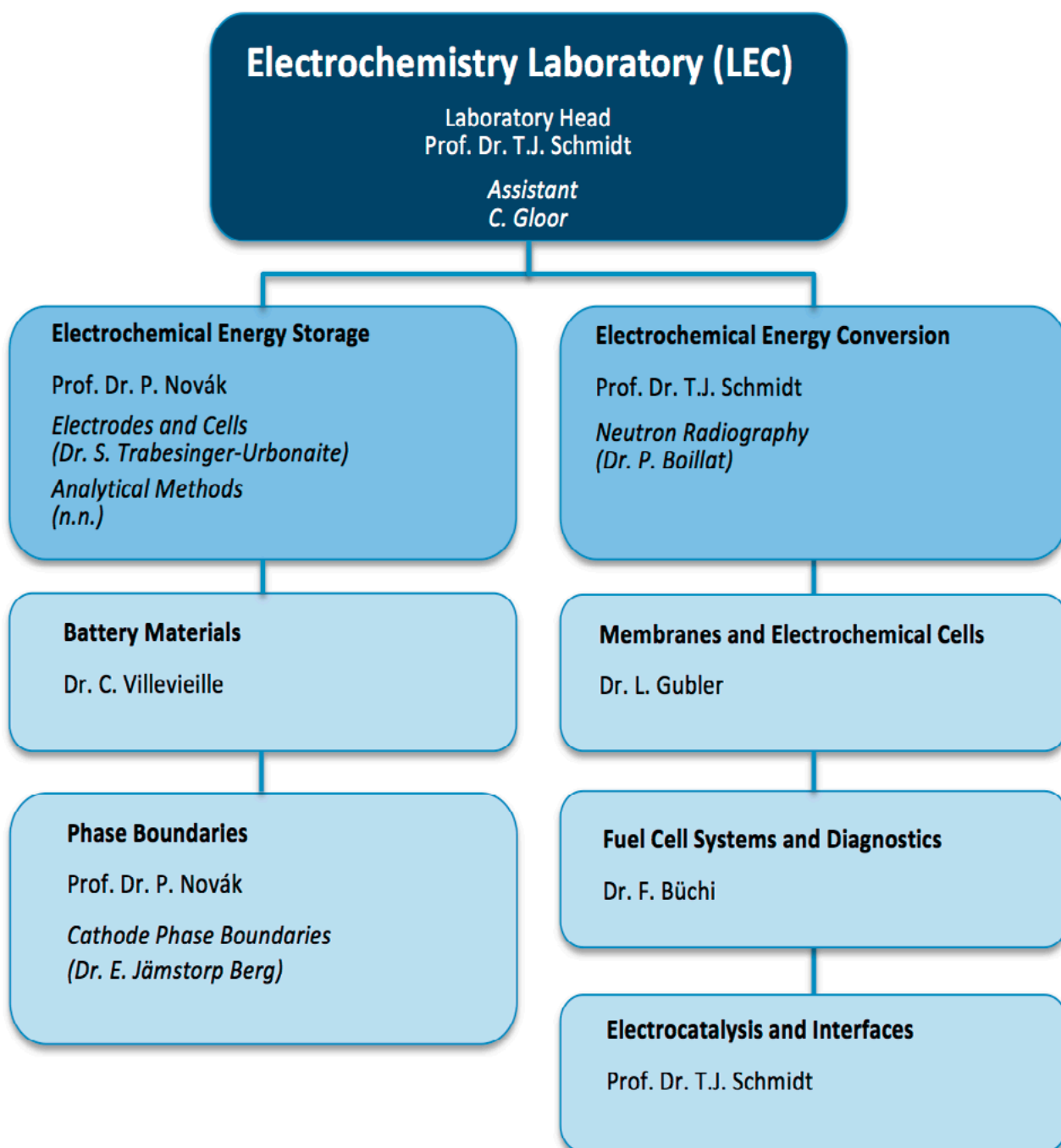
## References

- [1] A. Rabis, P. Rodriguez, T.J. Schmidt, *ACS Catal.* **2**, 864–890 (2012).
- [2] P. Strasser, *Nat. Chem.* **2**, 454–460 (2010).
- [3] R. Koch, *J. Phys. Cond. Matter* **6**, 9519–9550 (1994).
- [4] H. Galinski, T. Ryll, P. Reibisch, L. Schlagenhauf, I. Schenker, L.J. Gauckler, *Act. Mat.* **61**, 3297–3303 (2012).
- [5] M.K. El Jawad, B. Gilles, F. Maillard, *Electrocatalysis* **6**, 398–404 (2015).

# THE ELECTROCHEMISTRY LABORATORY

## FACTS & FIGURES

## STRUCTURE 2015



# PERSONNEL 2015

## Staff

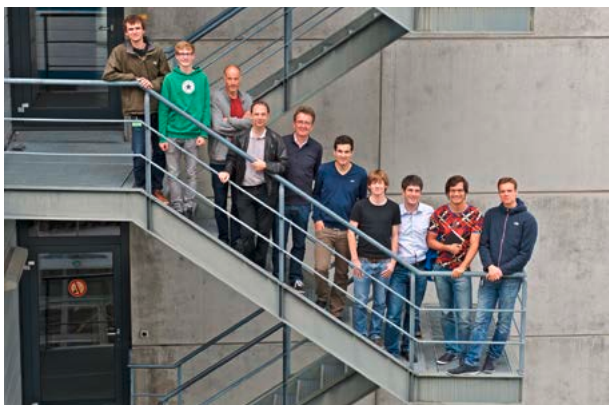
Dr. Daniel ABBOTT (Post Doctoral Researcher)  
 Martin AMMANN (Technician)  
 Dr. Erik J. BERG (Post Doctoral Researcher)  
 Dr. Juliette BILLAUD (Post Doctoral Researcher)  
 Dr. Pierre BOILLAT (Project Leader)  
 Dr. Christoph BOLLI (Post Doctoral Researcher)  
 Lukas BONORAND (Engineer)  
 Dr. Felix BÜCHI (Group Leader)  
 Kira BUZDIN (Technician)  
 Dr. Xi CHENG (Post Doctoral Researcher)  
 Dr. Magali COCHET (Scientist)  
 Dr. Julien DURST (Scientist)  
 Dr. Mario EL KAZZI (Scientist)  
 Dr. Jens ELLER (Scientist)  
 Dr. Emiliana FABBRI (Scientist)  
 Dr. Maria GEORMEZI (Post Doctoral Researcher)  
 Cordelia GLOOR (Assistant)  
 Thomas GLOOR (Technician)  
 Dr. Lorenz GUBLER (Group Leader)  
 Dr. Aurélie GUÉGUEN (Scientist)  
 Dr. Juan HERRANZ SALANER (Post Doctoral Researcher)  
 Christoph JUNKER (Technician)  
 Hermann KAISER (Technician)  
 Dr. Adrien LAMIBRAC (Post Doctoral Researcher)  
 Dr. Cyril MARINO (Scientist)  
 Christian MARMY (Technician)  
 Prof. Dr. Petr NOVÁK (Section Head & Group Leader)  
 Dr. Anastasia A. PERMYAKOVA (Post Doctoral Researcher)  
 Dr. Tiphaine POUX (Post Doctoral Researcher)  
 Dr. Alexandra PĂTRU (Post Doctoral Researcher)  
 Christian PETER (Engineer)  
 Dr. Rosa ROBERT SANCHEZ (Scientist)  
 Florian RUNTSCH (Engineer)  
 Dr. Sébastien SALLARD (Scientist)  
 Dirk SCHEUBLE (Engineer)  
 Prof. Dr. Thomas J. SCHMIDT (Laboratory Head)  
 Dr. Daniel STREICH (Post Doctoral Researcher)  
 Jürg THUT (Technician)  
 Dr. Sigita TRABESINGER-URBONAITE (Scientist)  
 Dr. Claire VILLEVIEILLE (Group Leader)

## PhD Students

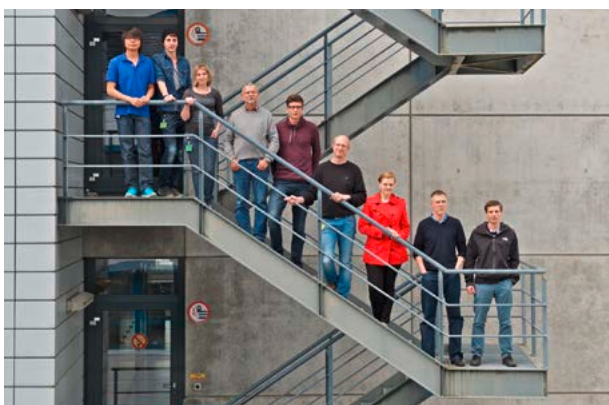
Albert ALBERT  
 Ugljesa BABIC  
 Tobias BINNINGER  
 Johannes BIESDORF  
 Lucien BOULET-ROBLIN  
 Joanna CONDER  
 Sebastian EBERHARDT  
 Tom ENGL  
 Giulio FERRARESI  
 Eibar Joel FLORES CEDEÑO  
 Antoni FORNER-CUENCA  
 Jonathan HALTER  
 Minglong HE  
 Sebastian HENNING  
 Baejung KIM  
 Daniela LEANZA  
 Maria Victoria MANZI OREZZOLI  
 Olga NIBEL  
 Yohan PARATCHA  
 Hai-Jung PENG  
 Mauro POVIA  
 Annett RABIS  
 Martin REICHARDT  
 Tomasz ROJEK  
 Sebastian SCHMIDT  
 Jakub SEWERYN  
 Véronique SPROLL  
 Michel SUERMANN  
 Susan TAYLOR  
 Sandra TEMMEL  
 Simon TSCHUPP  
 Leonie VOGT  
 Kay WALTAR



*The Electrochemistry Laboratory, May 2015.*



*Fuel Cells Systems and Diagnostics Group, May 2015.*



*Membranes and Electrochemical Cells Group, May 2015.*



*Electrocatalysis and Interfaces Group, May 2015*



*Section Electrochemical Energy Storage, December 2015.*

## DISSERTATIONS 2015

**Annett Rabis**



*The impact of metal oxides on the electrocatalytic activity of platinum catalysts*

Ph.D. Thesis No. 23106, ETH Zürich, November 2015.

Examiners: Prof. Dr. T.J. Schmidt, PSI Villigen/ETH Zürich  
Prof. Dr. Ch. Copéret, ETH Zürich  
Dr. E. Fabbri, PSI Villigen

**Tom Engl**



*Electrode degradation in high-temperature polymer electrolyte fuel cells: Characterization, Mechanisms and Mitigation*

Ph.D. Thesis No. 23084, ETH Zürich, November 2015.

Examiners: Prof. Dr. T.J. Schmidt, PSI Villigen/ETH Zürich  
Prof. Dr. A. Wokaun, PSI Villigen/ETH Zürich  
Dr. L. Gubler, PSI Villigen

# EXCHANGE STUDENTS, DIPLOMA THESES, SUMMER STUDENTS, GUEST SCIENTISTS

**Ahmet O. Tezel**

Norwegian University of Science and Technology,  
Trondheim, Norway

*SEI forming reactions on graphitic anodes in Li-ion batteries: Effect of anion receptor and NaPF<sub>6</sub> addition*  
July 2014 – July 2015 (Battery Materials).

**Iris Kováčsovics**

ETH Zürich

*Electrochemical studies of Mg or Ca doped HE-NMC as insertion material in Li-ion half- and full-cells*  
September 2014 – January 2015 (Battery Materials).

**Anna Tobler**

ETH Zürich

*Development and validation of a simple EIS model for Li-ion batteries*  
February – April 2015 (Battery Materials).

**Polychronis Patapis**

ETH Zürich

*Fuel cell characterization: hardware and software implementation and single cell testing*  
October 2014 – March 2015 (Membranes and Electrochemical Cells).

**Christian Hänsel**

ETH Zürich

*Lithium conducting polymer electrolytes with polysulfide barrier properties used as separator materials in Li/S batteries*  
Feb. – June 2015 (Membranes and Electrochemical Cells).

**Thomas Kiupel**

Hochschule Ansbach, Ansbach, Germany

*Characterization of an Electrochemical Hydrogen Compressor*  
February – August 2015 (Fuel Cell Systems and Diagnostics).

**Noemi Poyatos Salguero**

University of Granada, Granada, Spain

*Pt coverage of model catalysts: active vs inactive area and its consequences on ORR limiting currents in a flow cell*  
March – August 2015 (Electrocatalysis and Interfaces).

**Patricia Gröninger**

ETH Zürich

*Building and testing of an experimental fuel cell with an evaporative cooling concept*  
May – December 2015 (Neutron Radiography).

**Guillaume Gaudemer**

Grenoble INP Phelma, Grenoble, France

*Extensive characterization of radiation grafted membranes for the all-vanadium redox flow battery*  
May – July 2015 (Membranes and Electrochemical Cells).

**Yuya Yamashita**

University of Yamanashi, Yamanashi, Japan

*Perovskites for the oxygen evolution reaction*  
June – December 2015 (Electrocatalysis and Interfaces).

**Kazuhiro Takanohashi**

University of Yamanashi, Yamanashi, Japan

*Investigation of porous Ti-sinter materials for electrolyzer application by X-ray imaging*  
June – December 2015 (Fuel Cell Systems and Diagnostics).

**Mohamed Mahmoud Nasef**

University Teknologi Malaysia, Kuala Lumpur, Malaysia

*Exploration of novel grafted polymer structures for CO<sub>2</sub> separation applications*  
June – July 2015 (Membranes and Electrochemical Cells).

**Elaine Kelly**

Trinity College Dublin, Ireland

*Investigation into electrode materials for sodium-ion batteries*

June – August 2015 (Battery Materials).

**Simon Escobar Steinvall**

Imperial College London, London, UK

*Characterization of gas diffusion layer materials by X-ray imaging*

June – September 2015 (Fuel Cell Systems and Diagnostics).

**Ivan Abramovic**

ETH Zürich

*Validation of a mass transport model in thin-film rotating disk electrodes*

August – November 2015 (Electrocatalysis and Interfaces).

**Anna Gerlitz**

Westfälische Wilhelms-Universität, Münster, Germany

*Atomic layer deposition on LNMO electrode and investigation of related Na - spinel materials*

August – October 2015 (Battery Materials).

**Rémi Bérard**The Graduate School of Chemistry, Biology and Physics,  
Bordeaux, France*Hyform Project – Alimentation d'une pile à combustible par un reformeur d'hydrogène basé sur l'acide formique*  
August – October 2015 (Membranes and Electrochemical Cells).**Petra Hehet**

Ludwig-Maximilians-Universität, München, Germany

*Swift-heavy ion technique for the preparation of proton exchange membranes*

August – December 2015 (Membranes and Electrochemical Cells).

**Fabio Oldenburg**

Humboldt-Universität zu Berlin, Berlin, Germany

*Radiation grafted membranes for redox flow batteries*

September 2015 – May 2016 (Membranes and Electrochemical Cells).

## SEMINAR, INVITED SPEAKERS

### Dr. Philippe Adelhelm

Institute of Physical Chemistry, Justus-Liebig-University  
Giessen, Giessen, Germany

*From lithium to sodium batteries: Similarities and surprises*  
January 14, 2015.

### Prof. Brett Lucht

University of Rhode Island, Kingston RI, USA

*Electrolytes for lithium ion batteries: A mechanistic understanding*  
March 11, 2015.

### Prof. Bing-Joe Hwang

National Taiwan University of Science and Technology,  
Taipei, Taiwan

*Understanding of Li-rich layered oxide cathode materials for lithium ion batteries*  
May 29, 2015.

### Assoc. Prof. Fu-Ming Wang

National Taiwan University of Science and Technology,  
Taipei, Taiwan

*In situ formation of pentafluorophosphate benzimidazole anion mutually stabilizes high-temperature and high-voltage performance of Li-rich cathode ( $\text{Li}[\text{Ni}_x\text{Li}_{(1-2x)/3}\text{Mn}_{(2-x)/3}]\text{O}_2$  ( $0 \leq x \leq 0.5$ )) based lithium-ion batteries*  
May 29, 2015.

### Prof. Katsuyoshi Kakinuma

University of Yamanashi, Fuel Cell Nanomaterials Center,  
Yamanashi, Japan

*Electrochemical activity and durability of Pt catalysts supported on conducting ceramics with fused aggregated network structure*  
June 3, 2015.

### Prof. Junji Inukai

University of Yamanashi, Fuel Cell Nanomaterials Center,  
Yamanashi, Japan

*Oxygen inside/outside of an MEA*  
June 3, 2015.

**Mogens Mogensen**, Research Professor  
DTU Energy, Technical University of Denmark, Roskilde,  
Denmark

*Some proposals for improving characterization, performance and cost of PEMEC*  
June 30, 2015.

### Amir Niroumand

Eickerling Group, Simon Fraser University, Burnaby,  
Canada

*Intelligent fuel cell diagnostics*  
July 6, 2015.

### Prof. Marie-Cecile Pera / Prof. Daniel Hissel

Université de Franche-Comté, FEMTO-ST, FCLAB, Belfort,  
France

*Activities on fuel cell system developed at FCLAB*  
July 8, 2015.

### Dr. Michael Marino

Max-Planck-Institut für Festkörperforschung, Stuttgart,  
Germany

*Polyelectrolyte membranes for fuel cells and batteries*  
August 26, 2015.

### Dr. Mathias Reum

Senior Manager Research & Development, Proton Motor  
Fuel Cell GmbH, Puchheim, German

*Industrialization of PEM fuel cells – challenges and barriers*  
September 2, 2015.

**Dr. Yu Morimoto**

Toyota Central R&D Labs. Inc., Nagakute, Aichi, Japan

*Alternative PEFC catalysts for future commercial FCVs*  
September 18, 2015.

**Prof. Renaud Bouchet**

LEPMI-Université de Grenoble, Grenoble, France

*Materials for electrochemical storage; a focus on solid-state technologies as an innovative storage*  
September 23, 2015.

**Bernard Lestriez**

IMN Institut des matériaux de Nantes, Nantes, France

*Design of the composite electrode formulation for lithium batteries*  
October 16, 2015.

## AWARDS

Albert Albert

*Best Poster Prize Winner*

A. Albert, T.J. Schmidt, L. Gubler

*Stability of radiation grafted polymer electrolyte membranes for water electrolysis cells.*65<sup>th</sup> Annual Meeting of the International Society of Swiss Chemical Society Fall Meeting 2015, EPFL, Lausanne, September 4, 2015.

Xi Cheng

*2<sup>nd</sup> Poster Prize Winner*

X. Cheng, E. Fabbri, M. Nachttegaal, I.E. Castelli, M. El Kazzi, R. Haumont, N. Marzari, T.J. Schmidt

*Oxygen evolution reaction: correlation between electronic property and OER activity for  $La_{1-x}Sr_xCoO_3$  ( $0 \leq x \leq 1$ ) perovskite oxides.*

MARVEL review and retreat, EPFL, Lausanne, September 3–4, 2015.

Sebastian H. Eberhardt

*ECS Travel Grant for the 228<sup>th</sup> ECS Meeting, Phoenix, AZ, USA*

Maria Geormezi

*Best Poster Prize Winner*

M. Geormezi, P.A. Patapis, L. Bonorand, T.J. Schmidt, L. Gubler

*Electrochemical characterization of catalyst-coated radiation grafted membranes under different LT-PEFC operating conditions.*6<sup>th</sup> International Conference on Fundamentals and Development of Fuel Cells (FDfC2015), University of Toulouse, Toulouse, France, February 3–5, 2015.

Minglong He

*Best Oral Presentation Award*

M. He, K. Fic, E. Frackowiak, P. Novák, E.J. Berg

*In situ gas release investigation of active carbon based supercapacitors with an aqueous electrolyte.*6<sup>th</sup> International Conference on Carbon for Energy Storage/ Conversion and Environment Protection, Poznan, Poland, October 18–22, 2015.

Susan Taylor

*Best Poster Prize Winner*

S.M. Taylor, A. Pătru, T.J. Schmidt

*Influence of carbon surface modification on vanadium (V) reduction for redox flow cell applications.*

ECS Conference on Electrochemical Energy Conversion &amp; Storage with SOFC-XIV, Glasgow, United Kingdom, July 26–31, 2015.

## CONFERENCES – SYMPOSIA

**2<sup>nd</sup> Symposium of SCCER HaE Storage  
May 5, 2015.**

### *Heat and Electricity Storage – 2<sup>nd</sup> Symposium*

#### Organizers:

Thomas J. Schmidt, SCCER HaE Storage/Electrochemistry  
Laboratory  
Jörg Roth, Ursula Ludgate, SCCER Heat and Electricity  
Storage

#### Contributions from (in order of appearance):

Nigel Brandon, Imperial College, London, UK  
Claire Villevieille, Paul Scherrer Institut, Villigen,  
Switzerland  
Timothy Patey, ABB Schweiz AG, Baden, Switzerland  
Maurizio Barbato, SUPSI, Manno, Switzerland  
Stefan Zunft, DLR, Stuttgart, Germany  
Kevin Sivula, EPFL, Lausanne, Switzerland  
Christian von Olshausen, sunfire GmbH, Dresden ,  
Germany  
Christian Bauer, Paul Scherrer Institut, Villigen,  
Switzerland  
David Parra, University of Geneva, Geneva, Switzerland  
Peter Jansohn, Paul Scherrer Institut, Villigen,  
Switzerland



*From left to right. Front row: Cordelia Gloor, Claire Villevieille, Maurizio Barbato, Timothy Patey, Kevin Sivula, Ursula Ludgate, Petr Novák, Stefan Zunft. Back row: David Parra, Nigel Brandon, Christian von Olshausen, Christian Bauer, Thomas J. Schmidt, Jörg Roth, Peter Jansohn.*

## 31<sup>st</sup> PSI Electrochemistry Symposium May 6, 2015.

### *Electrochemical Energy Storage: A Key for Future Energy Systems*

#### Organizers:

Thomas J. Schmidt, Cordelia Gloor, Electrochemistry Laboratory  
Jörg Roth, Ursula Ludgate, SCCER Heat & Electricity Storage

#### Contributions from (in order of appearance):

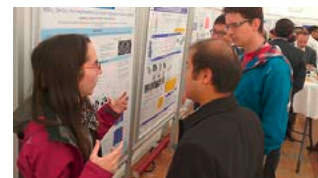
Nathan Lewis, California Institute of Technology, Pasadena, CA, USA  
Gabriele Centi, University of Messina, Italy  
Detlef Stolten, Research Center Jülich, Germany  
Jean-Marie Tarascon, Collège de France, Paris  
Martin Winter, University of Münster, Germany



From left to right: Gabriele Centi, Nathan East, Lorenz Gubler, Cordelia Gloor, Claire Villevieille, Thomas J. Schmidt, Ursula Ludgate, Detlef Stolten, Petr Novák, Martin Winter, Jean-Marie Tarascon, Jörg Roth, Felix N. Büchi



Registration, talks, poster session, lunch and discussions...



# REVIEW ACTIVITIES OF THE LABORATORY

## Journals

- A** ACS Applied Materials & Interfaces ♦ Advanced Energy Materials ♦ Advanced Functional Materials ♦ Advanced Materials ♦ Angewandte Chemie International Edition ♦ Applied Surface Science
- C** Carbon ♦ Chemical Science ♦ Chemical Reviews ♦ Chemistry of Materials ♦ ChemSusChem
- E** ECS Electrochemistry Letters ♦ Electrochemistry Communications ♦ Electrochimica Acta ♦ Energy and Environmental Science
- F** Fuel Cells
- I** International Journal of Hydrogen Energy
- J** Journal of the American Chemical Society ♦ Journal of the Electrochemical Society ♦ Journal of Fuel Cell Science and Technology ♦ Journal of Membrane Science ♦ Journal of Physical Chemistry ♦ Journal of Power Sources ♦ Journal of Solid State Electrochemistry ♦ Journal of Synchrotron Radiation
- N** Nature ♦ Nature Materials
- P** Physical Chemistry Chemical Physics
- R** RSC Advances
- S** Science ♦ Scientific Reports ♦ Solid State Ionics

## Organisations

- A** Agence National de Recherche, France ♦ Alexander von Humboldt-Stiftung, Germany
- D** Danish Council of Strategic Research ♦ Deutsche Forschungsgemeinschaft
- E** ETH Zürich Research Commission ♦ European Commission Research Executive Agency ♦ European Research Council
- F** FFG Österreichische Forschungsförderungsgesellschaft
- N** National Sciences and Engineering Research Council of Canada ♦ National Science Foundation, USA
- S** SNF (Schweizerischer Nationalfonds) ♦ Society in Science
- T** The Research Council of Norway
- Q** Qatar National Research Fund

## External Dissertations: Review Activities

Thomas J. Schmidt:

- P.S.G. Lou, EPF Lausanne
- S. Sondergaard, DTU Lyngby, Denmark
- F. Zhou, University of Aalborg, Denmark

Felix N. Büchi:

- Benjamin Straubhaar, Université de Toulouse, France

Petr Novák:

- Oliver Waser, D-MAVT, ETH Zürich

# INDUSTRIAL PARTNERS

## Collaborations with Industrial Partners

The Laboratory had the pleasure to collaborate with the following industrial partners during the year 2015:

- B** BASF SE, Ludwigshafen, Germany
- C** Cellera, Caesarea, Israel
- E** ElringKlinger, Dettingen, Germany
- I** IBM Zürich Research Laboratory, Rüschlikon ♦ IMERYS Graphite & Carbon, Bodio
- S** Saft SA, Bordeaux, France ♦ Siemens AG, Erlangen, Germany ♦ Swiss Hydrogen SA, Fribourg
- T** Toyota Motor Europe, Zaventem, Belgium
- U** UMICORE AG & Co. KG, Hanau, Germany

## DOCUMENTATION

Project Collaborations  
with External Partners

## BFE

P. Boillat Project leader	<i>In situ study of water transport processes in polymer electrolyte electrolyzers with neutron imaging</i>
F.N. Büchi Project leader	<i>High Pressure Polymer Electrolyte Electrolysis with Belenos Clean Power Holding, Biel/Bienne</i>
L. Gubler Project leader	<i>EL YDEG – Understanding of degradation signatures in water electrolyzers operated with variable input</i>
T.J. Schmidt Project leader	<i>Renewable Energies in Future Energy Supply (RENERG<sup>2</sup>)</i>

## CCEM

C. Bach, T.J. Schmidt Project leaders	<i>Renewable Energies in Future Energy Supply (RENERG<sup>2</sup>) with ETH Zürich, Empa Dübendorf, EPF Lausanne, ZAHW Winterthur</i>
F.N. Büchi Project leader	<i>ADMIST (Advanced Understanding of Micro Structures in Fuel Cells and Batteries through X-ray Imaging) with Laboratory for Nanoelectronics ETH Zürich</i>
L. Gubler Co-project leader	<i>Hy-Form: Formic acid – chemical storage of electrical energy and on-site hydrogen production for use in PEM fuel cells with EPF Lausanne, Granit Technologies SA, ZHAW Winterthur</i>
T.J. Schmidt Project leader	<i>DURACAT (Highly durable oxide-based catalysts for polymer electrolyte fuel cells) with ETH Zürich, CSEM Neuchâtel, University of Southampton UK and Umicore AG &amp; Co KG.</i>
T.J. Schmidt Principal investigator	<i>From tailored CO<sub>2</sub>-sorber to optimized CO<sub>2</sub> electrochemical reduction catalyst: building tools for converting waste CO<sub>2</sub> to valuable chemicals with ETH Zürich</i>

## EU

P. Boillat Project leader	<i>H<sub>2</sub>FC (Integrating European infrastructure to support science and development of hydrogen- and fuel cell technologies towards European strategy for sustainable competitive and secure energy)</i>
F.N. Büchi Project leader	<i>IMPALA (Improved PEMFC with advanced water management and gas diffusion layers for automotive application)</i>
F.N. Büchi Project leader	<i>Auto-Stack CORE (Automotive Fuel Cell Stack Cluster Initiative for Europe)</i>
L. Gubler Project leader	<i>NOVEL (Novel materials and system designs for low cost, efficient and durable PEM electrolyzers)</i>

**KTI**

P. Novák Work package leader	<i>Swiss Competence Center for Energy Research (SCCER) – Heat &amp; Electricity Storage Advanced batteries and battery materials</i>
T.J. Schmidt Director	<i>Swiss Competence Center for Energy Research (SCCER) – Heat &amp; Electricity Storage</i>
T.J. Schmidt Principal investigator	<i>Swiss Competence Center for Energy Research (SCCER) – Heat &amp; Electricity Storage Catalytic and electrocatalytic CO<sub>2</sub> reduction</i>
C. Villevieille Principal investigator	<i>Swiss Competence Center for Energy Research (SCCER) – Heat &amp; Electricity Storage Advanced batteries and battery materials</i>

**SNSF**

E.J. Berg Project leader	<i>Interphase formation on high voltage and energy Li-ion cathodes (Ambizione Energy)</i>
P. Boillat Project leader	<i>Synthesis and characterization of porous materials with patterned wettability for advanced fuel cell water management strategies</i>
F.N. Büchi Co-project leader	<i>NFP70: Designing multifunctional materials for proton exchange membrane fuel cells with Institute for Computational Physics, ZHAW Winterthur</i>
E. Fabbri Project leader	<i>Designing novel electrocatalysts for fuel cells and electrolyzers by tailoring perovskite surface properties SNSF Ambizione project</i>
L. Gubler Project leader	<i>Radiation grafted proton conducting membranes for high-temperature polymer electrolyte fuel cells</i>
L. Gubler Project leader	<i>Lithium conducting polymer electrolytes with polysulphide barrier properties</i>
P. Novák Project leader	<i>New oxyphosphates as high specific charge electrode materials for lithium-ion batteries</i>
P. Novák Project leader	<i>In situ research on new generation of electrochemical capacitors (Polish-Swiss research programme)</i>
S. Sallard Project leader	<i>Hybrid organic-inorganic lithium metal diphosphonates and derivatives, new insertion materials for Li-ion batteries</i>
T.J. Schmidt Project leader	<i>NCCR Marvel Experimental Platform Project Development of advanced electrocatalysts for water splitting: Correlation between electronic structure, surface properties and electrochemical activity</i>
T.J. Schmidt Project leader	<i>Designing nano-extended multimetallic aerogel fuel cell catalysts for oxygen reduction reaction with TU Dresden, Germany</i>
T.J. Schmidt, L. Gubler Project leader/Co-project leaders	<i>Redox flow electrochemistry for power delivery and cooling (REPCOOL)</i>
C. Villevieille Project leader	<i>Surface and interface investigations of high density energy electrodes for sodium-ion batteries</i>

## PSI Research Commission

L. Gubler Co-project leader	<i>Structure-Property Correlations of Ion-Containing Polymers for Fuel Cells</i> Cross Initiative with Dr. U. Gasser; Dr. S. Balog, Université de Fribourg
T.J. Schmidt Co-project leader	<i>Improved Insight into Catalysis Mechanisms via Nanopatterned Metal Structures (Nanocat)</i> Cross Initiative with Prof. J. Gobrecht; Prof. J.A. van Bokhoeven

## Industry

M. El Kazzi Project leader	<i>Analyses of lithium-ion battery electrodes</i> Toyota Motor Europe NV/SA, Brussels, Belgium
P. Novák Project leader	<i>Forschungsnetzwerk «Elektrochemie und Batterien»</i> BASF SE, Ludwigshafen, Germany
T.J. Schmidt Project leader	<i>Advanced degradation studies on PBI/H<sub>3</sub>PO<sub>4</sub> based MEAs for high temperature PEFCs</i> BASF SE, Ludwigshafen, Germany
T.J. Schmidt Project leader	<i>Strained Pt/Perovskites as a novel class of oxygen reduction electrocatalysts</i> Dysenos
S. Trabesinger Project leader	<i>Graphite für Lithiumionen-Batterien</i> Imerys Graphite & Carbon, Bodio
C. Villevieille Project leader	<i>Study of full cell reaction mechanism of lithium-ion batteries using 5 V spinel materials</i> Saft SA, Bordeaux, France

## Teaching Activities

### University Level Teaching

Prof. Dr. P. Novák	<i>Elektrochemie</i> ETH Zürich, HS 2015
Prof. Dr. T.J. Schmidt	<i>Renewable Energy Technologies II, Energy Conversion &amp; Storage</i> ETH Zürich, SS 2015
Prof. Dr. T.J. Schmidt	<i>Physical Electrochemistry &amp; Electrocatalysis</i> ETH Zürich, SS 2015

### Lecture Courses at other Schools

J. Biesdorf	<i>Neutron imaging of liquid water in fuel cells</i> European Technical School on Hydrogen and Fuel Cells 2015.
-------------	--------------------------------------------------------------------------------------------------------------------

## Contributions to Courses at Universities, FHL, and other Institutes

- L. Gubler *Renewable Energy Technologies II, Energy Conversion & Storage*  
ETH Zürich, May 5, May 12, May 19, May 26, 2015.
- L. Gubler *Energy Storage Systems*  
Lucerne University of Applied Sciences and Arts, March 4, 2015.

## Publications

### Books and Reviewed Book Chapters

- T. Engl, L. Gubler,  
T.J. Schmidt *Catalysts and Catalyst Layers in HT PEFCs in High Temperature Polymer Electrolyte Fuel Cells – Approaches, Status, Perspectives*  
Springer Science + Business Media LLC, New York, Q. Li, D. Aili, H. Hjuler, J.O. Jensen (Eds.), doi:10.1007/978-3-319-17082-4 (2015).

### Peer Reviewed Papers

- B.D. Adams, R. Black,  
Z. Williams, R. Fernandes,  
M. Cuisinier, E. Jämstorp Berg,  
P. Novák, G.K. Murphy,  
L. F. Nazar *Towards a stable organic electrolyte for the lithium oxygen battery*  
doi: 10.1002/aenm.201400867, *Adv. Energy Mater.* **5**, 11 pages (2015).
- D. Aili, A. Vasiliev, J.O. Jensen,  
T.J. Schmidt, Q. Li *Methyl Phosphate Formation as a Major Degradation Mode of Direct Methanol Fuel Cells with Phosphoric Acid Based Electrolytes*  
doi: 10.1016/j.jpowsour.2015.01.010, *J. Power Sources* **279**, 517–521 (2015).
- A. Albert, T.J. Schmidt, L. Gubler *Radiation grafted polymer electrolyte membranes for water electrolysis cells – characterisation of key membrane properties*  
doi: 10.1021/acsami.5b04618, *ACS Appl. Mater. Interf.* **7**, 22203–22212 (2015).
- E.J. Berg, C. Villevieille, D. Streich,  
S. Trabesinger, P. Novák *Rechargeable batteries: grasping for the limits of chemistry*  
doi: 10.1149/2.0081514jes, *J. Electrochem. Soc.* **162**, A2468–A2475 (2015).
- P. Bernardo, J.M. Le Meins,  
L. Vidal, J. Dentzer, R. Gadiou,  
W. Märkle, P. Novák, M.E. Spahr,  
C. Vix Guterl *Influence of graphite edge crystallographic orientation on the first lithium intercalation in Li-ion battery*  
doi: 10.1016/j.carbon.2015.05.001, *Carbon* **91**, 458–467 (2015).
- J. Biesdorf, P. Stahl,  
M. Siegwart, T.J. Schmidt,  
P. Boillat *When size matters: Active area dependence of PEFC cold start capability*  
doi: 10.1149/2.0871510jes, *Journal of the Electrochemical Society* **162**, F1231–F1235 (2015)
- J. Biesdorf, A. Forner-Cuenca,  
T.J. Schmidt, P. Boillat *Impact of hydrophobic coating on mass transport losses in PEFCs*  
doi: 10.1149/2.0861510jes, *Journal of the Electrochemical Society* **162**, F1243–F1252 (2015)
- T. Binninger, M. Garganourakis,  
J. Han, A. Pătru, E. Fabbri,  
O. Sereda, R. Kötz, A. Menzel,  
T.J. Schmidt *Particle-support interferences in small-angle X-ray scattering from supported-catalyst materials*  
doi: 10.1103/PhysRevApplied.3.024012, *Phys. Rev. Applied* **3**, 024012 (2015).

- T. Binninger, R. Mohamed, K. Waltar, E. Fabbri, P. Levecque, R. Kötzt, T.J. Schmidt  
*Thermodynamic explanation of the universal correlation between oxygen evolution activity and corrosion of oxide catalysts*  
doi: 10.1038/srep12167, *Sci. Rep.* **5**, 12167 (2015).
- P. Bleith, H. Kaiser, P. Novák, C. Villevieille  
*In situ X-ray diffraction characterization of  $Fe_{0.5}TiOPO_4$  and  $Cu_{0.5}TiOPO_4$  as electrode material for sodium-ion batteries*  
doi: 10.1016/j.electacta.2015.06.105, *Electrochim. Acta* **176**, 18–21 (2015).
- P. Bleith, W. van Beek, H. Kaiser, P. Novák, C. Villevieille  
*Simultaneous in situ XAS and XRD studies on battery materials: the case of  $Fe_{0.5}TiOPO_4$*   
doi: 10.1021/jp511042x, *J. Phys. Chem. C* **119**, 3466–3471 (2015).
- P. Boillat, A. Iranzo, J. Biesdorf  
*Layer by Layer Segmentation of Water Distribution from Neutron Imaging of Large Scale Cells*  
doi: 10.1149/2.0511506jes, *Journal of the Electrochemical Society* **162**, F531–F536 (2015).
- L. Boulet-Roblin, M. El Kazzi, P. Novák, C. Villevieille  
*Surface/interface study on full  $xLi_2MnO_3(1-x)LiMO_2$  ( $M = Ni, Mn, Co$ )/graphite cells*  
doi: 10.1149/2.0491507jes, *J. Electrochem. Soc.* **162**, A1297–A1300 (2015).
- Y. Buchmüller, R. Hafner, A. Wokaun, T.J. Schmidt, L. Gubler  
*From Electrochemical Interface to Interphase (2D → 3D) on Ionomer Membranes*  
doi: 10.1002/celc.201402332, *ChemElectroChem* **2**, 338–342 (2015).
- C. Bünzli, H. Kaiser, P. Novák  
*Important aspects for reliable electrochemical impedance spectroscopy measurements of Li-ion battery electrodes*  
doi: 10.1149/2.1061501jes, *J. Electrochem. Soc.* **162**, A218–A222 (2015).
- X. Cheng, E. Fabbri, M. Nachtegaal, I.E. Castelli, M. El Kazzi, R. Haumont, N. Marzari, T.J. Schmidt  
*The oxygen evolution reaction on  $La_{1-x}Sr_xCoO_3$  perovskites: A combined experimental and theoretical study of their structural, electronic, and electrochemical properties*  
doi: 10.1021/acs.chemmater.5b03138, *Chemistry of Materials* **27**, 7662–7672, (2015).
- J. Conder, S. Urbonaite, D. Streich, P. Novák, L. Gubler  
*Taming the polysulphide shuttle in Li-S batteries by plasma-induced asymmetric functionalization of the separator*  
doi: 10.1039/C5RA13197A, *RSC Adv.* **5**, 79654–79660 (2015).
- J. Durst, A. Rudnev, A. Dutta, Y. Fu, J. Herranz, V. Kaliginedi, A. Kuzume, A. Permyakova, Y. Paratcha, P. Broeckmann, T.J. Schmidt  
*Electrochemical  $CO_2$  Reduction – A Critical View on Fundamentals, Materials and Applications*  
doi: 10.2533/chimia.2015.762015, *Chimia* **69** (12), 769–76 (2015).
- S.H. Eberhardt, M. Toulec, F. Marone, M. Stampanoni, F.N. Büchi, T.J. Schmidt  
*Dynamic Operation of HT-PEFC: In-Operando Imaging of Phosphoric Acid Profiles and (Re)distribution*  
doi: 10.1149/2.0751503jes, *J. Electrochem. Soc.* **162**, F310–F316 (2015).
- S.H. Eberhardt, T. Lochner, F.N. Büchi, T.J. Schmidt  
*Correlating Electrolyte Inventory and Lifetime of HT-PEFC by Accelerated Stress Testing*  
doi: 10.1149/2.0591512jes, *J. Electrochem. Soc.* **162**, F1367–F1372 (2015).
- S.H. Eberhardt, F. Marone, M. Stampanoni, F.N. Büchi, T.J. Schmidt  
*Imaging Phosphoric Acid Migration in High Temperature Polymer Electrolyte Fuel Cells by X-Ray Tomographic Microscopy*  
doi: 10.1149/06917.0591ecst, *ECS Trans.* **69**, 591–599 (2015).
- M. El Kazzi, I. Czekaj, E.J. Berg, P. Novák, M.A. Brown  
*Investigation of Li-ion solvation in carbonate based electrolytes using NAPP*  
doi: 10.1007/s11244-015-0518-2, *Topics in Catalysis* **59** (5), 628–634 (2015).
- J. Eller, F. Marone, F.N. Büchi  
*Operando sub-second tomographic imaging of water in PEFC gas diffusion layers*  
doi: 10.1149/06917.0523ecst, *ECS Trans.* **69** 523–531 (2015).

- T. Engl, L. Gubler, T.J. Schmidt *Think different! Carbon corrosion mitigation strategy in high temperature PEFC – A durability study*  
doi: 10.1149/2.0681503jes, *J. Electrochem. Soc.* **162**, F291–F297 (2015).
- E. Fabbri, X. Cheng, T.J. Schmidt *Highly Active Ba<sub>0.5</sub>Sr<sub>0.5</sub>Co<sub>0.8</sub>Fe<sub>0.2</sub>O<sub>3-δ</sub> Single Material Electrode towards the Oxygen Evolution Reaction for Alkaline Water Splitting Applications*  
doi: 10.1149/06917.0869ecst, *ECS Trans.* **69** (17), 869–875 (2015).
- E. Fabbri, M. Nachttegaal, X. Cheng, T.J. Schmidt *Superior Bifunctional Electrocatalytic Activity of Ba<sub>0.5</sub>Sr<sub>0.5</sub>Co<sub>0.8</sub>Fe<sub>0.2</sub>O<sub>3-δ</sub>/Carbon Composite Electrodes: Insight into the Local Electronic Structure*  
doi: 10.1002/aenm.201402033, *Adv. Energy Mater.* **5** (2015).
- E. Fabbri, X. Cheng, T.J. Schmidt *Highly active Ba<sub>0.5</sub>Sr<sub>0.5</sub>Co<sub>0.8</sub>Fe<sub>0.2</sub>O<sub>3-δ</sub> single material electrode towards the oxygen evolution reaction for alkaline water splitting applications*  
doi: 10.1149/06917.0869ecst, *ECS Transactions* **69**, 869–875 (2015).
- A. Forner Cuenca, J. Biesdorf, L. Gubler, P.M. Kristiansen, T.J. Schmidt, P. Boillat *Engineered water highways in fuel cells: radiation grafting of gas diffusion layers*  
doi: 10.1002/adma.201503557, *Adv. Mater.* **27**, 6317–6322 (2015).
- J.L. Gómez-Cámer, P. Novák *Polyacrylate Bound TiSb<sub>2</sub> Electrodes for Li-Ion Batteries*  
doi: 10.1016/j.jpowsour.2014.09.087, *J. Power Sources* **273**, 174–179 (2015).
- J.L. Gómez-Cámer, H. Thuv, P. Novák *Electrochemical study of Si/C composites with particulate and fibrous morphology as negative electrodes for lithium-ion batteries*  
doi: 10.1016/j.jpowsour.2015.06.067, *J. Power Sources* **294**, 128–135 (2015).
- M. He, E. Castel, A. Laumann, G. Nussli, P. Novák, E. Berg *In situ gas analysis of Li<sub>4</sub>Ti<sub>5</sub>O<sub>12</sub> based electrodes at elevated temperatures*  
doi: 10.1149/2.0311506jes, *J. Electrochem. Soc.* **162**, A870–A876 (2015).
- M. Hess, T. Sasaki, C. Villeveille, P. Novák *Combined operando X-ray diffraction-electrochemical impedance spectroscopy detecting solid solution reactions of LiFePO<sub>4</sub> in batteries*  
doi: 10.1038/NCOMMS9169, *Nature Communications* **6**, 8169, 9 pages (2015).
- A. Iranzo, P. Boillat, J. Biesdorf, A. Salva *Investigation of the liquid water distributions in a 50 cm<sup>2</sup> PEM fuel cell: Effects of reactants relative humidity, current density, and cathode stoichiometry*  
doi: 10.1016/j.energy.2015.01.101, *Energy* **82**, 914–921 (2015).
- D. Kundu, R. Black, E.J. Berg, L.F. Nazar *A highly active nanostructured metallic oxide cathode for aprotic Li O<sub>2</sub> batteries*  
doi: 10.1039/C4EE02587C, *Energy Environ. Sci.* **8**, 1292–1298 (2015).
- W. Liu, A.-K. Hermann, N.C. Bigall, P. Rodriguez, D. Wen, M. Oezaslan, T.J. Schmidt, N. Gaponik, A. Eychmüller *Noble-Metal Aerogels – Synthesis, Characterization, and Application as Electrocatalysts*  
doi: 10.1021/ar.500237c, *Acc. Chem. Res.* **48**, 154–162 (2015).
- I. Mayrhuber, F. Marone, M. Stampanoni, T.J. Schmidt, F.N. Büchi *Fast X-Ray Tomographic Microscopy: Investigating Mechanisms of Performance Drops During Freeze Starts of Polymer Electrolyte Fuel Cells*  
doi:10.1002/celc.201500132, *ChemElectroChem.* **2**, 1551–1559 (2015).
- E. McCalla, A.M. Abakumov, M. Saubanère, D. Foix, E.J. Berg, G. Rousse, M.L. Doublet, D. Gonbeau, P. Novák, G. Van Tendeloo, R. Dominko, J.M. Tarascon *Visualization and impact of O–O peroxo-like dimers in high capacity layered oxides for Li-ion batteries*  
doi: 10.1126/science.aac8260, *Science* **350** (6267), 1516–1521 (2015).

- E. McCalla, A.S. Prakash, E. Berg, M. Saubanère, A.M. Abakumov, D. Foix, B. Klobes, M.T. Sougrati, G. Rousse, F. Lepoivre, S. Maryappan, M.L. Doublet, D. Gonbeau, P. Novák, G. Van Tendeloo, R.P. Hermann, J.M. Tarascon  
*Reversible Li-intercalation through oxygen reactivity in Li-rich Li Fe Te oxide materials*  
doi: 10.1149/2.0991507jes, J. Electrochem. Soc. **162**, A1341–A1351 (2015).
- E. McCalla, M.T. Sougrati, G. Rousse, E. Jämstorp Berg, A. Abakumov, N. Recham, K. Ramesha, M. Sathiya, R. Dominko, G. Van Tendeloo, P. Novák, J.M. Tarascon  
*Understanding the roles of anionic redox and oxygen release during electrochemical cycling of lithium-rich layered  $\text{Li}_4\text{FeSbO}_6$*   
doi: 10.1021/jacs.5b01424, J. Am. Chem. Soc. **137**, 4804–4814 (2015).
- G.R. Meseck, E. Fabbri, T.J. Schmidt, S. Seeger  
*Silicone Nanofilament Supported Nickel Oxide: A New Concept for Oxygen Evolution Catalysts in Water*  
doi: 10.1002/admi.201500216, Adv. Mater. Interfaces **2** (2015).
- Q. Meyer, S. Ashton, R. Jervis, D.P. Finegan, P. Boillat, M. Cochet, O. Curnick, T. Reisch, P. Adcock, P.R. Shearing, D.J. Brett  
*The Hydro-electro-thermal Performance of Air-cooled, Open-cathode Polymer Electrolyte Fuel Cells: Combined Localised Current Density, Temperature and Water Mapping*  
doi: 10.1016/j.electacta.2015.08.106, Electrochimica Acta **180**, 307–315 (2015).
- R. Mohamed, X. Cheng, E. Fabbri, P. Levecque, R. Kötz, O. Conrad, T.J. Schmidt  
*Electrocatalysis of Perovskites: The Influence of Carbon on the Oxygen Evolution Activity*  
DOI: 10.1149/2.0861506jes, J. Electrochem. Soc. **162**, F579–F586 (2015)
- H. J. Peng, S. Urbonaitė, C. Villevieille, H. Wolff, K. Leitner, P. Novák  
*Consequences of electrolyte degradation for the electrochemical performance of  $\text{Li}_{1+x}(\text{Ni}_a\text{Co}_b\text{Mn}_{1-a-b})_{1-x}\text{O}_2$*   
doi: 10.1149/2.0061513jes, J. Electrochem. Soc. **162**, A7072–A7077 (2015).
- M. Reichardt, S. Sallard, P. Novák, C. Villevieille  
*Lithium chromium pyrophosphate as an insertion material for Li-ion batteries*  
doi: 10.1107/S2052520615017539, Acta Crystallographica, Section B **71** (Pt 6), 661–667 (2015).
- R. Robert, C. Bünzli, E.J. Berg, P. Novák  
*Activation mechanism of  $\text{LiNi}_{0.80}\text{Co}_{0.15}\text{Al}_{0.05}\text{O}_2$ : surface and bulk operando electrochemical, DEMS, and XRD analyses*  
doi: 10.1021/cm503833b, Chem. Mater. **27**, 526–536 (2015).
- R. Robert, P. Novák  
*Structural changes and microstrain generated on  $\text{LiNi}_{0.80}\text{Co}_{0.15}\text{Al}_{0.05}\text{O}_2$  during cycling: effects on the electrochemical performance*  
doi: 10.1149/2.0721509jes, J. Electrochem. Soc. **162**, A1823–A1828 (2015).
- S. Sallard, E. Castel, C. Villevieille, P. Novák  
*A low-temperature benzyl alcohol/benzyl mercaptan synthesis of iron oxysulfide/iron oxide composite materials for electrodes in Li-ion batteries*  
doi: 10.1039/c5ta03155a, Mater. Chem. A **3**, 16112–16119 (2015).
- T. Sasaki, C. Villevieille, Y. Takeuchi, P. Novák  
*Understanding inhomogeneous reactions in Li-ion batteries: operando synchrotron X-ray diffraction on two-layer electrodes*  
doi: 10.1002/advs.201500083, Adv. Sci. **2**, 6 pages (2015).
- M.J. Schmid, J. Xu, J. Lindner, P. Novák, R. Schuster  
*Concentration effects on the entropy of electrochemical lithium deposition: implications for  $\text{Li}^+$  solvation*  
doi: 10.1021/acs.jpcc.5b07670, J. Phys. Chem. B **119**, 13385–13390 (2015).

- S. Schmidt, D. Sheptyakov,  
J.C. Jumas, M. Medarde,  
P. Benedek, P. Novák, S. Sallard,  
C. Villevieille  
*Lithium iron methylene diphosphonate: a model material for new organic-inorganic hybrid positive electrode materials for Li-ion batteries*  
doi: 10.1021/acs.chemmater.5b02595, *Chem. Mater.* **27** (23), 7889–7895 (2015).
- P. Stahl, J. Biesdorf, P. Boillat,  
J. Kraft, K.A. Friedrich  
*Water Distribution Analysis in the Outer Perimeter Region of Technical PEFC Based on Neutron Radiography*  
doi: 10.1149/2.0351507jes, *J. Electrochem. Soc.* **162**, F677–F685 (2015).
- M. Suermann, T.J. Schmidt,  
F.N. Büchi  
*Investigation of mass transport losses in polymer electrolyte electrolysis cells*  
doi: 10.1149/06917.1141ecst, *ECS Trans.* **69** (17), 1141–1148 (2015).
- S. Urbonaite, T. Poux, P. Novák  
*Progress towards commercially viable Li–S battery cells*  
doi: 10.1002/aenm.201500118, *Adv. Energy Mater.* **5**(16) 1500118 (2015).
- C. Villevieille,  
A. Gorzkowska-Sobas,  
H. Fjellvåg, P. Novák  
*Freeze-dried  $\text{Li}_x\text{MoO}_3$  nanobelts used as cathode materials for Li-ion batteries: a bulk and interface study*  
doi: 10.1016/j.jpowsour.2015.07.082, *J. Power Sources* **297**, 276–282 (2015).
- C. Villevieille, M. Ebner,  
J.L. Gómez Cámer, F. Marone,  
P. Novák, V. Wood  
*Influence of conversion material morphology on electrochemistry studied with operando X-ray tomography and diffraction*  
doi: 10.1002/adma.201403792, *Adv. Mater.* **27**, 1676–1681 (2015).
- C. Villevieille, X.J. Wang,  
F. Krumeich, R. Nesper,  
P. Novák  
 *$\text{MoS}_2$  coating on  $\text{MoO}_3$  nanobelts: a novel approach for a high specific charge electrode for rechargeable Li-ion batteries*  
doi: 10.1016/j.jpowsour.2014.12.129, *J. Power Sources* **279**, 636–644 (2015).
- C. Villevieille, P. Novák  
*New  $\text{MSnS}_2$  ( $M = \text{Cu}, \text{Fe}$ ) electrode family as dual-performance electrodes for Li-S and Li-Ion batteries*  
doi: 10.1149/2.0121503jes, *J. Electrochem. Soc.* **162**, A284–A287 (2015).
- L.O. Vogt, M. El Kazzi,  
E. Jämstorp Berg, S. Pérez Villar,  
P. Novák, C. Villevieille  
*Understanding the interaction of carbonates and binder in Na-ion batteries: a combined bulk and surface study*  
doi: 10.1021/cm5039649, *Chem. Mater.* **27**, 1210–1216 (2015).
- K. Waiz, S.A. Tschupp,  
M. Oezaslan, T.J. Schmidt,  
J. Gobrecht, J. van Bokhoven,  
Y. Ecinci  
*High-Resolution and Large-Area Nanoparticle Arrays Using EUV Interference Lithography*  
doi: 10.1039/C5NR00565E, *Nanoscale* **7**, 7386–7393 (2015).
- M. Worsdale, A. Rabis, E. Fabbri,  
T.J. Schmidt, D. Kramer  
*Conductivity Limits of Extrinsicly Doped  $\text{SnO}_2$  Supports*  
doi: 10.1149/06917.1167ecst, *ECS Trans.* **69** (17), 1167–1178 (2015).
- Z. Zhang, Y. Buchmüller,  
L. Bonorand, A. Wokaun,  
T.J. Schmidt, L. Gubler  
*Effects of temperature and catalysts on chemical degradation of radiation grafted membranes in the polymer electrolyte fuel cell*  
doi: 10.1002/fuce.201500019, *Fuel Cells* **15**, 610–618 (2015).

## Talks

### Invited Talks

- E.J. Berg *In situ gas analysis for rechargeable lithium batteries*  
MRS Spring Meeting, San Francisco, CA, USA, April 7, 2015.
- E.J. Berg *Development of differential electrochemical mass spectrometry (DEMS) and its application for Li-O<sub>2</sub> batteries*  
IBM Research Center, Almaden, CA, USA, April 9, 2015.
- E.J. Berg *In situ gas analysis for rechargeable lithium batteries*  
Chemistry colloquium, Oldenburg University, Oldenburg, Germany, July 20, 2015.
- E.J. Berg *In situ gas characterization of rechargeable lithium batteries*  
Advanced Functional Materials Seminar, Linköping University, Linköping, Sweden, September 10, 2015.
- E.J. Berg *In situ gas analysis for rechargeable lithium batteries*  
SIRBATT Workshop, Bilbao, Spain, September 29, 2015.
- J. Biesdorf *Neutron imaging of water in fuel cells: from differential cells to stacks*  
9<sup>th</sup> Int. Symposium Hydrogen and Energy, Emmetten, Switzerland, January 25–30, 2015.
- P. Boillat *Fuel Cell Diagnostics through Neutron Imaging*  
ECS Conference on Electrochemical Conversion and Storage, Glasgow, Scotland, July 30, 2015.
- P. Boillat *Neutron imaging of fuel cells and lithium batteries*  
Neutron Imaging Workshop, Journées de la Diffusion Neutronique, Evian, France, October 6, 2015.
- F.N. Büchi *Brennstoffzellen – Grundlagen*  
Schweizerischer Verein des Gas- und Wasserfaches SVGW, Schwerzenbach, February 28, 2013.
- L. Gubler *Radiation grafting: tailored ion-conducting membranes for electrochemical applications*  
Asilomar Conference on Advances in Polymers for Fuel Cells and Energy Devices, Pacific Grove CA, USA, February 10, 2015.
- L. Gubler *Radiation grafting: tailoring of ion-conducting membranes for electrochemical applications*  
University of Surrey, Department of Chemistry, Guildford, UK, February 23, 2015.
- L. Gubler *Ion-conducting membranes for energy devices prepared by radiation grafting*  
The University of Nottingham, Faculty of Engineering, Nottingham, UK, February 26, 2015.
- L. Gubler *Radiation grafting: tailoring of ion-conducting membranes for electrochemical applications*  
Max Planck Institute (MPI) for Solid State Research, Department of Physical Chemistry of Solids, Stuttgart, Germany, May 11, 2015.

- E. Fabbri *Challenges towards the development of metal oxide electrocatalysts as oxygen electrodes in polymer electrolyte and alkaline water electrolyzers*  
Technical University of Denmark (DTU), Risø campus, Lyngby, Denmark, August 10, 2015.
- J. Herranz *Current Challenges in Electrocatalyst Development for Fuel-to-Energy and Energy-to-Fuel Conversion Devices*  
Catalysis for Energy UK-CH Meeting, Harwell, England, October 5, 2015.
- P. Novák *What is 'battery science'? (Interplay of bulk and surface)*  
Seminar at the University of Southampton, Southampton, UK, March 6, 2015.
- P. Novák *Interface reactions in nonaqueous batteries: a journey from 3 to 5 Volts*  
Plenary lecture at the 11<sup>th</sup> ECHEMS Meeting, Bad Zwischenahn, Germany, June 16, 2015.
- P. Novák *Aktuelle und zukünftige Batterien: Realität vs. Wunschdenken*  
Weiterbildungsseminar des Forum VERA, Pfäffikon SZ, Switzerland, September 11, 2015.
- P. Novák *How to understand the electrochemistry of battery materials?*  
Keynote presentation at the 66<sup>th</sup> ISE Annual Meeting, Taipei, Taiwan, October 5, 2015.
- P. Novák *Development of battery materials: basics, unknown effects, and beyond*  
Keynote lecture at the 2<sup>nd</sup> Nordic Battery Conference (NORDBATT), Trondheim, Norway, December 2, 2015.
- P. Novák *Basics of battery materials, unknown effects, and beyond*  
Seminar at the Max Planck Institute for Solid State Research, Stuttgart, Germany, December 8, 2015.
- T.J. Schmidt *The Swiss Competence Center for Energy Research (SCCER) Heat & Electricity Storage*  
2<sup>nd</sup> Swiss Symposium Thermal Energy Storage, Luzern, January 16, 2015.
- T.J. Schmidt *The Swiss Competence Center for Energy Research (SCCER) Heat & Electricity Storage*  
Novatlantis Bauforum, Luzern, January 25, 2015.
- T.J. Schmidt *The Swiss Competence Center for Energy Research (SCCER) Heat & Electricity Storage*  
9<sup>th</sup> Int. Symposium Hydrogen and Energy, Emmetten, Switzerland, January 25–30, 2015.
- T.J. Schmidt *Electrolysis and Renewable Hydrogen as Basis for Power-to-Gas*  
Empa Akademie – Power to Gas in der Mobilität, Dübendorf, February 25, 2015.
- T.J. Schmidt *Oxygen Electrocatalysis Using Metal Oxides – News and Insights*  
MRS Spring Meeting 2015 – Symposium Development of Oxygen Reduction Reaction (ORR) and Oxygen Evolution Reaction (OER) Materials in Energy Storage and Conversion Systems, San Francisco, CA, USA, April 6–10, 2015.
- T.J. Schmidt *Oxygen Electrocatalysis in Fuel Cells and Electrolyzers*  
NCCR Marvel Junior Retreat, Männedorf July 7–10, 2015.
- T.J. Schmidt *Nanoparticles in Electrocatalysis*  
Nanosa15 – Nanoscale Assemblies of Semiconductor Nanocrystals, Metal Nanoparticles and Single Molecules: Theory, Experiment and Application, Dresden, Germany, August 24–28, 2015.
- T.J. Schmidt *The Oxygen Evolution Reaction – The Key for Efficient Hydrogen Production*  
ElectroChem2015, Delft, The Netherlands, September 28, 2015.

- T.J. Schmidt *New Oxygen Electrocatalysts for Fuel Cells and Electrolyzers*  
Meeting Danish Electrochemical Society 2015, Copenhagen, Denmark, October 1–2, 2015.
- T.J. Schmidt *ECS Short Course Polymer Electrolyte Fuel Cells*  
Phoenix, AZ, USA October 12, 2015.  
(T.J. Schmidt, H.A. Gasteiger)
- T.J. Schmidt *The Swiss Competence Center for Energy Research Heat & Electricity Storage: Background, Topics and Contributions from Paul Scherrer Institute*  
Joint Center for Energy Storage Research (JCESR), Argonne National Laboratory, Argonne, IL, USA, October 19, 2015.
- T.J. Schmidt *The Electrocatalysis of Oxygen Electrodes for Electrochemical Energy Conversion Devices*  
Materials Sciences Division, Argonne National Laboratory, Argonne, IL, USA, October 19, 2015.
- T.J. Schmidt *Global Trends and Activities in Fuel Cell R&D*  
PEFC Workshop HySA/Catalysis, University of Cape Town, Cape Town, South Africa, November 19, 2015.
- T.J. Schmidt *Quo Vadis High Temperature PEFC ?*  
University of Aalborg, Department of Energy Technology, Aalborg, Denmark, November 30, 2015.

## Contributed Talks

- A. Albert, T.J. Schmidt, L. Gubler *Properties and stability of radiation grafted polymer electrolyte membranes for water electrolysis cells*  
Pacific Polymer Conference 14, Kauai, Hawaii, USA, December 9–13, 2015.
- T. Binninger *In situ small-angle X-ray scattering for the analysis of electrochemical degradation of metal oxide supported Pt nanoparticles*  
227<sup>th</sup> ECS Meeting, Chicago, May 24–28, 2015.
- F.N. Büchi, I. Mayrhuber, T.J. Schmidt *Imaging Phosphoric Acid Migration in High Temperature Polymer Electrolyte Fuel Cells by X-Ray Tomographic Microscopy*  
228<sup>th</sup> ECS Meeting, Phoenix, AZ, USA, October 11–15, 2015.
- F.N. Büchi, M. Suermann, T.J. Schmidt *Imaging Phosphoric Acid Migration in High Temperature Polymer Electrolyte Fuel Cells by X-Ray Tomographic Microscopy*  
228<sup>th</sup> ECS Meeting, Phoenix, AZ, USA, October 11–15, 2015.
- X. Cheng, E. Fabbri, M. Nachtegaal, I.E. Castelli, M. El Kazzi, R. Haumont, N. Marzari, T.J. Schmidt *The oxygen evolution reaction on  $La_{1-x}Sr_xCoO_3$  perovskites: A combined experimental and theoretical study of their structural, electronic, and electrochemical properties*  
66<sup>th</sup> ISE Annual Meeting, Taipei, Taiwan, October 4–9, 2015.
- J. Conder, L. Gubler, P. Novák, S. Urbonaite *Taming the polysulfide shuttle in Li-S batteries: a functionalized separator obtained by plasma induced graft copolymerization*  
MRS Spring Meeting, San Francisco, CA, USA, April 6, 2015.
- J. Durst, A.A. Permyakova, Y. Paratcha, J. Herranz, T.J. Schmidt *Co-electrolysis cell configuration for CO<sub>2</sub> electrochemical reduction*  
228<sup>th</sup> ECS Meeting, Phoenix, AZ, USA, October 11–15, 2015.

- S.H. Eberhardt, F.N. Büchi, T.J. Schmidt *Accelerated stress testing of HT-PEFC: the effect of electrolyte loss on cell performance*  
5<sup>th</sup> European PEFC & H<sub>2</sub> Forum, Luzern, June 30 – July 3, 2015.
- S.H. Eberhardt, F. Marone, M. Stampanoni, F. N. Büchi, T.J. Schmidt *Imaging Phosphoric Acid Migration in High Temperature Polymer Electrolyte Fuel Cells by X-Ray Tomographic Microscopy*  
228<sup>th</sup> ECS Meeting, Phoenix, AZ, USA, October 11–15, 2015.
- J. Eller, F. Marone, F.N. Büchi *Transient in-operando tomographic imaging of water in PEFC gas diffusion layers*  
12<sup>th</sup> Symposium on Fuel Cell and Battery Modelling and Experimental Validation – ModVal 12, Freiburg-Munzingen, Germany, March 26–27, 2015.
- J. Eller, F. Marone, F.N. Büchi *3D Transient tomographic Imaging of the water distribution in polymer electrolyte fuel cells*  
Interpore Conference 2015, Padua, Italy, May 18–21, 2015.
- J. Eller, F. Marone, F.N. Büchi *Operando sub-second tomographic imaging of water in PEFC gas diffusion layers*  
228<sup>th</sup> ECS Meeting, Phoenix, AZ, USA, October 11–15, 2015.
- E. Fabbri, X. Cheng, T.J. Schmidt *Ba<sub>0.5</sub>Sr<sub>0.5</sub>Co<sub>0.8</sub>Fe<sub>0.2</sub>O<sub>3-δ</sub> Single Material Electrode towards the Oxygen Evolution Reaction*  
228<sup>th</sup> ECS Meeting, Symposium on Polymer Electrolyte Fuel Cells 15, Phoenix, AZ, USA, October 11–15, 2015.
- A. Forner-Cuenca, J. Biesdorf, L. Gubler, T.J. Schmidt, P. Boillat *Novel gas diffusion layers with patterned wettability*  
6<sup>th</sup> International Conference on Development and Fundamentals of Fuel Cells, Toulouse, France, February 4, 2015.
- A. Forner-Cuenca, J. Biesdorf, L. Gubler, T.J. Schmidt, P. Boillat *Advanced water management strategies: novel gas diffusion layers with patterned wettability*  
12<sup>th</sup> Symposium for Fuel Cell and Battery Modelling and Experimental Validation, Freiburg, Germany, March 27, 2015.
- A. Forner-Cuenca, J. Biesdorf, L. Gubler, T.J. Schmidt, P. Boillat *Engineering the water transport: diffusion layers with patterned wettability*  
228<sup>th</sup> ECS Meeting, Phoenix, AZ, USA, October 11–15, 2015.
- L. Gubler, O. Nibel, L. Bonorand *Redox flow battery membranes with improved vanadium-ion barrier properties*  
The International Flow Battery Forum (IFBF), Glasgow, UK, June 16–17, 2015.
- L. Gubler, O. Nibel, L. Bonorand, T.J. Schmidt *Redox flow battery membranes with improved vanadium-ion barrier properties*  
ECS Conference on Electrochemical Energy Conversion & Storage with SOFC-XIV, Glasgow, UK, July 26–31, 2015.
- S. Henning, J. Herranz, L. Kühn, A. Eychmüller, T.J. Schmidt *Bimetallic Aerogels: Nanostructured Oxygen Reduction Reaction Electrocatalysts*  
228<sup>th</sup> ECS Meeting, Symposium on Polymer Electrolyte Fuel Cells 15, Phoenix, AZ, USA, October 11–15, 2015.
- M. He, K. Fic, E. Frąckowiak, P. Novák, E.J. Berg *In situ gas release investigation of active carbon based supercapacitors with an aqueous electrolyte*  
6<sup>th</sup> International Conference on Carbon for Energy Storage/Conversion and Environment Protection, Poznan, Poland, October 18–22, 2015.
- M. He, P. Novák, E.J. Berg *In situ gas investigation for Li-ion batteries*  
Inorganic Chemistry Christmas Symposium, ETH Zürich, December 16, 2015.
- A. Lamibrac, J. Roth, F. Marone, F.N. Büchi *Investigation of liquid water transport in GDLs using X-ray tomographic microscopy*  
6<sup>th</sup> International Conference on Fundamentals and Development Fuel Cell (FDfC), Toulouse, France, February 3–5, 2015.

- A. Lamibrac, J. Roth, J. Eller,  
F. Marone, F.N. Büchi  
*Characterization of liquid water invasion in GDLs using X-ray Tomographic Microscopy*  
228<sup>th</sup> ECS Meeting, Phoenix, AZ, USA, October 11–15, 2015.
- Y. Paratcha, J. Herranz, J. Durst,  
A.A. Permyakova, T.J. Schmidt  
*CO<sub>2</sub>-reduction to syngas on Au-surfaces: a differential electrochemical mass spectrometry (DEMS) study*  
ECS Conference on Electrochemical Energy Conversion & Storage with SOFC-XIV,  
Glasgow, UK, July 26–31, 2015.
- A. Pătru, E. Fabbri, R. Kötz,  
T.J. Schmidt  
*New Oxide Catalyst Support Generation for PEFC – Application in MEAs, Performance and Stability Issues*  
ECS Conference on Electrochemical Energy Conversion & Storage with SOFC-XIV,  
Glasgow, UK, July 26–31, 2015.
- A. Pătru, J. Biesdorf,  
A. Forner Cuenca, E. Fabbri,  
P. Boillat, T.J. Schmidt  
*Performance and Stability of New Oxide Catalyst Supports under PEFC Operating Conditions*  
66<sup>th</sup> ISE Annual Meeting, Taipei, Taiwan, October 4–9, 2015.
- H. J. Peng, S. Urbonaite,  
C. Villeveille, H. Wolf, K. Leitner,  
P. Novák  
*Consequences of electrolyte degradation for the electrochemical performance of NCM battery materials*  
66<sup>th</sup> ISE Annual Meeting, Taipei, Taiwan, October 4–9, 2015.
- T. Poux, J.L. Gómez-Cámer,  
D. Cericola, T. Hucke, M.E. Spahr,  
P. Novák  
*Increasing the life time of Si/C composite electrodes for lithium-ion batteries*  
16<sup>th</sup> Topical ISE Meeting – Electrochemical Properties and Applications of Advanced Carbon Materials, Angra dos Reis, Brazil, March 22–26, 2015.
- D. Streich, P. Novák, M. El Kazzi  
*Complementary operando XPS and Raman spectroscopy of graphite cycled in ionic liquids*  
66<sup>th</sup> ISE Annual Meeting, Taipei, Taiwan, October 4–9, 2015.
- D. Streich, P. Novák, M. El Kazzi  
*Complementary operando investigations of graphite cycled in ionic liquids by XPS and Raman spectroscopy*  
228<sup>th</sup> ECS Meeting, Phoenix, AZ, USA, October 11–15, 2015.
- M. Suermann, T.J. Schmidt,  
F.N. Büchi  
*Experimental investigation of the influence of pressure on the performance of polymer electrolyte water electrolysis cells*  
ECS Conference on Electrochemical Energy Conversion & Storage with SOFC-XIV,  
Glasgow, UK, July 26–31, 2015.
- S.M. Taylor, A. Pătru, T.J. Schmidt  
*Oxygen Functionalised Carbon Surfaces – a Suitable Electrode Material for Vanadium (V) Reduction in Redox Flow Cell Applications*  
ECS Conference on Electrochemical Energy Conversion & Storage with SOFC-XIV,  
Glasgow, UK, July 26–31, 2015.
- S.E. Temmel, E. Fabbri, R. Kötz,  
D. Pergolesi, T. Lippert,  
T.J. Schmidt  
*Study of Pt electrocatalysts for the oxygen reduction reaction fabricated by pulsed laser deposition*  
European Fuel Cell Forum, Luzern, July 5–8, 2015.
- S.E. Temmel, E. Fabbri,  
D. Pergolesi, T. Lippert,  
T.J. Schmidt  
*Investigation of ORR activity of strained thin film Pt electrocatalyst produced by pulsed laser deposition*  
66<sup>th</sup> ISE Annual Meeting, Taipei, Taiwan, October 4–9, 2015.

## Patent Applications

- L. Gubler, O. Nibel, L. Bonorand *Electrolyte membrane with selective ion transport properties and a redox flow battery comprising an electrolyte membrane*  
Patent Application No. EP 2015P01713, 2015.
- A. Tezel, P. Novák, S. Sunde, A.M. Svensson *Pre-forming of primarily organic coating in THIFPB or PF5 containing electrolyte*  
Patent Application No. GB1517429.5, 2015.

## Posters

- A. Albert, T.J. Schmidt, L. Gubler *Stability of radiation grafted polymer electrolyte membranes for water electrolysis cells*  
SCS Fall Meeting, Lausanne, Switzerland, September 4, 2015.  
Best Poster Prize Winner
- E.J. Berg, M. He, E. Castel, A. Laumann, G. Nuspl, P. Novák *In situ gas analysis of  $\text{Li}_4\text{Ti}_5\text{O}_{12}$  based electrodes at elevated temperatures*  
8<sup>th</sup> International Conference on Advanced Lithium Batteries for Automobile Applications, Bilbao, Spain, September 30, 2015.
- E.J. Berg, M. He, K. Fic, E. Frąckowiak, P. Novák *Reactions on conductive carbons in non-aqueous carbonate electrolytes*  
6<sup>th</sup> International Conference on Carbon for Energy Storage/Conversion and Environment Protection, Poznan, Poland, October 18–22, 2015.
- J. Billaud, S. Sallard, P. Novák, C. Villevieille *Modified high energy lithium nickel-cobalt-manganese oxides (HE NCM) as cathodes for lithium-ion batteries*  
8<sup>th</sup> International Conference on Advanced Lithium Batteries for Automobile Applications, Bilbao, Spain, September 30, 2015.
- L. Boulet-Roblin, P. Borel, D. Sheptiakov, C. Tessier, P. Novák, C. Villevieille *Operando neutron powder diffraction of  $\text{LiNi}_{0.5}\text{Mn}_{1.5}\text{O}_4$  vs. graphite performed in a cylindrical cell*  
LiBD 7 – 7<sup>th</sup> Lithium Battery Discussion – Electrode Materials, Arcachon, France, June 21–26, 2015.
- X. Cheng, E. Fabbri, R. Haumont, T.J. Schmidt *Oxygen evolution reaction: correlation between electronic property and OER activity for  $\text{La}_{1-x}\text{Sr}_x\text{CoO}_3$  ( $0 \leq x \leq 1$ ) perovskite oxides*  
SCCER Heat and Electricity Storage – 2<sup>nd</sup> Symposium Paul Scherrer Institut, Villigen, May 5, 2015 and  
31<sup>st</sup> PSI Electrochemistry Symposium Electrochemical Energy Storage: A Key for Future Energy Systems Paul Scherrer Institut, Villigen, May 6, 2015.
- X. Cheng, E. Fabbri, M. Nachtegaal, I.E. Castelli, M. El Kazzi, R. Haumont, N. Marzari, T.J. Schmidt *Oxygen evolution reaction: correlation between electronic property and OER activity for  $\text{La}_{1-x}\text{Sr}_x\text{CoO}_3$  ( $0 \leq x \leq 1$ ) perovskite oxides*  
MARVEL review and retreat, Lausanne EPFL, September 3–4, 2015.  
Poster award 2<sup>nd</sup> prize.
- M. Cochet, A. Forner-Cuenca, D. Scheuble, J. Biesdorf, P. Boillat *Neutron imaging characterization of water and heat transport in an evaporative cooled fuel cell*  
2<sup>nd</sup> SCCER Mobility Annual Conference, Zürich, Switzerland, August 26–27, 2015.
- J. Conder, L. Gubler, P. Novák, S. Urbonaite *Taming the polysulfide shuttle in Li-S battery*  
7<sup>th</sup> Lithium Battery Discussion (LiBD 7)– Electrode Materials, Arcachon, France, June 21–26, 2015.

- G. Ferraresi, L. Czornomaz,  
P. Novák, C. Villevieille, M. El Kazzi  
*Surface investigation of n-doped Si thin films as anodes for Li-ion batteries*  
8<sup>th</sup> International Conference on Advanced Lithium Batteries for Automobile Applications, Bilbao, Spain, September 30, 2015.
- A. Forner-Cuenca, P. Gröninger,  
J. Biesdorf, L. Gubler, T. J. Schmidt,  
P. Boillat  
*Measuring the internal contact angle of gas diffusion layers,*  
6<sup>th</sup> International Conference on Development and Fundamentals of Fuel Cells, Toulouse, France, February 3–5, 2015.
- M. Geormezi, T.J. Schmidt,  
L. Gubler  
*Electrochemical characterization of catalyst-coated radiation grafted membranes under different LT-PEFC operating conditions*  
6<sup>th</sup> International Conference on Fundamentals and Development of Fuel Cells, Toulouse, France, February 3–5, 2015.  
Best Poster Prize Winner
- A. Guéguen, E.J. Berg, P. Novák  
*Dynamics of the porous carbonaceous O<sub>2</sub> electrode interface: a combined XPS and OEMS study,*  
LiBD 7 – 7<sup>th</sup> Lithium Battery Discussion - Electrode Materials, Arcachon, France, June 21–26, 2015.
- M. He, E. Castel, A. Laumann,  
G. Nuspl, P. Novák, E.J. Berg  
*In situ gas analysis of Li<sub>4</sub>Ti<sub>5</sub>O<sub>12</sub> based electrodes at elevated temperatures*  
LiBD 7 – 7<sup>th</sup> Lithium Battery Discussion – Electrode Materials, Arcachon, France, June 21–26, 2015.
- M. Hess, P. Novák, V. Wood  
*Challenges in determining the rate capability of battery materials*  
LiBD 7 – 7<sup>th</sup> Lithium Battery Discussion – Electrode Materials, Arcachon, France, June 21–26, 2015.
- A. Lamibrac, F. Marone, F.N. Büchi  
*Characterization of liquid water invasion in GDLs using X-ray Tomographic Microscopy*  
ModVal 12, Freiburg-Munzingen, Germany, March 26–27, 2015.
- G. Nagy, V. Sproll, U. Gasser,  
M. Obiols-Rabasa, S. Gustavsson,  
S. Balog, L. Gubler  
*Correlation between nano-structure and performance-related properties of radiation-grafted proton-conducting membranes*  
16<sup>th</sup> Swiss Soft Days, Villigen PSI, Switzerland, May 4, 2015.
- O. Nibel, T.J. Schmidt, L. Gubler  
*Ion conducting membranes for the vanadium redox flow battery (VRB) with improved barrier properties*  
Asilomar Conference on Advances in Polymers for Fuel Cells and Energy Devices, Pacific Grove CA, USA, February 8–11, 2015.
- P. Novák, M. Hess, C. Villevieille  
*Graphite revisited: new insights into lithium intercalation*  
18<sup>th</sup> International Symposium on Intercalation Compounds ISIC18, Strasbourg, France, June 1–4, 2015.
- V. Orava, O. Souček, P. Čendula,  
J. Schumacher, L. Gubler  
*Multi-phase modeling of a hydrogen generator coupled to a PEM fuel cell*  
12<sup>th</sup> Symposium on Fuel Cell and Battery Modelling and Experimental Validation (ModVal 12), Freiburg, Germany, March 26–27, 2015.
- H.J. Peng, S. Urbonaite,  
C. Villevieille, H. Wolf, K. Leitner,  
P. Novák  
*Cycling-related electrolyte (de-)composition in an EC/EMC based battery system.*  
LiBD 7 – 7<sup>th</sup> Lithium Battery Discussion – Electrode Materials, Arcachon, France, June 21–26, 2015.
- M. Reichardt, C. Villevieille,  
P. Novák, S. Sallard  
*Lithium chromium phosphate Li<sub>3</sub>Cr<sub>2</sub>(PO<sub>4</sub>)<sub>3</sub> as cathode material for Li-ion batteries*  
LiBD 7 – 7<sup>th</sup> Lithium Battery Discussion – Electrode Materials, Arcachon, France, June 21–26, 2015.
- T. Rojek, T.J. Schmidt, L. Gubler  
*Radiation grafted membranes for high-temperature polymer electrolyte fuel cells*  
Workshop on Ion Exchange Membranes for Energy Applications – EMEA 2015, Bad Zwischenhahn, Germany, June 22–24, 2015.

- S. Sallard, S. Schmidt,  
D. Sheptyakov, P. Novák,  
C. Villevieille *Lithium iron methylene diphosphonate, a new organic-inorganic hybrid material for Li-ion batteries*  
66<sup>th</sup> ISE Annual Meeting, Taipei, Taiwan, October 4–9, 2015.
- S. Schmidt, D. Sheptyakov,  
C. Villevieille, P. Novák, S. Sallard *Lithium iron methylene diphosphonate, a new organic-inorganic hybrid material for Li-ion batteries*  
LiBD 7 – 7<sup>th</sup> Lithium Battery Discussion – Electrode Materials, Arcachon, France, June 21–26, 2015.
- J. Seweryn, J. Biesdorf,  
T.J. Schmidt, P. Boillat *Neutron Radiography of PEM Water Electrolysis Cells,*  
ECS Conference on Electrochemical Conversion and Storage, Glasgow, Scotland, July 26–31, 2015.
- V. Sproll, U. Gasser, G. Nagy,  
S. Balog, T.J. Schmidt, L. Gubler *Grafting design: a way to the optimized proton exchange membrane?*  
13<sup>th</sup> Tihany Symposium on Radiation Chemistry, Balatonalmádi, Hungary, August 29 – September 3, 2015.
- S.M. Taylor, A. Pătru, T.J. Schmidt *Influence of carbon surface modification on vanadium (V) reduction for redox flow cell applications*  
ECS Conference on Electrochemical Energy Conversion & Storage with SOFC-XIV, Glasgow, UK, July 26–31, 2015.  
Best Poster Prize Winner
- S. Urbonaite, P. Novák *Search for perfect carbonaceous sulphur hosts for Li-S batteries*  
66<sup>th</sup> ISE Annual Meeting, Taipei, Taiwan, October 4–9, 2015.
- L.O. Vogt, M. El Kazzi, E.J. Berg,  
C. Marino, P. Novák, C. Villevieille *Understanding the interaction of the carbonates and binder in Na-ion batteries: a combined bulk and surface study*  
Congrès 2015 de la Société Chimique de France, Lille, France, July 4–9, 2015.

## Conferences & Workshops Organizations

- F.N. Büchi, T.J. Schmidt *15<sup>th</sup> Symposium on Polymer Electrolyte Fuel Cells PEFC 15*  
228<sup>th</sup> ECS Meeting, Phoenix, AZ, USA, October 11–15, 2015.  
Members of organizing committee
- L. Gubler *Symposium 4: Advances in Fuel Cells from Materials to Systems*  
66<sup>th</sup> ISE Annual Meeting, Taipei, Taiwan, October 4–9, 2015.  
Member of organizing committee
- J. Herranz, T.J. Schmidt *Symposium Low-Temperature Fuel Cells, Electrolyzers, and Redox Flow Cells*  
ECS Conference on Electrochemical Energy Conversion & Storage with SOFC-XIV, Glasgow, UK, July 26–31, 2015.  
Members of organizing committee
- T.J. Schmidt *31<sup>st</sup> PSI Electrochemistry Symposium: Electrochemical Energy Storage – A Key for Future Energy Systems*  
Paul Scherrer Institut, Villigen, May 6, 2015.

## Members in external committees

L. Gubler	<i>DTU Energy, Denmark</i> Selection Committee for the Position of Research Scientist
P. Novák	<i>Int. Meetings on Lithium Batteries LLC</i> Director
P. Novák	<i>CIC Energigune, Vitoria, Spain</i> Scientific Committee
T.J. Schmidt	<i>HySA/Catalysis, University of Cape Town, Cape Town, South Africa</i> Technical Steering Committee
T.J. Schmidt	<i>4M Centre – Mechanisms, Materials, Manufacturing and Management – Interdisciplinary Fundamental Research to Promote commercialization of HT-PEMFC, Technical University of Denmark, Lyngby, Denmark</i> Technical Steering Committee
T.J. Schmidt	<i>Competence Center Energy &amp; Mobility Switzerland</i> Steering Board
T.J. Schmidt	<i>The Electrochemical Society</i> Individual Membership Committee
T.J. Schmidt	<i>Federal Energy Research Commission (CORE), Switzerland</i> Member Working Group
T.J. Schmidt	<i>Swiss Hydrogen SA, Fribourg</i> Board of Directors
T.J. Schmidt	<i>European Academy of Sciences Advisory Council</i> Working Group Member Dedicated Energy Storage,
S. Trabesinger	<i>The Research Council of Norway (RCN)</i> Member of Peer Review Panel / Expert Evaluator
S. Trabesinger	<i>Qatar National Research Fund (QNRF)</i> Expert Evaluator
S. Trabesinger	<i>European Commission</i> Member of Peer Review Panel/Expert Evaluator

## Editorial Work

H.A. Gasteiger, A.Z. Weber,  
V.K. Ramani, T.F. Fuller,  
R.A. Mantz, H. Uchida,  
F.N. Büchi, M. Edmundson,  
C. Coutanceau, J.M. Fenton,  
S. Mitsushima, T.J. Schmidt,  
K. Shinohara, K. Swider-Lyons,  
D.J. Jones, B.S. Pivovar,  
K.E. Ayers, K.A. Perry,  
S.R. Narayanan, P. Strasser

*Polymer Electrolyte Fuel Cells 15*  
ECS Transactions **69** (17), The Electrochemical Society, Pennington, NJ,  
ISBN 978-1-62332-183-3 (2015).

C. Gloor, L. Gubler,  
T.J. Schmidt

*PSI Electrochemistry Laboratory Annual Report 2014*  
doi: 10.3929/ethz-a-007047464, ISSN 1661-5379

L. Gubler

*Electrochimica Acta*  
Guest Editor, Special Issue, 66<sup>th</sup> ISE Annual Meeting, Taipei, Taiwan, October 4–9, 2015.

T.J. Schmidt

*Journal of the Electrochemical Society / ECS Electrochemistry Letters*  
Associate Editor

T.J. Schmidt, J. Roth

*Energy Storage Research in Switzerland*  
The Swiss Competence Center for Energy Research Heat & Electricity Storage, Guest  
Editors *Chimia* **12** (2015).



